Molecular insights into the complex formed by the actin cytoskeleton related protein VASP and the inhibitory postsynaptic scaffolding protein gephyrin

Molekulare Einblicke in den Komplex, der durch das mit dem Aktin-Zytoskelett verwandte Protein VASP und Gephyrin, einem Gerüstprotein inhibitorischer postsynaptischer Strukturen, gebildet wird

Doctoral thesis for a doctoral degree
at the Graduate School of Life Sciences,
Julius-Maximilians-Universität Würzburg,
Section Biomedicine

submitted by

Anabel Pacios Michelena

from

Havana, Cuba

Würzburg 2020

Submitted on: ……………………………………………

Office stamp

Members of the Thesis Committee

Chairperson: Prof. Dr. Manfred Gessler

Primary Supervisor: Prof. Dr. Hermann Schindelin

Supervisor (Second): Prof. Dr. Carmen Villmann

Supervisor (Third): Dr. Sonja Lorenz

Date of Public Defense: ……………………………………………

Date of Receipt of Certificates: ……………………………………………

To my parents and my sister,
hope the distance has been worth it.

"Discovery consists of seeing what everybody has seen and thinking what nobody has thought."

— Albert von Szent-Györgyi, Nobel Prize in Physiology and Medicine 1937

Acknowledgements

I would like to express my immense gratitude to many people who supported me and encouraged me during this eventful journey towards the completion of my Ph.D.

First of all, I would like to highly thanks the GSLS for giving me this unique opportunity to study abroad and to accomplish one of my dreams of obtaining a Ph.D., a personal challenge I was dreaming off as a scientist. Not in doubt, the GSLS is a great organization because of its people to whom I am really grateful, the Dean Caroline Kisker, who I owe a special thanks also because of all the insights and fruitful suggestions in the lab; besides, to Felizitas, Katrin, Jenni, Sebastian Michael, Franz-Xaver, Stephan Schröder-Köhne, and, especially, Gabi for your support and guidance, particularly in the initial phase.

A special thanks to my first supervisor, Hermann Schindelin, who has been my mentor through all these years. Thank you for trusting in me and my motivation for science and for welcoming me to conduct this project. Thanks for your guidance, your fundamental questions that encourage me to analyze my data beyond the superficial facts, always challenging me to become a better scientist.

A great thanks to my second supervisor, Carmen Villmann, who opened up a new perspective to me, the exciting field of neurobiology, from whom I have learned a lot and who has supported my project in many ways. Thanks for welcoming me to your lab and allowing me to improve myself in the area of cellular biology, which I find fascinating.

To Sonja Lorenz, my third supervisor, thanks for accepting to be part of my supervisory Committee and to have always encouraging words for me.

To Vikram Kasaragod, who helped me to have a smooth initiation into the amazing world of gephyrin and for sharing with me some exciting projects.

To Hans Maric, who has acted as a supervisor to me and my project, always bringing factual thoughts and confidence with him.

Many thanks to Robert Blum for all he has taught me about viruses and gene silencing technology. Open discussions about how best to proceed are always welcome. Thank you very much for allowing me to work in your lab as one of your group.

To Bodo Sander for delivering in me all his expertise regarding the topic gephyrin, and always being there giving advice and ideas to follow in my project.

To Bettina Böttcher's group, especially Sam and Cihan who taught me the little I know of this passionate world of cryo-EM.

To Dan, who guided me through the process of particle reconstruction and software handling.

To the Strubis, as we name ourselves, for being such an amazing group of scientists and friends.

To Nicole Bader and Monika Kuhn for all your support and handling in the lab, to Bernhard Fröhlich and Roland Markert for all your IT-support, and Andrea Heinzmann and Teresa Frank for your diligence and help with the German administrative staff.

Special thanks to Theresa Klemm, who has become a friend through all these years, thanks for holding me up in my worst moments and encouraging me to continue. Thanks to your family and especially Conni, who accepted us as part of yours.

Thanks to my friends, who are my second family. Special thanks to Erick Miranda, who guided us through this unforeseeable process of adaptation to a completely different world, for becoming a real friend, and for sharing with me not only advice as a friend but also as a scientist.

Thanks to my family, who accepted my decision, despite knowing the sadness of being apart. And last but not least, a great thanks to my husband Ernesto, who unconditionally followed me on this journey with the only aim of wishing that my dreams come true. Thanks for always being there, as the cliché says: "through thick and thin, braving all storms" and for supporting me in your special way of having clever discussions about proteins and purifications even when it is far away from your programming passion.

SUMMARY

Gephyrin is a 93 kDa moonlighting protein, which is involved in the last two steps of the molybdenum cofactor (Moco) biosynthesis pathway while at the same time playing a central role in the anchoring, clustering and stabilization of glycine receptors (GlyRs) and γ-aminobutyric acid type A receptors ($GABA_A$Rs) at inhibitory synapses in the mammalian central nervous system (CNS). It is composed of two structured domains located at either end, the N-terminal G domain which trimerizes and the C-terminal E domain which dimerizes. Both domains are linked through an unfolded region of ~150 amino acids referred to as the linker region. While the G and E domains have been structurally characterized, the full-length protein could not be crystallized, presumably due to its long unstructured linker. Therefore, the full-length protein has been molecularly characterized *via* a combination of small-angle X-ray scattering (SAXS) and atomic force microscopy (AFM), showing that in solution, gephyrin is a conformationally flexible protein, which is present in different states including compact, as well as partially and full extended molecules. The protein is predominantly trimeric, mediated by the trimerization interface present in the G domain, while dimerization through its E domain is suppressed due to unknown reasons. Despite the previous SAXS and AFM studies, a high-resolution structure of the full-length protein is needed to better understand its function, in particular, how the formation of higher order oligomers in a synaptic context is regulated. In the context of this thesis, I am presenting the first attempt to determine the structure of the full-length gephyrin by cryo-electron microscopy (cryo-EM).

To obtain such a structure of gephyrin, the protein was heterologously expressed in *E. coli* and purified by different chromatographic techniques. The purified protein was subjected to the GraFix procedure to decrease conformational heterogeneity in the sample with the goal of facilitating data analysis. Consequently, the protein was subjected to ultracentrifugation in a continuous sucrose gradient in the presence of the crosslinker glutaraldehyde. After analyzing the fractions by SDS-polyacrylamide gel electrophoresis and negative stain visualization with a 120 kV Tecnai transmission electron microscope (TEM), data were recorded for selected fractions with a 300 kV Titan Krios TEM. The data were analyzed using the Relion 3.0 software and a preliminary model with a low resolution of 16 Å resolution was obtained. The resulting density map, which is clearly asymmetric, could be interpreted with one centrally located G-domain trimer and one E dimer linked. Additional density features may correspond to the third E-domain and the linker regions. To achieve higher resolution some strategies were initiated, such as the heterologous expression of gephyrin in insect cells. Despite the limited resolution, the data presented here are promising and set the stage for the future elucidation of a high resolution cryo-EM structure of full-length gephyrin.

Gephyrin was shown to be a mammalian target of the anti-malarial drugs artemisinins. This targeting affects its inhibitory postsynaptic anchoring function, since the drug binds to the universal receptor-binding pocket in gephyrin. Meanwhile, another mammalian target was identified, namely the enzyme pyridoxal kinase (PDXK). This enzyme is responsible for the synthesis of pyridoxal 5'-phosphate (PLP), which is the active form of vitamin B6, a fundamental cofactor in a wide range of metabolic pathways. PLP-dependent enzymes are also involved in the biosynthesis of various neurotransmitters, *e.g.* GABA by glutamic acid decarboxylase (GAD). Thus, inhibition of PDXK by artemisinins has the potential to affect inhibitory neurotransmission also via the presynaptic side. In the context of this thesis, I am going to present enzymatic data that describe the inhibition of PDXK by artemisinins. Two artemisinins, the parental compound artemisinin and the succinic acid derivative artesunate were shown to be competitive inhibitors characterized with K_i-values of 120 ± 2 μM and 1250 ± 5 μM, respectively.

Gephyrin ensures the accurate accumulation of neurotransmitter receptors in precise apposition to presynaptic neurotransmitter release sites, as this is required for efficient synaptic transmission. To accomplish this task gephyrin interacts intracellularly with cytoskeletal anchoring elements to provide a physical platform for maintaining receptors at synapses. Among the interaction partners of gephyrin are members of the enabled/vasodilator-stimulated phosphoprotein (Ena/VASP) family.

The Ena/VASP family in vertebrates is composed of three members: the mammalian enabled protein (Mena), mostly present in the CNS, the ena/VASP-like protein (Evl) and VASP. This family shares a tripartite structural organization consisting of highly homologous N-terminal and C-terminal parts (Ena-VASP homology domains 1 and 2, EVH1 and EVH2) that are separated by a central proline-rich region. Ena/VASP family members play a wide variety of functions regulating actin-related processes, such as epithelial cell adhesion, cell polarity, cell motility, axon outgrowth and guidance, neuritogenesis, as well as spine and synapse formation. Two studies described a direct binding between gephyrin and Mena/VASP. In an earlier study published in 2003, the *in vitro* interaction of Mena/VASP with gephyrin was analyzed identifying the E domain as being responsible for this interaction. However, three years later another study concluded that the VASP-binding site is present within the gephyrin linker. While there is an obvious controversy regarding the location of the VASP-binding site in gephyrin, the gephyrin-binding site in VASP had not been characterized previously.

In this thesis, I am presenting biochemical and *in cellulo* data confirming the direct interaction of the two proteins and, more importantly, mapping the specific interaction sites. Using analytical size exclusion (aSEC), native agarose gel (NAGE) and microscale thermophoresis (MST), the VASP-binding in gephyrin was mapped to the N-terminal part of its central linker, specifically residues P201-V255. At the same time, using the same techniques as well as cell-based assays, the gephyrin-binding site in VASP was localized to the very N-terminal part of the proline-rich region, specifically to residues P125-Q144. This stretch is highly conserved amongst the Mena/VASP proteins, particularly the acidic residues E136 and E137 and the basic residues K142 and R143. In colocalization experiments in HEK293 and COS-7 cells, I could demonstrate that mutating the acidic residues to alanine in the E136A/E137A double mutant significantly impaired complex formation, while binding of the (K142A/R143A) double mutant to gephyrin was not perturbed. This result was corroborated by co-immunoprecipitation experiments and MST measurements, hence residues E136 and E137 within the region P125-Q144 of Mena/VASP are critical for the gephyrin-VASP interaction. In addition, complex formation was thermodynamically characterized by MST revealing that this interaction is endothermic but entropically favored and is spontaneous only at temperatures $T > \Delta \boldsymbol{H}/\Delta \boldsymbol{S}$, exhibiting a high affinity reflected in a dissociation constant of 1 μM at physiological temperatures. Moreover, in cultured hippocampal and cortical neurons, VASP/Mena colocalizes with gephyrin at inhibitory postsynaptic sites.

The biological relevance of this interaction is currently investigated in shRNA-based Mena/VASP knockdown experiments in cultured hippocampal neurons in which gephyrin-$GABA_AR$ clustering and miniature inhibitory postsynaptic currents (mIPSCs) will be analyzed in the knock-down situation as well as in rescue experiments with Mena/VASP variants which are impaired in gephyrin binding. Hence, the work presented in this dissertation characterizes the Mena/VASP-gephyrin interaction in great detail and lays the groundwork to investigate the physiological consequences of this interaction.

ZUSAMENFASSUNG

Gephyrin ist ein multifunktionales 93 kDa-Protein. Dieses Protein katalysiert die letzten beiden Schritte des Biosynthesewegs des Molybdän-Cofaktors (Moco). Gleichzeitig spielt es eine zentrale Rolle bei der Verankerung, Clusterbildung und Stabilisierung sowohl von Glycinrezeptoren (GlyRs) als auch von γ-Aminobuttersäure-Typ-A-Rezeptoren ($GABA_A$Rs) die in inhibitorischen Synapsen im Zentralnervensystem (ZNS) von Säugetieren lokalisiert sind. Gephyrin aus zwei strukturierten Domänen, die sich an den Enden des Proteins befinden. Dabei bildet die N-terminale G-Domäne ein Trimer aus, und die C-terminale E-Domäne ein Dimer. Beide Domänen sind durch eine unstrukturierte Region von ca. 150 Aminosäuren verknüpft, die als Verknüpfung (*engl.* linker*)* bezeichnet wird. Während die G- und E-Domänen strukturell charakterisiert sind, konnte das Holo-Protein, vermutlich aufgrund seiner langen unstrukturierten Region noch nicht kristallisiert werden. Daher wurde das Protein durch eine Kombination aus Röntgenkleinwinkelbeuung (*engl.* small angle X-ray scattering, SAXS) und Rasterkraftmikroskopie (*engl.* atomic force microscopy, AFM) charakterisiert. Diese Experimente zeigten, dass Gephyrin in Lösung sowohl kompakte als auch extendierte Konformationen einnimmt. Dabei liegt es als Trimer vor, in dem die Trimerisierungsschnittstelle der G-Domäne erhalten bleibt, wohingegen die Dimerisierung der E-Domäne durch einen bisher unverstandenen Mechanismus unterdrückt wird. Aufgrund der limitierten Auflösung der SAXS und AFM Methoden, steht eine hochauflösende Struktur des nativen Proteins weiter aus, die es erlauben würde, das Protein endgültig auf molekularer Ebene zu charakterisieren. In dieser Arbeit stelle ich einen ersten Versuch vor, die Struktur von Gephyrin mittels Kryo-Elektromikroskopie (Kryo-EM) zu bestimmen.

Um die Kryo-EM-Struktur von Gephyrin zu erhalten, wurde es heterolog in *E. coli* exprimiert und mittels chromatographischer Methoden aufgereinigt. Das gereinigte Protein wurde der GraFix-Methode unterzogen, um eine Homogenität der Probe für die Datensammlung zu erreichen. Das bedeutet, dass das Protein während konstanter Ultrazentrifugation in Gegenwart des Vernetzers Glutaraldehyd einen linearen Saccharosegradienten durchlief. Nach Analyse der Fraktionen mittels SDS-PAGE und Negativkontrastierung wurde die Probe in einem 120-kV-Tecnai-Transmissionselektromikroskop (TEM) vorläufig charakterisiert. Nachfolgend wurden Daten ausgewählter Fraktionen in einem 300-kV-Titan-Krios-TEM aufgenommen. Die gesammelten Daten wurden mit der Relion 3.0-Software analysiert. Als Ergebnis erhielt man eine 3D-Dichtekarte mit einer nach wie vor limitierten Auflösung von 16 Å. Diese Karte zeigt ein asymmetrisches Partikel, das mit einem zentralen Trimer der G-Domäne und einem Dimer der E-Domäne interpretiert wurde. Darüber hinaus existierten zusätzliche Region in der Dichtekarte, die eventuell von der fehlenden dritten E-Domäne oder den drei Verknüpfungen hervorgerufen wurden. Allerdings können aufgrund der begrenzten

Auflösung diesbezüglich keine eindeutigen Aussagen getroffen werden. Um die Auflösung zu verbessern, wurden alternative Strategien initiiert, wie beispielsweise die heterologe Expression von Gephyrin in Insektenzellen, die potentiell die Homogenität der Probe verbessern. Die bisher präsentierten Daten sind vielversprechend und legen einen Grundstein für die zukünftige Aufklärung der Kryo-EM-Struktur von Gephyrin.

Es wurde unlängst gezeigt, dass Artemisinine, die momentan die erfolgreichsten Pharmazeutika zur Behandlung von Malaria sind, an das Gephyrinprotein des Wirts binden. Diese Wechselwirkung beeinflusst die inhibitorische postsynaptische Funktion, da das Medikament an die universelle Rezeptorbindungstasche von Gephyrin bindet. In der Gleichzeitig wurde ein weiteres Zielprotein im menschlichen Wirt entdeckt, das Enzym Pyridoxalkinase (PDXK). Dieses Enzym ist für die Synthese des Pyridoxal-5'-Phosphats (PLP) verantwortlich, der aktiven Form von Vitamin B6 ist, einem essentiellen Kofaktor in einer Vielzahl von biochemischen Prozessen. Dazu gehört auch die Biosynthese verschiedenster Neurotransmitter, u.a. GABA durch das PLP-abhängige Enzym Glutaminsäure-Decarboxylase (GAD). Somit kann eine Artemisinin-induzierte Inhibition dieses Enzyms die inhibitorischen Neurotransmission auch via die präsynaptische Seite beeinflussen. Im Rahmen dieser Arbeit, werde ich enzykinetische Charakterisierung des GAD-Enzyms sowie Inhibitionsstudien mit zwei Artemisininen, der parentalen Verbindung Artemisinin und dem Succinsäureesterderivat Artesunat, vorstellen. Die PDXK-Inhibition ist durch Inhibitionskonstanten (K_i) von 120 ± 2 µM bzw. 1250 ± 5 µM charakterisiert.

Die Verankerung inhibitorischer Neurotransmitterrezeptoren durch Gephyrin wird durch weitere Wechselwirkungen mit Elementen des Zytoskeletts, die Gephyrin ebenfalls eingehen kann, gewährleistet. Auf diese Weise ermöglicht Gephyrin eine genaue Akkumulation von Neurotransmitterrezeptoren in präziser Apposition zu den präsynaptischen Neurotransmitter-Freisetzungsstellen, was wiederum für eine effiziente synaptische Signalübertragung erforderlich ist. Unter den Elementen des Zytoskeletts, die durch ihre Interaktion mit Gephyrin diese Verankerungsfunktion vermitteln, sind u.a. Proteine der enabled/vasodilator stimulated phosphoprotein (Ena/VASP) Familie. In Wirbeltieren besteht die Ena/VASP-Familie aus drei Mitgliedern: dem enabled Protein aus Säugetieren (*engl.* mammalian enabled protein, Mena), das hauptsächlich im ZNS vorkommt, dem Ena/VASP-ähnlichen Protein (*engl.* ena/VASP-like protein) (Evl) und VASP. Die Mitglieder der Familie teilen eine dreigliedrige Strukturorganisation, die zwei hochhomologe N-terminale und C-terminale Regionen (Ena-VASP-Homologiedomänen 1 und 2 (EVH1 und EVH2)) beinhalten, sowie einen zentralen Prolin-reichen Bereich. Mitglieder der Ena/VASP-Familie weisen eine Vielzahl von Funktionen auf die Aktin-vermittelte Prozesse regulieren, wie z. B. Epithelzelladhäsion, Zellpolarität, Zellmotilität, Axonenwachstum und axonale Führung, Neuritogenese sowie Rückenmarkbildung und Synapsenbildung. In der Literatur existieren zwei Studien, die die direkte Bindung zwischen Gephyrin und Mena/VASP beschreiben. Im Jahr 2003 wurde die Wechselwirkung von Mena/VASP mit Gephyrin *in vitro* beschrieben, wobei die E-Domäne von Gephyrin als die die Wechselwirkung vermittelnde Region identifiziert wurde. Drei Jahre später kamen eine andere Studie jedoch zu dem Schluss, dass sich die VASP-Bindungsstelle stattdessen innerhalb der Gephyrin-Linker-Region befindet. Somit ist die Lokalisation der VASP-Bindungsstelle in Gephyrin bisher nicht eindeutig geklärt, und zudem wurde die Gephyrin-Bindungsregion in VASP noch nicht identifiziert.

In dieser Arbeit präsentiere ich biochemische und zellbiologische Daten, die eine direkte Wechselwirkung beider Proteine demonstrieren und die spezifischen Interaktionsstellen kartieren. Unter Verwendung von analytischer Größenausschlusschromatographie (*engl.* analytical size exclusion chromatography, aSEC), nativen Agarosegelen (*engl.* native agarose gel electrophoresis, NAGE) und Thermophorese im Mikromaßstab (*engl.* Microscale thermophoresis, MST) wurde die VASP-Bindungsstelle in Gephyrin auf den Bereich zwischen den Resten P201-V255 eingegrenzt. Unter Einbeziehung dieser Techniken und der Verwendung von Säugetierzellen wurde die Gephyrin-Bindungsstelle in VASP im N-terminalen Bereich der prolinreichen Region lokalisiert, konkret auf die Reste P125-Q144. Dieser Bereich ist innerhalb der Mena/VASP-Proteine hoch konserviert, u.a. sind die sauren Resten E136 und E137 sowie die basischen Resten K142 und R143 nahezu invariant. In Kolokalisationsexperimenten in HEK293- und COS-7-Zellen konnte ich zeigen, dass diese Wechselwirkung durch Mutationen der sauren Reste zu Alanin in der Doppelmutante E136A/E137A deutlich geschwächt wird, die Bindung der basischen Doppelmutante (K142A/R143A) an Gephyrin jedoch nicht beeinflusst wurde. Dieses Ergebnis wurde durch Co-Immunpräzipitationsexperimente und MST-Messungen bestätigt. Zusammenfassend lässt sich sagen, dass die Region P125-Q144 von entscheidender Bedeutung für die Wechselwirkung mit Gephyrin ist und innerhalb dieses Bereichs die Reste E136 und E137 eine wichtige Rolle spielen. Außerdem wurde die *in vitro* Komplexbildung durch MST thermodynamisch charakterisiert. Die Bindung zwischen VASP und Gephyrin ist ein endothermer Prozess der spontan bei $T > \Delta \boldsymbol{H} / \Delta \boldsymbol{S}$ abläuft und durch eine relative hohe Affinität mit einer Dissoziationskonstant von ca. 1 µM bei einer Temperatur im physiologischen Bereich. Darüber hinaus kolokalisieren VASP/Mena in kultivierten hippocampalen und kortikalen Neuronen an inhibitorischen postsynaptischen Kontakten mit Gephyrin.

Die biologische Relevanz dieses Komplexes wird in laufenden Experimenten unter Verwendung von shRNAs untersucht, welche die Expression von Mena/VASP in kultivierten hippocampalen Neuronen unterbindet. Außerdem werden die Auswirkungen dieser Unterbindung auf die Gephyrin/$GABA_AR$-Cluster und auf die Miniatur-inhibitorischen postsynaptischen Ströme (*engl.* miniature inhibitory postysynaptic currents, mIPSCs) getestet. Zusammenfassend lässt sich sagen, dass die in dieser Dissertation vorgestellten Experimente unser Verständnis für die Wechselwirkung zwischen Mitgliedern der Mena/VASP Familie und Gephyrin *in vitro* und in zellbasierten Experimenten umfangreich charakterisiert und die Grundlagen legt, um die physiologische Bedeutung dieser Interaktion für die Architektur postsynaptischer zu analysieren.

Index

I Introduction

I.1 Synapses

Synapses constitute the essential information-processing units of neural circuits, thus conferring the basis of all brain functions. A synapse can be either electrical or chemical, depending on the kind of signal being transmitted[1]. In a chemical synapse, the electrical signal generated via the activation of voltage-gated calcium channels in the presynaptic neuron, is converted into a chemical signal, the release of specific neurotransmitters which interact with selected receptors located in the plasma membrane of the postsynaptic cell[1]. Once the neurotransmitter is released, it initiates an electrical response, also known as a secondary messenger pathway, that may either excite or inhibit the postsynaptic neuron. Chemical synapses can be classified according to the neurotransmitter released into glutamatergic (excitatory), GABAergic (inhibitory), cholinergic (vertebrate neuromuscular junction) as well as dopaminergic (releasing dopamine) and adrenergic (releasing norepinephrine)[1]. Due to the complexity of the receptor signal transduction network, chemical synapses can have diverse effects on the postsynaptic cell[1].

In an electrical synapse, however, there is a gap junction where the presynaptic and postsynaptic cell membranes are connected by special channels capable of passing an electric current, and therefore causing voltage changes in the presynaptic cell to induce voltage changes in the postsynaptic cell. This facilitates the rapid transfer of signals from one cell to the next one[1].

Chemical synapses in the central nervous system (CNS) connect a presynaptic axonal terminal with a postsynaptic dendrite[1]. For the chemical signal to be transmitted, vesicles containing the neurotransmitters fuse with the plasma membrane of the presynaptic terminal and release their content into the synaptic cleft[2]. Once in the synaptic cleft, the neurotransmitters bind to the extracellular part of the cognate ligand-gated ion channels embedded in the membrane of the postsynaptic cell. This binding results in a conformational change which leads to channel opening and triggers ion influx or efflux in response to the respective ion concentrations in the microenvironment. Ion influx is observed if the extracellular ion concentration exceeds the cytosolic concentration, and, conversely, an efflux occurs, if the intracellular concentration is higher than the extracellular concentration. These fluxes result in local changes of the membrane potential, eliciting inhibitory postsynaptic potentials (IPSPs) or excitatory postsynaptic potentials (EPSPs), depending on the resulting membrane potential. Synapses exerting EPSPs and IPSPs at the postsynaptic cell are called excitatory and inhibitory synapses, respectively[1]. The following chapters will focus on inhibitory synapses in mammals.

I.2 Assembly of inhibitory synapses: Glycine and $GABA_A$ receptors

Proper synapse mechanisms involve the synchronized accumulation of the neurotransmitter release machinery at presynaptic sites and, in apposition, at postsynaptic locations the clustering of appropriate receptors. In the synaptic cleft, inhibitory signals are mediated by glycine and γ-aminobutyric acid (GABA) as neurotransmitters, and the glycine and γ-aminobutyric acid type A receptors (named GlyR and $GABA_AR$, respectively) at the postsynaptic cell membrane[1].

GlyR and $GABA_AR$ belong to the Cys-loop superfamily of pentameric ligand-gated chloride channels (pLGIC), with, especially in case of the $GABA_ARs$, having a great diversity in their subunit composition[3,4]. Both inhibitory neurotransmitter receptors can assemble into either hetero- or homopentamers. Recently, the main structural features of these receptors have been reviewed[5,6]. These receptors share a common architecture (Figure I.1) and are composed of an extracellular domain (ECD) formed by ten β-strands that fold into a twisted β-sheet, a transmembrane domain (TMD) comprised of four α-helices which are interconnected by two intracellular loops and an extracellular loop.

Recently, the structures of the GlyR α1 and GlyR α3 homopentamers, in combination with allosteric modulators, analgesic potentiators and agonists as well as antagonists have been elucidated using X-ray crystallography and cryo-electron microscopy (cryo-EM)[7-10]. These findings shed light into the function of these Cys-loop family members, as well as their gating mechanism. The first crystal structure of a $GABA_AR$ was that of a β3-homopentamer in the presence of the protease inhibitor benzamidine, which turned out to be an agonist of the receptor[11]. The structure is similar to others pLGICs (Figure I.1) in which the ECD presents the binding site for the natural agonist GABA and drugs, such as the benzodiazepines, while allosteric modulators such as endogenous neurosteroids, like pregnanolone and pregnenolone, bind to the TMD[11-15].

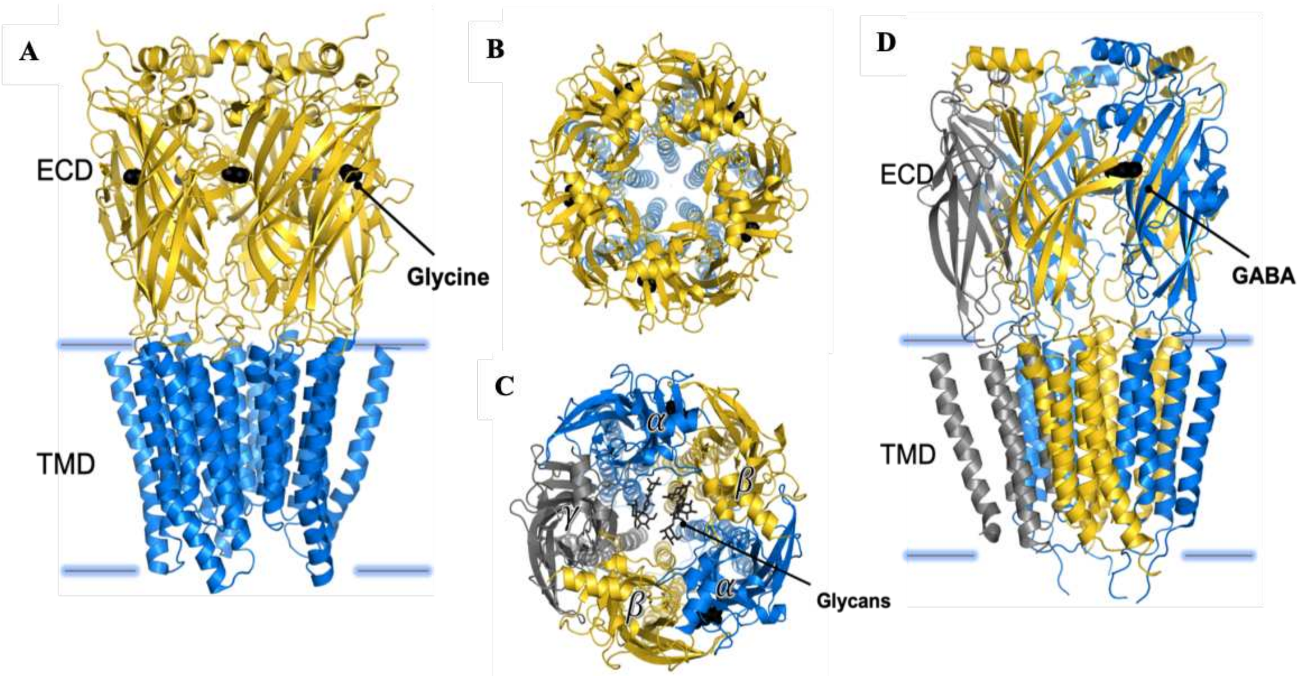

Figure I.1 Structures of ligand-gated glycine (GlyR) and γ-aminobutyric acid type A receptors ($GABA_AR$). (A) *Cartoon representation of a side view of the homopentameric α3 GlyR in complex with glycine, as elucidated by X-ray crystallography (PDB: 5TIN). The transmembrane domain (TMD) is displayed in blue and the extracellular domain (ECD) in yellow. Glycine is represented by black spheres.* ***(B)*** *Top view of the homopentameric α3 GlyR.* ***(C)*** *Top view of the heteropentameric α1β3γ2 $GABA_AR$ as elucidated by cryo-EM (PDB: 6HUP). The α1 chains are represented in blue, the β3 chains in yellow and the γ2 chain in gray. N-linked glycans present in the a1-chains are shown as black sticks.* ***(D)*** *Side view of the heteropentameric α1β3γ2 $GABA_AR$ in complex with GABA, which is represented with black spheres and is located in the two α-β interfaces of the ECD. The subunits are color coded as in (C).*

The majority of the GlyRs are composed of α-subunits (α1- α4) and only a single β-subunit[3], in such a way that the heteropentameric receptors are composed of either two α and three β[16] or two β and three α subunits[17,18]. $GABA_A$Rs, on the other hand, are more heterogeneous in their subunit diversity than the GlyRs. They are assembled from 19 different subunits derived from eight different subunit classes named α, β, γ, δ ε, π, ρ, and Θ[19]. The most common $GABA_A$Rs are composed of two α, two β, and single γ or δ subunit[19]. The receptor subunit composition varies within and across different brain regions and endows receptors with different functionalities[20], *e.g.* different kinetics of channel opening and closing. The presence of specific subunits also mediates distinct protein interactions with synapse-organizing molecules, scaffolding proteins and intracellular signaling molecules[20]. For instance, the $GABA_A$Rs α4-6 and δ subunits are present at extrasynaptic sites where the concentration of GABA is ambient, having higher agonist affinity and longer open times than their synaptic counterparts and responding to lower GABA concentrations (μM range), thus contributing to tonic inhibition in the CNS[21]. In contrast, the α1-3, β2-3, and γ2 subunits are localized at post-synaptic sites where they predominantly mediate phasic inhibition, in response to higher concentrations of GABA (mM range) due to short life burst (< 1ms) release of the neurotransmitter from presynaptic terminals[20,21].

Recently, cryo-EM structures of heteromeric $GABA_A$Rs were elucidated, specifically, a human α1β2γ2 receptor[15], a rat α1β1γ2 heteropentamer[14], and the human α1β3γ2 receptor[21,22]. All structures provided valuable insights into the binding of the agonist GABA that occupies the canonical neurotransmitter binding site which is contributed by the α-β interface, and other diverse modulators, as well as the interaction with membrane lipids. The structures show a clockwise α–β–α–β–γ arrangement of the subunits when viewed from the extracellular side (Figure I.1c), in agreement with previous biochemical data[22,23]. Also, the presence of two glycosylation sites originated from residue Asn111, present in all α subunits of $GABA_A$Rs, should be mentioned. This post-translational modification (PTM) is a unique structural feature of heteropentameric $GABA_A$Rs, possibly conferring specific stoichiometries, a conserved arrangement of the α subunits within the heteropentamer, and receptor permeability.

Neurotransmitter receptors are recruited and stabilized at inhibitory postsynapses by scaffolding proteins. The scaffolding protein gephyrin was shown to interact with post-synaptically localized $GABA_A$Rs containing the α1-3 subunits[24-26], and also possibly those containing the α5 subunit[27] and the β2-3 subunits[28]. Besides, the $GABA_A$R γ2 subunit has proven to be crucial for the clustering of $GABA_A$Rs and gephyrin at the post-synaptic membrane, although it does not interact directly with gephyrin[29]. In case of the GlyRs, its β-subunit is the only subunit able to interact with gephyrin[30]. The next chapter will focus on specific structural and functional aspects of what is currently known regarding gephyrin as a scaffolding protein.

I.3 Structure and general functions of gephyrin

Postsynaptic scaffolding molecules are key components in the organization of functional synapses. They ensure the accurate accumulation of neurotransmitter receptors in precise apposition to presynaptic release sites, as this is required for reliable synaptic transmission. Gephyrin is a 93 kDa-scaffolding protein first identified when it co-purified with the GlyR from rat spinal cord[31]. It ensures the anchoring, clustering and stabilization of GlyR and $GABA_A$R at inhibitory postsynapses in the mammalian CNS[29,32].

Gephyrin is composed of three distinct regions: folded N and C terminal domains as well as a central flexible linker (Figure I.2a)[33-36]. The residue numbering presented here refers to the P1 splice variant; in the next chapter, I will describe the alternative splicing of gephyrin and which isoform was employed in this work (see chapter I.4)). The N-terminal G domain contains the first 180 amino acids and adopts a trimeric structure with a classical Rossmann fold in each monomer (Figure I.2b). This domain is homologous to the bacterial MogA protein[37] and the plant Cnx1G domain[36,38], hence for simplicity purposes it will be referred to as GephG. The E domain, located at the C-terminal end comprises residues 318 to 736 and, in isolation, forms a dimer (Figure I.2c)[33,39]. This domain is evolutionarily related to the bacterial MoeA protein[40] and plant Cnx1E domain[41], hence it will be named GephE. In the context of the full-length (FL) protein the trimerization of GephG is maintained, contrary to GephE dimerization that, due to an unknown mechanism, is prevented (Figure I.2 d)[34].

GephE can be structurally subdivided into four subdomains, named I to IV; notably, subdomain III shares a similar architecture with the N-terminal GephG arguing for an evolutionary relationship and reflecting the fact that the product of the G-domain is the substrate of the E-domain (Figure I.2c). Due to the oligomeric states of the GephG and GephE domains, it was proposed that the FL protein forms a planar hexagonal scaffold, which provides anchoring points for the receptors on the membrane-proximal side and on the opposite side links to cytoskeletal elements[40,42].

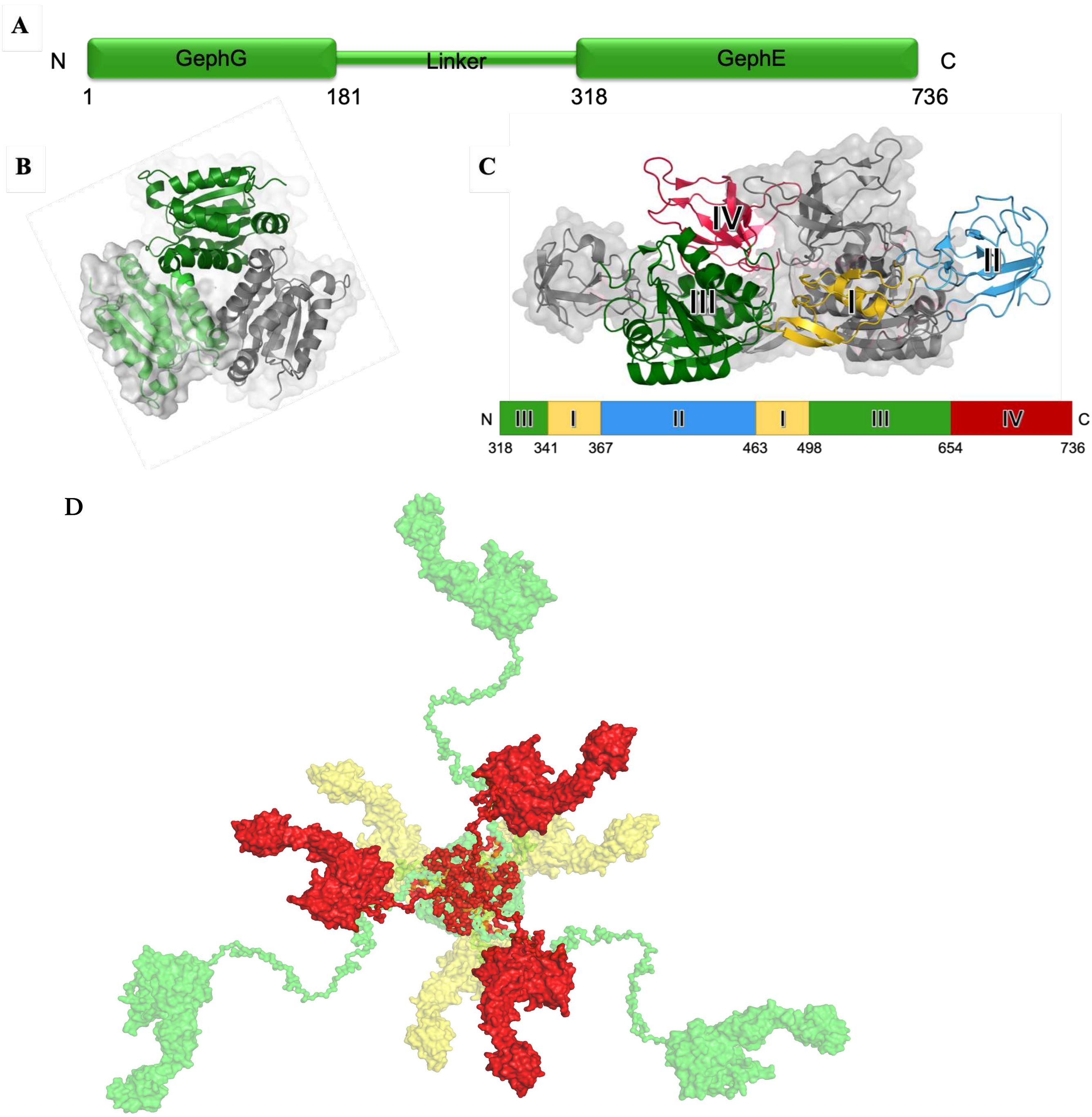

Figure I.2 ***Structure of gephyrin. (A)*** *Schematic representation of the domain architecture of gephyrin. The FL protein is numbered according to the human P1 splice variant nomenclature.* ***(B)*** *Crystal structure of the N-terminal GephG trimer where each monomer is shown in cartoon representation (green, dark green and gray, respectively) with an 80% transparent surface representation in gray (PDB: 1JLJ).* ***(C)*** *Crystal structure of the C-terminal GephE dimer where one monomer is shown in cartoon and surface representation in gray, and the other one in cartoon representation only, but colored according to its four subdomains (schematic representation of the subdomains is shown below the crystal structure) (PDB: 2FU3).* ***(D)*** *Surface view of the FL-gephyrin models derived by SAXS [34]. Represented in green is the completely extended conformation, in red the moderately extended conformation and in yellow the compact conformation. The GephG trimer is always located at the center and the monomeric GephE connected by the more or less extended linker follows the threefold symmetry imposed during the analysis.*

Gephyrin also exerts different other functions, for instance, its enzymatic activity is crucial for the final steps of molybdenum cofactor (Moco) biosynthesis, namely the insertion of the metal into the organic moiety of the cofactor[39,43-46]. Also, it regulates mTOR signaling through a direct interaction with mTOR[47], and plays a structural role during the transport of GlyR and $GABA_AR$ to the membrane[48-51].

I.4 Alternative splicing of gephyrin

The gephyrin genes (*GPHN*) are encoded on chromosome 14 (q23.3) in humans and 12 in mice. This gene has a complex intron-exon structure consisting of 29 exons, from which nine involve alternative splicing (Figure I.3)[52,53]. In 2008, a new nomenclature was proposed to simplify the alternative splicing phenomena in gephyrin (Figure I.3) (for review, see Ref. 54). Since the C2 and C6 splice cassettes (according to the former nomenclature) appear in all gephyrin isoforms expressed *in vivo*, the corresponding exons are constitutively spliced rather than alternatively spliced.

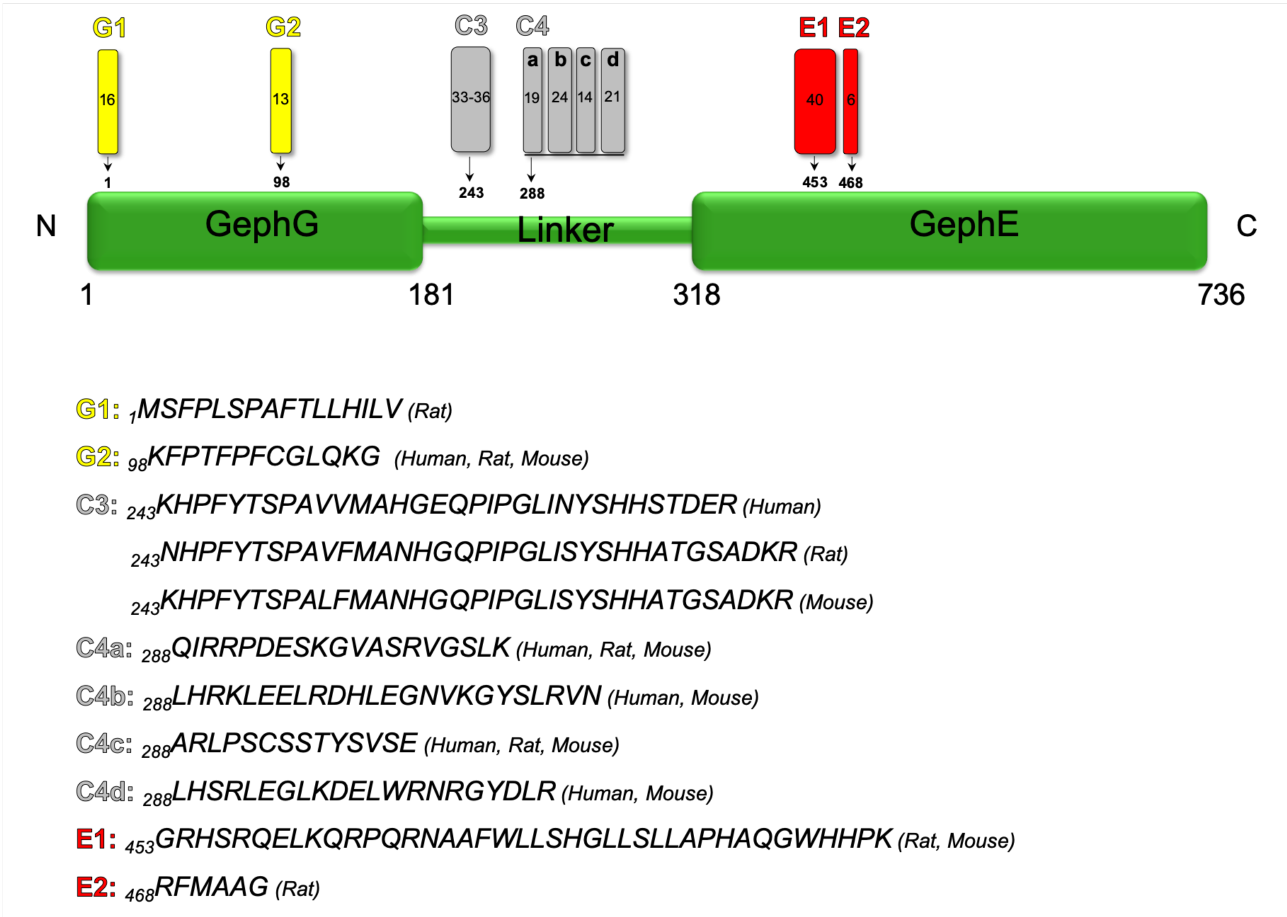

Figure I.3 Schematic representation of alternative splicing of gephyrin in vertebrates. *The gephG splice cassettes are shown in yellow, cassettes in the linker region in gray and gephE cassettes in red. The number within the box indicates the cassette's length, while the number underneath the arrow the position of the insertion. The sequence corresponding to each cassette is given below, indicating in brackets the species where it was identified. For an extended review of the alternative splicing of gephyrin, please see Ref. 54.*

In vertebrates, the GephG and GephE domains are encoded by exons 3-7 and 16-29, respectively, whereas the central exons 8, 13, and 14 encode the linker region[53]. Gephyrin is differentially expressed between neuronal and non-neuronal tissues, but also exhibits a differential expression pattern in different regions of the brain[53]. The differences in the primary sequence of the protein alter its structure and determine its subcellular localization, thereby modulating its activity during Moco biosynthesis as well as its neurotransmitter receptor anchoring function[55-58].

GephE domain splice variants have been not been studied in detail, contrary to GephG and linker region splice variants. In the GephG domain, insertion of the G2 cassette (previously referred to as the C5 or C5′ cassette) limits gephyrin cluster size and alters its oligomeric state[59]. In this isoform, which is enriched in non-neuronal tissues[55], the splice cassette G2 composed of a 13 amino acids, is inserted into GephG in such a way that it interferes with the GephG trimerization interface, hence compromising not only the co-localization of gephyrin with the GlyR β subunit[56] but also its enzymatic activity during Moco biosynthesis[57].

Most of the additions and/or modifications of the exons, however, affect the linker region, containing two splice sites with a total of five different cassettes (C3 and C4a-d) (Figure I.3)[52,53]. This divergence mainly influences the clustering behavior of gephyrin[35]. For instance, the isoform containing the C3 splice cassette modulates the oligomeric state of gephyrin and its interaction with the GlyR β-subunit, reducing the affinity 10-fold, in comparison to the corresponding C4c-containing neuronal variant and gephyrin without a splice cassette, according to a study conducted in *Spodoptera frugiperda* 9 (Sf9) insect cells[35]. Gephyrin isoforms containing the C3 splice cassette are highly abundant in liver[55,58], kidney[53] and glia[57] in vertebrates, where they are primarily involved in Moco biosynthesis[58], while these variants are absent in neurons[60].

In contrast, gephyrin variants carrying the C4 type are present in neurons, with cassettes C4c and C4d being more abundant than cassette C4a[55]. The splice cassette C4c does not affect GlyR binding[35] and none of the insertion of the C4 cassettes impair Moco biosynthesis[57]. The gephyrin isoform used in this work is the splice variant P2, which contains the cassette C4c (14 amino acids stretch with the sequence ARLPSCSSTYSVSE which are present as residues 289 to 302).

I.5 Posttranslational modifications of gephyrin

Posttranslational modifications (PTMs) of gephyrin may be important for modulating its function and localization at inhibitory postsynaptic densities. Such modifications might affect the structure and scaffolding properties of gephyrin, its trafficking and half-life, and finally its ability to interact with partner proteins.

Mass spectrometric analyses of rat and mouse brains revealed that gephyrin has 22 common phosphorylation sites, which represent the major PTMs founded in this protein[35,61,62]. Most of the phosphorylation sites are located in the linker region, except for Thr324, which resides in GephE. These modifications might induce conformational changes by affecting the structure of the linker or the neighboring GephG and GephE domains, thereby altering the clustering, trafficking and binding properties of gephyrin[61,62].

Among these sites, Ser268 and Ser270 represent two major phosphorylation sites, which are targeted by glycogen synthase kinase 3ß (GSK 3ß) and the extracellular signal-regulated kinases 1 and 2 (ERK 1/2)[61,62], respectively, that can synergistically influence the amplitude and frequency of GABAergic miniature inhibitory postsynaptic currents (mIPSCs) through changes in gephyrin clustering[61,62]. Thus, signaling pathways regulating gephyrin clustering properties can alter the strength of GABAergic signals. Furthermore, the observation of collybistin-dependent phosphorylation of gephyrin Ser270 by cyclin-dependent kinases[63] suggested that there is a convergence of signaling pathways on this critical residue. In line with this, the phosphorylation at Ser268 was found to crosstalk with SUMOylation at Lys148 and Lys724, as well as acetylation at Lys666[64]. These modifications are determinants of gephyrin clustering and hence the density of $GABA_A$Rs, thereby regulating GABAergic synaptic transmission[64].

PTMs of the GlyRs and $GABA_A$Rs confer further plasticity to the inhibitory synapse. Phosphorylation of Ser403 in the GlyR β-subunit is one of the most remarkable ones, since this amino acid resides in the core binding motif mediating the gephyrin-GlyR β interaction[65]. Ser403 is phosphorylated by protein kinase C resulting in a downregulation of the gephyrin-GlyR β interaction, hence modulating the gephyrin-mediated formation, maintenance and plasticity of inhibitory postsynapses[65]. Regarding the $GABA_A$Rs, Thr375 of the α1 subunit has been proposed as a putative phosphorylation site, resulting in a downregulation of the gephyrin-$GABA_A$R α1 interaction in binding experiments with phospho-mimetic mutants[25].

Regarding dephosphorylation of gephyrin much less in known. A direct interaction between gephyrin and protein phosphatase 1 has been observed in co-immunoprecipitation experiments[66]. However, different studies yield contradictory data whether dephosphorylation decreases or increases postsynaptic gephyrin clustering[61,63,66].

In addition to phosphorylation, palmitoylation and acetylation as mentioned before for Lys666 represent other common PTMs of gephyrin[61,67]. Palmitoylation helps to anchor gephyrin to the membrane. Therefore, gephyrin palmitoylation, either downstream or upstream of phosphorylation events, might contribute to the anchoring of gephyrin to the PSD and also to the recruitment of GABAergic synapse-specific molecules such as neuroligin2 and collybistin. It was shown that the residues undergoing palmytoilation are Cys212 and Cys284, which are targeted by the Asp-His-His-Cys (DHHC)-12 palmitoyltransferase, which is localized to the Golgi apparatus and dendritic shafts, and directly interacts with gephyrin[68].

Proteolytic degradation of gephyrin by calpain, a Ca^{2+}-dependent cysteine protease, also seems to be regulated by Ser268 and Ser270 phosphorylation of gephyrin[61,62]. In biochemical and cell-based experiments, Ser268 and Ser270-phosphorylated gephyrin seems to be susceptible to degradation by calpain, thus limiting its availability for postsynaptic clustering. Hence, the proteolytic degradation of gephyrin provides a turnover mechanism for the dynamic regulation of gephyrin scaffolds and hence GABAergic transmission.

I.6 Molybdenum cofactor biosynthesis by gephyrin

Molybdenum-dependent enzymes can be grouped into two categories depending on the cofactor composition and catalytic function, the bacterial nitrogenases containing an ironmolybdenum cofactor (Fe-Moco) in the active site, and those containing the molybdenum cofactor (Moco), which consists of a pterin-based organic moiety ligating a mononuclear Mo-center via the two S-atoms of a dithiolene group (for review see 69). The molybdenum cofactor (Moco) is essential for the survival of nearly all organisms, since molybdenum-dependent enzymes are crucial for autotrophic and heterotrophic organisms (reviewed in 46). These enzymes, such as nitrate reductases, sulfite oxidase and xanthine oxidoreductases, are required for the reduction of nitrate to nitrite, the oxidation of sulfite to sulfate, and the catabolism of purine nucleotides, respectively, where the Moco defines the catalytic center[69]. Gephyrin acts as a moonlighting protein having a fundamental role in the last two steps during Moco biosynthesis, which result in the incorporation of the metal into the pterin derivative[39,43-46].

In humans as in almost all other organisms, Moco biosynthesis takes place in a metabolic multistep pathway. In the first step, molybdenum cofactor synthesis 1A (MOCS1A) and MOCS1B rearrange the educt guanosine triphosphate to form a cyclic pyranopterin monophosphate. In the subsequent step MOCS2A/B and MOCS3 produce the metal-ligating dithiolene moiety in the pyran ring (reviewed in 70). The final two steps are carried out by gephyrin, where GephG catalyzes the penultimate step in which the apo-pyranopterin [44,45,71] is adenylated involving ATP-hydrolysis. The product of this reaction is transferred to GephE, where the metal (molybdenum) is inserted into the dithiolene group of the pterin coupled to the deadenylation of the AMP-MPT dinucleotide, resulting in active Moco[39,72,73].

In this sense, GephG and GephE are homologous to the bacterial MogA[37] and MoeA[40] proteins respectively, however, in the course of evolution these two distinct enzymatic activities were fused in a single protein, since MogA and MoeA in bacteria are independent enzymes. Meanwhile, GephG and GephE are also homologous to the plant Cnx1 G and E domains[36], enzymatic units that carry out the respective biosynthetic steps in plants. Interestingly, in Cnx1 the G and E domains are interconnected via a short linker in an inverted arrangement with the E domain preceding the G domain. Obviously, there is an evolutionary pressure dictating the fusion of both catalytic domains, which presumably allows for an easier transferring of the product of the G domain catalyzed reaction to the active site in the E domain where it serves as educt and may also dictate a preferred spatial arrangement of the two domains[73].

Human mutations in the enzymes responsible for Moco biosynthesis result in an autosomal recessive disorder, referred to as Moco deficiency, which is accompanied by severe neurological symptoms and usually leads to early childhood death[74]. The majority of mutations affect the first two steps, specifically the enzymes MOCS1 and MOCS2, however, two mutations have been identified in gephyrin, which both result in a severe form of Moco deficiency[75].

I.7 Roles of gephyrin in inhibitory postsynapse formation and maintenance

Gephyrin was originally identified as a protein which simultaneously binds to glycine receptors and tubulin at postsynaptic densities[52,76]. Hence, it was named gephyrin derived from the Greek word *gephyra* which means "bridge". Years later, it was also realized that gephyrin is crucially involved in the clustering of $GABA_A$Rs[48,50]. In the CNS, gephyrin clusters selectively at postsynaptic sites of glycinergic, GABAergic and mixed glycinergic/GABAergic synapses[77].

The clustering of GlyRs at postsynapses seems to be strictly dependent on gephyrin clustering since the insertion of the gephyrin-binding motif of the GlyR β loop into other membrane proteins is sufficient for co-clustering with gephyrin[51]. Specifically, the gephyrin-induced clustering of the receptors is triggered by the high-affinity binding of the GlyR β loop to GephE in close proximity of its dimerization[33,59]. This binding seems to be modulated by conformational changes in gephyrin arising from the phosphorylation-dependent binding of Pin1 within the linker region[78], suggesting that the gephyrin-GlyR clusters are dynamically regulated by specific protein kinases. Gephyrin also plays a central role in the intracellular trafficking of the GlyRs, as gephyrin proteins were found to be co-transported with GlyRs to the plasma membrane[79]. Therefore, the binding of GlyR to gephyrin seems to be crucial for the intracellular transport of the receptors[79-81], the regulation of their lateral diffusion in the synaptic membrane[82,83] as well as their interaction with the cytoskeleton[84]. The ability of gephyrin to move in and out of postsynaptic clusters[81,85] suggests that this postsynaptic scaffold protein is dynamically regulated by activity-dependent mechanisms, trans-synaptic molecules and specific intracellular interactors.

Although gephyrin also binds to $GABA_A$Rs, it plays distinct roles at glycinergic synapses compared to GABAergic synapses. Whereas all heteropentameric GlyRs bind gephyrin, only a subset of $GABA_A$Rs exhibit direct interactions with gephyrin, namely those containing the α1, α2 and α3 subunits. Therefore, the subsynaptic localization of gephyrin in GABAergic synapses depends on the $GABA_A$R composition. In this sense, gephyrin is critical for the clustering of α1/2/3-containing $GABA_A$R at synaptic sites, but not for the extrasynaptic clustering of $GABA_A$Rs, such as those containing α4 subunits that are expressed in thalamic neurons[86]. Similarly, $GABA_A$Rs containing the α5 subunit do not cluster in association with gephyrin[87], rather their membrane distribution is regulated by activated radixin[88]. However, recent studies imply a possible regulation of the synaptic localization of $GABA_A$Rs-containing α5 subunits propitiating dendritic outgrowth and spine maturation by gephyrin[27]. At GABAergic synapses, interactions of gephyrin with extracellular matrix proteins have been implicated in the targeting of GABAergic terminals to the axon initial segment of pyramidal cells[89]. In this regard, the composition of $GABA_A$Rs is also critical for synapse formation and regulation via gephyrin. In genetic experiments, the deletion of the gene encoding the γ2 subunit, elicited a disruption of $GABA_A$Rs clusters, which appear to be dispersed on the cell surface at postsynaptic sites. This dispersal of receptor clusters is mirrored in gephyrin, which was also found not be clustered anymore[90,91]. Likewise, the deletion of the α1 as well as the α3 subunits, triggers gephyrin cluster disassembly, resulting in a disperse intracellular distribution of gephyrin, thus indicating that these deletions prevent the postsynaptic targeting and localization of gephyrin[86,92]. Besides, the presence of only the α2 subunit is sufficient to regulate the localization of $GABA_A$Rs containing this subunit via gephyrin binding[93]. So far, there is no clear evidence of gephyrin being involved in the intracellular trafficking of $GABA_A$Rs. However, some studies indicate that the trafficking of $GABA_A$Rs as well as of gephyrin into and out of the plasma membrane might be regulated by palmitoylation[68,94-96]. This suggests that the interaction with gephyrin might merely occur at the cell membrane where it dynamically regulates the properties of $GABA_A$R clusters[97].

The interaction between gephyrin and the GlyRs as well as $GABA_A$Rs are mediated by GephE and the large highly unstructured intracellular loop region connecting transmembrane helices 3 and 4 (TM3-TM4) of receptors, respectively. All crystal structures of GephE in complex with the core binding region of either receptor exhibited a general stoichiometry of 1:1, although several studies employing isothermal titration calorimetry (ITC) suggested two binding sites of GlyR to gephyrin with different affinities[33,35,98-100]. Therefore, it is still under debate whether the gephyrin-GlyR interactions are mediated by two binding sites, *i.e.* a high affinity and a low affinity binding site. While the gephyrin-GlyR β loop interaction is moderately strong with reported dissociation constants varying from the high nM to the low μM range[33,98,101,102], interactions with the $GABA_A$Rs are significantly weaker. Amongst the $GABA_A$Rs, the α1 and α3 FL TM3-TM4 loops bind the tightest with reported K_d-values of 17 and 5.3 μM, respectively[24-26].

These dissociation constants, under physiological conditions will be significantly enhanced due to avidity effects, since the receptors are oligomers containing at least two gephyrin-binding subunits and also the oligomeric state of gephyrin. Besides, the encounter between the receptors and gephyrin is governed by two-dimensional diffusion as not only the receptors are constrained to the cell membrane but also gephyrin is recruited to the lipid bilayer. Finally, the subunit diversity of the $GABA_A$Rs may be crucial to regulate $GABA_A$R clustering across different regions of the brain, either relying on gephyrin as scaffolding protein or on other receptor-anchoring mechanisms.

Synapse formation is a process not yet fully understood. In GABAergic synapses, and possibly also at glycinergic synapses, the presence of neuroligin 2 appears to be critical for synaptogenesis[103]. Neuroligin 2 is a transmembrane protein enriched at inhibitory postsynapses which plays a critical role in the regulation of the correct apposition of receptors to the presynaptic neurotransmitter release machinery across the synaptic cleft through its interaction with neurexin proteins[104,105]. In *in vitro* experiments, it has been observed that α neurexins, as well as specific splice variants of the β neurexins, namely those containing the S4 cassette, selectively induce the formation of GABAergic synapses as well as the clustering of neuroligin 2, gephyrin and $GABA_A$Rs containing the γ2 subunit in transfected COS cells which were co-cultured with dissociated neurons[106]. Conceivably, the use of mutant mice lacking either gephyrin, collybistin, neuroligins and GlyRs/$GABA_A$Rs might be useful to understand the interplay of these proteins during synaptogenesis. Although deficiencies in neurotransmitter receptor clustering appear to be lethal, as observed in mutational experiments where gephyrin knock-out mice die within the first few hours with hyperexcitability symptoms attributed mainly to defects in neurotransmission defects at inhibitory synapses[107]. Besides, in gephyrin-deficient mice whose Moco biosynthesis was partially rescued by the transgenic expression of Cnx1 (the plant orthologue of gephyrin for Moco biosynthesis), the outcome was similar, indicating that the presumably still impaired receptor clustering was the crucial factor for the lethal phenotype[108]. These last studies demonstrate the crucial role of gephyrin as a scaffolding protein which helps to establish and maintains inhibitory postsynaptic specializations and is also involved in their regulation.

I.8 Neurological disorders associated with gephyrin dysfunctions

Base on the critical role of gephyrin in the organization of the GABAergic and glycinergic synapses, it is not surprising that various neurological disorders have been linked to dysfunctions of this scaffolding protein.

Alzheimer's disease is the most prevalent neurodegenerative disorder affecting *circa* 50 million patients worldwide[109]. Although a clear link between gephyrin and this disease has been established[110,111], the precise function of the protein is not well understood. While some studies associate this pathology with a decrease in GABAergic signaling related to globally reduced gephyrin levels in both spared and susceptible regions[63], other studies show an excitatory/inhibitory imbalance caused by the β-amyloids that are characteristic for this disease and induce an increased GABA synthesis in astrocytes[112]. This is in line with another study that shows there is an upregulation in the expression of gephyrin, resulting in an anomalous accumulation of the protein in patients suffering from Alzheimer's disease[62]. In this case, the enriched fraction of gephyrin is present in the β-amyloid plaques and neurofibrillary tangles, where gephyrin was detected as insoluble low-molecular weight proteins (40-kDa, 50-kDa, 60-kDa and 70-kDa) in immunoreactive assays with antibodies recognizing the linker region and the E domain. Nonetheless, further proteomic studies are necessary to better characterize these aberrant gephyrin fractions.

The neurological condition best characterized on the molecular level, which is associated with gephyrin impairment, is hyperekplexia. This disease is characterized by a pronounced startle response to tactile or acoustic stimuli and hypertonia. Hyperekplexia has been related to an impairment in glycinergic synapses associated mainly with mutations in the genes encoding for the GlyR α1 and β subunits[113], but also $GABA_AR$-associated proteins such as the guanine nucleotide exchange factor collybistin (ARHGEF9)[114] and gephyrin[115]. Rees and colleagues found a missense mutation (A28T) in one patient causing an amino acid substitution (N10Y) near the N-terminus of gephyrin. This amino acid substitution, although located in GephG and therefore not directly impacting gephyrin binding to the GlyR, may impair the association of gephyrin with other intracellular proteins such as elements of the cytoskeleton that mediate its scaffolding function.

Other neurological disorders associated with gephyrin mutations are autism, seizures and schizophrenia. These syndromes have been connected to inherited hemizygous microdeletions encompassing exons 3-5 of gephyrin, encoding GephG[116]. Curiously, a transcriptomic study showed a correlation between the transcriptomic profile of autism and schizophrenia, with a downregulation of the IQSEC3 gene, which encodes for a guanine nucleotide exchange factor specific to inhibitory postsynapses that binds gephyrin via GephG[117,118].

In temporal lobe epilepsy (TLE), gephyrin was reported to be downregulated according to immunohistochemistry and immunofluorescence data from patients suffering from this condition[119]. These findings were supported by animal studies, where the authors found that gephyrin protein levels gradually decreased during both the acute and latent periods of the disease. Although gephyrin levels started to increase again during the chronic phase of the disease, they never reached the normal level in comparison to the control group. TLE is characterized by an overall increase in excitatory (glutamatergic) neurotransmission[120,121], whereas GABA release is decreased[121].

The stiff-person syndrome is an autoimmune disease characterized by progressive rigidity and stiffness. During the progress of this condition, the organism develops autoimmunity against several proteins connected to inhibitory synapses. Most of the cases present autoantibodies against the GABA-synthetizing enzyme glutamic acid decarboxylase (GAD)[122], although patients have been reported with autoimmunity against gephyrin[123] and the $GABA_AR$-associated protein (GABARAP)[124].

Finally, in patients suffering from Down syndrome there is also an over-inhibition of synaptic function due to an increase in GABAergic synapses, affecting the excitatory/ inhibitory balance in the brain[125,126]. However, a direct implication of gephyrin dysfunction in this case has not been established.

I.9 Gephyrin interacting partners

Besides the gephyrin interaction with the $GABA_AR$ α1-3 and the GlyR β subunits, which allow the anchoring of the receptors to the iPSD, around 10 different intracellular proteins have been described to directly interact with gephyrin, and most of these do so via the GephE and the linker region (for a recent review see Ref. 127). Table I.1 summarizes the known intracellular synaptic proteins interacting with gephyrin.

Table I.1 Summary of intracellular synaptic proteins interacting with gephyrin

Intracellular Interactor	*Binding domain*	*Synaptic function*	*References*
VASP/ Mena	Linker/E domain	Axon guidance and neuronal migration.	128,129
Tubulin	Linker	Major microtubule cytoskeletal protein.	76,130
Profilin 1/2	E domain	Mediates actin-dependent $GABA_A$ receptor packing density and dynamics.	128,131
Neuroligin 2	E domain	Assembly of synaptic specialization by association with neurexins forming a cell adhesion system and recruitment of gephyrin.	132
IQSEC 3	G domain	IQSEC3 promotes inhibitory synapse formation in an Arf-GEF activity-dependent manner.	118,133
DYNLL- 1/2	Linker (aa205-212)	Involved in axonal trafficking of synaptic proteins.	80,134,135
GABARAP	Linker	Clustering of $GABA_A$ receptors.	136,137
Collybistin	Linker (aa319-329)	Involved in the transport, clustering and maintenance of gephyrin and $GABA_ARs$ at inhibitory synapses.	138,139
Pin 1	Linker (aa188-201)	Regulates the neuroligin 2-gephyrin interaction and negatively modulates inhibitory synaptic transmission.	78,140
RAFT1	Linker or E domain	A kinase that participates in signaling pathways controlling mRNA translation.	47
InSyn1/2	Unclear	Unknown function. Regulates GABAergic inhibition.	141

I.10 Antimalarial small drugs interact with gephyrin

Arteminisinins are anti-malarial drugs originally used in traditional Chinese medicine and derived from the plant *Artemisia annua*[142]. From a chemical perspective, these compounds are sesquiterpene lactones containing an endo-peroxide bridge (Figure I.4 a). Nowadays, the use of artemisinin in combination therapies with other drugs is the state-of-the-art drug regimen to fight malaria caused by *Plasmodium falciparum*[143]. These treatments involve artesunate, a succinic acid derivative of artemisinin, in combination with amodiaquine or mefloquine, and also artemether in combination with lumefantrine[144].

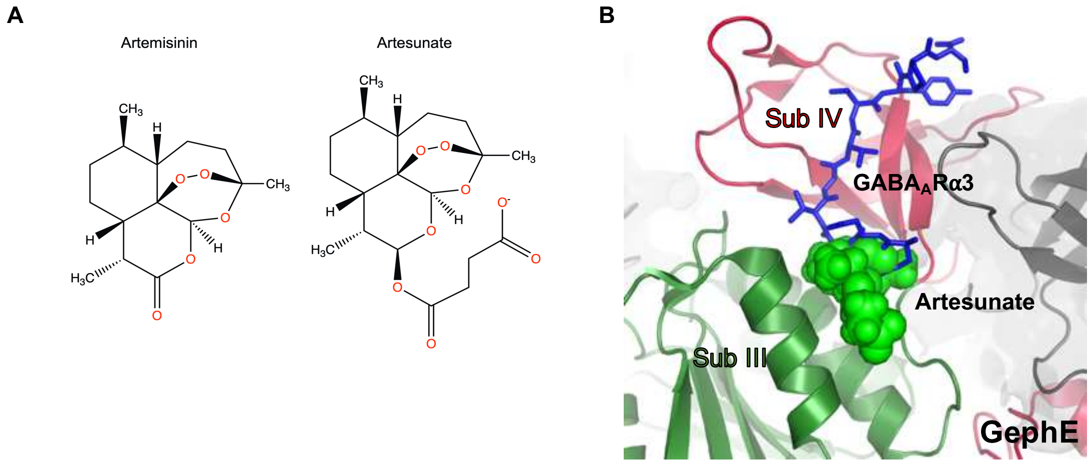

Figure I.4 Artemisinins bind to the universal receptor binding-pocket in GephE. (A) *Chemical structures of artemisinin and its derivative artesunate.* ***(B)*** *Enlarged view of the receptor binding pocket in GephE comprised by the subunits III (green) and IV (red). The gephyrin structure is shown in cartoon representation, the $GABA_AR$ α3 peptide in blue sticks and artesunate as green spheres (PDB: 6FGC, 6HSN).*

In recent years, gephyrin was identified as a primary mammalian target of artemisinins[145]. This interaction was identified while investigating the effect of artemisinins in the trans-differentiation of glucagon-producing pancreatic Tα cells into insulin-secreting Tβ cells by regulating GABA signaling[145]. Hence, it was suggested to exhibit an anti-diabetic potential, however, further studies have questioned this effect[146,147].

After the identification of the interaction between artemisinins and gephyrin, this binding was structurally characterized by our group[148]. After elucidating the structure of the complex artemisinin-gephyrin, it was shown that these small drugs target the N-terminal region of the universal receptor-binding pocket in GephE, inhibiting important hydrophobic interactions between gephyrin and residues ^{368}FNI^{370} of the $GABA_AR$ α3 subunit and ^{398}FSI^{400} of the GlyR β subunit (Figure I.4 b), which represent critical determinants of the gephyrin-receptor complex as these include the key aromatic residue at the first position of the consensus binding motif that engages in a stacking interaction with Phe330 of GephE, an essential prerequisite for the scaffolding function of gephyrin[33]. Through ITC measurements and a supported membrane sheet assay, it was demonstrated that these compounds negatively affect the gephyrin-receptor interaction. In this regard, the inhibitory neurotransmission signal is affected as was demonstrated later by electrophysiological experiments that revealed a significant decrease in glycinergic currents in the presence of these compounds, with a strict dependence on gephyrin[148]. Furthermore, receptor and gephyrin clustering studies displayed a strong and time-dependent decrease in $GABA_AR$ and gephyrin cluster sizes when artemisinins were administered[148]. In addition, artemisinins showed a time-dependent neurotoxic effect, in line with previous observations of cytotoxic effects of these compounds when administered in high doses[149,150].

I.11 Artemisinins modulate inhibitory neurotransmission also by interacting with pyridoxal kinase

In addition to their anti-parasitic activity, artemisinins have additionally been implicated in multiple cellular pathways including a variety of cancers, they exhibit immunomodulatory effects and act as anti-viral and anti-microbial effectors[143,151-153]. These clinically approved drugs have been demonstrated to penetrate the blood-brain barrier[154], thus exerting, at high doses, neurotoxic effects tested not only in animal and cell based experiments[150,155], but also in humans[149,156,157].

Due to this broad range of activities, it is not surprising that artemisinins have multiple mammalian targets[158,159]. It has been demonstrated that besides gephyrin[145,148], artemisinins also bind to pyridoxal kinase (PDXK)[145]. This essential enzyme catalyzes the synthesis of pyridoxal 5'-phosphate (PLP), the active form of vitamin B6. PLP serves as the essential cofactor for around 160 distinct human enzymatic activities which are involved in a wide variety of crucial cellular processes like cellular detoxification reactions and metabolic processes such as amino acid, carbohydrate and lipid metabolism, as well as neurotransmitter biosynthesis including the inhibitory neurotransmitters GABA and glycine[160-162]. GABA and glycine are synthesized by the PLP-dependent enzymes GAD and serine hydroxymethyl transferase (SHMT), respectively.

To better characterize the effects of artemisinins on basic neurobiological pathways, our lab recently investigated the mechanism of action of these drugs on PDXK. These studies included the crystallographic characterization of artemisinin-binding to the PDXK-active site, as well as biochemical and electrophysiological experiments, which demonstrated adverse effects of these drugs on GABA levels, thereby modulating inhibitory neurotransmission via the presynaptic site[163].

The structure of the artesunate-PDXK complex revealed that the drug-binding site partially overlaps with the substrate (PL)/product (PLP) binding site, thus suggesting an inhibitory action of the drug towards this enzyme (Figure I.5). *Ex vivo*, electrophysiological recordings in hippocampal slices, showed a statistically significant decrease in mIPSC after artemisinin administration in line with the gephyrin-mediated effects of the artemisinins. Curiously, at increased artemisinin concentrations a statistically significant decrease in the firing frequency was also observed, which indicates an impairment in the presynaptic terminals. This was confirmed by directly measuring the GAD activity in brain tissues, which revealed a reduction in the amount of GABA produced by this enzyme in the presence of these small drugs[163].

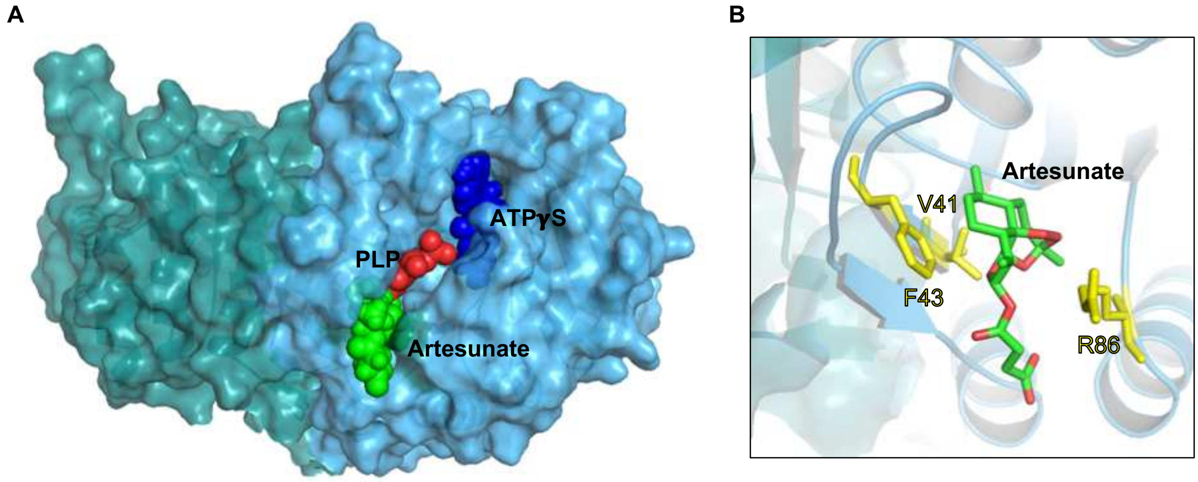

Figure I.5 ***PDXK in complex with artesunate. (A)*** *Artesunate interacts within the substrate-binding pocket of PDXK, thereby presumably affecting its catalytic activity. The PDXK dimer is shown in surface representation with one chain in petrol and the other in cyan. Artesunate (green), PLP (red) and ATPγS (blue) are displayed in sphere representation.* ***(B)*** *Zoom-in into the artesunate binding-pocket. The residues F43, V41 and R86 (yellow C-atoms) are involved in the artesunate (green C-atoms) binding (PDB: 6YK1, 3KEU).*

Besides modulating inhibitory neurotransmitter receptor clusters at postsynapses via their interactions with gephyrin, artemisinins are therefore also targeting inhibitory signal transmission by binding to the enzyme PDXK. This indirectly also affects neurotransmitter biosynthesis on the pre-synaptic side as the reduced levels of vitamin B6 impair the number of inhibitory neurotransmitters being produced by the GAD enzyme.

I.12 Gephyrin and its connection to the cytoskeleton

Cytoskeletal elements are key players in a variety of processes involving the transport and motility in the intracellular environment. In neurons, microtubules and microfilaments are not only essentials for neurogenesis, but also are involved in transporting components of the pre- and postsynaptic membrane from their site of synthesis towards the periphery[1].

Scaffolding molecules also interact with cytoskeletal anchoring elements to provide a physical platform for maintaining receptors at synapses and regulating downstream signaling pathways to adjust the molecular composition of the postsynaptic machinery necessary to sustain synaptic plasticity. In this sense, the reported direct binding of gephyrin to microtubules[76,130] and to the light chain of the microtubule motor protein dynein (DYNLL-1/2)[80] seems logical, however, the absence of microtubules in the direct vicinity of post-synaptically located gephyrin casts doubt on the functionality of this interaction as part of gephyrin's anchoring function. The inhibitory synapse also contains specific microtubule-associated components such as GABARAP ($GABA_A$ receptor associated protein), a microtubule and gephyrin ligand[137]. As actin filaments extend into the immediate vicinity of postsynaptic specializations a link to components or interactors of microfilaments would be of functional relevance. Hence the reported direct binding of gephyrin to actin-cytoskeleton associated proteins, namely, profilin 1, neuronal profilin 2a and the microfilament adaptors of the Mena/VASP family including neuronal Mena is noteworthy. Both profilin isoforms and Mena form complexes with gephyrin, at least *in vitro*[128].

Pharmacological studies suggested a role for both, microfilaments and microtubules in determining the size and number of GlyR clusters at the postsynaptic membrane[164]. For instance, in cultured spinal neurons at day *in vitro* 6 (DIV 6), when actin fibers are treated with cytochalasin D or any other depolymerizing alkaloid, the number of gephyrin clusters is affected[165-167]. Contrary, when actin microfilaments are depolymerized in mature spinal cord (DIV 10) or hippocampal neurons, the number of gephyrin clusters is not altered; although the average cluster sizes is drastically decreased[165,166].

I.13 The gephyrin-vasodilator stimulated-phosphoprotein (VASP) interaction

The neural isoforms of the Ena/VASP (enabled/Vasodilator Stimulated Phosphoprotein) family have been identified as interactors of gephyrin in neurons[128]. Ena/VASP proteins, which bind to uncapped actin filaments, would thereby act as adaptor proteins mediating the interaction between gephyrin and actin filaments.

Two studies regarding the interaction between gephyrin and VASP have already been published[80,81]. In 2003, Giesemann and collaborators studied the biding between these two proteins using co-immunoprecipitation, co-sedimentation and immunohistochemical data[128,129]. They identified through co-immunoprecipitation that the region responsible for the interaction in gephyrin is located in GephE. However, a few years later, Bausen and collaborators investigated this interaction by taking a different approach. In this case, they used GST-pull downs and co-localization assays to determine the binding region[129]. They found that the interacting region does not involve GephE, but instead the linker, specifically, a stretch encompassing the residues from 181 to 243, since a mutant lacking this region failed to co-localize with gephyrin in HEK293 cells.

On the other hand, regarding the interaction site of VASP, even less is known. Bausen *et al.* proposed, based on sequence homology, that the EVH1 domain (Ena/Vasp homology domain 1) harbors the binding site for gephyrin, since this region recognizes and binds to proteins containing the consensus sequence D/EFPPPPXD/E (abbreviated as "FPPPP" or "FP4"). This interaction is used to recruit Ena/VASP proteins to focal complexes and adhesions[168] but not to the leading edge of actin filaments[169]. However, upon closer examination the stretch of proline residues within the gephyrin linker region features the sequence "$_{187}$PSPPPPLS$_{194}$", which does not exactly fit to the canonical binding sequence. In this regard it is important to note that the phenylalanine is critical to maintain the interaction with the EVH1 domain as seen in crystal structures of this domain in complex with peptides derived from the metabotropic glutamate receptor 1α (mGluR) and the actin assembly-inducing protein (ActA)[170,171]. Nevertheless, one exception to this rule has been reported, namely the Tes protein (Testin LIM domain protein) that binds to the EVH1 domain of Mena proteins through its LIM domain. The LIM domain contains a unique double-zinc finger motif with a conserved distribution of cysteine and histidine residues in Lin-11, Isl-1 and Mec-3 (LIM) gene products, and in a competitive manner with zyxin binds to the same binding region on the EVH1 domain[172,173].

I.14 Ena/VASP family: Structure and function

The ena/VASP family consists of two orthologs identified in the invertebrates *Drosophila melanogaster* and *Caenorhabditis elegans*, one in the mycetozoan *Dictyostelium discoideum*, and the three vertebrate family members VASP, Mena, and EVL (Ena-VASP-like)[174-179].

The three vertebrate ena/VASP proteins, Mena, VASP, and EVL, share conserved domains (Figure I.6)[174]. Starting from the N-terminus, the EVH1 domain binds to proteins that typically contain one or more EVH1-binding sites with an optimal core consensus motif of "FP4"[180], such as vinculin[181,182], lamellipodin[183], zyxin[184], migfilin[185] and paladin[186], however, unconventional EVH1 ligands have been reported as mentioned before[173].

This domain is followed by a proline-rich central region (named Pro-rich) that contains binding sites for Src-homology 3 (SH3) and WW domains present in various signaling and scaffolding proteins The Pro-rich part is the most divergent region of the family and hence may have different binding partners and mechanisms of regulation. For instance, Enabled (Ena) binds to the SH3 domains of the Abelson tyrosine kinase (Abl), Src, and the carboxy-terminal SH3 domain of Drk[177,187,188], while EVL binds to the SH3 domains of Lyn, N-Src, Abl, and the WW domain of FE-65 (adaptor protein localized in nucleus)[189]. In contrast, Mena does not bind to the SH3 domain of N-Src, but is bound by the SH3 domain of IRSp53, Abl, Arg, Src, and the WW domain of FE65[174,190,191]. Besides, all ena/VASP family members contain proline-rich-binding sites for the small G-actin-binding protein profilin, and this binding is independent of their phosphorylation status[192,193]. Profilin II, the major profilin isoform expressed in brain tissues, binds as a dimer with high affinity to VASP but with low affinity to PI(4,5)P2. In contrast, profilin I has opposite binding preferences[194].

Mena family members feature a C-terminal EVH2 domain that contains G and F-actin binding sites (TLM and FAB, respectively, in Figure I.6) and a coiled-coil (CC) region that mediates tetramerization of all family members[195-197]. While the EVH1 and 2 domains are folded as demonstrated by their crystal structures[198,199], the central Pro-rich is mainly unstructured.

While *Drosophila* Ena has an additional glutamine-rich core region (Q-rich) of so far unknown function[177], vertebrate Mena has an additional region containing 13 repeats of the 5 amino acid residues leucine-glutamate-arginine-glutamate-arginine (LERER) within a 91-residue span located in between the EVH1 domain and proline-rich core[174]. The function of the LERER motif is currently still unknown. Mena contains a tyrosine phosphorylation site within an exonic variant (+EXON, Figure I.6) and all vertebrate ena/VASP proteins are substrates for the Ser/Thr protein kinases A and G and share a conserved N-terminal protein kinase A (PKA)-site[174,189,200]. *Drosophila* Ena is a substrate for the Abl and contains at least six sites for tyrosine phosphorylation[188]. In contrast, there are no reported phosphorylation sites in the *Dictyostelium* VASP and *C. elegans* UNC-34.

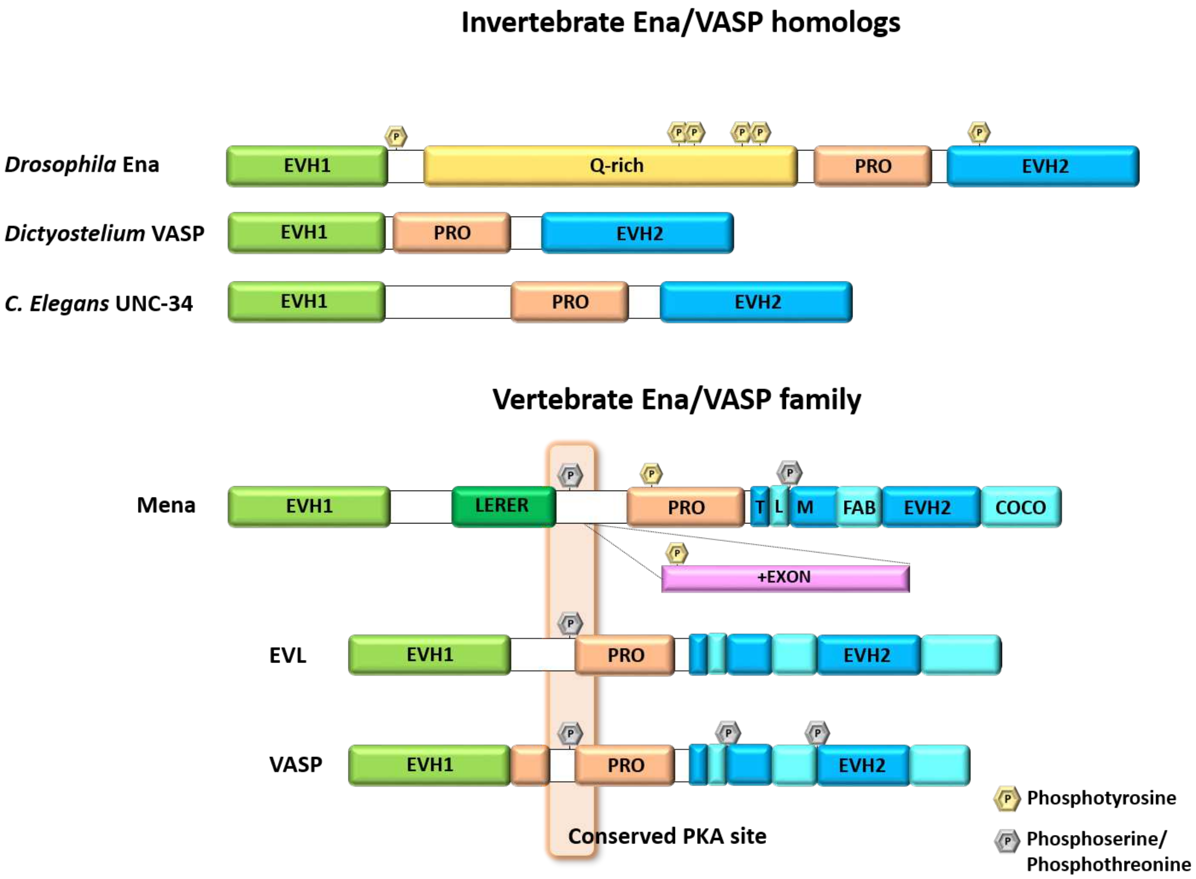

Figure I.6. Domain organization in the ena/VASP family. *The ena/VASP family includes two orthologs identified in the invertebrates Drosophila melanogaster and Caenorhabditis elegans, one in the mycetozoan Dictyostelium discoideum, and the three mammalian family members VASP, Mena, and EVL (Ena-VASP-like) [174,177-179]. All members share a conserved domain architecture consisting of a proline-rich core region (PRO), flanked by two distinct structured entities called Ena-VASP homology domains (EVH1 and EVH2, respectively). Drosophila Ena has an additional glutamine-rich core (Q-rich). Vertebrate Mena has an additional region containing repeats of the amino acid residues LERER and a neuronal specific alternative exon (+EXON) containing a tyrosine phosphorylation site.*

Members of the ena/VASP family have overlapping functions in cytoskeletal remodeling and the maintenance of cell polarity. They promote actin filament elongation and protect the barbed end of growing actin-filaments against capping proteins, thus regulating actin-related processes such as epithelial cell adhesion as well as axon outgrowth and guidance[201]. Each of the three proteins can support many ena/VASP-dependent cellular functions such as filopodial protrusion[202,203], formation of functional endothelial barriers[204], or stimulation of actin-based motility of the intracellular pathogen *Listeria monocytogenes*[205]. They primarily function as actin filament elongation factors, rather than nucleator factors[196,201]. Thus, depletion of individual ena/VASP proteins produces shorter and more densely branched filament networks, whereas overexpression causes the opposite effect[201,206].

Ena/VASP proteins localize within cells to areas of dynamic actin reorganization such as the leading edge of lamellipodia and at the tips of filopodia and other actin-dependent intracellular structures such as cell-cell contacts, focal adhesions, and in periodic puncta along stress fibers[174,189,207]. All these processes depend upon regulated cytoskeletal remodeling and implicate the ena/VASP family as a key linkage between signaling pathways and actin dynamics.

I.15 Ena/VASP family: Neuronal functions

Filopodia are characteristic for cells displaying exploratory behavior and are thought to sense guidance cues and pilot the growth cone[208,209]. Ena/VASP proteins have been implicated in integrating guidance signals into appropriate changes in cytoskeletal dynamics and are key regulators of filopodia formation and dynamics. These proteins are concentrated at areas of dynamic actin remodeling and have a well-established role in filopodia formation and elongation[207,208], likely functioning in multiple steps during nervous system development. Roles for Ena/VASP in neurulation[207,210], neuronal migration[211-213], dendritic morphology[214,215], and synapse formation[216-218] have been demonstrated. In addition, evidence suggests that both ena/VASP proteins present in *C. elegans* play a role in axon regeneration in this organism[219].

In mice, deletion of Mena caused axonal guidance defects in the formation of the corpus callosum, hippocampal commissure, pontocerebellar fiber bundles[207] and optic nerve formation[210]. Mena/VASP/EVL triple knockout mice exhibited stunted optic nerves that extended into the brain but failed to form the optic chiasm[203]. Contrary, the inhibition of ena/VASP function in *Xenopus laevis* retina by transfection of the FP4-Mito construct, typically used for tagging ena/VASP to mitochondria instead of to the leading edge, did not affect axon guidance, but did reduce actin filament elongation rates and terminal arborization[220]. Mena/VASP double knockout mutants display defects in the formation of several axon fiber tracts in the central and peripheral nervous system, including defects in all of the major forebrain commissures[210]. Also, analysis of mice lacking all three paralogs of ena/VASP reveals an unexpected requirement for these proteins in neuritogenesis in the cortex, leading to a block of cortical axon fiber tract formation[211]. This defect was shown to arise from a failure of ena/VASP-deficient cortical neurons to form neurites and can be rescued by overexpression of intrinsic factors, such as mDia2 and myosinX, or extrinsic ones, such as laminin, that induce filopodia formation. However, although filopodia are necessary, they are not sufficient for neuritogenesis, since dynamic microtubules are also required for neurite formation[203].

Interestingly, in ena/VASP double knockout mice, these proteins were required for neuritogenesis within the cortex, but not for other neuronal types, such as retinal ganglia, hippocampal neurons and dorsal root ganglia[221,222]. This suggests that signals absent from the cortex but present in structures that form axons promote ena/VASP-independent neurite initiation. One such factor is the extracellular matrix protein laminin which is largely absent from the cortex but is found in areas where ena/VASP-independent neuritogenesis occurs. Neuritogenesis is rescued by plating ena/VASP deficient primary cortical neurons on laminin but not fibronectin or collagen[203]. The existence of extrinsic (such as laminin) or intrinsic (such as mDia2 and myosinX) mechanisms that overcome the requirement for ena/VASP in neuritogenesis may also explain why this defect is not observed in mutants of the invertebrate ena/VASP orthologues.

D. melanogaster and *C. elegans* each have a single ena/VASP ortholog, Ena and UNC-34, respectively. Genetic studies in invertebrates implicated that the loss of ena/VASP function leads to subtle defects in axon guidance. Strikingly, ena/VASP appears to function downstream of both attractive and repulsive guidance cues, sometimes within the same cell. In worms, UNC-34 functions downstream of UNC-40/DCC (acronym for *Deleted in Colorectal Cancer*) and UNC-5, the two Netrin receptors in *C. elegans*[223,224]. Netrin receptors, present in vertebrates as well as invertebrates, are required for cell growth activity and axon migration during development[225]. Loss of UNC-34 partially suppresses the morphological phenotypes induced by a gain-of-function mutation in UNC-40/DCC[224], as well as axon repulsion induced by ectopic expression of UNC-5[223]. Genetic evidence also implicated *Drosophila* Ena in Netrin-mediated guidance[226]. In both flies and worms, ena/VASP appeared to function downstream of the repulsive guidance receptor Robo/Sax3, a molecule that binds directly to ena/VASP through an EVH1-binding site found on its cytoplasmic tail[227-229]. Genetic data also suggests that *D. melanogaster* Ena and D-abl may act antagonistically downstream of certain axon guidance receptors[227,230]. Other evidence implicated D-lar, a receptor tyrosine phosphatase that antagonizes D-Abl function in peripheral nervous system guidance[230], to be linked to Ena function. Deletion of either Ena or D-lar induced similar phenotypes in which intersegmental peripheral nerves failed to branch at the correct position and instead avoided their muscle target and extended beyond their normal branching point[230].

Not only that, in hippocampal neurons ena/VASP was found to be critical to form and extend filopodia, in response to Netrin-1 signaling upon PKA activation[231]. These results provide evidence that mammalian ena/VASP proteins directly regulate filopodial dynamics in response to guidance cues and are regulated by the activation of second messenger pathways (Netrin-1/DCC) that control growth cone behavior[231]. All three vertebrate family members are regulated by PKA, and, at least VASP, is known to be also phosphorylated by protein kinase G (PKG)[174,189,232-234]. While the family members display different PKA/PKG phosphorylation sites, they all contain one highly conserved PKA site located in between the EVH1 domain and the Pro-rich region (Figure I.6). Interestingly, many axon guidance molecules are regulated by downstream signaling depending on the status of cyclic nucleotide within growth cones[235]. For instance, in hippocampal neurons syndecan-2, a transmembrane heparan sulfate proteoglycan, activates PKA via neurofibromin and subsequently PKA phosphorylates ena/VASP, promoting filopodia and spine formation[216].

Ena/VASP proteins have been also implicated in spine formation. In studies performed with the use of FP4-mito constructs, it could be demonstrated that neurofibromin and ena/VASP proteins contributed to dendritic spine formation, perhaps through the regulation of filopodia formation[216]. VASP was shown to regulate actin polymerization in dendritic spines to modulate spine and synapse formation, synapse density, size, and morphology as well as spine head enlargement[217]. In cell-based experiments, the endogenous VASP knockdown produced a significant reduction in the density of spines and number of synapses, whereas the expression of a siRNA-resistant VASP rescued this defect. VASP puncta colocalized with SV2 and PSD95 clusters and VASP expression promoted a similar increase in the amount of PSD95, Homer, and Shank in spines, thus suggesting that VASP modulates the level of PSD-scaffolding proteins in spines. Additionally, VASP increased the number and retention of surface GluR1-containing α-amino-3-hydroxy-5-methyl-4-isoxazole propionic acid receptors (AMPARs) in spines to potentiate synaptic strength. The effect of VASP on synaptic GluR1 levels and its localization to spines were shown to be mediated by its EVH1 and EVH2 domains, thus suggesting that these domains may also be important for VASP function in the development of spines and synapses. Indeed, deletion of either the EVH1 or EVH2 domain of VASP significantly impaired spine and synapse formation[217].

In summary, the ena/VASP proteins are critical for nervous system development and dynamics, due to their involvement in vital processes like spine formation, expansion and modulation of synaptic strength, as well as the roles they play during neurulation, neuritogenesis, neuronal migration and dendritic morphology.

II Aims of the project

In mammals the anti-malarial drug artemisinin and its semi-synthetic derivatives artesunate and artemether target the inhibitory synapse-related proteins gephyrin and PDXK, the enzyme responsible for the biosynthesis of vitamin B6. Published work from the Schindelin lab recently demonstrated that the targeting of gephyrin by artemisinins affects its inhibitory neurotransmission from the postsynaptic side. Unpublished data further indicate that artemisinin-induced inhibition of PDXK affects the biosynthesis of GABA by the vitamin B6-dependent enzyme glutamic acid decarboxylase (GAD) and thus interferes with inhibitory neurotransmission presynaptically. To comprehensively describe the inhibition of PDXK by artemisinins, this thesis aims to enzymatically and biochemically characterize the binding of these drugs to PDXK.

A second aim of this thesis addresses the three-dimensional structure of gephyrin. While its N-terminal and C-terminal domains have been structurally well characterized, the large highly disordered central linker region introduces proteolytic susceptibility and renders the FL protein recalcitrant to crystallization. A low-resolution structure of gephyrin was derived by applying a combination of SAXS and AFM methodologies. Nevertheless, a high-resolution structure of the intact protein which would show how the terminal domains are arranged relative to each other, whether the linker is completely disordered or may be responsible to mask the dimer interface in the E-domain and how the two active sites in the terminal domains are arranged relative to each other is urgently needed. Hence, a concise effort has been made to derive the structure of gephyrin by electron-cryo microscopy (cryo-EM). Starting with sample optimization involving the gradient fixation (GraFix) approach and incorporating biochemical optimization steps, a first low resolution structure could be derived.

Several proteins have been described to interact with gephyrin, however, only a few of these interactions have been characterized at the molecular level. Notable exceptions are the interactions between gephyrin and the GlyRs and $GABA_A$Rs, however, how gephyrin is linked to acting filaments remains unclear. Although it is known that gephyrin interacts with the actin-related protein VASP, one of the three members of the ena/VASP family of proteins, the particular regions involved in this interaction remain unmapped and the physiological role of this interaction is only poorly defined. With the aim of bridging this gap in our knowledge, the work presented here biochemically and functionally characterizes the complex formed between VASP as well as other members of the ena/VASP family and gephyrin. With the aid of biochemical, biophysical and cell-based approaches, the amino acid regions harbored in gephyrin and VASP that are responsible of this binding were defined, and the affinity and thermodynamic parameters of this complex were determined. Lastly, initial experiments to functionally characterize the interaction between VASP and gephyrin are described.

III Materials & Methods

III.1 Materials

III.1.1 Chemicals, reagents and media

The following list contains the chemicals used in this thesis (Table III.1). All buffers and solutions were prepared with ultrapure water generated by a TKA GenPure system.

Table III.1 Chemicals, reagents and media

Chemical	Supplier
4-(2-hydroxyethyl)-1-piperazineethanesulfonic acid (HEPES)	Carl Roth
4’, 6-diamidino-2-phenylindole (DAPI)	Thermo Fisher Scientific
Acetic acid	Carl Roth
Acrylamide/Bis-acrylamide (37.5:1)	Carl Roth
Adenosine 5’-triphosphate magnesium salt (Mg-ATP)	Sigma-Aldrich
Agar	Carl Roth
Agarose HEEO ultra quality	Carl Roth
Agarose NEEO ultra quality	Carl Roth
Alexa Fluor 647 protein labeling kit	Thermo Fisher Scientific
Ammonium persulfate (APS)	Carl Roth
Ampicillin (Amp) sodium salt	Carl Roth
Artemisinin	Sigma-Aldrich
Artesunate	Sigma-Aldrich
B27 499 supplement	Invitrogen
Benzamidine hydrochloride	Carl Roth
Bovine serum albumin (BSA)	Sigma-Aldrich
Bromophenol blue sodium salt	Carl Roth
Chloramphenicol (Cam)	Carl Roth
Chloroquine diphosphate salt	Sigma-Aldrich
cOmplete™, EDTA-free protease inhibitor cocktail	Sigma-Aldrich (Roche)
Coomassie Brilliant Blue G-250	Carl Roth
Coomassie Brilliant Blue R-250	Carl Roth
D-sucrose	Carl Roth
Diethylaminoethyl (DEAE)-dextran	Thermo Fisher Scientific
Dithiothreitol (DTT)	Carl Roth
Dnase I	Invitrogen
Dulbecco’s Modified Eagle Medium (DMEM)	Gibco
Ethanol	Carl Roth
Ethylenediaminetetraacetic acid (EDTA)	Carl Roth
Fetal complete serum (FCS)	Gibco
Gibco Opti-MEM	Gibco
Glucose	Invitrogen
GlutaMAX	Gibco
Glutamine	Invitrogen

Glutaraldehyde, 25% solution	Carl Roth
Glycerol	Carl Roth
Glycine	Carl Roth
Hydrochloric acid (HCl)	Carl Roth
Imidazole	Carl Roth
Isopropyl-β-D-thiogalactopyranoside (IPTG)	Carl Roth
Kanamycin sulfate (Kan)	Carl Roth
Lipofectamine 2000	Thermo Fisher Scientific
Lysogeny broth (LB) medium	Carl Roth
Magnesium chloride ($MgCl_2$)	Carl Roth
Mowiol 4-88	Carl Roth
NBT/BCIP substrate	Sigma-Aldrich
Neurobasal medium	Invitrogen
Orange G	Sigma-Aldrich
Penicillin/streptomycin	Gibco
Phenylmethylsulfonyl fluoride (PMSF)	Carl Roth
Pierce™ ECL western blotting substrate	Thermo Fisher Scientific
Poly-L-ornithine	Invitrogen
Potassium chloride (KCl)	Carl Roth
Potassium dihydrogen phosphate (KH_2PO_4)	Sigma-Aldrich
Pyridoxal hydrochloride	Sigma-Aldrich
Sodium chloride (NaCl)	Carl Roth
Sodium dodecyl sulfate (SDS)	Carl Roth
Sodium hydroxide (NaOH)	Carl Roth
Sodium phosphate dibasic (Na_2HPO_4)	Sigma-Aldrich
Sodium pyruvate	Gibco
Tetramethylethylenediamine (TEMED)	Carl Roth
Tris-(hydroxymethyl)-aminomethane (Tris)	Carl Roth
Trypsin	Invitrogen
Tween-20	Carl Roth
Uranyl acetate	Agar scientific
β-Mercaptoethanol (βmE)	AppliChem
HRV-14, 3C protease	In-house production

III.1.2 Consumables and instruments

The list of consumables excludes general glass and plastic bottles and containers.

Table III.2 Consumables

Type	Model	Supplier
Centrifugal concentrator	Amicon® Ultra-0.5, 4 and 15 mL	Merck Millipore
Centrifuge tube	Cellstar® centrifuge tube – 15 and 50 ml	Greiner Bio-One
Cuvettes	Rotilabo® -single-use	Carl Roth
Dialysis membranes	Spectra/Por®	Spectrum Laboratories
Filter paper		Sartorius
Gloves	Nitril gloves	Star Lab
Microwell 96 plates	Nunc	Thermo Scientific

Mini-PROTEAN® TGX™ precast gels	4-20% gradient gel	Bio-Rad Laboratories
Monolith NT.115 premium capillaries		NanoTemper Technologies
Nitrocellulose membrane		Amersham
Optical quality sealing foil	VIEWsealTM	Greiner Bio-One
Parafilm® M	2 in. x 250 ft	Sigma-Aldrich
Pipette tips	Pipette tips – 10, 200, 1000 l	Mettler-Toledo
Polymerase chain reaction (PCR) tubes	Multiply®-Pro cup 0.2 ml, Multiply®-µStrip 0.2 ml chain, 8-Lid chain, flat	Sarstedt
Polyvinylidene difluoride (PVDF) membrane		Amersham
Reaction tubes	SafeSeal tube – 0.5, 1.5 ml clear and 2 ml brown	Sarstedt
Sterile filter	Acrodisc® sterile filter for syringe – 0.22 and 0.45 µm	Pall
Syringes	Omnifix® syringes – 1, 5, 10 and 20 ml	B. Braun

Table III.3 Instruments

Instrument	**Model**	**Supplier**
Agarose gel electrophoresis system	Mini-Sub® Cell GT System	Bio-Rad Laboratories
Autoclave	Systec V-150	Systec
Balance	XS 6002S Dual Range	Mettler Toledo
Balance, analytical	XS 105 Dual Range	Mettler Toledo
Biological Safety Cabinet	Class II Safe 2020	Thermo Fisher Scientific
Block thermostat	Rotilabo® block thermostat H 250	Carl Roth
CD cuvette	Cylindrical absorption cuvette, path length 1 mm	Hellma Analytics
Cell disruption system	M-110P	Microfluidics
Centrifuges	5417 R 5424 5804 R 5430 R	Eppendorf
Centrifuges	Avanti J-26 XP Avanti J-HC	Beckman Coulter
Crossover tweezers N5 Stainless steel. 0.10 x 0.06 mm tip	Dumont HP	Agar Scientific
Electrophoresis	Mini-PROTEAN Tetra Cell	Bio-Rad Laboratories
Electrophoresis power supply	PowerPac™ Basic	Bio-Rad Laboratories
FPLC systems (Protein purification)	ÄKTA™ pure 25 ÄKTA™ avant 25 ÄKTA™ purifier 10	GE Healthcare
Gel Imaging UV	Universal Hood 2 II	Biorad
Gel-drying device	GelAir Gel Dryer	Bio-Rad Laboratories

Gradient master instrument		BioComp
Grid box		Agar scientific
Imaging system	Odyssey	LI-COR Biosciences
Imaging system	ChemiDoc™ MP Imaging System	Bio-Rad Laboratories
Incubator	B15 Compact Incubator	Heraeus
Incubator (CO_2)	CB 210	Binder
Incubator (CO_2)	Hera Cell 240	Thermo Fisher Scientific
Laminar flow hood Class II		Thermo Fisher Scientific
Magnetic stirrer	MR 3002	Heidolph Instruments
Microplate reader	Clariostar®	BMG LABTECH
Microscope	IX81	Olympus
Microscope	DM IL LED	Leica
Microscope confocal laser scanning system	FV1000	Olympus
Microscope spectral detector	FVD10 SPD	Olympus
Microwave		Privileg
Mini Trans-Blot cell		Bio-Rad Laboratories
Monolith	NT.115Pico	NanoTemper Technologies
PCR-cycler	Mastercycler® EPgradient S Mastercycler® pro S	Eppendorf
pH meter	BlueLine 14 pH	SCHOTT
Pipette (Multichannel)	Pipet-Lite Multi Pipette L8-20XLS+	Mettler-Toledo
Pipettes	XLS+ LTS PIPET 0.1-2 L XLS+ LTS PIPET 0.5-10 L XLS+ LTS PIPET 2-20 L XLS+ LTS PIPET 20-200 L XLS+ LTS PIPET 100-1000 L	Mettler-Toledo
Plasma Cleaner		Harrick Plasma
Plunge freezer	FEI Vitrobot Mark IV	IST Austria
Rotors for Beckman Coulter centrifuges	JLA 16.250 JA-25.50 JS-5.0 JLA-8.100	Beckman Coulter
Shaking incubators	ISF-1-W ISF-1-X LT-X	Kühner
Spectrophotometer	BioPhotometer	Eppendorf
Spectrophotometer	NanoDrop ND 1000	Peqlab
Thermomixer	Thermomix comfort	Eppendorf
Transmission electron microscope	120 kV FEI Tecnai G2	IST Austria
Transmission electron microscope	200 kV Cryos Titan	Thermofisher
Ultracentrifuge	Swinging-Bucket Rotor SW 60 Ti Optima L-100XP	Beckman Coulter

Ultracentrifuge	Optima L-100XP	Beckman Coulter
Ultrapure water system	TKA GenPure	Thermo Fisher Scientific
UV imaging system	Gel Doc™ XR System	Bio-Rad Laboratories
Vortex mixer	Vortex-Genie 2	Scientific Industries
Water bath		GFL

III.1.3 Chromatography columns and resins

Table III.4 Chromatography columns and resins

Type	Model	Supplier
Affinity matrix for intein-chitin isolation	Chitin Resin	New England Biolabs
Analytical size exclusion chromatography (SEC) FPLC columns	Superose™ 6 increase 10/300 GL (Superose 6 increase) Superdex™ 200 10/300 GL (SD 200 10/300) Superdex™ 75 10/300 GL (SD75 10/300)	GE Healthcare
Column body	Econo-Column®	Bio-Rad Laboratories
Immobilized metal-ion affinity chromatography resin	Protino® Ni-IDA	MACHEREY-NAGEL
Ion exchange columns	MonoQ® 10/100 GL MonoS® 10/100 GL	GE Healthcare
Preparative SEC FPLC column	HiLoad™ 16/600 Superdex™ 200 pg (SD 200 16/600)	GE Healthcare
	HiLoad™ 16/600 Superdex™ 75 pg (SD75 16/600)	GE Healthcare

III.1.4 Cloning materials and enzymes

Table III.5 Cloning kits and chemicals

Chemical and/or kit	Supplier
2'-Deoxyadenosine 5'-triphosphate (dATP), sodium salt solution 100 mM	Thermo Fisher Scientific
2'-Deoxycytidine 5'-triphosphate (dCTP), sodium salt solution 100 mM	Jena Biosciences
2'-Deoxyguanosine 5'-triphosphate (dGTP), sodium salt solution 100 mM	Thermo Fisher Scientific
2'-Deoxythymidine 5'-triphosphate (dTTP), sodium salt solution 100 mM	Thermo Fisher Scientific
Bovine serum albumin (BSA)	New England Biolabs
Calf intestinal phosphatase (CIP)	New England Biolabs
CutSmart buffer 10x	New England Biolabs
Dpn I	New England Biolabs
EcoRI HF	New England Biolabs
GC buffer (PCR)	New England Biolabs

GeneRuler™ 1 kb DNA Ladder	Thermo Fisher Scientific
Gibson Assembly kit	New England Biolabs
HindIII HF	New England Biolabs
Midori Green Advance	Biozyme Scientific
NEBuffer™ 2 (Cloning)	New England Biolabs
Nucleospin gel and PCR cleanup kit	Macherey-Nagel
Nucleospin plasmid kit	Macherey-Nagel
PageRuler™ prestained protein ladder	Thermo Fisher Scientific
Phusion® high fidelity DNA polymerase	Thermo Fisher Scientific
Polyethyleneglycol 4000	Carl Roth
Q5-Site directed mutagenesis kit	New England Biolabs
Standard Taq Reaction Buffer	New England Biolabs
T4 DNA ligase	New England Biolabs
T4 DNA ligase buffer 10x	New England Biolabs
T4 DNA polymerase	New England Biolabs
T4 kinase (PNK)	New England Biolabs
Taq DNA polymerase	New England Biolabs

III.1.5 Bacterial strains and plasmids

Table III.6 Plasmids for protein expression in bacterial and mammalian cells

Construct name	Vector	Tag	Uniprot/ protein sequence	Antibiotics	Aim	Author/Supplier
Gephyrin-FL	pET28b	N-His	Q03555/ 1-763	Kanamycin	Protein purification	Bodo Sander
GephE	pTWIN	N-Intein	Q03555/ 318-763	Ampicillin	Protein purification	Eun Young Lee
GephG	pET28b	N-his	Q03555/ 1-181	Kanamycin	Protein purification	Bodo Sander
Green fluorescent protein (GFP)-Gephyrin	pEGFPC2	N-GFP	Q03555/ 1-763	Kanamycin / Neomycin	Expression in mammalian cells	Eun Young Lee
His-VASP	pQE30	N-his	P70460/ 1-337	Ampicillin	Protein purification	Frank Gertler
His-VASP (Evh1)	pQE30	N-his	P70460/ 1-115	Ampicillin	Protein purification	-
His-VASP (Evh1Pro)	pQE30	N-his	P70460/ 1-208	Ampicillin	Protein purification	-
His-VASP (Evh2)	pQE30	N-his	P70460/ 220-337	Ampicillin	Protein purification	-
His-VASPΔ125-144	pQE30	N-his	P70460/ 1-115	Ampicillin	Protein purification	-
His-VASP (E136A/E137A)	pQE30	N-his	P70460/ 1-115	Ampicillin	Protein purification	-

His-VASP (K142A/R143A)	pQE30	N-his	P70460/ 1-115	Ampicillin	Protein purification	-
wtVASP	prk5	N-flag	P70460/ 1-337	Ampicillin	Mammalian cell-based studies	-
VASP(evh1)	prk5	N-flag	P70460/ 1-115	Ampicillin	Mammalian cell-based studies	-
VASP(evh1-pro)	prk5	N-flag	P70460/ 1-208	Ampicillin	Mammalian cell-based studies	-
VASP(pro)	prk5	N-flag	P70460/ 116-219	Ampicillin	Mammalian cell-based studies	-
VASP(evh2)	prk5	N-flag	P7046/ 220-337	Ampicillin	Mammalian cell-based studies	-
VASPΔ125-144	prk5	N-flag	P70460	Ampicillin	Mammalian cell-based studies	-
VASP(E136A/E137A)	prk5	N-flag	P70460	Ampicillin	Mammalian cell-based studies	-
VASP(K142A/R143A)	prk5	N-flag	P70460	Ampicillin	Mammalian cell-based studies	-
Mena	prk5	N-flag	Q03173	Ampicillin	Mammalian cell-based studies	Synthetic Gene (ATG: biosynthetics GmbH)
wtPDXK	pETM14	N-his	Q8k183	Kanamycin	Protein purification	Nicole Bader
PDXK(R86W)	pETM14	N-his	Q8k183	Kanamycin	Protein purification	Nicole Bader
PDXK(V41W)	pETM14	N-his	Q8k183	Kanamycin	Protein purification	Nicole Bader
PDXK(F43R)	pETM14	N-his	Q8k183	Kanamycin	Protein purification	Nicole Bader
PDXK(V41W/F43R)	pETM14	N-his	Q8k183	Kanamycin	Protein purification	Nicole Bader

Linker201-255 peptide synthetized and kindly provided by Dr. Hans Maric, sequence: ^{201}PHKQTEDKGVQCEEEEEEKKDSGVASTEDSSSHITAAALAAKIPDSIISRGVQV^{255}

Mena cDNA (GenBank: NM_001083121.2) synthetized and cloned into a pUC vector by ATG: Biosynthetics GmbH.

Table III.7 Bacterial strains

Organism	Strain	Genotype	Usage	Supplier
Escherichia coli (E. coli)	DH5α	F^- φ80 *lac*ZΔM15 Δ(*lac*ZYA-*arg*F)U169 *rec*A1 *end*A1 *hsd*R17(rK$^-$, mK$^+$) *pho*A *sup*E44 λ^- *thi*-1 *gyr*A96 *rel*A1	Cloning, plasmid amplification	Invitrogen
E. coli	BL21(DE3)	F^- *ompT gal dcm lon hsdSB(rB– mB–) λ(DE3 [lacI lacUV5-T7p07 ind1 sam7 nin5]) [malB+]K-12(λS)*	Protein expression	Invitrogen
E. coli	BL21-CodonPlus^R (DE3)-RIL	F^- *ompT hsdS*(rB$^-$ mB$^-$) *dcm*$^+$ Tet^r *gal* λ(DE3) *endA* Hte[*argU ileY leuW* **Cam^r**]*	Protein expression	Stratagene
E. coli	SoluBL21	Not provided	Protein expression	Novagen
E. coli	BL21-CodonPlus (DE3)-RP	F^- ompT hsdS(r$^-$ m$^-$) dcm$^+$ Tet^r gal λ(DE3) endA Hte [argU proL BB **Cam^r**]*	Protein expression	Novagen

*Concentration of antibiotic used for selection: chloramphenicol 34 μg/ml.

III.1.6 Oligonucleotides

All listed primers were ordered form Sigma-Aldrich®. Abbreviations are given in the last row of the table.

Table III.8 List of primers used for generation of bacterial and mammalian expression constructs

Name	Sequence (5'- 3')
EVH1_115 fw	TAATAAGGTGGGCCTCCC
EVH1_115 rv	TCCTTCCAAGGCCTCTA
EVH2_222 fw	AATAGTGGGGGTTCCGGGG
EVH2_337 rv	GGATCCGTGATGGTGATGGTG
LP_prk5 fw	GCAGAAGCTTGGCC
LP_prk5_FLAG rv	CTTATCGTCGTCATCCTTGTAATCCATGGGGAATTCAATCGATAGAAC
Vasp_FLAG_SLIC_prk5 fw	CTACGATTGAATTCCCCATGGATTACAAGGATGACGACGATAAGATGAGCGAGACGG
Vasp_SLIC_prk5 rv	ATGGCGGCCAAGCTTCTGCTTATTAGGAGTCATCACTGGAGC
Vasp_115_SLIC_prk5 rv	ATGGCGGCCAAGCTTCTGCTTATTATCCTTCCAAGGCCTC
Pro-rich_FLAG_SLIC_prk5 fw	CTATCGATTGAATTCCCCATGGATTACAAGGATGACGACGATAAGGGTGGGCCTCCCCC
Pro-rich_SLIC_prk5 rv	ATGGCGGCCAAGCTTCTGCTTATTATGGGGCCCCGGAACC
Vasp_208_SLIC rv	ATGGCGGCCAAGCTTCTGCTTATTATGTAGGGAGTGGGG

EVH2_FLAG_SLIC_prk5 fw	CTATCGATTGAATTCCCCATGGATTACAAGGATG ACGACGATAAGGGCCTGGCTGCT
VASP_deletion_P125 rv	GGGTGCTGGGGCT
VASP_deletion_Q144 fw	CCGGAGCATATGGAGC
VASP_ E136A/E137A rv	GGAGGGACCATTCTGG
VASP_E136A/E137A fw	CCAGCAGCGCTGGAACAACAGAAAAGG
VASP_ K142A/R143A rv	GTTCCAGCTCCTCTGG
VASP_K142A/R143A fw	AACAGGCAGCGCAGCCGGAGCATATG
PDXK (R86W) fw*	CTCACTGGTTACACGTGGGACAAGTCTTTCCTG
PDXK (R86W) rv*	CAGGAAAGACTTGTCCCACGTGTAACCAGTGAG
PDXK (V41W) fw*	GATGCCGTGAACTCTTGGCAGTTTTCAAACC
PDXK (V41W) rv*	GGTTTGAAAACTGCCAAGAGTTCACGGCATC
PDXK (F43R) fw*	GTGAACTCTGTGCAGCGTTCAAACCACACAGG
PDXK (F43R) rv*	CCTGTGTGGTTTGAACGCTGCACAGAGTTCAC
PDXK (V41W/ F43R) fw*	GATGCCGTGAACTCTTGGCAGCGTTCAAACCACA CAGG
PDXK (V41W/ F43R) rv*	CCTGTGTGGTTTGAACGCTGCCAAGAGTTCACGG CATC

* The design of these oligonucleotides and the molecular cloning for obtaining these constructs was done by Ms. Nicole Bader, who kindly provided these constructs for the performance of this study.
Abbreviations: forward primer (fw), reverse primer (rv)

III.1.7 Cell lines, animals and antibodies

For primary neuronal cultures: CD-1 mice (Charles River, Sulzfeld, Germany) were used. The animals were transferred into the animal facility of the Institute for Clinical Neurobiology (Würzburg, Germany). Experiments were approved by the local veterinary authority (*Veterinäramt der Stadt Würzburg*) and the Ethics Committee of Animal Experiments, *i.e. Regierung von Unterfranken, Würzburg* (License numbers 55.2-2531.01-09/14; 55.2.2-2532.2-536). Mice were housed in cages with filter top (EU Direction 2010/63/EU) with access to water and food ad libitum at a 12 hours light/dark rhythm with lights on at 6.30 a.m. Pregnant female mice were sacrificed by overdose exposure to CO_2 and hippocampal cells were prepared from embryos at stage E16.

Table III.9 Cell lines

Cell line	Description
HEK293	Human embryonic kidney 293. ATCC® CRL-1573™
COS-7	*Cercopithecus aethiops* kidney. ATCC® CRL-1651™

Table III.10 Antibodies

Antibody	Catalog number/Clon	Supplier
Alexa Fluor 488-conjugated goat anti-rabbit IgG	115-546-003	Dianova
Alexa Fluor 647-conjugated donkey anti-chicken	703-605-155	Dianova
Anti-Flag	9A3	Cell signaling
Anti-Gephyrin	ab181382	Abcam
Anti-Gephyrin	147111/mAb7a37	Synaptic Systems
Anti-Mena	MAB2635	Merck
Anti-Synapsin 1 & 2	106006	Synaptic Systems
Anti-VASP	orb163147	Biorbyt
Cy3-conjugated goat anti-mouse	115-165-003	Dianova
GFP-trap MA (magnetic agarose) beads	gtma-100	Chromotek
Goat anti-mouse IgG	31320	Thermo Fisher
Goat anti-rabbit IgG	G-21079	Thermo Fisher
Horseradish peroxidase (HRP)-conjugated goat anti-mouse IgG	115-035-008	Dianova
HRP-conjugated goat anti-rabbit IgG	111-035-045	Dianova

III.1.8 Software, server and databases

Table III.11 Software, server and databases

Name	Usage	Source
ESPript 3.0	Depiction of sequence similarity after sequence alignment by ClustalW	[236] http://espript.ibcp.fr
ExPASy ProtParam	Protein parameters	[237]
GraphPad Prism 7.0	Interaction assay data analysis	GraphPad Software, La Jolla California USA, www.graphpad.com
ImageJ	Image processing and analysis	National Institute of Health
Inkscape 0.92	Figures design	www.inkscape.org,

		free open source software
Kalign website	Multiple Sequence alignment	[238]
MARS data analysis software	Enzymatic assays data analysis	BMG Labtech
Microsoft Office 365 ProPlus Excel, Word	Activity assay data analysis Word processing	Microsoft Office
MO.Affinity Analysis version 2.3	Advanced data analysis for MST interaction assays	NanoTemper Technologies
MO.Control	MST planning and assay setup	NanoTemper Technologies
ODYSSEY	Imaging software	LI-COR
Origin	Data analysis software	OriginLab
Pep-Fold server	Peptide folding prediction	[239,240]
Protein Data Bank (PDB)	Protein structures	rcsb.org, [241]
PubMed (NCBI)	Literature research	ncbi.nlm.nih.gov/pubmed/
PyMOL	3D visualization and graphical depiction of structures	[242]
RaptorX	Protein structure prediction	[243]
Relion 3.0	Determining cryo-EM structures	[244]
siRNA at Whitehead	Designing of siRNA	[245]
SnapGene	DNA, Protein sequence handling generation of primers	SnapGene software (from GSL Biotech; available at snapgene.com)
UCSF Chimera	3D visualization and graphical depiction of structures	[246]
UNICORN	Aekta control and data analysis	GE Healthcare
UniProt	Information about proteins	uniprot.org, [247]

III.2 Methods

III.2.1 Molecular biology

III.2.1.1 PCR amplification

For PCR amplification of inserts and vectors I used the Phusion Polymerase Kit (NEB), following the instructions of the manufacturer.

Briefly, I designed primers with overlapping 5’ overhangs, in both the insert and the vector, for the next step in cloning. The PCR reaction was set up in a total volume of 20 µL reaction using a 2-fold dilution of the Phusion Polymerase Master Mix, 1 µL of each primer (fw and rv at a concentration of 10 µM) and 10 ng of template DNA.

The PCR conditions used were:

Step	Temperature °C	Time seconds
Initial denaturation	98	30
25 Cycles	98	10
	50-65	30
	72	30 seconds / kb
Final extension	72	120
Hold	4	

III.2.1.2 Site-directed mutagenesis and gene modification

For the insertion of stop codons, shortening of constructs and gene modifications I regularly used the Q5 Site-directed Mutagenesis Kit (NEB, E0552S), following the instructions of the manufacturer.

Briefly, I designed primers suitable for the substitution, deletion or insertion of nucleotides into the gene. The reaction was set up in 20 µL reaction using a 2-fold dilution of the Q5 Hot Start High-Fidelity Master Mix, 1 µL of each primer (fw and rv at a concentration of 10 µM) and 10 ng of template DNA.

The PCR conditions used were:

Step	Temperature °C	Time seconds
Initial denaturation	98	30
25 Cycles	98	10
	50-65	30
	72	30 seconds / kb
Final extension	72	120
Hold	4	

Afterwards, 1 µL of the PCR product was subjected to a DpnI digestion together with phosphorylation and ligation reactions, using the enzyme cocktail KLD provided with the kit. This reaction ran for 30 minutes at room temperature.

Lastly, 5 µL aliquot of the resulting mixture was used for the transformation into chemically competent *E. coli* DH5α cells.

III.2.1.3 Cloning strategy via SLIC

For sub-cloning of the GOI (Gene Of Interest) into different vectors, I used the SLIC method (Sequence and Ligation independent Cloning)[248]. Basically, this technic takes advantage of *in vitro* homologous DNA recombination and single-strand annealing.

Briefly, I designed two pairs of primers (one for the linearization of the vector and other one for the amplification of the GOI), with 12-15 nucleotides annealing overhangs. After PCR (chapter III.2.1.1), the products were treated with the restriction enzyme DpnI for 1 hour at 37 °C to eliminate the template DNA and increase the ligation efficiency. Then, the PCR products were purified using the PCR Clean-up Kit (Macherey-Nagel) and the DNA concentration was measured using a spectrophotometer (Nanodrop ND1000, PEQLAB).

For the cloning procedure, I first treated the insert and the vector separately with T4 DNA polymerase in NEB-2-buffer plus BSA at room temperature for 30 minutes. The set up for 50 µL reaction was as follow: 5 µL NEB 2 buffer (NEB) and 1.5 µL T4 DNA polymerase (NEB), using 1 µg of DNA and adjusting the volume with distilled (dd) H_2O. Afterwards, I quenched the reaction using 1 µL of 100 µM dCTP and put the sample on ice. Then, I proceeded with the chemical transformation.

Alternatively, the Gibson Assembly Kit (NEB) was used in some cases, following the manufacturer instructions, to improve the ligation efficiency.

III.2.1.4 Cloning strategy via restriction enzyme digestion

The sub-cloning of genes into other vectors was done by restriction enzyme digestion. For that, 2 µg of DNA were treated for 2 hours at 37 °C with 1 µL of each restriction enzyme diluted in the appropriate buffer (usually CutSmart buffer). After 2 hours, 0.2 µL of calf intestinal phosphatase (CIP) was added to the reaction which continued for another 2 hours. Then, the GOI and the vector were separated by running them on a 1% agarose gel. The desired band was cut from the gel and purified using a PCR clean up kit. The DNA concentration was measured in a spectrophotometer (Nanodrop ND1000, PEQLAB). Afterward, the gene was further phosphorylated for the subsequent ligation. For the phosphorylation reaction 100 ng of DNA were incubated with the T4 kinase (PNK) enzyme in PEG 4000 at a final concentration of 5% (w/v) and the reaction mixture was adjusted to 25 µL with ddH_2O and incubated at 37 °C for 30 minutes, and then heat inactivated (65 °C for 20 minutes), before starting the ligation reaction. After cooling on ice, 1 µL of T4 DNA ligase was added to this mixture which was incubated at 16 °C overnight.

III.2.1.5 DNA analysis by gel electrophoresis and ultraviolet–visible spectroscopy

DNA quality and composition were assessed by DNA agarose gel electrophoresis. The gels contained 1% (w/v) NEEO ultra-quality agarose, 1x TAE buffer and Midori Green Advance (3 µL/ 50 mL gel). DNA samples were mixed with 6x DNA loading buffer (final concentration: 1x) and subjected to gel electrophoresis in 1x TAE buffer for 30 min at a voltage of 100 V. DNA fragments were visualized with the electrophoresis gel imaging cabinet Universal Hood II (Biorad) using a laser exciting the fluorescence of Midori Green which had intercalated in the respective DNA fragments. DNA length was estimated by comparison with a DNA ladder (GeneRuler 1 kbp). DNA concentrations were determined by ultraviolet-visible (UV-VIS) spectroscopy using a spectrophotometer (Nanodrop ND1000) and assuming an extinction coefficient ε_{DNA}(260 nm) of 0.02 mL/µg·cm.

III.2.1.6 Chemical transformation

Aliquots of 50 µL chemically competent *E. coli* DH5α cells were incubated with 10-100 ng of target DNA on ice for 30 minutes. Afterward the cells were subjected to a 90 s heat shock in a Thermomixer. Subsequently, the cells were incubated on ice for three minutes, before 250 µL LB medium were added and the bacteria were shaken at 200 rpm and a temperature of 37°C for 60 minutes. Afterward an aliquot was added to either 5 mL, 50 mL or 100 mL LB medium in appropriately sized flasks with the required antibiotics. The volume of LB medium was chosen depending on the purpose as follows: Pre-cultures for expression tests (50 mL), purification of DNA (5 mL) or precultures for obtaining protein for scaled-up purification (100 mL). All samples were incubated overnight at 37 °C. In case of aiming to obtain single colonies for analysis of plasmid sequences, a 100 µL aliquot was added to an LB-agar plate containing the appropriate antibiotic(s) for selection.

III.2.1.7 Plasmid isolation

Single colonies obtained after chemical transformation were transferred to LB-medium with the appropriate antibiotics. The cultures were shaken overnight at 200 rpm at 37°C and centrifuged at 4,000 g for 10 min at 4°C. The cell pellet was subjected to DNA isolation protocol following the manufacturer instructions of the NucleoBond Plasmid Kit (Macherey-Nagel). The resulting DNA was sent for sequencing with specific or standard primers to the Microsynth SeqLab (https://srvweb.microsynth.ch).

III.2.2 Recombinant protein expression

The pre-culture cell suspension was used to scale up of the culture, using a 1:100 dilution, into 2 L of LB medium in 5 L flasks for heterologous protein production. The cultures were kept at 37°C for around 4-5 hours or until an OD_{600nm} of ~ 0.8 was reached. Afterward, the expression of protein was induced with IPTG (1 mM final concentration). Depending on the protein, each construct had its own conditions for optimum production of protein, which are summarized in Table III.12.

Table III.12 Expression strains, times and temperatures after induction with IPTG for different proteins.

Protein construct	*Vector/ Antibiotic*	*E. coli* strain	Temperature (°C) & Duration (h)
Gephyrin-FL	pET28b/ Kan	BL21-CodonPlus^R (DE3)-RIL (Cam)	15 °C 16-18h
GephE	pTWIN1/ Kan	BL21-CodonPlus^R (DE3)-RIL (Cam)	30°C 16-18h
GephG	pET28b/ Kan	BL21(DE3)	20°C 16-18h
hisVASP	pQE30/ Amp	SoluBL21	37°C 5h
hisVASPΔ125-144	pQE30/ Amp	SoluBL21	37°C 5h
hisVASP(E136A/E137A)	pQE30/ Amp	SoluBL21	37°C 5h
hisVASP(K142A/R143A)	pQE30/ Amp	SoluBL21	37°C 5h
hisVASP(evh1)	pQE30/ Amp	SoluBL21	37°C 5h
hisVASP(evh2)	pQE30/ Amp	BL21-CodonPlus^R (DE3)-RP (Cam)	20°C 16-18h

wtPDXK	pETM14/ Kan	SoluBL21	30°C 16-18h
PDXK(V41W)	pETM14/ Kan	SoluBL21	30°C 16-18h
PDXK(R86W)	pETM14/ Kan	SoluBL21	30°C 16-18h
PDXK(F43R)	pETM14/ Kan	SoluBL21	30°C 16-18h
PDXK(V41W/F43R)	pETM14/ Kan	SoluBL21	30°C 16-18h

III.2.3 Protein purification

III.2.3.1 Cell lysis and affinity chromatography

For cell lysis, the pellet from 16 L of culture was resuspended in 200 mL lysis buffer (for buffers, see Table III.13) supplemented with one tablet of the Roche EDTA-free cOmplete protease inhibitor cocktail, 100 µl DNase I solution (~250 UI/µL), 75 mg of PMSF and 150 mg of benzamidine hydrochloride at 4°C. Cells were lysed in two cycles using a mechanical cell disruptor at ~1500 bar and the lysate was cleared by centrifugation (1 h 35,000 g, at 4°C). The supernatant with the N-terminal 6xHis-tagged protein was applied twice to a gravity flow column containing (4-7 g) Protino® Ni-IDA resin followed by two washing steps, with 100 ml of one of them high salt buffer and the next one with 25-50 mM imidazole. The subsequent protein elution step (80 ml) was performed using in elution buffer containing 250 mM imidazole. In the case of GephE, with the N-terminal Intein tag, the sample was applied to 35 mL bed volume of chitin agarose beads and the elution was performed by a pH shift from pH 8.0 to pH 7.0. Affinity chromatography was performed at 4°C (except for GephE where it was performed at room temperature), collecting the column flow through of each step on ice. After analysis of aliquots representing the different purification steps by SDS polyacrylamide gel electrophoresis (SDS-PAGE), the elution fractions containing the protein of interest were pooled and equilibrated by adding a Low salt buffer (Table III.13) for further purification step by ion exchange chromatography.

Table III.13 Buffers for cell lysis and affinity chromatography

Name	**Gephyrin-FL**	**GephG**	**GephE**	**hisVASP (evh1) and (evh2)**
Lysis buffer	50 mM HEPES pH 8.0, 500 mM NaCl, 10 % glycerol 5 mM βmE	50 mM Tris-HCl pH 8.0, 250 mM NaCl, 5 mM βmE	20 mM Tris-HCl pH 8.5, 500 mM NaCl, 5 mM βmE	20 mM Tris-HCl pH 7.0, 200 mM KCl, 2mM $MgCl_2$, 1mM EGTA, 20 mM Imidazole, 1 mM DTT
Equilibration buffer	50 mM HEPES pH 8.0, 500 mM NaCl	50 mM Tris-HCl pH 8.0, 250 mM NaCl	Same as Lysis buffer	20 mM Tris-HCl pH 7.0, 200 mM KCl, 2 mM $MgCl_2$, 1 mM EGTA, 20 mM Imidazole
Wash buffer	50 mM HEPES pH 8.0, 500 mM NaCl, 10 mM Imidazole 5 mM βmercaptoethanol	50 mM Tris-HCl pH 8.0, 1 M NaCl, 5 mM βmE	50 mM HEPES pH 8.0, 500 mM NaCl, 10% glycerol, 1 mM EDTA, 5 mM βmE	Same as Lysis buffer

Wash buffer 1	50 mM HEPES pH 8.0, 300 mM NaCl, 50 mM imidazole 5 mM βmE	50 mM Tris-HCl pH 8.0, 250 mM NaCl, 25 mM imidazole, 5 mM βmE	50 mM HEPES pH 7.0, 150 mM NaCl, 10 % glycerol, 1 mM EDTA, 5 mM βmE	-
Elution buffer	50 mM HEPES pH 8.0, 250 mM NaCl, 250 mM imidazole 5 mM βmE	50 mM Tris-HCl pH 8.0, 250 mM NaCl, 250 mM imidazole, 5 mM βmE	50 mM HEPES pH 8.0, 80 mM NaCl, 1 mM EDTA, 5 mM βmE	20 mM Tris-HCl pH 7.0, 200 mM KCl, 2mM $MgCl_2$, 1mM EGTA, 250 mM imidazole, 1 mM DTT
Dilution or Low salt buffer	20 mM HEPES pH 8.0, 1 mM EDTA, 5 mM βmE	-	-	20 mM Tris-HCl pH 7.0, 1 mM DTT

Regarding the PDXK (and related mutants), a different strategy was followed for purification. The cell pellet from 8 L of culture was resuspended in 150 mL of lysis buffer (50 mM Tris-HCl pH 8.0, 300 mM NaCl, 5 mM βmE), supplemented with one tablet of the Roche EDTA-free cOmplete protease inhibitor cocktail and 20 µl DNase I solution (~250 UI/µL) at 4°C. After cell disruption in two cycles using a mechanical cell disruptor at ~1500 bar the lysate was cleared by centrifugation (30 minutes 75,000 g, at 4°C). The supernatant with the N-terminal 6xHis-tagged protein was incubated in a beaker with 5 g of Protino® Ni-IDA resin for 1 hour at 4 °C, followed by two washing steps, one with 100 ml high salt buffer (equals to lysis buffer but with 1 M NaCl instead of 300 mM), and the second with 50 mL of washing buffer 2 (50 mM Tris-HCl pH 8.0, 250 mM NaCl, 20 mM imidazole, 5 mM βmE). The subsequent protein elution step (100 ml) was performed using the elution buffer containing 250 mM imidazole (50 mM Tris-HCl pH 8.0, 250 mM NaCl, 250 mM imidazole, 5 mM βmE). The eluted protein was subjected to dialysis overnight at 4 °C in the presence of 3C protease (5 µg of protease/mg of protein).

III.2.3.2 Ion exchange and size exclusion chromatography

For the GephG and GephE constructs, usually size exclusion chromatography (SEC) following the affinity chromatography was sufficient for protein purification. The column (SD 200 16/600) was equilibrated with storage buffer (see Table III.14) before the concentrated proteins (c ~10mg/ml) were applied. Samples from the elution fractions were analyzed by SDS-PAGE and the ones containing pure protein were pooled, concentrated, aliquoted and flash frozen in liquid nitrogen for further storage at -80°C.

Table III.14 Buffers for ion exchange chromatography and size exclusion chromatography

Name	**Gephyrin-FL**	**GephG**	**GephE**	**hisVASP, (Evh1), (Evh2), Δ125-144, (E136A/E137A), (K142A/R143A)**
Buffer A	20 mM HEPES pH 8.0, 1 mM EDTA, 5 mM βmE	-	-	20 mM Tris-HCl pH 7.0, 80 mM NaCl, 1 mM DTT
Buffer B	20 mM HEPES pH 8.0, 2 M NaCl, 1 mM EDTA, 5 mM βmE	-	-	20 mM Tris-HCl pH 7.0, 1 M NaCl, 1 mM DTT

Storage buffer	20 mM HEPES pH 8.0, 150 mM NaCl, 5% glycerol, 5 mM βmE	50 mM Tris-HCl pH 8.0, 150 mM NaCl, 5 mM βmE	20 mM HEPES pH 8.0, 150 mM NaCl, 5 mM βmE	20 mM Tris-HCl pH 7.0, 200 mM NaCl, 5% glycerol, 5 mM DTT

Gephyrin-FL was purified using an additional anion exchange chromatography step (column MonoQ 10/100 GL) before the final SEC step. The column was pre-equilibrated with buffer A and eluted with a 30-column volume (CV) linear gradient of buffer A to 30% buffer B. The VASP variants (hisVASP, hisVASP(evh1), hisVASP(evh2), hisVaspΔ125-144, hisVasp(E136A/E137A) and hisVasp(K142A/R143A)) were purified using an additional cation exchange chromatography step (column MonoS 10/100 GL) prior to SEC. After the affinity chromatography, the proteins were diluted with low salt buffer (Table III.13) to obtain a salt concentration of ~80 mM. The proteins were then applied to the respective ion exchange column pre-equilibrated with buffer A and eluted with a 20 CV linear gradient of buffer A to 100% buffer B. Fractions containing the protein were pooled, concentrated and further purified by SEC (SD 200 16/600 GL). Pure protein fractions were then handled and stored as described above.

For the purification of PDXK (wild-type and mutants), following the overnight dialysis, the protein was subjected to SEC using a SD 200 16/600 GL column. The column was pre-equilibrated with 25 mM Tris-HCl pH 8.0, 150 mM NaCl, 5 mM βmE. The fractions were analyzed by SDS-PAGE and those with a purity > 95% were pooled and stored as described above.

III.2.4 Biochemical and biophysical analyses

III.2.4.1 UV/Vis spectrophotometry

DNA and protein concentrations were measured spectrophotometrically using the NanoDrop™ 1000 instrument. Prior to each measurement, a blank was performed utilizing the corresponding buffer of the sample. DNA absorbance was measured at 260 and 280 nm and the purity of the samples was determined by the ratio of the absorbances at 260 nm and 280 nm. For protein concentrations (mg ml^{-1}) the absorbance at 280 nm with a path length of 1 cm was measured and divided by the calculated extinction coefficients at A280 for each protein (1g/l), assuming all Cys residues being in the reduced state. Extinction coefficients and molecular weights of each protein construct were obtained from the ExPASy ProtParam website[237] and are listed in Table III.15.

Table III.15 Extinction coefficients and molecular weights

Protein	Extinction coefficient (10^3 $M^{-1}cm^{-1}$) assuming all Cys residues are in the reduced state	Molecular weight (kDa)
GephFL	31.4	84.0
GephG	7.0	22.0
GephE	22.0	45.0
HisVASP	33.4	42.1

HisVASP(Evh1)	20.9	14.2
HisVASP(Evh2)	2.98	10.9
HisVaspΔ125-144	27.9	39.9
HisVasp(E136A/E137A)	33.4	42.0
HisVasp(K142A/R143A)	33.4	42.0
wtPDXK	35.1	31.4
PDXK(V41W)	35.2	36.9
PDXK(R86W)	35.2	36.9
PDXK(F43R)	35.1	31.4
PDXK(V41W/F43R)	35.2	36.9

III.2.4.2 SDS-polyacrylamide gel electrophoresis

For the analysis of proteins by SDS-PAGE a 15% acrylamide gel was usually used. Basically, the 15 % acrylamide solution for the running gel was made with a 30% acrylamide solution, 1.5 M Tris pH 8.8 and 10% SDS. The 5 % acrylamide solution for the stacking gel was made with the 30% acrylamide solution, 1.0 M Tris pH 6.8 and 10% SDS. As catalyzers of the polymerization reaction 14 µL TEMED (Sigma-Aldrich) and 50 µL of 10% (w/v) ammonium persulfate solution were used for every 5 mL of polyacrylamide gel made.

The gel was set up with the wing clamp assembly (Bio-Rad). In cases where a gradient gel was needed, precast Mini-PROTEAN® TGX™ Precast Gels (Bio-Rad) were used. Gels were run at 200 V for 40 minutes at room temperature. For protein detection, a Coomasie G 250 staining solution (80 mg of Coomasie G 250 in 1 L of ddH2O acidified with 3 mL of 37% HCl) was used, and after heating in a microwave at 800 W for 60 sec and a subsequent 5 minutes incubation, distaining was done in water with an initial heating step in the microwave.

III.2.5 Interaction studies: Mapping the interaction site

III.2.5.1 Analytical size exclusion chromatography

Analytical size exclusion (aSEC) was used for analyzing the formation of a complex by the visualization of a left shift in the elution volume with respect to the elution volumes of the binary components. Protein mixtures were incubated in a 1:1 molar ratio in a range of concentrations (50-100 µM) for 1 hour at 4°C followed by high speed centrifugation at 10,000 g for 10 minutes. Afterward, a 100 µL aliquot was analyzed by using a Superdex 200 pg 10/30 GL or a Superdex 75pg 10/30 GL or a Superose 6 Increase column (all from GE Healthcare) depending on the molecular weight of the analyzed proteins and the separation range of the column. aSEC was performed in a buffer containing 50 mM Tris pH 7.5 150 mM NaCl 5 mM βmE at 4 °C at a flow rate of 0.5 mL/min. Complex formation was either directly detected on the chromatograms by following the absorbance at 280 nm and 260 nm as a function of time, or by SDS-PAGE analysis of selected fractions.

III.2.5.2 Native agarose gel shift assay (NAGE)

Protein mixtures were incubated for one hour at 4°C in assay buffer (50 mM Tris pH 7.5 150 mM NaCl 5 mM βmE), and then mixed with Orange G dye (Carl Roth) (60% glycerol 0.1‰

Orange G) in a 5:1 volumetric ratio. Samples were loaded on a 1% agarose gel (HEEO ultra quality agarose, Carl Roth) which contained 25 mM Tris and 200 mM glycine pH 7.5. Electrophoresis was carried out in a horizontal electrophoresis unit (Vari-Gel MAXI Horizontal Gel System, Carl Roth) at 4°C and a constant voltage of 90 V for 90 minutes. Gels were stained for 45 minutes in PAGE staining solution (1‰-5‰ Coomasie R250, 50% ethanol 10% acetic acid) and distained overnight in PAGE distaining solution (10% ethanol 5% acetic acid) for visualization of the proteins.

III.2.5.3 Cell-based experiments with gephyrin and VASP expressed in HEK293 cells

III.2.5.3.1 Cell culture co-transfection of HEK293 cells for co-immunoprecipitation assays

HEK293 human embryonic kidney cells (ATCC® CRL-1573™) were cultured in 10 cm dishes (2*10^6 cells seeded per dish) and grown in minimal essential medium (MEM) supplemented with 10% fetal complete serum (FCS), 200 mM GlutaMAX, 100 mM sodium pyruvate, and 50 U/mL penicillin/streptomycin under standard growth conditions at 37°C and 5% CO_2. Cells were transiently transfected with GFP-gephyrin and flag-VASP (or the respective fragments/variants) using a modified calcium phosphate co-precipitation method. Briefly, a mixture of 10 µg of each plasmid DNA, $CaCl_2$, 0,1xTE buffer and 2xHBS (50 mM HEPES, 12 mM glucose, 10 mM KCl, 280 mM NaCl, 1.5 mM Na_2HPO_4) was applied to the cells. GFP-gephyrin and flag-VASP plasmids were used at an equal molar ratio. Media was exchanged after 6 h. Cells were harvested 72 h after co-transfection by centrifugation at 135 g.

III.2.5.3.2 Co-immunoprecipitation assay of proteins expressed in HEK293 cells

After harvest HEK 293 cells were lysed in TBS buffer pH 8.0 containing 2 mM EDTA and 1% Triton X-100. 600 µL of cell lysate were added to 25 µL of prewashed GFP-Trap MA beads followed by overnight incubation at 4 °C with rotational agitation. On the following next day, the beads were washed three times with 400 µL of wash buffer (50 mM Tris-HCl pH 8.0 160 mM NaCl 5 mM EDTA 1% Triton X-100). After washing, 30 µL of 2X SDS-sample loading buffer was added to the beads followed by heating at 70°C for 5 minutes. A magnetic field was applied to the beads and the supernatant was loaded on an SDS-PAGE. To analyze the co-immunoprecipitation (co-IP), a Western blot (WB) was performed.

III.2.5.3.3 Western blot analysis

For the WB nitrocellulose membranes were used, which were first put into transfer buffer (25 mM Tris/HCl pH 8.3 190 mM glycine, 20% ethanol) for 5 minutes, while the SDS-PAGE was ongoing. Next, the gel together with the pre-activated membrane were assembled in the Mini Trans-Blot cell. The transfer of the proteins from the gel to the membrane was achieved by applying an electric current of 300 mA for 1 hour at 4°C.

To block the nitrocellulose membrane, it was incubated for 1 hour in TBS (50 mM Tris/HCl pH 7.5 150 mM NaCl)-Albumin Fraction V 2.5% (w/v) followed by washing with TBS-T (50 mM Tris/HCl pH 7.5, 150 mM NaCl, 0.05% (w/v) Tween-20).

Afterward, the membrane was incubated overnight with the primary antibody at 4°C (usually diluted 1:1000 in TBS buffer following the manufacturer's instructions). The

primary antibody was an anti-gephyrin antibody (ab181382, Abcam) and/or an anti-flag antibody (Cell signaling, 9A3).
The next day, two 5 min rinsing steps with TBS were conducted followed by two rinsing steps with TBS-T of equal duration. Subsequently, the blots were incubated with the secondary antibody (usually diluted 1:10000 in TBS). As secondary antibodies anti-rabbit-IgG and/or anti-mouse-IgG were used for the detection of gephyrin and flag-specific bands, respectively. After incubation with the secondary antibody, the blots were washed three times with TBS-T, 10 min each and the blots were developed by chemiluminescence detection using the NBT/BCIP and bands were detected over color development.

III.2.5.3.4 Colocalization analysis of gephyrin and VASP proteins expressed in HEK293 cells

III.2.5.3.4.1 Cell culture and co-transfection of HEK293 cells for immunofluorescence staining

HEK293 human embryonic kidney cells were cultured on 14 mm glass coverslips (50,000 cells seeded per coverslip) pre-coated with poly-L-ornithine (1.5 µg/mL) and grown in minimal essential medium (MEM) supplemented with 10% FCS, 200 mM GlutaMAX, 100 mM sodium pyruvate, and 50 U/mL penicillin/streptomycin under standard growth conditions at 37°C and 5% CO_2. Cells were transiently transfected with GFP-gephyrin and flag-VASP (or its fragments/variants) using a modified calcium phosphate co-precipitation method. Briefly, a mixture of 1 µg of each plasmid DNA, $CaCl_2$, 0,1xTE buffer and 2xHBS (50 mM HEPES, 12 mM glucose, 10 mM KCl, 280 mM NaCl, 1.5 mM Na_2HPO_4) was added to the cells. GFP-Gephyrin and flag-VASP plasmids (1 µg of each plasmid DNA) were used at an equal molar ratio. Media was exchanged after 6 h of co-transfection. Immunocytochemical staining was performed 72 h after co-transfection.

III.2.5.3.4.2 Immunofluorescence staining of HEK293 cells and visualization

72 h after co-transfection the cells were fixed for 10 min with 4% paraformaldehyde (PFA) at room temperature. Then, the cells were washed carefully quickly three times with PBS (137 mM NaCl, 2.7 mM KCl, 8 mM Na_2HPO_4, and 2 mM KH_2PO_4, pH 7.4) and blocked for 30 min with 5% (v/v) goat serum and 0.2% Triton X-100 in PBS. For staining, the fixed cells were incubated for 60 min with an anti-flag monoclonal antibody (dilution 1:1000) and after washing, for another 60 min with the secondary antibody, a Cy3-conjugated goat anti-mouse antibody (dilution 1:500). Cells were incubated for 5 min with 4', 6-diamidino-2-phenylindole (DAPI; stock solution: 1 mg/mL in methanol; final working dilution: 1 µg/mL) at room temperature and mounted on glass slides with Mowiol 4-88. Images were acquired using an inverted Olympus IX81 microscope equipped with an Olympus FV1000 confocal laser scanning system, a FVD10 SPD spectral detector and diode lasers of 405 nm (DAPI), 495 nm (eGFP-gephyrin), and 550 nm (Cy3-flag-VASP) (Olympus, Tokyo, Japan). The image shown in this thesis were acquired with an Olympus UPLSAPO 60x (oil, numerical aperture 1.35) objective.

III.2.5.4 Quantification of gephyrin and VASP colocalization in COS cells

III.2.5.4.1.1 Co-transfection and immunofluorescence of COS-7 cells

COS-7 (*C. aethiops* kidney) cells (ATCC® CRL-1651™) were cultured on 14 mm glass coverslips (50,000 cells seeded per coverslip) pre-coated with poly-L-ornithine (1.5 µg/mL) and grown in MEM supplemented with 10% FCS, 200 mM GlutaMAX, 100 mM sodium pyruvate, and 50 U/mL penicillin/streptomycin under standard growth conditions at 37°C and 5% CO_2. Cells were transiently transfected with GFP-gephyrin and flag-VASP (or their fragments/variants). Briefly, a mixture of 1 µg of each plasmid DNA, 30 µL of PBS and 62 µL of DEAE-dextran were mixed and applied to the cells. GFP-gephyrin and flag-VASP encoding plasmids were used at an equal molar ratio. The cells were incubated for 30 minutes in an incubator at 37 °C, and afterward the medium was exchanged with the 3 mL medium to 12 µL of chloroquine were added. The cells were again incubated for 2-3 hours at the same temperature and then the medium was exchanged to medium without chloroquine for a final time. Immunocytochemical staining was performed for 72 h after co-transfection following the protocol previously described for the HEK293 cells (chapter III.2.5.3.4.2). To analyze the colocalization, 25 different pictures were recorded with an Olympus confocal microscope and the grade of colocalization was measured in ImageJ using the JaCoP plugin[249,250]. Statistical analysis was done in GraphPad Prism, version 7.0 (GraphPad Software, La Jolla California USA, www.graphpad.com).

III.2.5.5 Colocalization analyses in primary neuronal cells

III.2.5.5.1Primary hippocampal neuron culture preparation

Primary cultures of hippocampal neurons at day *in vitro* 21 (DIV 21) were prepared for confocal microscopy from CD-1 mice (Charles River, Sulzfeld, Germany; source: chapter III.1.7) at embryonic day 16 (E16). Hippocampi were incubated with 0.5 mg/mL trypsin and 10 µg/mL DNase I in PBS containing 10 mM glucose for 15 min at 37 °C. After washing once in DMEM supplemented with 10% (v/v) FCS, 25 µg/mL pyruvate and 2 mM glutamine, cells were dissociated by trituration. Supernatants were centrifuged at 60 g for 10 min and the cells were seeded in DMEM supplemented as described above at a density of 150,000 cells per well onto a 14 mm-glass coverslip coated with poly-L-ornithine (1.5 µg/mL). After 3 h the medium was replaced with Neurobasal medium containing 2 mM glutamine, 25 µg/mL pyruvate and 2 % (v/v) B27 499 supplement. All media contained 50 IU/mL penicillin and 50 µg/mL streptomycin. The local veterinary authority and the Committee on the Ethics of Animal Experiments (*Regierung von Unterfranken*) authorized the experiments (License numbers 55.2-2531.01-09/14; 55.2.2-2532.2-536).

III.2.5.5.2 Immunofluorescence staining of primary hippocampal neurons and visualization

Primary hippocampal neurons were staining against gephyrin, VASP and synapsin. Immunostaining was carried out as described before (chapter III.2.5.3.1), only introducing minor changes, as described next. After fixation with 4% PFA and 4% sucrose in PBS, the cells were incubated for 10 min in 50 mM NH_4Cl solution in PBS. After three washing steps with PBS, 50 µL of 0.1 mM glycine were added onto the coverslip. Then, the washing with PBS was repeated followed by the blocking step which was carried out as described before (III.2.5.3.4.2).

After fixation, the cells were analyzed with primary antibodies against gephyrin (mouse monoclonal antibody, clone mAb7a37, dilution 1:500), VASP (rabbit polyclonal antibody, dilution 1:500) and synapsin 1 & 2 (chicken polyclonal antibody, dilution 1:500). The secondary antibodies were Alexa Fluor 488-conjugated goat anti-rabbit IgG (dilution 1:250), Alexa Fluor 647-conjugated donkey anti-chicken (dilution 1:250) and Cy3-conjugated goat anti-mouse (dilution 1:250). Fluorescence imaging was conducted with a laser scanning confocal microscope (Fluorview FV 1000, Olympus) using a 63X objective. All pictures were acquired as single confocal sections in sequential scanning mode for simultaneous multi-channel fluorescence imaging and were averaged four times to reduce the noise.

III.2.5.6 Binding studies by microscale thermophoresis (MST)

III.2.5.6.1 Fluorescence labeling of the bait protein

For the labeling of the protein Alexa Fluor 647 was used as fluorophore using the Alexa Fluor 647 Protein Labeling Kit from company Thermo Fisher Scientific according to the manufacturer's instructions. The labeling reaction relies on succinimidyl esters (NHS esters) that react sub-stoichiometrically with primary amines so that on average only 1 lysine of the protein react with the dye.

The labeling reaction was performed in 20 mM HEPES pH 8.0 150 mM NaCl at room temperature for 60 min in the dark. The proteins used were 1 mg of gephyrin or 2 mg of VASP (VASP was previously subjected to dialysis overnight at 4 °C to exchange the buffer from 20 mM Tris pH 7.0 to 20 mM HEPES pH 8.0).

Unreacted dye was removed with the dye removal column supplied with the kit which was equilibrated with the same buffer. The degree of labeling was determined using UV/VIS spectrophotometry at 650 and 280 nm. For determining the degree of labeling, Equation III.A and Equation III.B were used.

Equation III.A

$$Protein\ concentration\ (M) = {\lfloor A280nm - (A650nm * 0.03) \rfloor * dilution\ factor} \Big/ {\xi protein}$$

Equation III.B

$$moles\ dye\ per\ mole\ protein = {A650nm * dilution\ factor} \Big/ {239000 * protein\ concentration\ (M)}$$

Where 0.03 is the correction factor to account for absorption of the dye at 280nm, and 239,000 is the molar extinction coefficient in units of $M^{-1}\ cm^{-1}$ of the Alexa Fluor 647 dye at 650 nm.

III.2.5.6.2 MST measurements

Labeled gephyrin was adjusted to a concentration of 2 nM in HEPES buffer pH 7.5, 150 mM NaCl supplemented with 0.05 % Tween 20. The ligand VASP or related proteins (EVH1, Δ125-144, E136A/E137A, K142A/R143A) were dissolved in the same buffer, and a series of 16 twofold dilutions were prepared using the same buffer, producing ligand concentrations ranging from 200 µM to 52 nM. For the measurement, each ligand dilution was mixed with one volume of labeled gephyrin, which led to a final gephyrin concentration of 1 nM and final ligand concentrations ranging from 100 µM to 26 nM.

The same set up was performed using labeled VASP and unlabeled gephyrin or the linker201-255 peptide as ligand. In this case, the final VASP concentration was 1 nM and the final ligand concentration ranged from 150 µM to 9.2 nM (gephyrin) and 500 µM to 30.5 nM (linker201-255 peptide).

The samples were incubated for 30 min, followed by centrifugation at 10,000 g for 10 min, and each supernatant was loaded into a Monolith NT.115 Premium Capillary. MST was measured at 36 °C using a Monolith NT.115Pico instrument. Instrument parameters were adjusted to 5% LED power and high MST power. Data of three independently pipetted measurements were processed with the MO. Affinity Analysis software version 2.3 (NanoTemper Technologies) using an MST-on time 2.5 s signal and further analyzed using GraphPad Prism version 7.0 (GraphPad Software, La Jolla California USA, www.graphpad.com).

III.2.5.6.3 MST binding assays at different temperatures

To measure binding at different temperatures, basically the same procedure as described previously (chapter III.2.5.6.2) was followed. In this case, the labeled protein was gephyrin, at the same concentration as before and the ligand concentration was ranging from 1.0 mM to 52 nM. The final concentration of gephyrin was 1 nM and the VASP concentrations were in the range from 500 µM to 26 nM. MST was again measured using the Monolith NT.115Pico instrument at temperatures of 22 °C, 25 °C, 28 °C, 30 °C, 32 °C and 36°C. The instrument parameters were set and the analysis was conducted as described before (chapter III.2.5.6.2).

III.2.5.6.4 Van't Hoff plot and calculation of thermodynamic parameters

To determine the thermodynamic parameters the association constants K_a (equal to $1/K_d$) obtained at different temperatures were plotted against the reciprocal value of the absolute temperature in a van't Hoff plot[251] which should show a linear relationship. From the experimental points a linear regression was calculated using the program Excel (Microsoft Office). From the slope of the line the molar enthalpy ΔH° of the binding reaction was determined according to the equation slope= $-\Delta H^\circ/R$ and from the intercept with the y-axis the molar entropy ΔS° according to the equation intercept= $\Delta S^\circ/R$ with R being the universal gas constant (1.987 cal/mol*K). The free energy ΔG° of the interaction at the different temperatures was calculated using the equation: $\Delta G^\circ = -RT\ln K_a$.

III.2.5.6.5 MST binding assays at different salt concentrations

For testing the binding at different salt concentrations, basically the same procedure as previously described (chapter III.2.5.6.2) was used. In this case, the labeled protein was gephyrin at the same concentration as described before while the ligand concentration was varied between 200 µM to 52 nM. The final concentrations in the measurements of gephyrin was 1 nM and VASP was used in the range from 100 µM to 5.2 nM. The proteins were diluted and incubated in HEPES buffer pH 7.5 supplemented with 0.05 % Tween 20 with NaCl concentration of 50 mM, 100 mM, 150 mM, 250 mM, 350 mM and 500 mM. MST was measured using a Monolith NT.115Pico instrument at 36°C. The instrument parameters and data analysis were as described before (chapter III.2.5.6.2).

III.2.6 Functional studies

III.2.6.1 Design of interfering RNA molecules

The design of interfering small hairpin RNA (shRNA) molecules followed the instructions of the Systems Bioscience manual for shRNA cloning and expression in lentivectors. Briefly, for designing the shRNA, the siRNA platform at the Whitehead Institute at the Massachusetts Institute of Technology (http://sirna.wi.mit.edu) was used. The input GenBank sequences were NM_001282021.1 and NM_001083121.2, corresponding to the *Mus musculus* VASP mRNA and *Mus musculus* Mena mRNA, respectively. From the resulting sequences of 19 shRNAs with the specified length of 19 nucleotides, potentially good candidates were chosen according to the GC content which was set to be in the range of 40%-55%, the absence of a thermodynamically stable secondary structure with a ΔG value below 0 kcal/mol and exhibiting less than 70% of identity with other mRNA sequences in the RefSeq database (Appendix I). Table III.16 summarizes the shRNA sequences, cloned in sense and antisense direction respect to the eGFP (Figure III.2), used for the knockdown of VASP or Mena expression and the scrambled shRNA (designed with https://www.invivogen.com/sirnawizard/scrambled) to be used as control.

Table III.16 shRNA for knockdown of Mena/VASP proteins in murine neuronal cells

Name	Sequence	Target
VASP shRNA #1 fw	GCAGGTGGTTATCAACTGTCTTCCTGTCAGACT CGGTTTGAGTCCTTTCATTTTT	NM_001282021.1 *Mus musculus* VASP mRNA
VASP shRNA #1 rv	AAAAATGAAAGGACTCAAACCGAGTCTGACAG GAAGACAGTTGATAACCACCTGC	
VASP shRNA #2 fw	GATCCGAGCCAAACTCAGGAAAGTCTTCCTGT CAGACTCGGTTTGAGTCCTTTCATTTTT	
VASP shRNA #2 rv	AAAAATGAAAGGACTCAAACCGAGTCTGACAG GAAGACTTTCCTGAGTTTGGCTC	
Mena shRNA #1 fw	GGGTTCAGCAGAGTACATACTTCCTGTCAGAC CCAAGTCGTCTCATGTATTTTTT	NM_001083121.2 *Mus musculus* Mena mRNA
Mena shRNA #1 rv	AAAAAATACATGAGACGACTTGGGTCTGACAG GAAGTATGTACTCTGCTGAACCC	
Mena shRNA #2 fw	GGATGCTAGACAGGTGTATCTTCCTGTCAGAC CTACGATCTGTCCACATATTTTT	
Mena shRNA #2 rv	AAAAATATGTGGACAGATCGTAGGTCTGACAG GAAGATACACCTGTCTAGCATCC	
Mena shRNA #3 fw	GACAGGTGTATGGTCTCAACTTCCTGTCAGACT GTCCACATACCAGAGTTTTTTT	
Mena shRNA #3 rv	AAAAAAACTCTGGTATGTGGACAGTCTGACAG GAAGTTGAGACCATACACCTGTC	
Mena shRNA #4 fw	GGTCTATGATGATGCCAATCTTCCTGTCAGACC AGATACTACTACGGTTATTTTT	
Mena shRNA #4 rv	AAAAATAACCGTAGTAGTATCTGGTCTGACAG GAAGATTGGCATCATCATAGACC	

scrambled (Scr) shRNA fw	GACCGAGAACGGATATACACTTCCTGTCAGAC TGGCTCTTGCCTATATGTTTTTT	Non-target. control
Scr shRNA rv	AAAAAACATATAGGCAAGAGCCAGTCTGACAG GAAGTGTATATCCGTTCTCGGTC	

As a general rule of thumb, the shRNA contains the restriction sites at each end for cloning into the lentiviral vector, the sense strand, then a loop, then the antisense strand, followed by a terminator sequence (Figure III.1).

```
RS              Sense Strand              Loop          Antisense Strand           Terminator   RS
5' GATCCNNNNNNNNNNNNNNNNNNNNNCTTCCTGTCAGANNNNNNNNNNNNNNNNNNNNNTTTTTG 3'
       3' GNNNNNNNNNNNNNNNNNNNNNGAAGGACAGTCTNNNNNNNNNNNNNNNNNNNNNAAAAACTTAA 5'
```

__Figure III.1 Schematic representation of the shRNA structure.__ The sense and antisense strands were designed with the siRNA platform (http://sirna.wi.mit.edu). The loop and terminator sequences are as suggested according to the "Systems Bioscience for shRNA cloning and expression in lentivectors" manual. RS: restriction enzyme target sites. In case of VASP shRNA the RS cleaved by BamHI and for Mena shRNA the RS is recognized by EcoRI.

III.2.6.2 Lentiviral vector for silencing Mena/VASP expression in hippocampal neurons

The lentivector for transfecting hippocampal neurons using an adenoviral infection protocol was designed by Dr. R. Blum. Briefly, this vector (Figure III.2) contains the human U6 small nuclear promoter (U6) and the human H1 promoter (H1), specific for RNA polymerases III, since they naturally direct the synthesis of small, highly abundant non-coding RNA transcripts. Furthermore, it contains a specific neuronal protomer for calcium/calmodulin-dependent protein kinase II (αCAMKII) upstream of the gene encoding for eGFP to easily identify infected neurons. The VASP shRNA was cloned downstream of the H1 promoter and the Mena shRNA is located downstream of the U6 promoter.

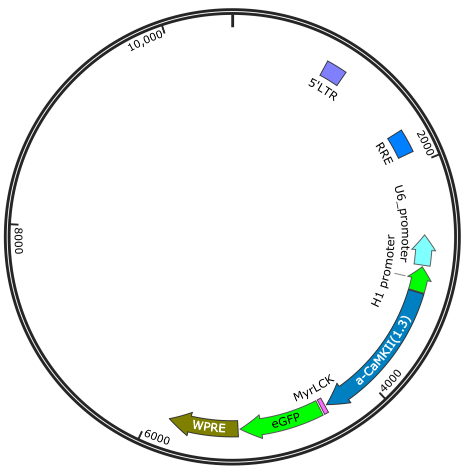

__Figure III.2 Schematic representation of the lentivector pFCK1.3.__ The vector has a size of 10500 bp and contains the H1 and U6 promoter in antisense to the calcium/calmodulin-dependent protein kinase II (αCAMKII) promoter/ eGFP protein. The shRNAs are cloned downstream of the H1 and/or U6 promoter, while the eGFP protein helps to identify the neuron cells positively transfected with the vector.

III.2.6.3 Determining Mena/VASP knockdown efficiency in HEK293 cells

For determining the efficiency of the respective shRNA initial tests were conducted in HEK293 cells. In order to this, HEK293 cells were cultured in 3 cm dishes ($1{,}8 \times 10^6$ cells seeded per dish) and grown in MEM supplemented with 10% FCS, 200 mM GlutaMAX, 100 mM sodium pyruvate, and 50 U/mL penicillin/streptomycin under standard growth conditions at 37°C and 5% CO_2. Cells were transiently transfected with the *pFCK* vector containing the shRNA and either *prk5*_flag-tagged VASP or *prk5*_flag-tagged Mena. As controls the empty pFCK1.3 vector and a vector containing a Scr shRNA were used. For co-transfection, lipofectamine 2000 was used. The protocol was as follows: 100 ng of flag-tagged VASP or flag-tagged Mena plus 1 µg of pFCK1.3-shRNA were dissolved in 200 µL Opti-MEM prewarmed at 37 °C and the mixture was incubated for 5 minutes. Meanwhile in separate vials 2 µL of lipofectamine 2000 were added to 200 µL of Opti-MEM and incubated as well for 5 minutes. Then, both solutions were mixed and resuspend by vortexing, followed by incubation for 30 minutes at 37 °C and then added dropwise to the cultures. After 16 hours of incubation the cells were washed with supplemented DMEM medium and cells were harvested 72 h after co-transfection. VASP or Mena expression was analyzed by WB targeting the flag epitope and by visualizing the bands with HRP-conjugated anti-mouse/rabbit IgG secondary antibodies using the Pierce ECL Western Blotting Substrate.

III.2.6.4 Virus packing, titration and transduction into primary cultured hippocampal neuron cells

Production of lentiviral particles was performed by H. Troll and Dr. R. Blum, Institute of Clinical Neurobiology, Würzburg. As lentiviral expression vector (transfer vector), a modified version of pFCK1.3 containing our shRNA was used[252]. Lentiviral particles were produced in HEK293T cells. The lentiviral expression vector was co-transfected with a pseudo-typing vector (pMD2.G), expressing vesicular stomatitis virus G (VSV-G) protein, and the packaging vector pCMVΔR8.91[253] using lipofectamine 2000.

Lentiviral particles were separated from the supernatant by ultracentrifugation (UC) and stored at −80°C in 50 mM Tris–HCl, pH 7.8, 130 mM NaCl, 10 mM KCl, 5 mM $MgCl_2$[254]. For transduction of hippocampal neurons, a multiplicity of infection (m.o.i.) of 20 was typically used. Neuronal transduction was performed during cell seeding.

III.2.6.5 Quantification of the number and size of gephyrin clusters in hippocampal neurons

Primary cultured neuron cells were prepared as described above (chapter III.2.5.5). Gephyrin cluster numbers and sizes were assessed by ImageJ using the "Integrated Morphometry Analysis" tool, calculating the number, area, average intensity, total intensity, perimeter, radius, and shape factor of single objects. Statistical analysis was performed with GraphPad Prism version 7.0 (GraphPad Software, La Jolla California USA, www.graphpad.com). Statistical significance was assessed with one or two-way ANOVA. All values from quantitative data represent the mean ± SEM from *n* independent experiments.

III.2.7 Enzymatic characterization of PDXK in the presence and absence of artemisinins

III.2.7.1 Michaelis-Menten kinetics

PDXK activity was measured following the procedure described by Churchich[255] with minor modifications. Briefly, the assay was conducted in 10 mM HEPES buffer pH 7.3 at 37°C with 100 mM KCl, 1 mM $MgCl_2$, 1 mM Mg-ATP and 50 µg/mL BSA. PDXK samples (wt and mutants) were used at a concentration of 20 µg/mL (0.56 µM), and the substrate PL was added in a concentration range from 10 µM up to 600 µM. The activity was measured following the increase in absorbance at 388 nm due to PLP formation (extinction coefficient of 4900 $M^{-1}cm^{-1}$) in a microplate reader CLARIOstar (BMG LABTECH). K_m and k_{cat} values were calculated by a Lineweaver-Burk plot[256]. All experiments were carried out in triplicates. Analysis of the data was performed using GraphPad Prism version 7.0 (GraphPad Software, La Jolla California USA, www.graphpad.com).

III.2.7.2 Characterization of the mechanism of inhibition by Dixon plots and determination of K_i and IC_{50} values of artemisinin and artesunate

For the estimation of the K_i value, the assays were performed under the same conditions, using PL concentrations of 50 µM and 150 µM, respectively. Artesunate and artemisinin were used in 2-fold serial dilutions starting at a concentration of 2.5 mM and 0.156 mM, respectively. The data were fit to a Dixon plot[257] by using a linear regression analysis ($p< 0.0001$) of the inverted velocity values. The K_i parameter for the inhibitors artesunate and artemisinin can be extracted from the intersect between the two lines corresponding to the individual PL concentrations used in the assays. According to the intersection of the lines, the mechanism of inhibition was estimated in the Dixon plot.

For determining the IC_{50} values, the values of inhibitor concentration were transformed to a logarithmic scale and fitted using a nonlinear regression fit with a variable slope. IC_{50} values were calculated as the concentration of inhibitor that results in a velocity half way between the minimal and maximal values of the curve. The assays were performed in triplicates. Curve-fitting procedures and statistical analysis were performed using GraphPad Prism version 7.0 (GraphPad Software, La Jolla California USA, www.graphpad.com).

III.2.7.3 Enzymatic characterization of the residues involved in artemisinin binding in PDXK

The enzymatic assays of PDXK (wt and mutants) were performed as described before in the presence of artesunate at 1.5 mM. Analysis of the data was performed using GraphPad Prism version 7.0 (GraphPad Software, La Jolla California USA, www.graphpad.com). To assess the statistical significance of the enzymatic assays, the normality distribution of the data was initially determined by a D'Agostino & Pearson normality test. After passing the normality test, the statistical significance was determined by a paired t-test. For all statistical tests, the p values correspond to *$p<0.05$; **$p<0.01$; ***$p<0.001$; ****$p<0.0001$; ns is not significant. Statistical analyses were performed by using values from four independent experiments.

III.2.8 Structural biology studies

III.2.8.1 Sample preparation for cryo-EM

For protein sample preparation for cryo-EM, the GraFix Method[258] developed by H. Stark and colleagues was employed. Briefly, the protein was freshly repurified by SEC prior to crosslinking and UC. The SEC was carried out in a SD 200 10/300 column using the buffer 20 mM HEPES pH 8.0, 150 mM NaCl, 5 mM βmE. A final protein concentration around 1-5 mg/mL was desired. The protein at 1mg/mL was then applied to the top of a continuous sucrose gradient containing glutaraldehyde at a final concentration of 0.1% (see below for experimental details). Consequently, the protein will be crosslinked as it migrates through the sucrose gradient.

For fractionation a 10-40 % sucrose gradient was prepared as follows: Two sucrose solutions in Hepes buffer (20 mM Hepes pH 7.5, 150 mM NaCl and 5 mM βmE) at concentrations of 10% and 40% (w/v) were prepared. To the 40% sucrose solution glutaraldehyde was added to a final concentration of 0.1%. Afterwards, two gradient tubes were prepared simultaneously; one containing glutaraldehyde and the other without glutaraldehyde, which will serve as control for the localization of the protein in the different fractions. For gradient preparation 11 mm x 60 mm centrifugation tubes were used (Beckman Coulter). The gradient was prepared by first adding the less dense sucrose solution to the bottom of the tube with a syringe, and carefully adding the denser solution on top. During centrifugation the denser solution will displace the less dense one at the bottom of the tube. Afterwards, the tubes were gently closed and applied to a Gradient Master instrument (BioComp). To generate a 10-40 % gradient, the following program parameters were selected: duration of 70 sec, tilt angle of 86° and speed of 16 rpm. Next, the tubes were stored at 4 °C for one hour to stabilize the gradient and finally 300 µL of protein were gently applied to the top of the gradient.

The samples were run overnight (~18 hours) at 86418 g and 4 °C using the swinging-bucket SW 60 Ti rotor (Beckman Coulter) in an Optima L-100XP (Beckman Coulter) ultracentrifuge. The following day the samples were aliquoted into 100 µL samples, taken consecutively from the top of the tube with the pipette and then analyzed by SDS-PAGE (Mini-PROTEAN® TGX™ 4-20% gradient precast gels) to determine which fractions were suitable for the negative staining (NS) and, ultimately, cryo-EM.

III.2.8.2 Adsorbing samples on the carbon substrate and negative staining

For adsorbing the protein sample on carbon-covered grid, the Side Blotting Method[259] was used. Briefly, the edge of the grid was gripped with a pair of crossover tweezers (Dumont HP crossover tweezers N5 Stainless steel. 0.10 x 0.06 mm tip, Agar Scientific), and 3.5 µL of sample were applied to the support surface. The self-made carbon-covered grid (thickness around 0.8 nm) was previously cleaned in a Plasma Cleaner (Harrick Plasma) for 1 minute. The sample was allowed to adsorb to the grid surface for 1 min. Then, the edge of the grid was brought into contact with a sheet of filter paper (Whatman) to remove excess liquid by capillary action.

Afterwards, 3 x 20 µL drops of ultrapure water were placed on a sheet of parafilm. Next the carbon surface of the grid was gently brought into contact with the drop to lift off a small droplet onto the surface of the grid. Afterwards the edge of the grid was positioned to touch the filter paper again to allow capillary action to pull off the liquid. This wash step was repeated three times before proceeding with staining. For that, three 20 µL drops of uranyl acetate solution at 2 % (w/v) were placed on a sheet of laboratory film. By gentle touch the carbon surface of the grid contacted the drop to lift off a small droplet onto the top surface of the grid. Subsequently, the edge of the grid was brought into contact with filter paper to allow capillary action to draw off the liquid. The staining step was repeated three times with a 5 min incubation in the final step before again touching the edge of the grid with filter paper to draw off the liquid. Finally, the grid was allowed to air dry before storage in a grid box waiting for further analysis under the microscope. NS grids were visualized in the 120 kV FEI Tecnai G2 transmission electron-microscope (TEM) at a magnification of 52,000 x, corresponding to a pixel size of 2.201 Å. For every NS grid, around 10 different images were recorded to visualize the quality of the protein particles to afterward decide which of them go to plunge-freeze grids.

III.2.8.3 Cryo-EM

Negative stained fractions that looked nice were selected for the preparation of cryo-grids. Cryo-grids were prepared in duplicates at different serial dilutions of 1:5, 1:25 and 1:125 starting from material with a concentration of 3 mg/ml. Plunge-freezing was performed at approximately 100% humidity and 4 °C. Afterwards, the cryo-grids were stored in liquid nitrogen prior to analysis in the 120 kV FEI Tecnai G2 TEM.

When this preliminary analysis indicated that the particles were of sufficient quality, data were collected. The second cryo-grid of each duplicate pair was further analyzed in the 300 kV Titan Krios TEM equipped with a Falcon II direct electron detector at a magnification of 75,000 x, corresponding to a calibrated pixel size of 1.0635 Å. A number of 500 micrographs were collected during 12 hours.

III.2.8.4 Computational analysis for particle reconstruction

The dataset was analyzed using the Relion 3.0 software[244]. I manually picked around 1000 particles from a small set of micrographs to train the software for auto-picking and subsequent 2D classification. Selected 2D classes were used as templates for auto-picking of particles from all micrographs. Two rounds of reference-free 2D classification were performed and well-aligned 2D classes were selected for subsequent 3D reconstruction. An initial reference-free 3D model was generated in RELION 3.0 using the stochastic gradient descent (SGD) methodology. Selected particles were 3D-refined and Bayesian polishing of particles was performed. Next, the polished particles were classified into five 3D volumes without particle alignment. Particles with the highest resolution were combined and 3D-refined using a soft-mask and solvent-flattened Fourier shell correlations. After the 3D model was refined, post-processing was performed. The known structures of GephG and GephE (PDB entries: 1JLJ and 2FU3, respectively) were docked sequentially in the resulting map using the Chimera software[246].

IV Results

IV.1 Biochemical characterization of the pyridoxal kinase artemisinin-binding pocket

To perform the enzymatic characterization of PDXK, the wt as well as its mutants were purified as described in the previous chapter (III.2.3). A usual yield of 22 mg of protein per L of culture was achieved. After SEC (Figure IV.1 and appendix IX.4), the PDXK variants were flash frozen in liquid nitrogen and stored at a concentration of around 12.5 mg/mL until further use.

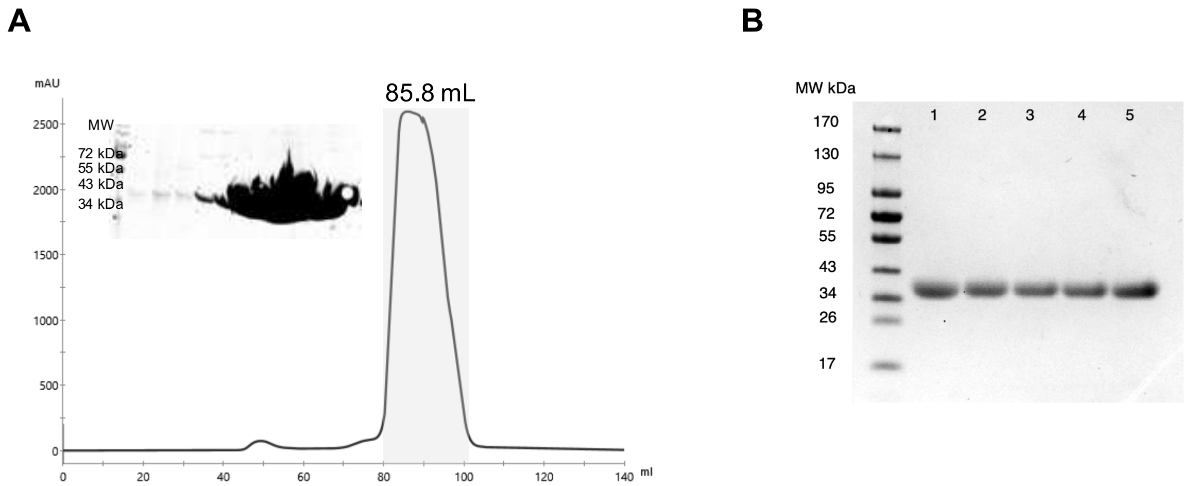

Figure IV.1 Size exclusion chromatography of PDXK. (A) *Sample purity was analyzed by SDS-PAGE (15% gel) and fractions within the shaded area were pooled to use in further analysis.* ***(B)*** *Comparison of the recombinant purified PDXK variants in a 4-20 % gradient gel. From left to right: (1) wtPDXK, (2) R86W, (3) V41W, (4) F43R and (5) V41W/F43R.*

To analyze PDXK kinetically, a set of enzymatic assays were performed in the presence of a constant excess concentration of 1 mM Mg-ATP, the second substrate, and a dilution curve of PL, the first substrate. The K_m and k_{cat} parameters for PL under the assay conditions were measured as 26.0 ± 5.4 µM and 0.143 ± 0.003 s^{-1}, respectively with a turnover number of 0.164 ± 0.006 s^{-1} (Figure IV.2). These parameters are similar to respective values obtained for other PDXK enzymes (K_m ~ 3-50 µM)[255,260-263].

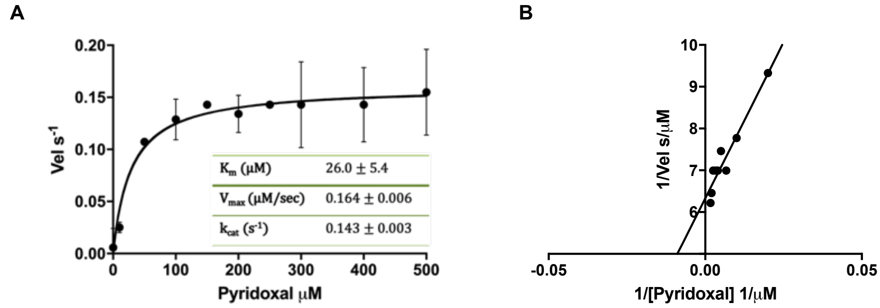

Figure IV.2 Michaelis-Menten kinetics of PDXK. (A) *The assay was performed in triplicates. Each point in the curve represents the mean ± SD.* ***(B)*** *Lineweaver-Burk or double reciprocal plot. Data were transformed to reciprocals and fitted to a lineal regression. The equation of the curve is y= 158.5x + 6.09 (R^2=0.9184), where the slope is equal to K_m/V_{max} and the intercept is equal to $1/V_{max}$. The analysis of the data was performed using GraphPad Prism version 7.0.*

To evaluate the inhibitory potency of artemisinin and artesunate towards PDXK a series of enzymatic assays were conducted. Dixon plots revealed that in both cases, artesunate and artemisinin, the data for each substrate concentration fall on straight lines that cut each other at the left of the vertical axis and intersects at [I]=-K_i and 1/Vel=1/V_{max}, which is typical for a competitive inhibition mechanism[257]. As shown in Figure IV.3, artesunate has a K_i of 1250 ± 5 μM and artemisinin of 120 ± 2 μM. Accordingly, the IC_{50} values for artesunate and artemisinin are 1445 ± 1.4 μM and 229 ± 1.3 μM, respectively. Obviously, artemisinin is at least a 6-fold more potent inhibitor than artesunate.

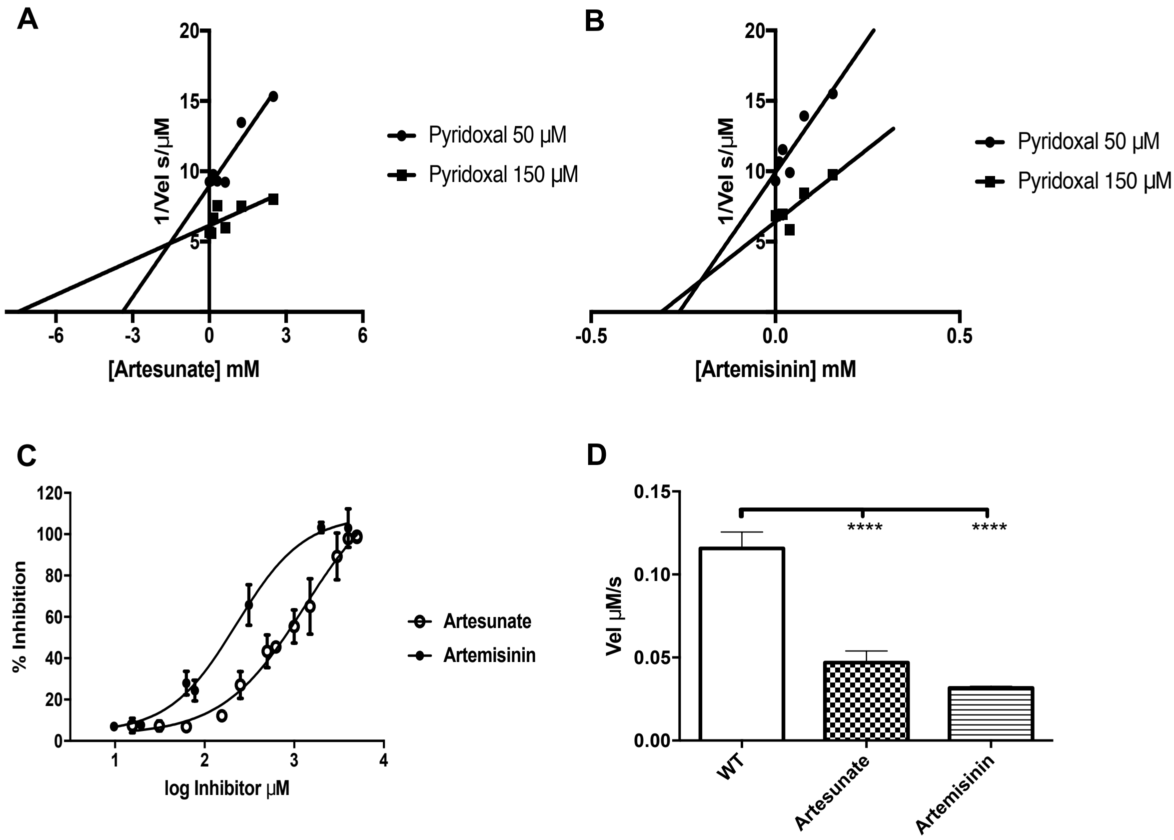

***Figure IV.3 Characterization of PDXK inhibition by artesunate and artemisinin. (A & B)** Dixon plots of PDXK in the presence of artesunate and artemisinin, respectively. **(C)** IC_{50} values of artemisinin and artesunate are derived from the inhibition curves of PDXK, where the percent inhibition is plotted against the logarithm of the inhibitor concentration. The assays were performed in triplicates and the analysis of the data was performed in GraphPad Prism version 7.0. **(D)** Enzymatic activity of wtPDXK in the presence of artesunate and artemisinin at concentrations of 1.5 mM (artesunate) and 156 µM (artemisinin), respectively. Data were obtained in triplicates, and are presented as mean ± SEM. The statistical analysis was done using a paired t-test (p values are: *p<0.05; **p<0.01; ***p<0.001; ****p<0.0001).*

Due to the inhibitory effect of these drugs, the PDXK-catalyzed turnover rate decrease ~3-fold (Figure IV.3d), reaching values of 0.047 ± 0.007 s^{-1} and 0.032 ± 0.001 for artesunate and artemisinin, respectively, compared to 0.116 ± 0.01 s^{-1} in the absence of these compounds. Statistical analyses revealed a significant reduction in enzymatic activity in the presence of the artemisinins, where the enzymatic or turnover velocity (Vel), is defined as the mean number of product molecules generated by a single enzyme per unit time.

After a closer examination of the artesunate-binding pocket in the crystal structure of the PDXK-artesunate-ATP complex (Figure I.5), it was possible to evaluate which residues are involved in the binding of this drug. Artesunate-binding is mediated by V41 and F43 (Figure I.5b), which generate a hydrophobic pocket into which artesunate binds, being stabilized through π-π stacking interactions with the aromatic residues F43 and Y84. Additionally, the carboxylate moiety of artesunate is engaged in an electrostatic interaction with the guanidinium side chain of R86. These observations prompted us to engineer and purify the R86W, V41W and F43R single mutants as well as the double mutant V41W/F43R.

As shown in Figure IV.4a, the V41W and F43R mutations drastically decreased the turnover numbers of the enzyme (0.04 ± 0.006 s^{-1} for V41W and 0.016 ± 0.001 s^{-1} for F43R), even in the absence of artesunate, compared to wtPDXK (0.080 ± 0.004 s^{-1}). This might be because these residues are also involved in the binding of the substrate PL, therefore the catalytic function of the enzyme is impaired by these mutations. This is not the case for the R86W mutation, which displays a turnover number of 0.080 ± 0.005 s^{-1} (Figure IV.4a & c), the same number observed for the wt.

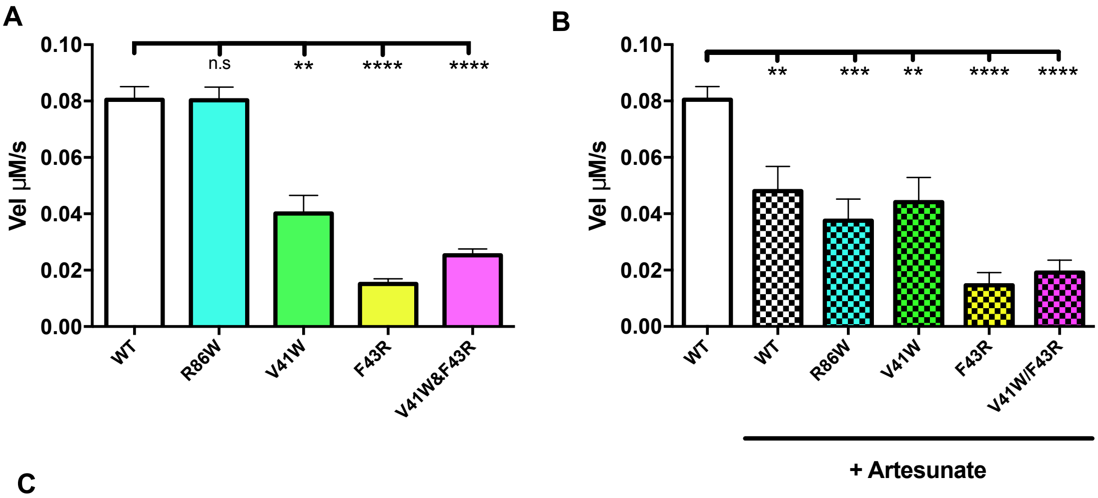

C

Enzyme	Vel µM/s	Vel µM/s + Artesunate
wtPDXK	0.080 ± 0.004	0.047 ± 0.007
R86W	0.080 ± 0.005	0.038 ± 0.008
V41W	0.040 ± 0.006	0.044 ± 0.009
F43R	0.016 ± 0.001	0.014 ± 0.005
V41W/ F43R	0.019 ± 0.004	0.024 ± 0.002

Figure IV.4 Enzymatic activity of PDXK and related mutants in the absence and presence of artesunate. *The turnover rates of PDXK variants (wt and mutants) are represented in the absence **(A)** and presence **(B)** of 1.5 mM artesunate. (*p<0.05; **p<0.01; ***p<0.001; ****p<0.0001). The assays were done in triplicates and the data are represented as mean ± SEM. Statistically significant differences were analyzed using a paired t-test. **(C)** Summary of the turnover ratios for the different PDXK variants in the absence and presence of artesunate. The data were processed using the GraphPad Prism software.*

However, in the presence of the artesunate the V41W and F43R variants yield similar turnover rates of the enzyme in the presence of artesunate with values of 0.044 ± 0.009 for V41W and 0.014 ± 0.005 for F43R s^{-1} compared to 0.040 ± 0.006 and 0.016 ± 0.001 s^{-1}, respectively, in its absence (Figure IV.4). Likewise, in case of the V41W/F43R double mutant, a similar turnover number was observed, with values of 0.024 ± 0.002 s^{-1} in the presence of artesunate and 0.019 ± 0.004 s^{-1} in its absence.

In contrast, the R86W mutation did not affect the inhibitory action of these drugs (Figure IV.4). A comparison of the turnover numbers of the enzyme indicated that enzyme activity was equally affected as in the wt; in the presence of artesunate the turnover number was 0.047 ± 0.007 s^{-1} for the wt and 0.038 ± 0.008 s^{-1} for the R86W variant. This would suggest that the electrostatic interaction between the succinic acid side chain of artesunate and the guanidinium group of the R86 observed in the crystal structure, is not a crucial contact for the inhibitory action of artesunate.

IV.2 Towards a structural characterization of gephyrin by cryo-EM

Although crystal structures of the terminal domains of gephyrin have been derived[33,36], there is only limited information on the architecture of the FL protein. A few years ago, Sander *et al.* elucidated a low-resolution structure of gephyrin in solution combining SAXS-analysis with AFM experiments[34]. According to this study, gephyrin should behave as a trimer in solution taking advantage of its GephG interface for trimerization, while the GephE dimerization apparently is prevented in the context of the FL protein. Since gephyrin so far could not be crystallized, presumably due to its large unstructured, proteolytically sensitive central linker, cryo-EM appears to be a better strategy to determine a structure of the intact protein that goes well beyond the resolution of the SAXS-derived models.

For protein sample preparation for cryo-EM, the GraFix Method[258] as developed by H. Stark and colleagues was employed with slight modifications. After optimization of the protocol regarding sucrose gradient concentration (10-30%, 10-40%), protein concentration (1.0, 2.0 and 3.0 mg/mL), crosslinker concentration (0.05- 0.1%) and time (14-18 hours) as well as speed (80,000- 86,500 g) during UC, the parameters described below were used in this work.

To initiate these experiments, always freshly purified protein following SEC was used and gephyrin was further fractionated using a 10-40% continuous sucrose gradient. During UC, the protein was subjected to crosslinking with glutaraldehyde at a final concentration of 0.1% (v/v) of a protein solution with a concentration of 3 mg/ml. According to the results of the GraFix procedures, as visualized by SDS-PAGE (Figure IV.5a), I chose fractions 13 and 14 for initial negative stain EM experiments. These fractions revealed a clear and single protein band for the non-crosslinked sample corresponding to a size of ~ 90 kDa, as expected for the monomeric protein and one higher molecular mass peak well above the 170 kDa marker band for the crosslinked sample. For comparison, the gephyrin trimer is expected to have a molecular weight of 270 kDa and the observed band presumably corresponds to the trimer. Negative stain EM experiments were carried out with uranyl acetate as contrasting agent at a concentration of 2% (w/v) on carbon-coated grids. The negative stained micrographs of fraction 14 showed aggregated protein and heterogeneous sample with particle sizes ranging from 10 nm to 15 nm, while fraction 13 was homogeneous with a particle size of ~7 nm, and showed only a few aggregates. Therefore, fraction 13 was chosen for further cryo-EM experiments. For that, I prepared cryo-grids in duplicates using concentrations around 1 mg/mL.

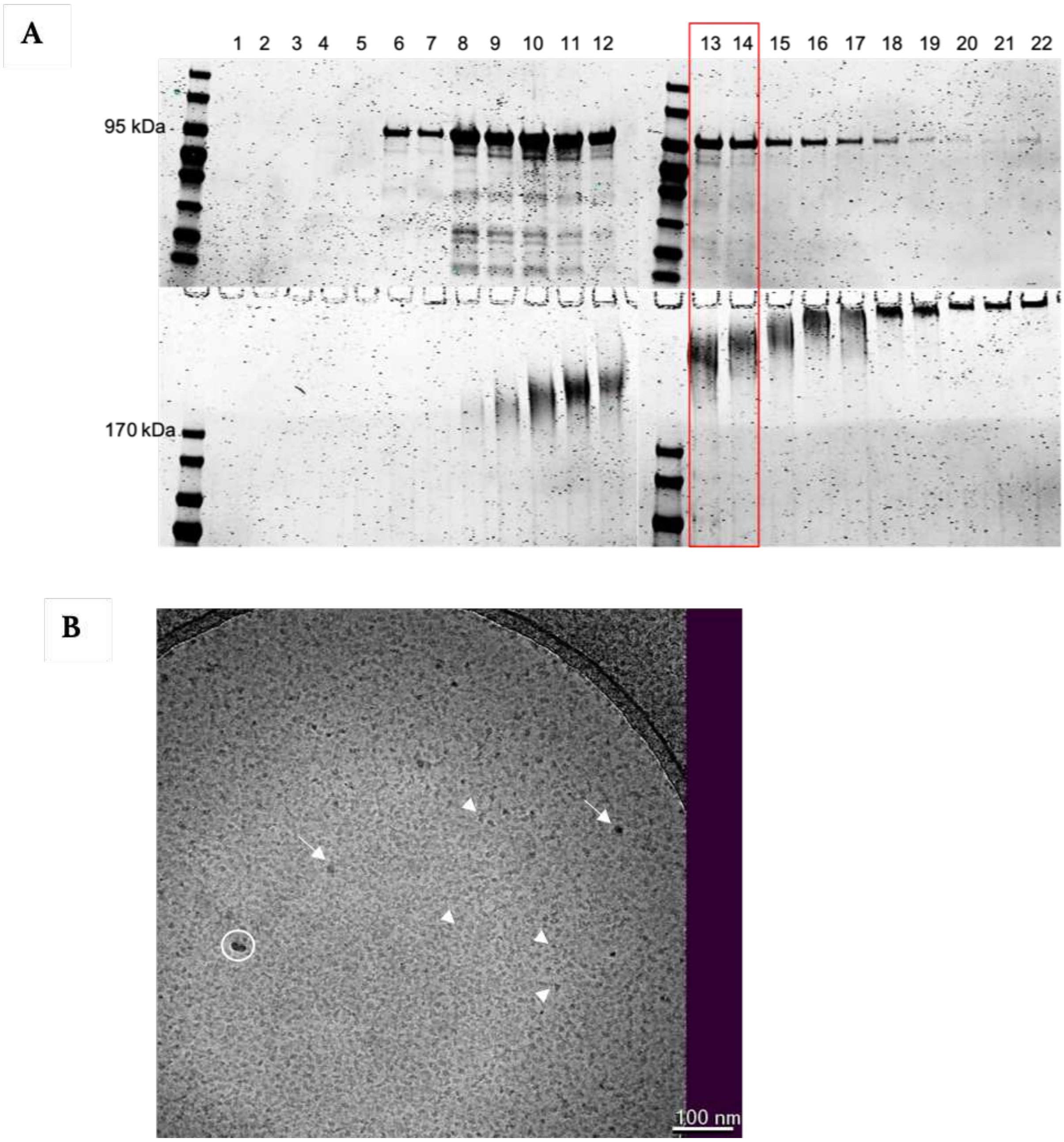

Figure IV.5 Preparation of gephyrin samples by the GraFix method and analysis of crosslinked gephyrin particles by negative stain EM. *(A) SDS-PAGE analysis of the fractions after GraFix from a 10-40% sucrose gradient after crosslinking with 0.1% glutaraldehyde (upper panel: non-crosslinked sample, lower panel: crosslinked sample). SDS-PAGE was performed in a 4–20% Mini-PROTEAN® TGX™ precast protein gel. (B) Cryo-grid micrograph of fraction 13 analyzed with a 120 kV Tecnai G2 electron microscope at a magnification of 52,000 x corresponding to a pixel size of 2.201 Å. Some of the individual particles are highlighted with arrowheads, while selected larger aggregates are marked with arrows. Some ice was also observed in some of the micrographs (marked by the white circle).*

On the electron micrographs after negative staining fraction 13 appeared quite homogeneous and well behaved (Figure IV.5b). This fraction exhibited an average particle size of ~7 nm, and, according to SDS PAGE, presumably represented particles corresponding to the gephyrin trimer (Figure IV.5a, lower panel). Based on a molecular weight of 270 kDa one would estimate a particle size of 8.55 nm, assuming a protein density of 1.37 g/cm^3 and a perfectly spherical shape[264]. Given that gephyrin most likely adopts an anisometric shape, the observed value seems reasonable.

The results of this preliminary analysis indicated that the particles were of sufficient quality to collect data with the 300 kV Titan Krios TEM, which is equipped with a Falcon II direct electron detector. 500 micrographs were collected during a 12-hour data collection at a magnification of 75,000, corresponding to a calibrated pixel size of 1.0635 Å (Figure IV.6a). The dataset was analyzed using the RELION 3.0 software[244]. I manually picked around 1000 particles from a small set of micrographs to train the software for auto-picking and subsequent 2D classification. After that two rounds of reference-free 2D classification were performed and well-aligned 2D classes (Figure IV.6b) were selected for subsequent 3D reconstruction. After 3D classification, the particles with the highest resolution were combined and 3D-refined using soft-mask and solvent-flattened Fourier shell correlations (Figure IV.6d). The 3D refined model had a resolution of 18.8 Å, and, after post-processing, the resolution could be slightly extended to 16.0 Å (Figure IV.6c-d). The map was superimposed with the crystallographic models of the trimeric GephG (PDB: 1JLJ) and dimeric GephE (PDB: 2FU3) using the Chimera software (Figure IV.6e). Although the map was not of high resolution, in the superimposition, the 3D volume of the particles was of the correct size to accommodate a gephyrin trimer. More precisely a trimer of GephG could be modeled in the more central part of the map, while a GephE dimer could be fitted on one side of the GephG trimer, while smaller density features on the opposite side were not accounted for. With a GephG trimer and a GephE dimer, the model is obviously missing the third GephE monomer (46 kDa), and the three linkers connecting each G and E domain with a total molecular weight of 3 x 16 kDa (48 kDa). Obviously, there are still unassigned regions in the map, in particular a larger feature on the opposite side of the GephG trimer with respect to the GephE dimer, which could represent the location of the third GephE monomer (Figure IV.6e). The results are promising to further continue in this direction to elucidate the structure of FL gephyrin.

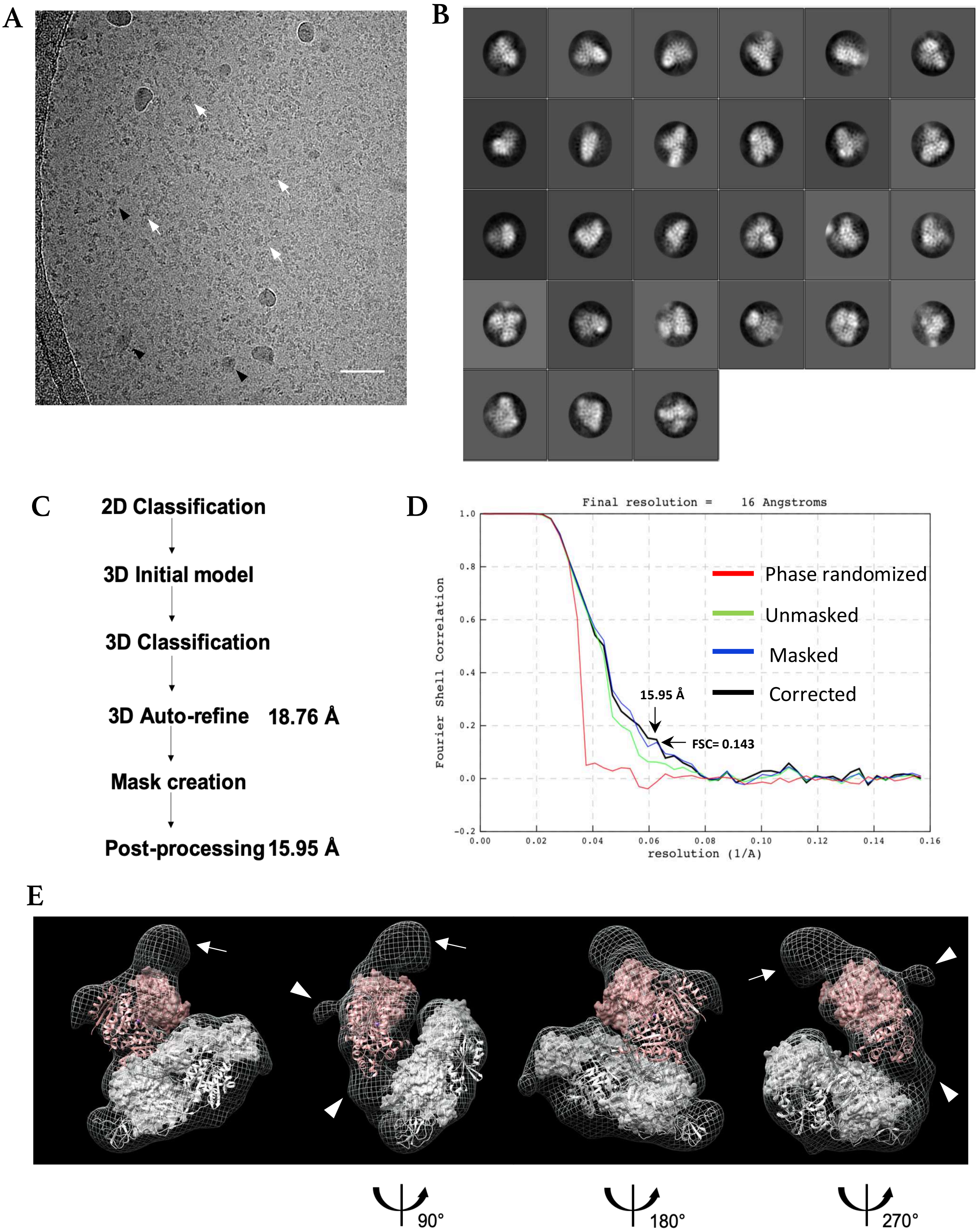

Figure IV.6 ***Cryo-EM of the gephyrin particles.*** *(A) Representative micrograph of fraction 13 of gephyrin obtained with a 300 kV Titan Krios TEM. Selected particles are highlighted with white arrows, while larger aggregates of gephyrin are indicated by black arrowheads. Scale bar: 100 nm.* ***(B)*** *Representative 2D-classes derived from 67,865 particles, which were chosen for 3D reconstruction.* ***(C)*** *Workflow of the data processing with the RELION 3.0. software.* ***(D)*** *Fourier shell correlation (FSC) graph showing the resolution obtained after post-processing of the 3D model in RELION 3.0. Applying the 0.143 criterion yields a resolution of 15.95 Å.* ***(E)*** *CryoEM map (white mesh)* *contoured at a level of 0.012 for a map size of 100^3 voxels and superimposed with the crystal structure of GephG trimer (PDB: 1JLJ shown in pink with two monomers in ribbon representation and the other in surface representation) and one GephE dimer (PDB: 2FU3 with a correlation of 0.91, shown in white with one monomer in ribbon representation and the other monomer in surface representation) using Chimera. Unassigned density volumes possibly representing the third GephE monomer are indicated with arrows and additional regions which might correspond to the linker are indicated by arrowheads.*

IV.3 VASP construct design

Based on the domain architecture of VASP and a secondary structure prediction with the software RaptorX[243], I designed different constructs with the aim of mapping the gephyrin-binding site in VASP. Table IV.1 summarizes the different constructs and lists the success or failure of each construct during expression and purification.

Table IV.1 VASP constructs and success or failure during expression and purification

Protein	Tag	Construct	Expression	Purification
wtVASP	nHis	EVH1 PRO-rich EVH2 1 380	✓	✓
EVH1	nHis	EVH1 1 115	✓	✓
EVH2	nHis	EVH2 225 380	✓	✓
Pro-rich	nHis	Pro-rich 116 225	✗	✗
EVH1-Pro	nHis	EVH1 PRO-rich 1 208	✓	✗
Δ125-144	nHis	EVH1 125 144 PRO-rich EVH2 1 380	✓	✓
E136A/E137A	nHis	E136A/E137A EVH1 PRO-rich EVH2 1 380	✓	✓
K142A/K143A	nHis	K142A/R143A EVH1 PRO-rich EVH2 1 380	✓	✓

The expression of all the constructs was successful except for the constructs containing the Pro-rich region (Table IV.1), presumably because it is mainly unstructured and prone to degradation. All these constructs were cloned into the pQE30 vector and expressed in *E. coli* with an N-terminal His-tag to allow Ni-affinity chromatography as first step of purification.

IV.4 Protein purification

For the purification of FL-VASP and its variants EVH1, EVH1-Pro, EVH2, Δ125-144, E136A/E137A and K142A/R143A, a general strategy was performed using Ni-Affinity chromatography followed by ion exchange chromatography and, as last step, SEC. The fractions from the SEC were analyzed by 15% SDS-PAGE and the fractions with >95% purity were pooled for further experiments (Figure IV.7). As the EVH1-Pro construct is prone to degradation, it was not further used for the *in vitro* studies. In the case of FL-gephyrin as well as the GephG and GephE domains, they were purified following protocols previously described by colleagues[33,34,36]. Briefly, for purifying gephyrin and GephG a Ni-affinity chromatography followed by ion exchange chromatography and as last step SEC were performed. In contrast, GephE protein was purified using a Chitin-affinity chromatography followed by removal of the tag and a final SEC (Figure IV.7). As for the VASP proteins, fractions with >95% of purity as judged by 15% SDS-PAGE were pooled and used for further experiments.

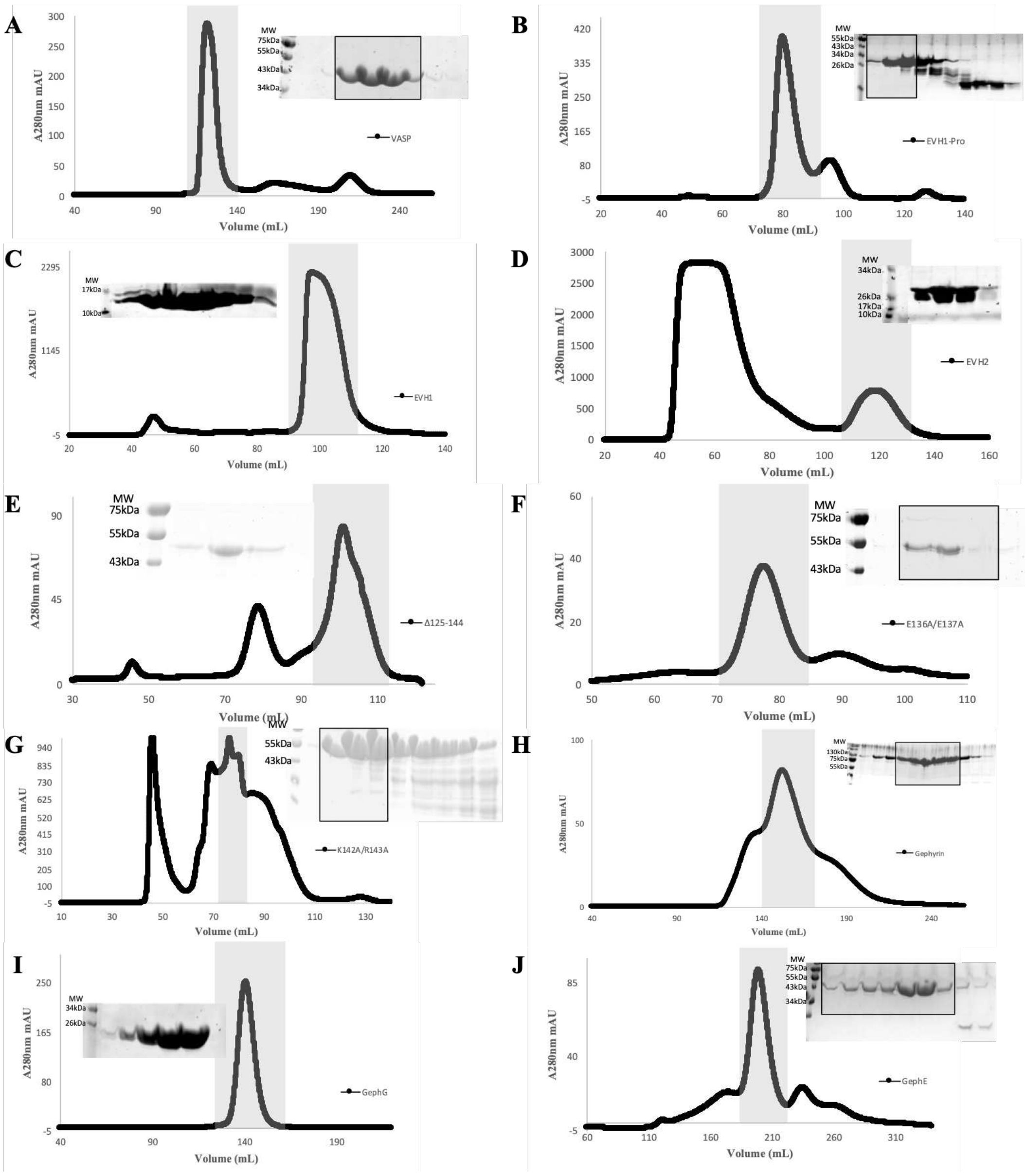

Figure IV.7 Size exclusion chromatograms of the proteins used in this study. *(A) VASP, (B) VASP(EVH1-Pro), (C) Evh1, (D) Evh2, (E) Δ125-144, (F) E136/E137, (G) K142A/R143A, (H) gephyrin, (I) GephG, (J) GephE. Sample purity was analyzed by SDS-PAGE (15% gels) and fractions within the shaded areas were pooled to use in further analysis.*

The typical yields obtained from each purification and the concentrations to which the proteins were stored until further use are summarized in Table IV.2. Usually, a pooled fraction of 1-2 mg/mL was concentrated using centrifugal concentrator tubes with a molecular cut-off appropriate for each protein to reach the proper concentration in which the protein was stored, as described in chapter III.2.3.2.

Table IV.2 Yield and storage concentration of protein usually obtained per purification

Protein	Yield (mg protein/ L culture)	Storage Concentration (mg/mL)
GephFL	0.88	14
GephG	3.00	24
GephE	3.00	24
VASP	1.75	20
Evh1	4.70	25
Evh2	3.13	25
Δ125-144	2.00	20
E136A/E137A	1.80	20
K142A/R143A	1.70	20

IV.5 Mapping the VASP-binding site in gephyrin

The VASP-binding site in gephyrin has been a topic of interest, being investigated previously by two different groups[128,129]. Giesemann *et al* and Bausen *et al.* studied the interaction between gephyrin and VASP and made efforts to elucidate the binding region in gephyrin through co-IP, GST-pulldown and co-localization experiments. However, the VASP-binding site in gephyrin is still not well defined since the two studies came to different conclusions, mapping the binding site to either GephE (Ref. 128) or to the linker region (Ref. 129).

In my thesis, I performed NAGE and aSEC experiments to verify the interaction between VASP and gephyrin in an *in vitro* setting and to map the VASP-binding site in gephyrin.

In aSEC experiments, the chromatography profile shows the presence of a complex in the form of a small shoulder at an earlier elution volume (12.84 ml) when VASP and gephyrin in their full-length form were incubated, but not when FL-VASP was incubated with the individual domains of gephyrin (GephG and/or GephE) (Figure IV.8a-d).

In the same way, in NAGE assays, a shift of the VASP and gephyrin proteins towards each other was detected when the complex was analyzed, which was absent when instead of FL-gephyrin only GephG or GephE were used (Figure IV.8g). These results indicated that neither GephG nor GephE domains are responsible for mediating the interaction of gephyrin with VASP, which suggests that the linker region is responsible for VASP binding. The interaction was further analyzed by NAGE using a peptide derived from linker of gephyrin encompassing residues P201 to V255, referred from now on as Linker201-255. Figure IV.8h reveals a shift in the VASP migration upon incubation with increasing concentrations of the peptide.

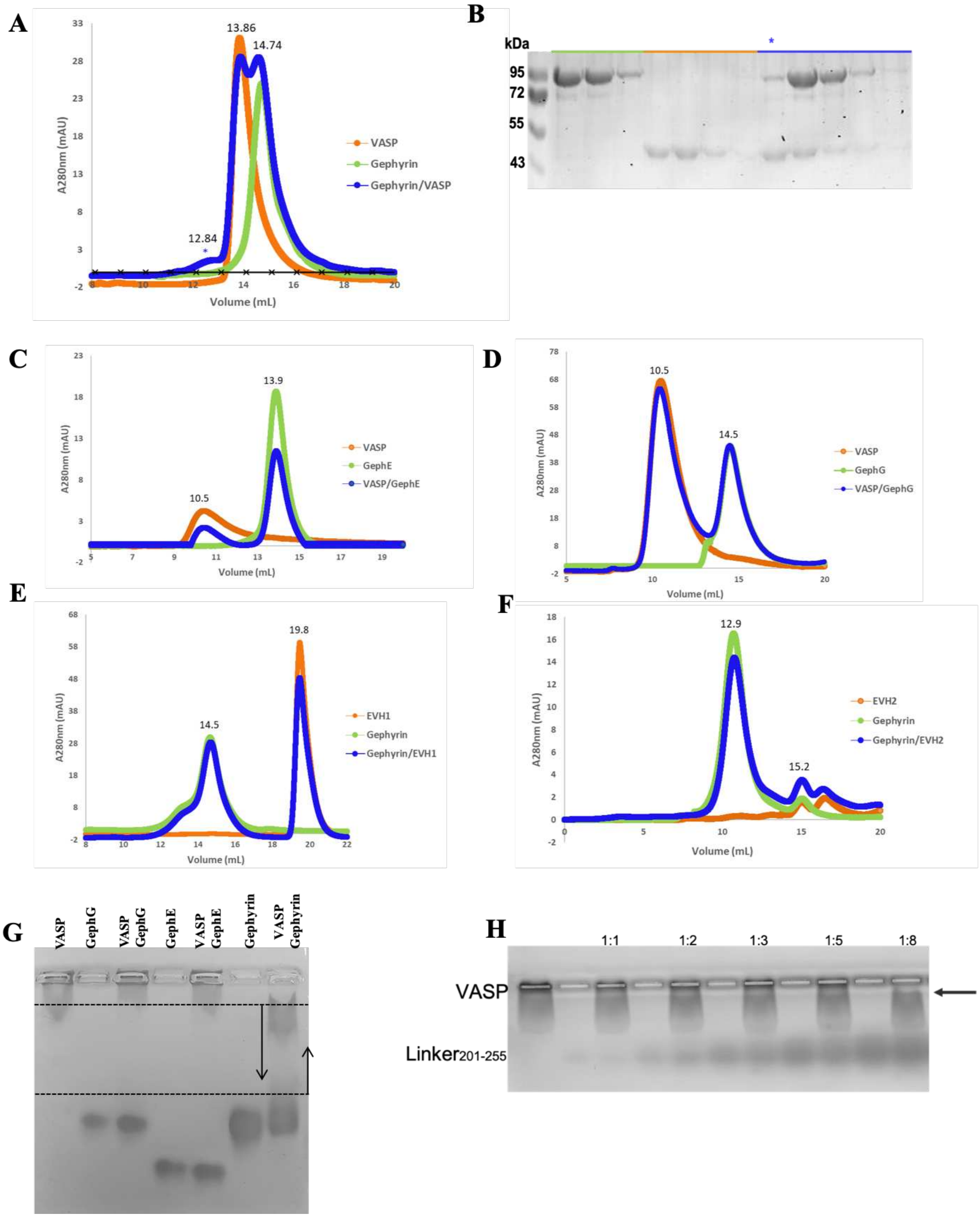

Figure IV.8 aSEC and NAGE of the gephyrin-VASP with the full-length proteins and shortened constructs. (A) *aSEC of FL-VASP and gephyrin on a Superose 6 increase 10/30 GL column. Protein concentrations were 100 µM at a 1:1 molar ratio.* ***(B)*** *15 % SDS-PAGE of fractions from the different aSEC runs as indicated with the corresponding color. The fraction corresponding to the VASP-gephyrin complex running at the leading shoulder of the left peak in the chromatogram is labeled with an asterisk.* ***(C)*** *aSEC of GephE with the FL-VASP analyzed on Superdex 200 10/30 GL column. Protein concentrations were 100 µM at a 1:1 molar ratio.* ***(D)*** *aSEC of GephG with the FL-VASP analyzed on Superdex 200 10/30 GL column. Protein concentrations were 100 µM at a 1:1 molar ratio.* ***(E)*** *aSEC of EVH1 with FL-gephyrin analyzed on a Superdex 200 10/30 GL column. Protein concentrations were 100 µM at a 1:1 molar ratio.* ***(F)*** *aSEC of EVH2 with FL-gephyrin analyzed on Superdex 200 10/30 GL column. Protein concentrations were 100 µM at a 1:1 molar ratio.* ***(G)*** *NAGE of FL-VASP with GephG, GephE and FL-gephyrin. Protein concentrations were 50 µM at a 1:1 molar ratio. The mixture was pre-incubated for 1 hour at 4°C and the gel ran at 90 V for 2 hours at 4°C.* ***(H)*** *NAGE of FL-VASP with the Linker201-255 peptide. The VASP* *concentration was 50 μM and the molar ratios (VASP: Linker201-255) were 1:1, 1:2, 1:3, 1:5 and 1:8. Samples were pre-incubated for 1 hour at 4°C and the gel was run at 90 V for 2 hours at 4°C.*

Once I had corroborated the interaction between the two proteins and had identified a region within the linker region as the responsible binding site, I analyzed the affinity of the complex. For that I used MST by using AlexaFluor 647-labelled VASP as the target protein and recombinant purified gephyrin or synthetic Linker201-255 peptide as ligand. The binding affinity at the near-physiological temperature (36 °C) was 0.82 ± 0.16 μM (R^2= 0.9108) and 4.11 ± 0.79 μM (R^2= 0.9658) for gephyrin and the Linker201-255 peptide, respectively (Figure IV.9a).

The same experiment was performed using AlexaFluor 647-labelled gephyrin as the target and VASP as the titrant. In this case, the K_d at the same temperature was measured as 1.43 ± 0.4 μM (R^2= 0.9758) (Figure IV.9b). In summary, the affinity of the interaction between gephyrin and VASP at near physiological temperature is around 1 μM.

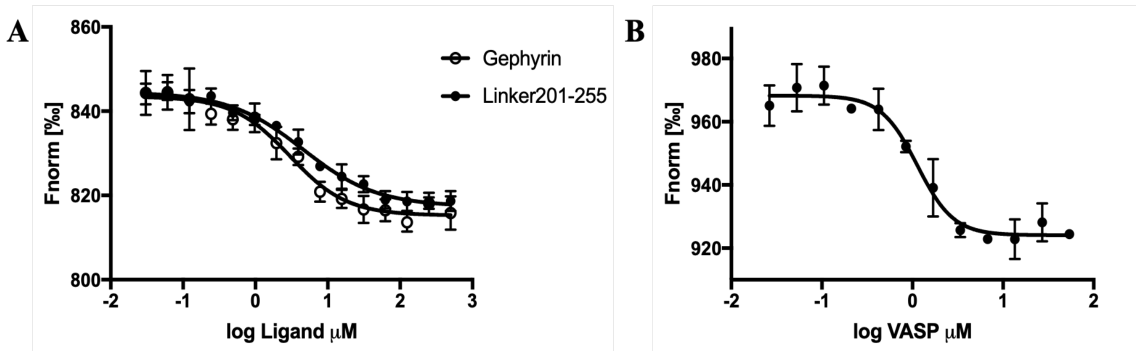

***Figure IV.9 MST of the interaction between gephyrin and VASP. (A)** MST of gephyrin (●) or the Linker201-255 peptide (●) used as ligand with AlexaFluor647-VASP as target. The temperature of the assay was 36°C. Error bars represent the s.d. derived from n=3 experiments. **(B)** MST of VASP as ligand with AlexaFluor647-gephyrin as target. The temperature of the assay was again 36°C. Error bars represent the s.d. from n=3 experiments. Data were exported from the MO.Affinity Analysis software and were analyzed with GraphPad Prism.*

IV.6 Mapping the gephyrin-binding site in VASP

Once I narrowed down the VASP-binding site in gephyrin to the region encompassing residues 201-255 in the linker, I wanted to identify the gephyrin-binding site in VASP. This was of special interest since this had not been investigated before. Unfortunately, the instability and/or lack of expression of the constructs containing the Pro-rich region (Table IV.1, Figure IV.7), at least when expressed in *E. coli*, prevented *in vitro* testing by aSEC and NAGE to directly probe whether this region is the responsible for mediating the interaction. However, aSEC experiments did not suggest binding for fragments containing either the EVH1 or EVH2 domains, arguing against an involvement of these domains of VASP as interaction sites of gephyrin (Figure IV.8e & f). This reinforced the need to overcome the absence of proteins containing the Pro-rich region in these studies.

To address this limitation, I expressed both full-length proteins and fragments derived thereof in mammalian cells and performed co-IP and colocalization experiments. HEK293 cells were co-transfected with an eGFP-gephyrin fusion protein and flag-tagged wtVASP as well as its individual domains: flag-VASP(EVH1), flag-VASP(EVH2), flag-VASP(Pro), flag-VASP(EVH1-Pro). Co-IP assays using eGFP-gephyrin as the bait protein confirmed that VASP was co-precipitating with gephyrin as did the two constructs containing the Pro-rich region, flag-VASP(Pro) and flag-VASP(EVH1-Pro) (Figure IV.10a). In contrast, the isolated terminal VASP domains, EVH1 and EVH2, did not coprecipitate with gephyrin. These results demonstrated that the interacting region of VASP must be located within the Proline-rich region.

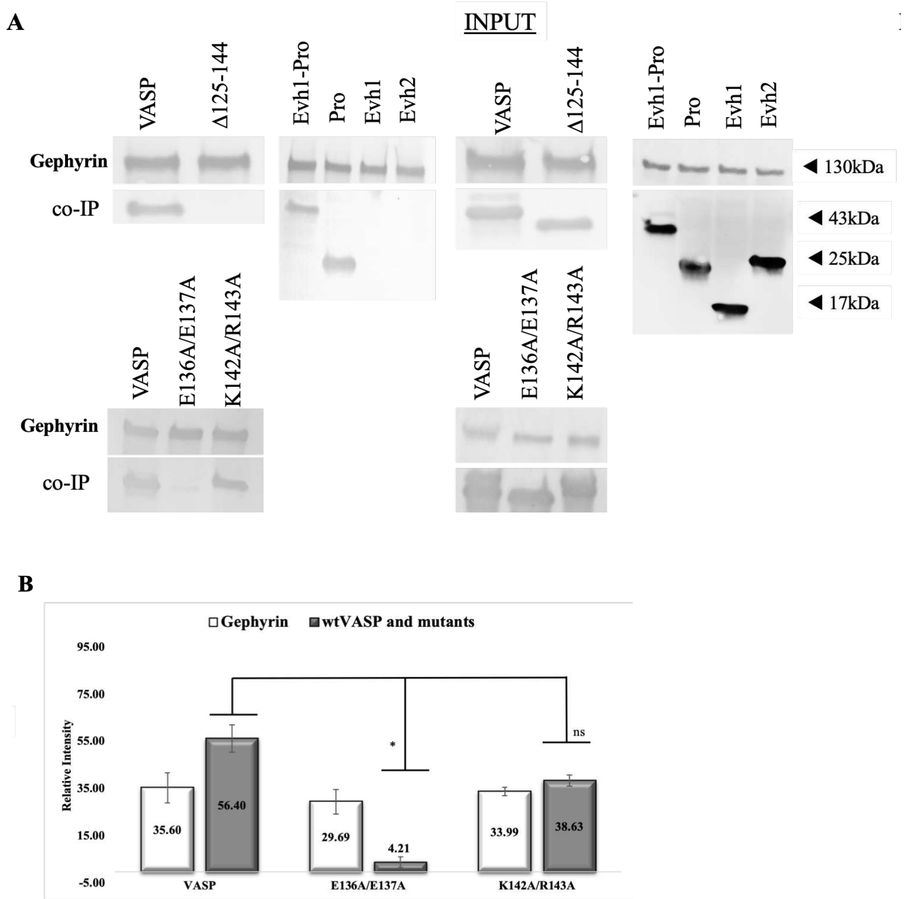

Figure IV.10 Coprecipitation assays of GFP-gephyrin with flag-VASP (and/or fragments and mutants). ***(A)*** *HEK293 cells were co-transfected using the $CaCl_2$ method with GFP-gephyrin and flag-VASP, or its fragments EVH1, EVH2, EVH1-Pro, Pro as well as the VASP mutants Δ125-144, E136A/E137A and K142A/R143A. After 72 hours in culture the cells were harvested and immunoprecipitation was carried out with GFP-magnetic beads using gephyrin as the bait protein. VASP and related proteins were visualized with an anti-flag antibody.* ***(B)*** *Co-IP of VASP was significantly decreased in the presence of the E136A/E137A mutant. The bar graph shows a quantification of the co-IP of VASP, E136A/E137A and K142A/R143A as shown in the lower gel on the left-hand side in (A). Quantification was done from three individual experiments. The images were analyzed in ImageJ for calculating the relative intensities. The data were statistically analyzed using the Kruskal-Wallis non-parametric test (*, $p<0.05$ (0.015); ns= not significant) in GraphPad Prism version 7.00 (www.graphpad.com).*

This was further confirmed in co-localization experiments utilizing HEK293 cells. For this, as described before, HEK293 cells were co-transfected with an eGFP-gephyrin fusion protein and flag-tagged wtVASP as well as its individual domains. After 72 hours in culture, the cells were fixed and immunofluorescence-labelled and images were recorded in a confocal microscope. In the colocalization experiments, I detected a decreased co-localization of both proteins, when gephyrin was co-expressed with mutants of VASP lacking the Pro-rich region (Figure IV.11).

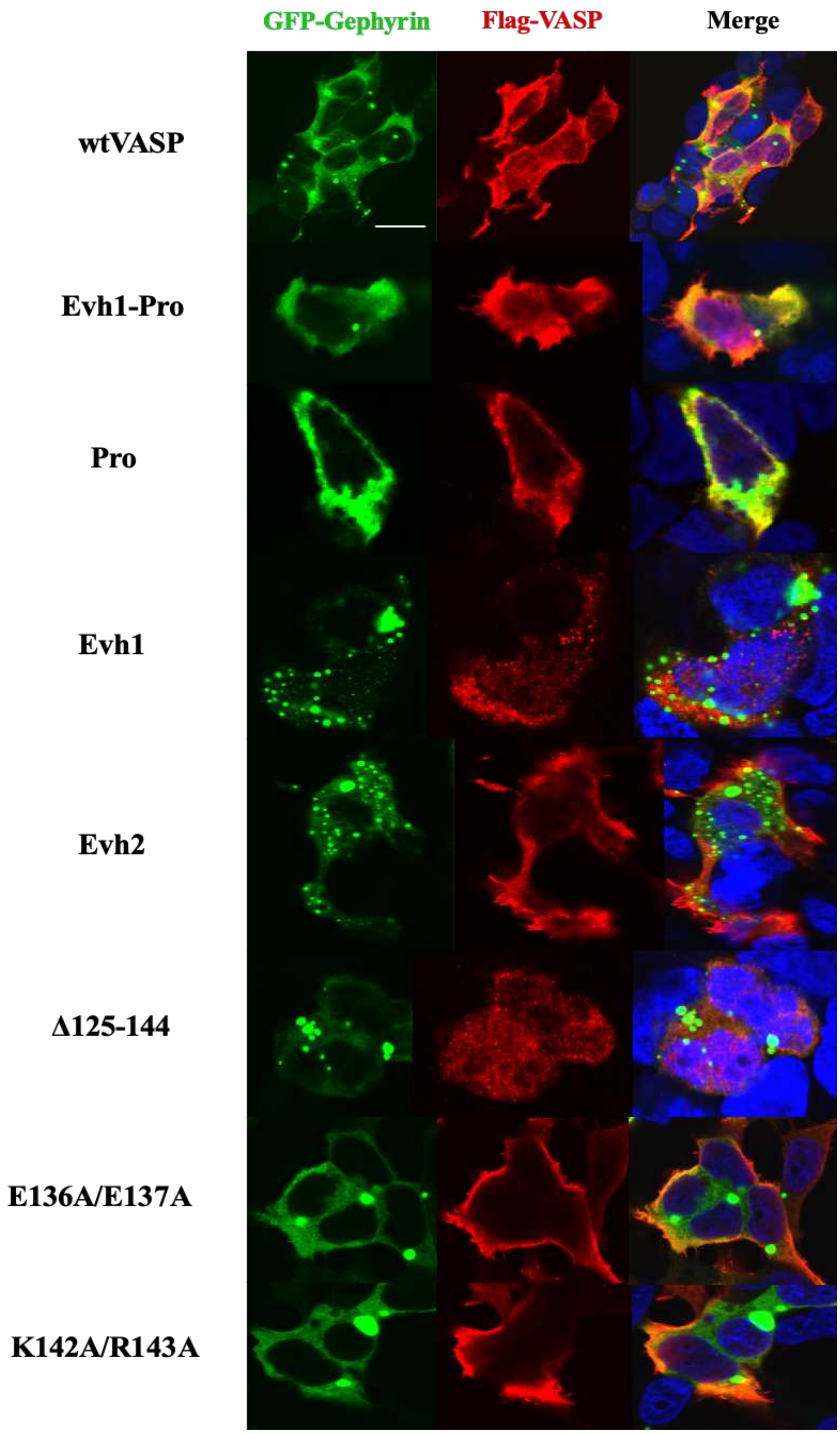

Figure IV.11 ***Colocalization of GFP-gephyrin and flag-VASP, its fragments or variants in HEK293 cells.*** *Cells were co-transfected using the $CaCl_2$ method with GFP-gephyrin plus flag-VASP (and its fragments EVH1, EVH2, EVH1-Pro, Pro or FL-VASP variants Δ125-144, E136A/E137A, K142A/R143A. After 72 hours in culture the cells were immuno-stained. The green color represents GFP-gephyrin and the red color flag-tagged VASP while colocalization* *is indicated by an orange-yellow color. The images were recorded with an Olympus confocal microscope at 60-fold magnification. Scale bar: 20 µm.*

Based on the initial results identifying the Pro-rich region of VASP, the VASP sequence was analyzed in a multiple-sequence alignment comparing human and murine VASP as well as different Mena isoforms. The latter were added since I could demonstrate that Mena also co-localizes with gephyrin in neurons[128]. The multiple sequence alignment identified two highly conserved regions, the well-known Profilin-binding segment (underlined in blue) and a second highly conserved region encompassing residues P125-Q144 (underlined in red) located just at the beginning of the Pro-rich core region (Figure IV.12a). This observation led me to postulate that these residues mediate the interaction with gephyrin. To confirm my hypothesis I performed, as already described above, the co-IP and colocalization assays with a deletion variant of VASP lacking residues 125-144, referred to as flag-VASPΔ125-144. This truncated VASP protein was no longer able to co-precipitate and to co-localize with gephyrin (Figure IV.10a, Figure IV.11), thus confirming that this 20-residue long region harbors the interaction site for gephyrin.

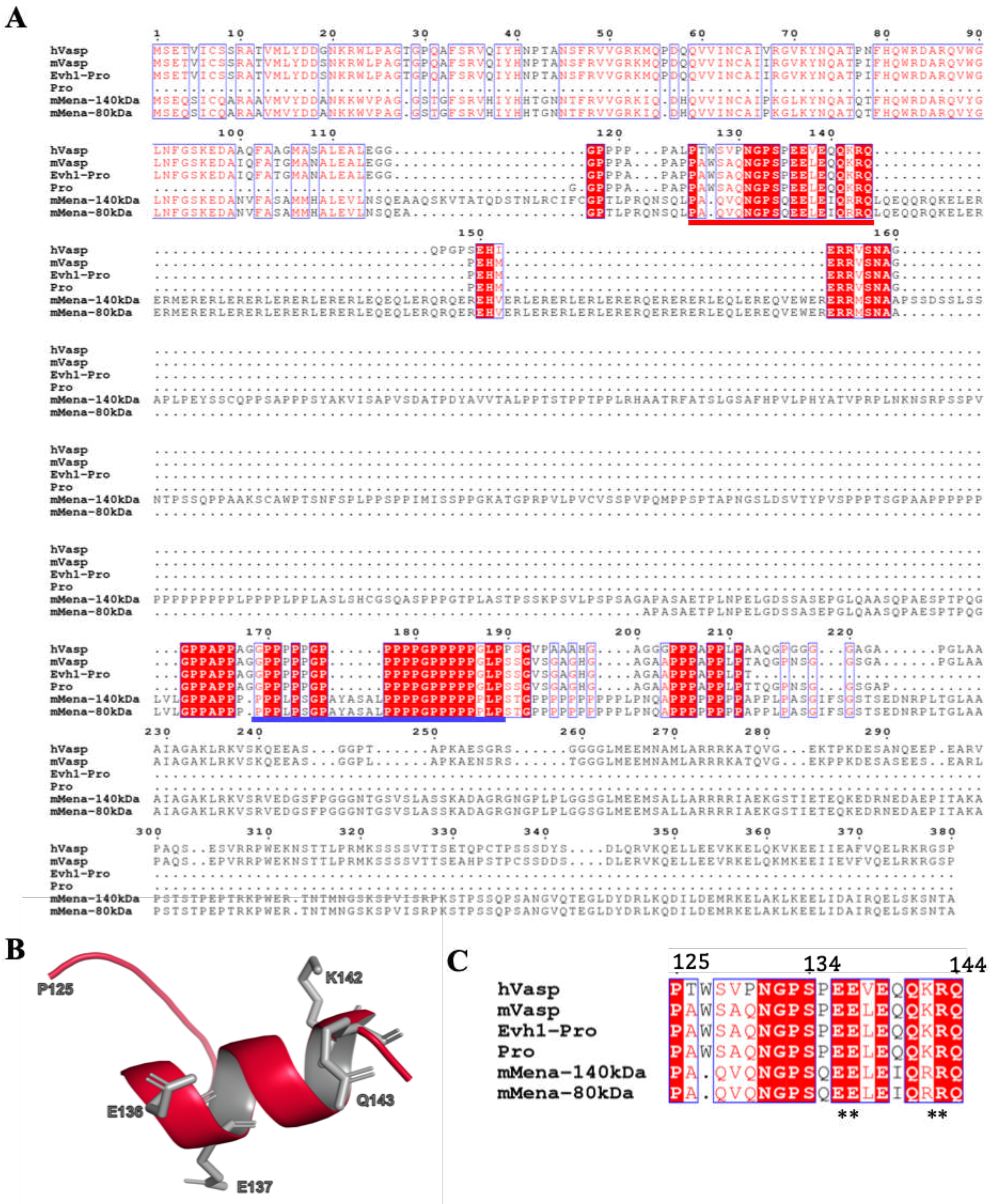

*Figure IV.12 **Multiple-sequence alignment of neuronal Mena isoforms and VASP.** **(A)** Multiple sequence alignment of murine neuronal Mena isoforms (UNIPROT: Q03173) and human and murine VASP (UNIPROT: P500552 and P70460), as well as the shortened constructs (Evh1-Pro and Pro) analyzed in the cell-based experiments. The putative gephyrin-binding site is underlined in red and the known Profilin-binding site in blue. Overlaid with a red background are residues which are strictly conserved and displayed in red are residues which are type conserved within this protein family. The multiple-sequence alignment was generated with the Kalign software. **(B)** Predicted three-dimensional structure of the putative gephyrin-binding site (peptide P125-Q144 from mVASP) as modelled with the PEP-FOLD software. Strictly conserved acidic and basic residues which were mutated in the constructs E136A/E137A and K142A/R143A are displayed in stick representation. **(C)** Sequence alignment of the putative gephyrin-binding site. Strictly conserved acidic and basic residues which were mutated in the constructs E136A/E137A and K142A/R143A are highlighted by black asterisks below the sequences.*

After identifying the putative gephyrin-binding region within VASP, I wanted to further characterize it by identifying residues which are critical for the interaction. Residues 125-144 were predicted to form a loop followed by an α-helix (Figure IV.12b). Upon closer examination, I noted the presence of two consecutives acidic residues at positions 136 and 137 in hVASP and two sequential basic residues at positions 143 and 144 in hVASP, which are conserved throughout the ena/VASP family. Their high degree of conservation could indicate that the residues mediate interactions with gephyrin (Figure IV.12a, c), possibly via electrostatic interactions. To check the involvement of these residues in the interaction with gephyrin, I engineered two double point mutants, flag-VASP(E136A/E137A) and flag-VASP(K142A/R143A), and co-transfected them with GFP-gephyrin in HEK293 cells. As shown in Figure IV.10a, the E136A/E137A double variant almost completely lost the ability to interact with gephyrin, since hardly any co-precipitation of the two proteins could be detected. On the other hand, the K142A/R143A variant only slightly diminished the co-precipitation, hence these residues were considered not to be critical for the interaction. Quantification of the co-IP data showed a significant decrease in the relative intensity from 56.4 ± 5.9 (wtVASP) to 4.2± 2.3 in the case of the E136A/E137A mutant, while only a slight, statistically insignificant decrease was observed for the K142A/R143A mutant to 38.6 ± 2.4 (Figure IV.10b). The same effects were also observed in co-localization experiments in HEK293 cells, where VASP-gephyrin colocalization was drastically diminished in the presence of the E136A/E137A double mutant (Figure IV.11).

To test whether these observations derived from HEK293 cells are also valid in another cell line, I co-transfected the same plasmids into COS-7 cells and quantified the level of co-localization of VASP within the gephyrin blobs. To perform the quantification, 25 images each representing a single cell were recorded per condition. These data are summarized in Appendix II, and in Figure IV.13, one representative image is shown per condition.

Colocalization was quantified in ImageJ using the JaCoP plugin by calculating the Pearson's correlation coefficient (Appendix III) and the results were statistically analyzed in GraphPad Prism using a One-way ANOVA test followed by Dunnett's multiple comparisons test. The results revealed no statistically significant differences in co-localization between gephyrin and either VASP or the constructs containing the Pro-rich region, flag-VASP(Pro), flag-VASP(EVH1-Pro) (Figure IV.13). In contrast, for the individual domains EVH1 and EVH2, the deletion mutant Δ125-144 and the double mutant E136A/E137A a highly significant reduction in colocalization was observed ($P<0.0001$). In case of the double mutant K142A/R143A colocalization was slightly diminished but this reduction did not reach statistical significance.

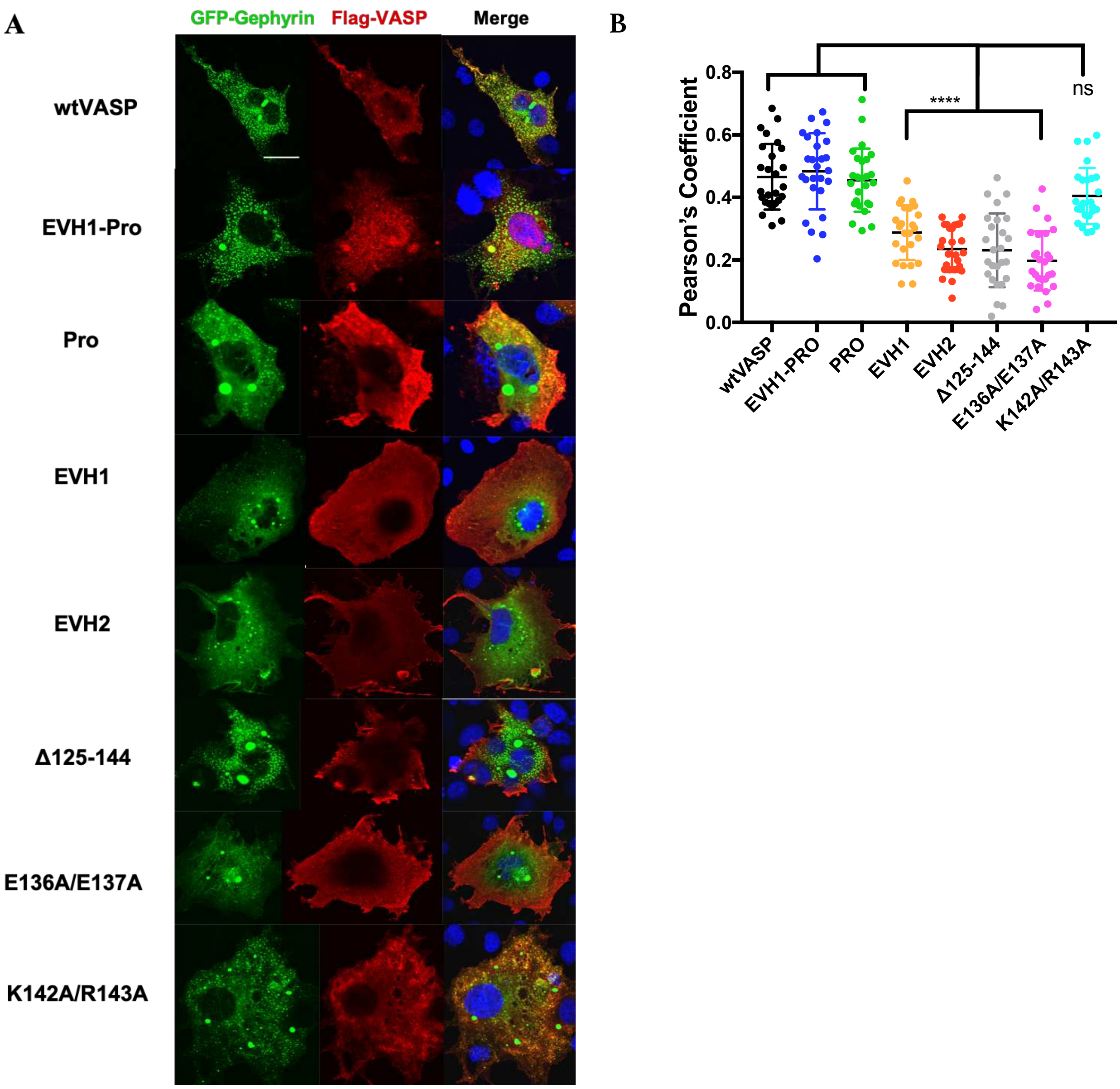

Figure IV.13 Co-localization analysis of VASP and gephyrin. (A) *Representative images of GFP-gephyrin (green, left) and flag-VASP (red, center) stained cells and the merged image (right).* ***(B)*** *Plot of the corresponding Pearson correlation coefficients measuring co-localization. Pearson analysis included a minimum of 25 cells per condition. Statistical tests were conducted using a One-way ANOVA with a Dunnett's multiple comparisons test (**** $p<0.0001$, ns= not significant). Scale bar, 10 µm.*

I corroborated these results by measuring the binding affinity between the two VASP mutants to AlexaFluor647-gephyrin in comparison to wtVASP. Figure IV.14 shows that the interaction is completely abolished in the presence of the Δ125-144 deletion mutant (no K_d-value can be derived), thus confirming that this region is essential for the interaction between the two proteins. While the interaction was also drastically affected by the substitution of the glutamic acid residues with alanine (E136A/E137A, K_d= 30.81 ± 6.38 µM, R^2= 0.9835), replacing the basic residues with alanine (K142A/R143A) barely altered the binding affinity between VASP and gephyrin (K_d=1.65 ± 0.42 µM, R^2= 0.8928).

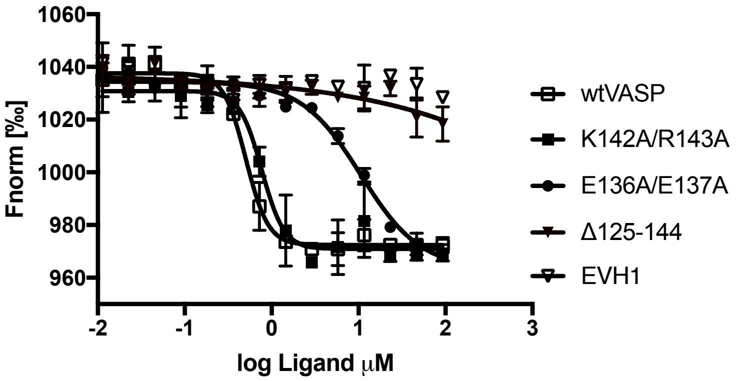

VASP	Kd µM	R^2
wtVASP	**1.43 ± 0.40**	**0.9319**
K142A/R143A	**1.65 ± 0.42**	**0.8928**
E136A/E137A	**30.81 ± 6.38**	**0.9835**
Δ125-144	**-**	**-**
EVH1	**-**	**-**

Figure IV.14 Residues Δ125-144 are critical for the interaction with gephyrin, with the acidic residues E136 and E137 playing an important role. *MST assays of VASP and its mutants (Δ125-144, E136A/E137A, K142A/R143A) binding to AlexaFluor647-gephyrin as target. The EVH1 construct was used as a negative control. The temperature of the assay was 36°C, the error bars represent the s.d. for n=3 experiments. The data were exported from the MO.Affinity Analysis software and were analyzed with GraphPad Prism software.*

IV.7 Thermodynamic characterization of the gephyrin-VASP interaction

To derive thermodynamic parameters for the gephyrin-VASP interaction, the MST assay was performed at different temperatures (from 22 °C to 36°C) to determine the K_d value at every temperature (Figure IV.15a, c). While the K_d-value was ~100 µM at room temperature, with increasing temperature the affinity increased, reaching a value in the low micromolar range at near physiological temperature (Figure IV.15). The natural logarithms (ln) of the different association constant values K_a (which equals $1/K_d$) were then plotted against the reciprocal temperature to derive the thermodynamic parameters, the molar enthalpy $\Delta H°$ and molar entropy $\Delta S°$ according to the van't Hoff plot[251] (Figure IV.15b). Specifically, $\Delta H°$ and $\Delta S°$ were derived from the slope and intercept, respectively, of a straight line described by the equation ($\ln(K_a) = -24.03*1/T + 13.56$ ($R^2 = 0.8253$)), which was derived from a linear regression analysis. From the different K_a-values, the $\Delta G°$ values at the different temperatures were calculated (Figure IV.15c) by applying the equation $\Delta G° = -RT\ln K_a$. This analysis showed that the interaction occurs spontaneously only at temperatures $T > \Delta H°/\Delta S°$, hence the reaction is endothermic but is driven by an increase in entropy.

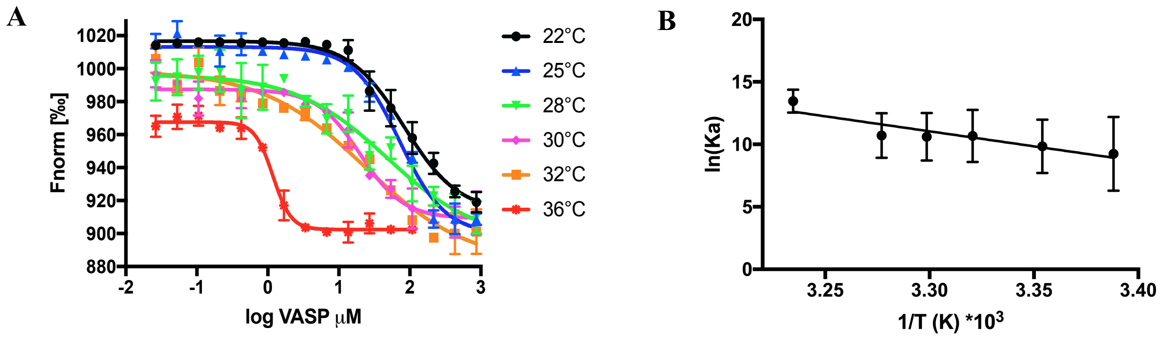

C

Temp (°C)	K_d (µM)	Temp (K)	ΔG kcal/mol	ΔH (kcal/mol)	ΔS (cal/mol*K)
22	97.68 ± 19.12	295.15	-5.42	47.79	26.94
25	53.55 ± 8.49	298.15	-5.83		
28	23.25 ± 8.05	301.15	-6.39		
30	24.71 ± 6.72	303.15	-6.39		
32	22.37 ± 5.93	305.15	-6.49		
36	1.43 ± 0.40	309.15	-8.27		

Figure IV.15 The Gephyrin-VASP interaction is thermodynamically spontaneous only when T> $\Delta H/\Delta S$, exhibiting a low micromolar affinity at near-physiological temperature. *(**A**) MST assays of VASP as a ligand and AlexaFluor647-gephyrin as the target, carried out at different temperatures (22 °C, 25 °C, 28 °C, 30 °C, 32 °C and 36 °C). Error bars represent the s.d. from n=3 experiments. (**B**) Van't Hoff plot derived from the data obtained at the different temperatures resulting in a straight line described by $\ln(K_a)= -24.03*1/T + 13.56$ ($R^2= 0.8253$) derived by linear regression analysis. The data were extracted from the MO.Affinity Analysis software and analyzed with GraphPad Prism software. (**C**) Data were extracted from the MST assays conducted at different temperatures. The molar enthalpy ΔH was calculated from the slope and the molar entropy ΔS from the intercept of the van't Hoff plot shown in (B) with the molar free energy calculated according to $\Delta G°=-RT\ln K_a$.*

IV.8 The stability of the complex is modulated by the salt concentration

Since the interaction between VASP and gephyrin involves at least the two acidic residues at positions 136 and 137 of the murine VASP protein, I investigated whether this interaction is affected by the salt concentration present in the medium. For that I performed different MST assays using VASP as the ligand protein binding to AlexaFluor647-gephyrin and tested the affinity of the interaction at different salt concentrations at 36 °C. When the interaction was tested at NaCl concentrations below 150 mM the proteins started to precipitate and formed aggregates, thus preventing data collection. Therefore, I only tested concentrations starting from 150 mM NaCl up to 500 mM NaCl. This experiment demonstrated that the interaction is indeed affected by the salinity in the medium, but, surprisingly, the affinity of the interaction increases at higher salt concentration (Figure IV.16) which argues against electrostatic interactions being the main driving force for complex formation. One possible explanation would be that ordered water molecules surrounding one or both of the binding partners are displaced upon complex formation, thus leading to the observed increase in entropy and that this process is favored at higher salt concentrations.

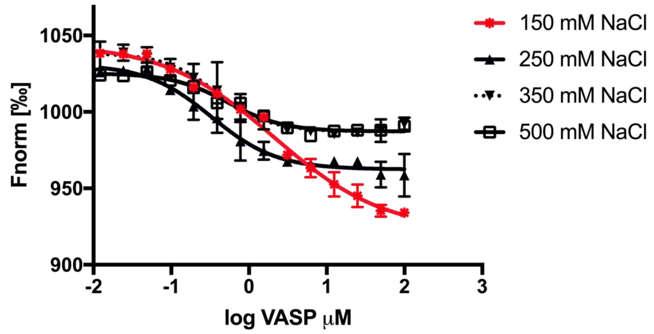

Salt Concentration	K_d µM	R^2
150 mM	1.42 ± 0.19	0.9812
250 mM	0.29 ± 0.06	0.9435
350 mM	0.44 ± 0.11	0.9142
500 mM	0.52 ± 0.13	0.9119

Figure IV.16 Salt-dependence of the VASP-gephyrin interaction. *MST assays of VASP as ligand and AlexaFluor647-gephyrin as the target, carried out at 36 °C using different salt concentrations (150 mM, 250 mM, 350 mM and 500 mM NaCl), error bars= s.d., n=3. The data was recovered from the MO.Affinity Analysis software and analyzed with GraphPad Prism software.*

IV.9 Mena/VASP colocalizes with gephyrin at synapses in hippocampal and cortical neurons

To study the impact of the interaction between gephyrin and Mena/VASP proteins at synaptic sites, the cell-based studies in HEK293 and COS-7 cells were extended to hippocampal and cortical neurons. In previous studies, the colocalization of Mena with gephyrin was tested in spinal cord and hippocampal neurons[128,129]. The preparation of spinal cord neurons is difficult to handle and the yield is typically low. I therefore chose hippocampal neurons as these were previously studied to directly compare the results as well as cortical neurons to have a second neuronal cell type. Hippocampal cultures have been used widely for visualizing the subcellular localization of endogenous or expressed proteins, for investigating protein trafficking and for defining the molecular mechanisms underlying the development of neuronal polarity, dendritic growth and synapse formation[265]. Hippocampal and cortical neurons are phylogenetically similar, since the hippocampus can be considered to be phylogenetically primitive cortical complex, which is located in the temporal lobe of humans and in the caudal portion of the rodent forebrain[265]. The main difference is that hippocampal networks tend to have more network spikes than cortical networks[266]. Therefore, since cortical neuron culture preparation is easy to handle and the yield is higher compared to hippocampal preparations, cortical neuron cultures were also prepared in the lab to test Mena colocalization with gephyrin.

In a first step primary cultures of hippocampal and cortical neurons were prepared from mice at E16 and were cultured until DIV21 followed by analysis with confocal microscopy. As synaptic marker synapsin was used. Synapsins belong to a family of neuronal phosphoproteins involved mainly in neurotransmitter release, by reversibly tethering synaptic vesicles to the actin cytoskeleton in the presynaptic terminals[267]. Immunofluorescence staining was performed using monoclonal antibodies (chapter III.1.7) to detect the synaptic marker protein synapsin, either VASP (hippocampal neurons) or the two predominantly isoforms of Mena (~80 kDa and ~140 kDa, cortical neurons) and gephyrin. According to the different fluorophores used in the secondary antibody staining, VASP is pictured in green, gephyrin in purple and synapsin in cyan (Figure IV.17a), while in the cortical neurons, Mena can be observed in purple, gephyrin in green while synapsin retains the cyan color (Figure IV.17b). When the three proteins are co-localizing the signal is visualized as white spots. As shown in Figure IV.17, focusing on the dendrites, where pre-synapses are in apposition to postsynaptic sites, the presence of white spots (highlighted by arrowheads) indicates that VASP/Mena proteins colocalize with gephyrin at synaptic sites, in both hippocampal and cortical neurons.

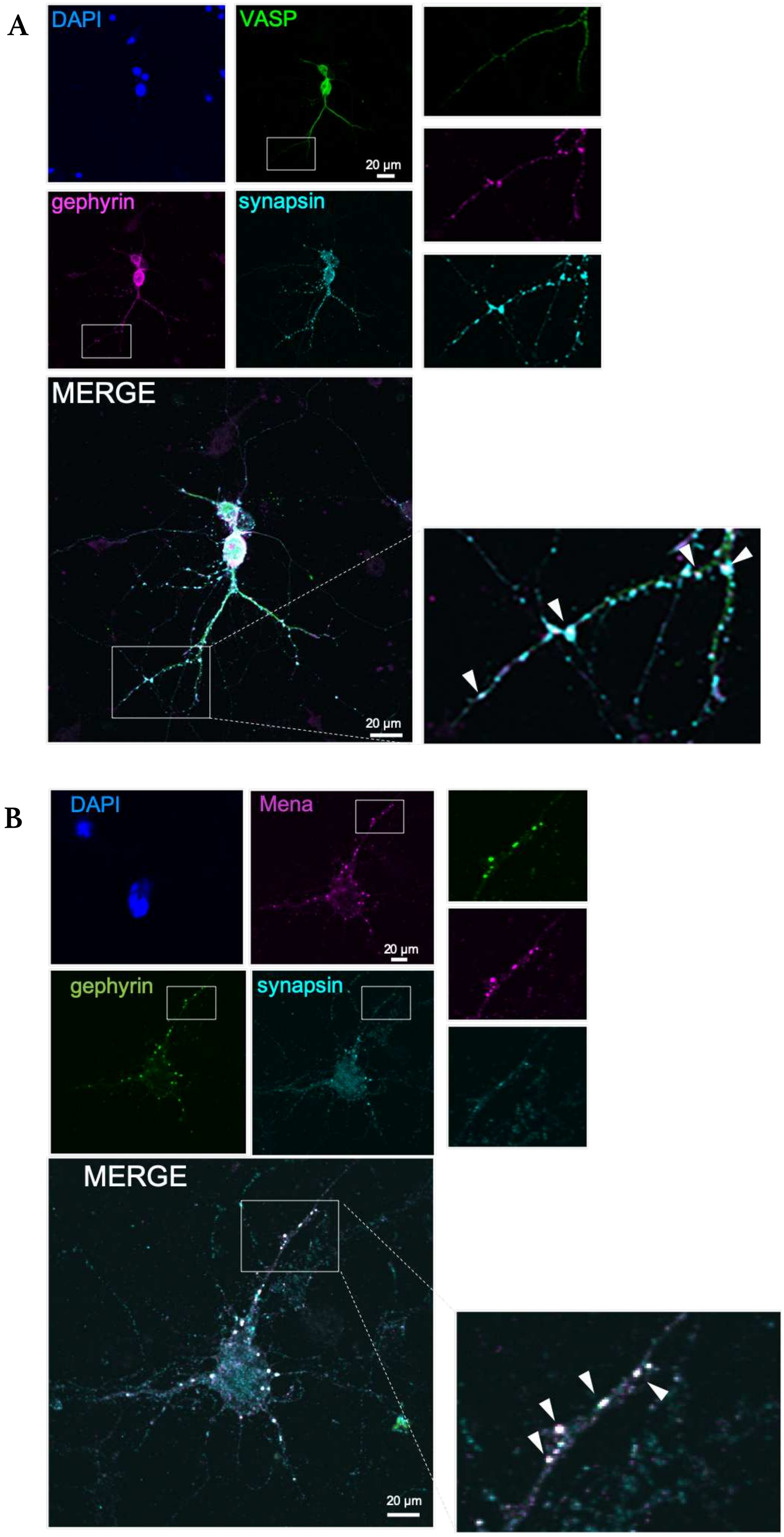

Figure IV.17 VASP/Mena proteins colocalize with gephyrin at hippocampal and cortical inhibitory synapses. (A) *Primary culture of hippocampal neurons at DIV 21. VASP and gephyrin colocalize at postsynaptic sites as indicated by white spots (indicated by the arrowheads) representing the simultaneous presence of synapsin, VASP and gephyrin.* ***(B)*** *Primary culture of cortical neurons at DIV 21. Mena and gephyrin colocalize as shown by white spots (indicated by the arrowheads) representing the simultaneous presence of synapsin, Mena and gephyrin. Scales bar: 20μm.*

Once, the co-localization of gephyrin and Mena/VASP proteins at synaptic sites was established, the next question to be answered will be to find out whether Mena/VASP are modulating gephyrin cluster size and density and hence regulating synaptic plasticity. To answer this, I designed shRNA constructs as described in chapter III.2.6.1. The shRNAs were initially tested in HEK293 cells co-transfected with the murine VASP sequence and the vector pFCK1.3 containing the coding region for the shRNAs. From a total of four different constructs, two of them shown effective knockdown (Figure IV.18) and were selected for further tests in cultured hippocampal neurons. The selected shRNAs consist of the same shRNA sequence (mentioned above in chapter III.2.6.1) and their only difference is that the shRNA is positioned in sense or antisense direction, with respect to the GFP construct used to label the neurons where the plasmid is being expressed.

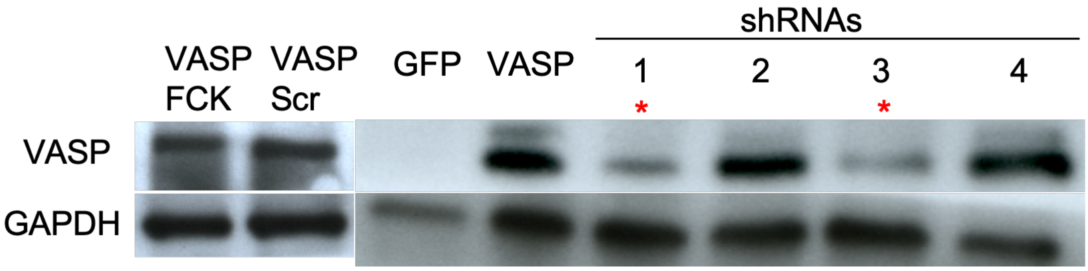

Figure IV.18 shRNA tests in HEK293 cells co-transfected with the murine VASP gene and pFCK1.3 containing the different shRNAs. *VASP protein is visualized by WB using an anti-flag antibody. As housekeeping gene glyceraldehyde-3-phosphate dehydrogenase (GAPDH) was used. From left to right the co-transfections are as follow; VASP/FCK: murine VASP together with empty vector pFCK1.3; VASP/Scr: murine VASP with a pFCK1.3 vector containing a Scr-shRNA; GFP transfected cells; murine VASP transfected cells; lines 1-4 are the different shRNAs tested in co-transfection with murine VASP. Lane 1: sense shRNA-5'GCAGGTGGTTATCAACTGT-3', lane 2: sense shRNA-5'GAGCCAAACTCAGGAAAGT-3', lane 3: antisense shRNA-5'GCAGGTGGTTATCAACTGT-3', lane 4: antisense shRNA-5'GAGCCAAACTCAGGAAAGT-3'. The shRNAs chosen for further experiments are number 1 and 3 (highlighted with red asterisks).*

The same procedure is currently taking place with the murine Mena gene, and the next steps will be to test the knockdown efficacy in cultured hippocampal neuron cells. Once, the shRNAs prove to efficiently knock down Mena/VASP expression in neurons, experiments for measuring the gephyrin cluster size and density as well as electrophysiological recording of mIPSCs will be performed.

V Discussion

V.1 Modulation of inhibitory neurotransmission by artemisinins

PDXK is of fundamental importance as its reaction product PLP is a critical cofactor in *circa* 160 different metabolic transformations. These corresponding enzymes catalyze diverse reaction during the synthesis of carbohydrates, amino acids, lipids, etc[160-162]. Of particular note in this context, PDXK is also critical for the biosynthesis of neurotransmitters, since most of the enzymes which synthesize neurotransmitters are PLP-dependent enzymes, such as GAD, the enzyme catalyzing GABA from glutamate and SHMT, which converts serine into glycine. Hence the synthesis of both inhibitory neurotransmitters, GABA and glycine, requires proper vitamin B6 levels and is indirectly dependent on the proper function of PDXK. Interestingly, additional vitamin B6-dependent enzymes including histidine decarboxylase, aromatic-L-amino-acid decarboxylase (also known as DOPA decarboxylase), glutamate pyruvate transaminase and glutamate oxaloacetate transaminase are involved in the biosynthesis of additional neurotransmitters, namely histamine, serotonin, dopamine and catecholamines, as well as being involved in the metabolism of glutamate[268-270], the main excitatory neurotransmitter. The data presented here clearly show how artemisinins modulate PDXK activity. Specifically, artemisinin and its succinic acid derivative artesunate competitively inhibit PDXK with K_i values of 120 ± 2 µM and 1250 ± 5 µM, respectively.

Interestingly, artemisinins play a dual role in modulating inhibitory synapses. As described here, at presynaptic terminals, it binds to PDXK thereby slowing down the biosynthesis of the cofactor PLP, thus limiting the biosynthesis of the neurotransmitters GABA[163] and presumably also glycine. At the same time, this drug also interferes with the postsynaptic receptor-scaffold architecture through its direct interaction with gephyrin, which impedes the binding and clustering of $GABA_A$Rs[148].

These dual neuronal targets might partially cause the neurotoxic effects of the artemisinins observed in cells, animals and humans[149,150,155-157], but the existence of other neuronal targets cannot be excluded. In this regard, the studies with PDXK and gephyrin might serve as starting point for future structure-based drug design, with the aim to optimize this lead compound for the treatment of malaria, while at the same avoiding its neurotoxic effects and improving its pharmacological properties.

Moreover, one of the major challenges in drug design to treat neurological diseases is to cross the blood-brain barrier. Artemisinins might represent a good starting point for drug design, since they efficiently cross this barrier[154]. Therefore, the crystallographic data of artemisinins in complex with mammalian targets as gephyrin and PDXK might represent a starting point for future rational drug design efforts against severe neurological disorders; for instance, those associated with dysfunctional gephyrin-mediated neurotransmission, such as Alzheimer's disease, autism, schizophrenia, epilepsy and hyperekplexia [99,110,111,115,116,119,271] or states in which there is an excess of inhibitory neurotransmitters.

V.2 Cryo-EM structure of gephyrin

From a structural point of view, gephyrin is a highly interesting protein combining two folded domains linked via a long and intrinsically unstructured linker. The protein is ubiquitously expressed and carries out two completely independent functions, namely to catalyze the last two steps during Moco biosynthesis and to orchestrate a scaffolding function at inhibitory postsynaptic specializations. How these functions are conducted in the context of its three-dimensional structure remains only poorly defined. Gephyrin was first identified by its co-purification with the GlyR[31]. The protein is composed of an N-terminally located GephG domain that trimerizes and a C-terminally positioned GephE domain that dimerizes. The two domains are linked via a ~150 residue long unstructured region, which confers to the entire structure high flexibility and vulnerability to degradation[33,35,36,52]. The N-terminal GephG was the first part of the structure to be structurally characterized by Schwarz *et al.* who reported its crystal structure in 2001 (Figure V.1a)[36]. This study revealed that this domain is composed of a central 6-stranded β-sheet surround by 8 α-helices arranged in a Rossmann fold[272]. Three monomers were arranged into a trimer via interactions between residues in α5, β4, α7, a 3_{10}-helix and the loop connecting β3 with α4 (Figure V.1a). This was followed a few years later by the crystal structure of GephE which revealed a dimer arrangement (Figure I.2). Each monomer is composed of 4 subdomains (denoted by Roman numerals I-IV) with subdomain III having the same fold as GephG (Figure V.1b)[33]. However, exhaustive efforts to elucidate a crystal structure of the full-length protein were unsuccessful, as the protein is recalcitrant to crystallisation.

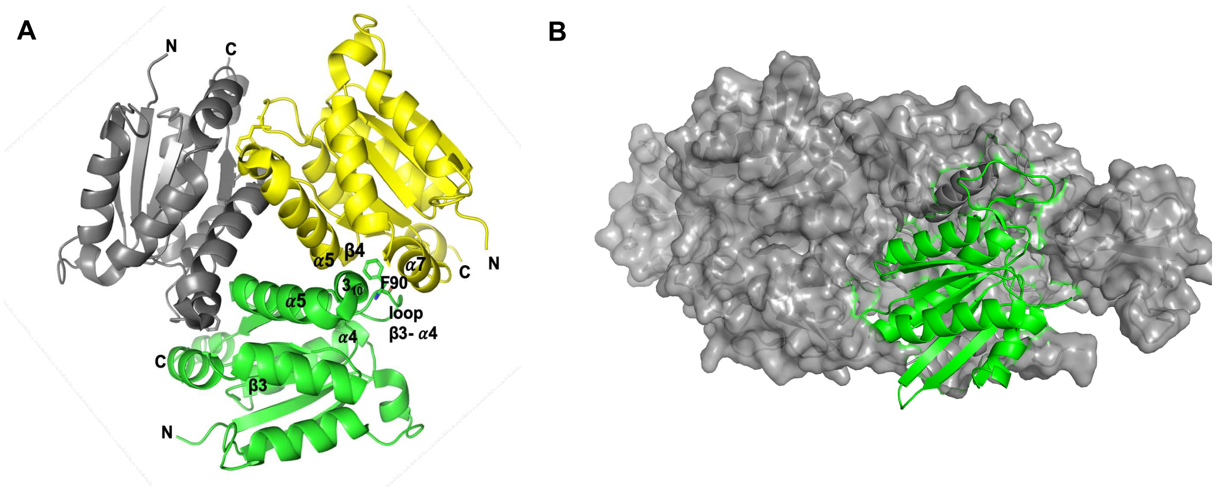

Figure V.1 Schematic representation of the GephG trimerization interface and the Rossmann fold in each GephG monomer and subdomain III of GephE. (A) *GephG trimerization interface. Monomers are in cartoon representation in colors green, yellow and gray, respectively. The interface for trimerization is formed by residues in α5, β4, α7, a 3_{10}-helix and the loop connecting β3 with α4. The domain is composed of a central 6-stranded β-sheet surround by 8 α-helices arranged in a Rossmann fold. (PDB: 1LJL)* ***(B)*** *GephE dimer in surface representation. In one monomer subdomain III is highlighted in cartoon representation (green) showing the Rossmann fold. (PDB: 2FU3)*

The so far only visualization of the full-length protein was reported by Sanders *et al.*, who reported a low-resolution structure of the protein derived by combining SAXS with AFM methodologies and imposing C_3 symmetry during SAXS data analysis (Figure I.2)[34]. In their work, they used rat gephyrin (splice variant P2) heterologously expressed in *E. coli*. Their study revealed that the protein is highly flexible and adopts multiple conformations with different degrees of compactness ranging from compact states in which GephG and GephE are in contact to each other over partially to fully extended states. Curiously, in the context of the full length protein, the trimerization of GephG is conserved while dimerization of GephE is prevented. Consequently gephyrin predominantly forms a trimer in solution with GephG acting as its structural core (Figure I.2).

Since gephyrin so far did not crystallize and SAXS only provided a low-resolution structure, I tried to obtain higher resolution structural insights using a cryo-EM approach. To accomplish this, I studied the same isoform as Sanders *et al.* in their SAXS study. Firstly, I tried with purified protein, however, the degree of heterogeneity was too high, therefore I implemented crosslinking conditions followed by fractionation of the purified protein. In the process to reduce the flexibility of gephyrin and to obtain a more homogeneous sample, suitable for cryo-EM data collection, I applied the GraFix method, which is used as a routine method for sample preparation for cryo-EM[258]. Despite these steps the resolution of the maps is still quite limited and did not significantly improve during refinement. Consequently, interpretation of the data should be considered preliminary. Nonetheless, in the resulting low resolution structure exhibiting a resolution of ~16 Å as judged by the FSC criterion of 0.143, I obtained particles that superimposed quite well with the known structures of GephG and GephE, respectively (Figure IV.6). Compared to the SAXS-structure the most striking difference is a clear absence of C_3 symmetry beyond the core of the protein formed by GephG since the three GephE domains do not follow the threefold symmetry. Instead it appears as if two GephE monomers come together to form a dimer that ressembles the crystallographically observed GephE dimer. Additional density in the cryo-EM structures could possibly represent the missing GephE and/or the three linkers, however, I cannot rule out the possibility that the monomeric GephE together with the adjoining linker is missing completely due to proteolytic degradation of the protein.

With the current sample it appears to be really challenging to derive a structure of the protein at a sufficiently high enough resolution to allow for the generation of an atomic model, even with the implementation of cryo-EM techniques. Possible reasons of the low resolution obtained can be incorrect particle picking at the beginning of data analysis, particles not being properly centered during 2D classification and insufficient homogeneity of the protein sample, despite the implementation of the GraFix protocol or possibly even caused by crosslinking.

Presumably a higher sample quality and homogeneity will be mandatory to improve the resolution. This could be achieved for instance by being even more selective in the fractions being collected during the different chromatography steps, *e.g.* only taking those fractions that correspond to the most central area under the peak after the SEC run, in the extreme case only taking the peack fraction. Furthermore, different glutaraldehyde and protein concentrations as well as the use of other bifunctional crosslinkers, *e.g.* maleimide and N-hydroxysuccinimide ester, during the GraFix procedure may help to improve the homogeneity of the sample.

On the biochemical side, an alternative approach will be to express gephyrin in insect cells which might facilitate the preparation of a more homogeneous protein sample. There is one report in the literature describing the expression of gephyrin from insect cells[35]. In this study, Herweg and Schwarz compared different splice variants of gephyrin obtained and purified from Sf9 insect cells. In contrast to gephyrin assembling predominantly into a trimer when expressed in *E. coli*, they also found a hexameric form of gephyrin.

Furthermore, they reported a higher compactness of the linker region as judged by partial proteolysis and differential scanning calorimetry experiments. Consequently, expression of gephyrin in insect cells constitutes an interesting alternative approach to investigate the structure of the full-length protein by cryo-EM.

V.3 The interaction between ena/VASP proteins and gephyrin

Gephyrin is the central scaffolding protein at inhibitory synapses and directly interacts with GlyRs as well as $GABA_ARs$[48,50,52,76] and these interactions were described in atomic detail[33,101]. Central to its scaffolding function is the simultaneous interaction with cytoskeletal elements, however, these interactions have not been characterized in as much detail biochemically, and structural data on how gephyrin is connected to the cytoskeleton do not exist. In the context of this thesis, I derived biochemical, biophysical and cell biological data that confirm and characterize in detail the interaction between gephyrin and members of the ena/VASP protein family. Since ena/VASP proteins most likely act as anti-capping factors of actin filaments, thereby promoting growth of actin filament at barbed ends, these data significantly advance our understanding of the link between gephyrin and actin filaments.

The first reports investigating the interaction between VASP and gephyrin showed that gephyrin interacted with VASP through its E domain[128]. Giesemann and colleagues demonstrated a direct binding by co-IP experiments, where they co-transfected HeLa cells with either flag-tagged gephyrin or flag-tagged GephE and probed WBs for the presence or absence of VASP in immunoprecipitations obtained with an anti-flag antibody. This finding was in agreement with observations that Cnx1, the plant homologue of gephyrin, binds actin via its E domain[273]. I therefore tested for a direct interaction between GephE and VASP in aSEC and NAGE experiments, however, I could not detect any binding (Figure IV.8), in contrast to FL-gephyrin where an interaction was observed. In subsequent NAGE and MST experiments with a peptide representing most of the N-terminal end of the linker region encompassing residues 201-255 (Linker201-255), I could clearly demonstrate that this region is interacting with VASP (Figure IV.8, Figure IV.9). This finding is in agreement with a study published by Bausen *et al.* in 2006, in which they concluded via pull-down studies, co-IP and co-localization methods[129] that the interacting region is contained within the linker, specifically, they mapped the interaction to residues 181-243. Combining my data with this study yields residues 201-243 as the ena/VASP binding region in gephyrin.

While the N-terminal part of the linker in gephyrin had been correctly identified as the region mediating the interaction with VASP, nothing was known about the residues in VASP which are responsible for the interaction with gephyrin. I could demonstrate that VASP is interacting with gephyrin through a stretch of residues located at the very N-terminal end of the proline-rich region, contrary to what Bausen *et al.* had previously suggested based on sequence analyses[129]. This study proposed that the region of interaction might be contained within the EVH1 domain, since it is known that this domain binds to proteins containing the amino acid sequence Phe-Pro-Pro-Pro-Pro, referred to as FP4 motif reflecting the one-letter code of the involved amino acids[180]. This assumption was based on the presence of the sequence $_{188}$SPPPPLSPPP$_{197}$ located within that part of the linker (residues 181-243) which mediates the binding to VASP. One drawback of this hypothesis was the absence of the leading phenylalanine which is replaced with serine. The importance of the leading Phe is demonstrated by: (1) An AP4-mito construct fails to mistarget Mena and VASP proteins to mitochondria in contrast to the FP4 parental sequence. (2) The crystal structure of Mena Evh1 domain in complex with an FP4 motif reveals that the N-terminal Phe engages in critical π-cation interactions [169,212] (Figure V.2). Bausen *et al.* did not discuss the alternative alignment of the FP4 pentapeptide with residues 193-197 in which the N-terminal leucine would correspond to the leading phenylalanine and the first proline would be replaced with serine, however, my data demonstrating an interaction with the Linker201-255 peptide and a lack of interaction with the isolated EVH1 domain not only rule out the original AP4 sequence but also the LP4 pentapeptide.

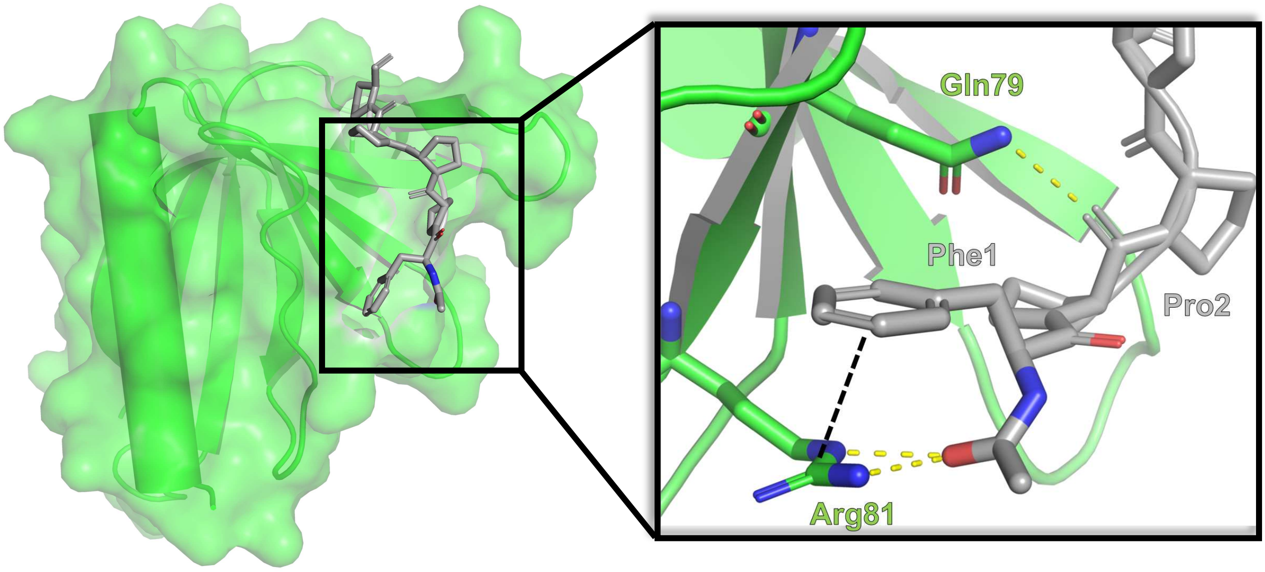

Figure V.2 Structure of the Mena Evh1 domain in complex with the FP4 motif of the actin assembly-inducing protein (ActA). *The Evh1 domain is shown in green cartoon and surface representation and the peptide (FP4) in gray sticks. The Phe at position 1 of FP4 is critical for the stabilization of the complex by engaging in π-cation interactions with the Arg81 side chain of the Evh1 (PDB: 1EVH).*

A multiple sequence alignment of ena/VASP family members revealed (Figure IV.12) that the proline-rich region is the most variable domain in this protein family, however, there are two short but highly conserved stretches present in all ena/VASP family members known to interact with gephyrin[128,129]. One of them is the well-known profilin-binding site[192], whereas the other region, which is comprised of residues P125 to Q144 has no assigned function. I therefore hypothesized that this region might represent the binding site for gephyrin. After deletion of this sequence stretch I could no longer detect an interaction between gephyrin and VASP in co-localization and co-IP assays. Furthermore, MST data demonstrated that residues 125-144 are crucial for the binding since the Δ125-144 deletion drastically reduced the affinity of this interaction (Figure IV.14), thus confirming that these residues are responsible for the interaction with gephyrin.

To identify specific amino acids involved in the interaction of VASP with gephyrin, I used a biochemical and cell biological approach by mutating highly conserved charged residues in the 125-144 stretch of VASP. Specifically, two consecutives, negatively charged residues (E136 and 137) were replaced with alanine, as were two positively charged residues (K142 and R143). While the latter residues could be replaced without impairing binding, substitution of the highly conserved glutamic acid residues, E136 and E137, were almost as severe as the Δ125-144 variant. Due to the involvement of ionic residues I speculated that complex formation resulted in the formation of salt bridges involving E136 and E137 interacting with oppositely charged residues (arginine and lysine) in the N-terminal region of the linker in gephyrin. This hypothesis was probed by conducting MST measurements at different salt concentrations. Opposite to my assumption, increasing the ionic strength enhanced the binding affinity, indicating that the interaction between the two proteins is mainly governed by the hydrophobic effect and van der Waals forces. A closer examination of the P125-Q144 stretch in VASP reveals that this region comprises hydrophobic residues which are conserved amongst the ena/VASP family such as P125, A126, G132, P133 and a type-conserved aliphatic residue (V or L) at position138. These residues, besides their contribution to the stability and the conformation of the structure, might engage in hydrophobic interactions with the linker of gephyrin. As reflected in the MST measurements, the affinity of the gephyrin-Mena/VASP interaction increases with increasing salt concentration (Figure IV.16) and also with increasing temperature (Figure IV.15), which is a typical behavior for predominantly hydrophobic interactions[274,275]. Therefore, the conservation of these hydrophobic residues within the Mena and VASP proteins, might provide suitable binding determinants for the interaction of Mena/VASP with gephyrin.

Furthermore, since complex formation is an endothermic process driven solely by entropic forces, there is an enthalpy-entropy compensation that renders the interaction spontaneous. This mechanism is not uncommonly observed in thermodynamic binding studies of biological systems[276-278], and analyses of calorimetric data for protein–ligand binding[279,280] leave no doubt that it is a genuine and common physical phenomenon. The enthalpy–entropy compensation may be due to the formation and disruption of weak noncovalent interactions. This compensation mechanism is influenced by multiple factors, such as the flexibility of the ligand-binding site or of the surrounding, the changes in intermolecular forces during the binding process and the structural and thermodynamic properties of the solvent including the hydrophobic effect, solvation/desolvation energies and the local water structure [281-283].

Nonetheless, the knowledge I derived in my thesis regarding the affinity and thermodynamic of the complex together with the prior experience in the characterization of the apo-gephyrin, might help in the design of SEC-MALS, SAXS and cryo-EM experiments aimed at determining the stoichiometry and structure of the ena/VASP-gephyrin complex, which remains so far unknown.

On the other hand, the colocalization of Mena with gephyrin was previously observed in cultured spinal cord neurons[128], however, it was not clear if this colocalization takes place at synaptic sites. Hence I carried out colocalization experiments which revealed that Mena is located in apposition to presynaptic sites in hippocampal neurons, thus suggesting a colocalization with gephyrin at synaptic densities[129]. The data I generated corroborate this colocalization in both hippocampal as well as in cortical neurons, where both proteins interact at iPSDs since they colocalize at synaptic sites (Figure IV.17).

In general, the linker of gephyrin contains binding sites for around 10 different gephyrin interactors[47,80,130,139,284], thus the vast majority of its binding partners recognize segments within the linker (Figure V.3a). For example, residues 205-212 are responsible for the interaction with DYNLL (Dynein LC8 Light Chain)[80,134], residues 319-329 for the recruitment of collybistin[138,139] and the phosphorylation-dependent binding of peptidyl prolyl cis-trans isomerase Pin1 is mediated by residues 188-201[78].

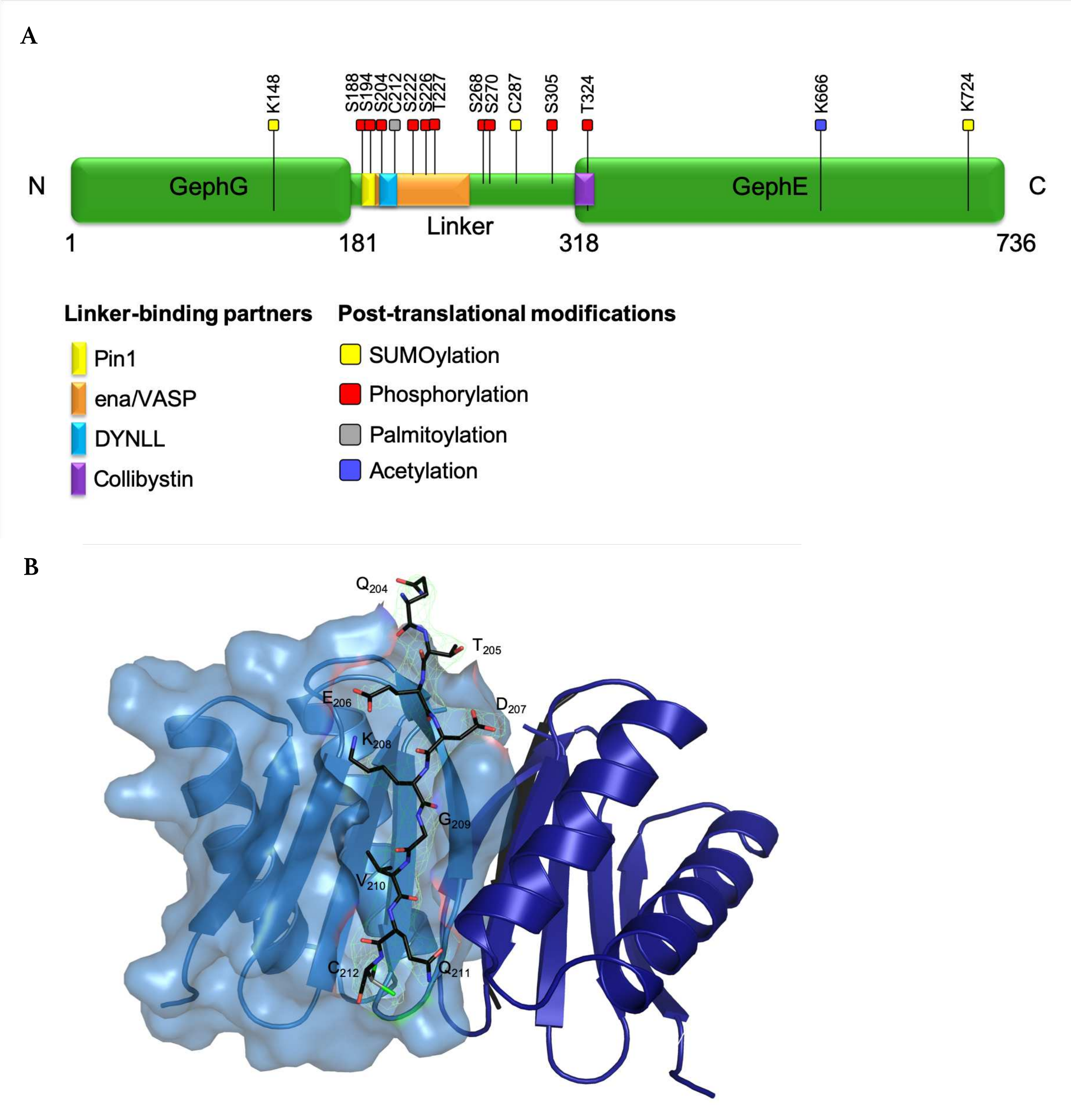

Figure V.3 Schematic representation of post-translational modifications of gephyrin and binding sites located in the linker region together with the only known structure of a binding partner (DYNLL1) in complex with the linker (residues 205-212). (A) *Schematic representation of gephyrin. The main post-translational modifications (PTMs) are shown by lines with a colored head indicating the type of PTM as indicated in the legend. The residue number of each modified side chain is located above each arrow line. The relative positions where the different linker-binding partners interact are represented by a color legend as indicated below the scheme.* ***(B)*** *DYNLL1 dimer in complex with the gephyrin linker peptide T205-C212. The monomers are represented in dark and light blue, respectively, and one of them is also shown in surface representation. The linker peptide is shown in stick representation, superimposed with its electron density (green). The figure was kindly provided by Dr. Bodo Sander.*

Strikingly, the VASP binding site (residues 201-243), as far as it is currently mapped, coincides with the DYNLL 1/2 recognition motif, which is also located in the linker region[80,134,135], specifically at residues 205-212. This raises the possibility that binding of either protein to gephyrin could modulate the interaction with the other protein, resulting in either mutually exclusive binding or enhanced binding due to cooperative effects.

The interaction between gephyrin and DYNLL 1/2 was first discovered by Fuhrmann *et al.* using the yeast-two hybrid method[80]. They narrowed down the binding site to the region encompassing residues 181-243. Subsequently, Navarro-Lérida and co-workers further refined the binding site to a 9-residue peptide corresponding to residues Thr205-Cys212 (Figure V.3)[134]. Five years later, Eun Young Lee, a former member of the Schindelin group, derived in her dissertation (unpublished data) the crystal structure of this peptide in complex with the DYNLL (Figure V.3b)[135]. The DYNLL 1/2 proteins are auxiliary subunits of dynein motor-cargo protein complexes, which play a central role in the intracellular transport of a wide range of biomolecules and organelles along microtubules, such as RNA molecules[285], the glucocorticoid receptor[286] and transmembrane receptors, exocytotic vesicles, endosomes and autophagosomes[287,288], thus regulating essential processes like neuronal migration[289], organelle biogenesis and signaling pathways[290].

Based on this general function the DYNLL 1/2 subunits were proposed to function as cargo adaptors, facilitating the transport of GlyR-containing vesicles through their interaction with gephyrin, which, in turn, binds to the receptor[81]. Indeed, sedimentation and co-IP experiments confirmed a co-transport of gephyrin-GlyR complexes as demonstrated by time-lapse video microscopy[81]. However, DYNLL 1/2 proteins are localized at the edges of synapses rather than at their centers[80]. In this work I could demonstrate that Mena/VASP proteins also colocalize with gephyrin within synaptic puncta. Regarding the question as to whether the two gephyrin ligands compete for the same binding site or enhance their respective interactions with gephyrin one can only speculate in the absence of additional data. Competitive binding would be in line with the co-transport of gephyrin-GlyR-vesicles along microtubules into the immediate vicinity of postsynaptic sites and a subsequent binding of gephyrin to ena/VASP proteins at synaptic sites. In contrast one could envision synergistic binding to take place when gephyrin-GlyR-vesicles are required for the final step in their journey to synaptic sites, which, due to the absence of microtubules in dendritic spines, presumably involves the actin cytoskeleton (Figure V.4).

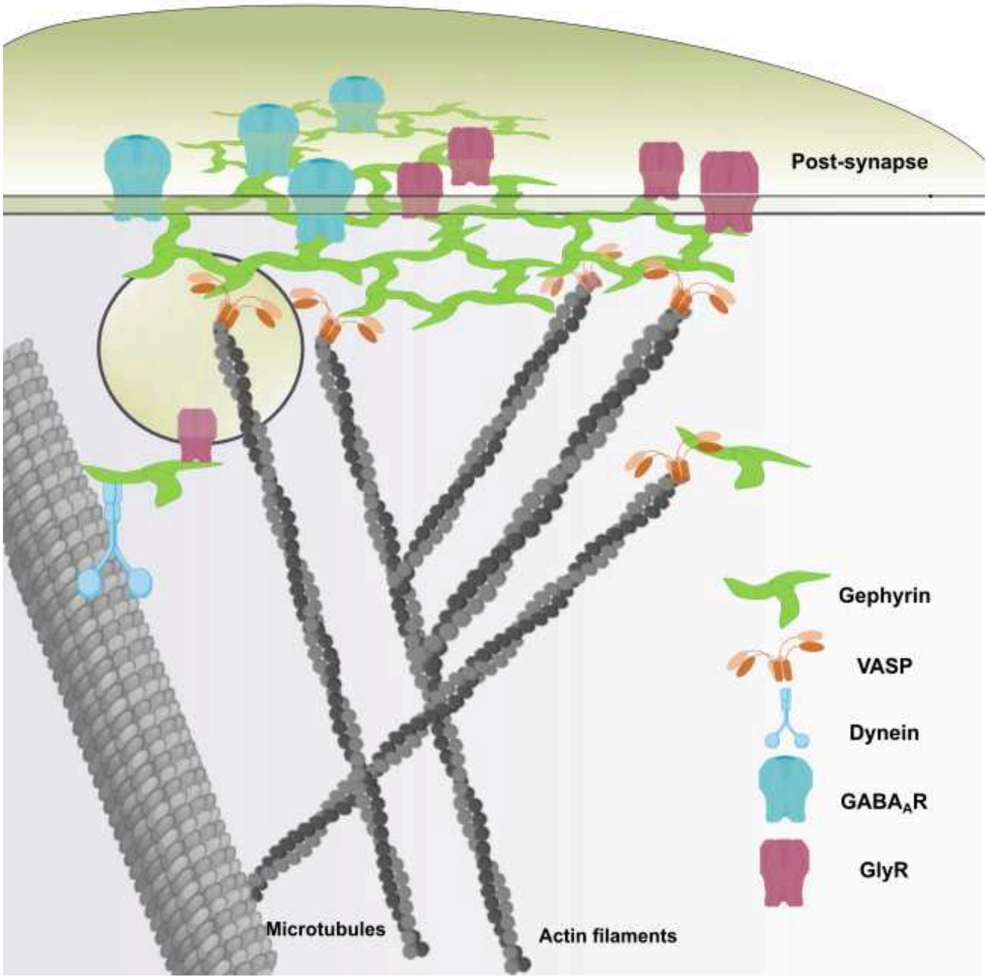

Figure V.4 In GABAergic and glycinergic postsynapstic sites, gephyrin clusters are stabilized by actin-microfilaments through ena/VASP proteins. *Schematic representation of GABAergic and glycinergic synapses showing gephyrin clusters stabilized by actin-microfilaments through interactions with ena/VASP proteins. Meanwhile gephyrin trimers are also co-transported together with GlyRs via dynein along microtubules to synaptic sites.*

One of the earliest identified binding partners of gephyrin is tubulin as gephyrin was found to directly bind to microtubules with nanomolar affinity[130]. In contrast, up to this day there are no reports of a direct interaction between gephyrin and actin filaments. Instead, the interaction is supposed to be indirect and to be mediated via actin-associated proteins. In this regard, direct interactions of gephyrin with either profilin or members of the Mena/VASP family are considered to be crucial elements tying gephyrin to the actin-cytoskeleton[128]. The association of gephyrin with the actin-cytoskeleton can serve both as a transport mechanism to recruit gephyrin-receptor complexes to synaptic sites, and as an anchoring of gephyrin to the actin-cytoskeleton, , thereby restricting the mobility of the gephyrin scaffold and the associated neurotransmitter receptors, which would otherwise diffuse freely in the lipid bilayer, which is essential for proper function of the inhibitory postsynapses (Figure V.4).

Ena/VASP family members have redundant functionalities promoting actin filament elongation by acting as anti-capping proteins[201]. It was demonstrated that the Mena protein is positioned at the tip of the growth cone of filopodia[207] where it triggers actin polymerization and hence filopodia elongation. As demonstrated in this thesis, gephyrin interacts with VASP at iPSDs since they colocalize at synaptic sites (Figure IV.17). Therefore, it might be possible that at synaptic sites, VASP stabilizes the structure of gephyrin (Figure V.4), thereby supporting its scaffolding function, and through PTMs on either protein the density and size of gephyrin clusters is modulated, which, in turn, contributes to the dynamic and plasticity of $GABA_A$Rs and GlyRs at iPSDs.

Ena/VASP proteins, as already mentioned, function as anti-capping factors promoting the actin filament elongation. Hence, another plausible hypothesis might be that the interaction with gephyrin at synaptic puncta abrogates their capping function, thereby inhibiting the continuous microfilament elongation once the barbed end of actin-filaments reaches synaptic sites. Therefore, this mechanism might regulate the elongation of filopodia during synaptogenesis, ultimately contributing to synaptic plasticity. To demonstrate that gephyrin indeed impedes the ena/VASP anti-capping function, several standard *in vitro* methods exist to test the ena/VASP anti-capping function in the presence and absence of gephyrin. Among them are actin-polymerization assays using a pyrene-modified actin and total internal reflection fluorescence (TIRF) microscopy[291,292]. Basically, these methods will help to visualize ena/VASP-mediated actin-polymerization by observing an increase in fluorescence over time (Figure V.5). In case that gephyrin prevents actin-polymerization, filament growth will stop, which would result in no further fluorescence increase.

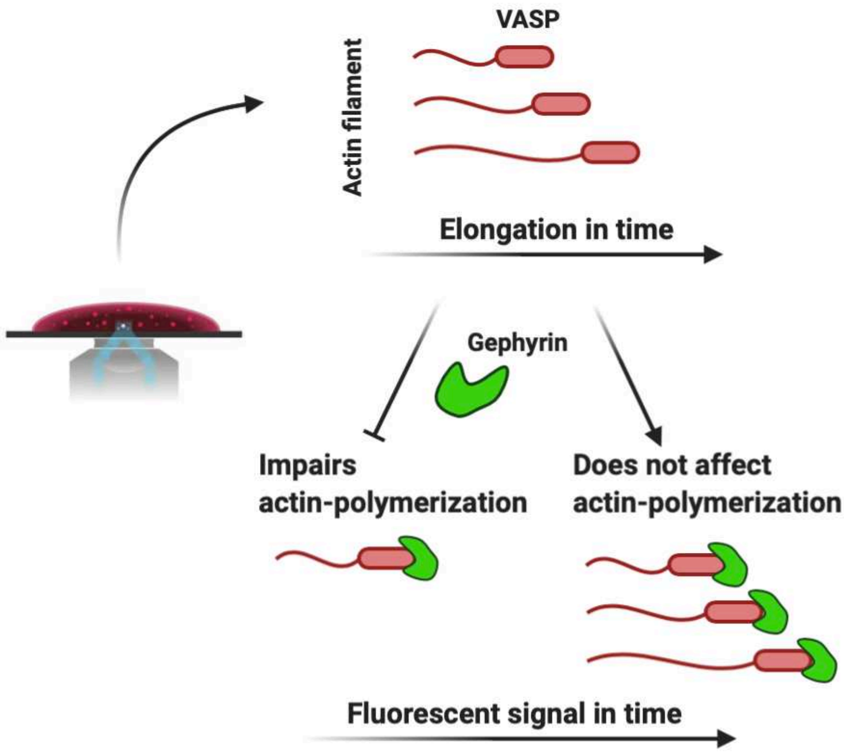

Figure V.5 Schematic representation of a TIRF experiment outcome. *If gephyrin abrogates the ena/VASP anti-capping function, actin-microfilament elongation will be impeded (left), while actin filaments will continue to grow if gephyrin binding does not influence the anti-capping function of ena/VASP (right).*

In addition, the linker also harbors most of the sites where gephyrin is modified via PTMs (Figure V.3a), including phosphorylation, SUMOylation, acetylation and palmitoylation. In the case of phosphorylation, 22 different sites in gephyrin have been identified, of which only one is located outside the linker, namely T324 in GephE[35,64,293]. Particularly well studied have been the phosphorylation events taking place at S268 and S270, which modulate gephyrin cluster density and size[61,62]. These sites are located in relatively close proximity of residues 201-243, the ena/VASP binding region, hence there could be cross-talk between these phosphorylation sites and the gephyrin-ena/VASP interaction.

Gephyrin dephosphorylation at Ser270 regulates dendrite growth and branching by modifying GABAergic, but not glutamatergic transmission[294]. Studies in cultured hippocampal neurons indicated that gephyrin assemblies at synapses are in the dephosphorylated state at positions S268 and S270 as demonstrated by Tyagarajan *et al*[61,62]. Those residues are phosphorylated via ERK- and GSK3β-dependent pathways, respectively, and upon phosphorylation by these kinases the density and size of gephyrin clusters decreases, resulting in a calpain-mediated degradation of gephyrin, which in turn affects the amplitude and frequency of GABAergic mIPSCs. Accordingly, in a study conducted by Bausen *et al*[66] using phosphatase inhibitors, the number and size of gephyrin clusters was also reduced. Although these phosphorylation sites are not directly within the ena/VASP interacting region, it might be that these proximal PTMs regulate the compactness of gephyrin and especially its linker, and hence the exposure of the ena/VASP binding site. Furthermore, within residues 201-255 there are additional phosphorylation sites such as S204, S222, S226 and T227 (Figure V.3a), however, the role and regulation of these phosphorylation sites remains poorly understood at present. In any case, VASP certainly binds to non-phosphorylated gephyrin, since I could demonstrate an interaction in my *in vitro* studies where neither gephyrin nor VASP are post-translationally modified.

Whether PTMs will enhance or diminish binding remains an open question at present. To address this question binding experiments using phosphorylated gephyrin or variants mimicking phosphorylations such as S268D and S270D could be performed to investigate how these PTMs modulate the interaction *in vitro*. Besides, one could check the status of gephyrin phosphorylation in colocalization experiments by probing the presence of gephyrin which is phosphorylated at S270 in cell-based colocalization experiments with VASP by using the mAb7a antibody[63]. This antibody recognizes the epitope 264-276 of gephyrin including the phosphorylation at residue 270 and is widely used to detect brain specific 93 kDa S270-phosphorylated gephyrin.

On the side of VASP it should be noted that it harbors a phosphorylation site near the binding region at S157 (Figure V.6). Phosphorylation of this residue abrogates the interaction of VASP with the SH3 domain-containing proteins Abl, Src and αII-spectrin[189,295]. This modification also controls the cellular distribution of VASP, promoting a localization at the leading-edge in migrating cells[296,297] and at the tip of the growth cone in filopodia, thereby promoting filopodia and spine formation[216]. S157 is a conserved phosphorylation site within the vertebrate ena/VASP family including VASP, Mena and EVL, and this residue is phosphorylated by PKA[231,234]. In summary, although there are no PTM sites within the interacting region of either protein, formation of the gephyrin-VASP complex might be modulated through nearby PTMs. Consequently, future experiments should be conducted to elucidate the role of phosphorylations and other PTMs in modulating the interaction between VASP and gephyrin and how these PTMs regulate dynamic processes at inhibitory postsynapses.

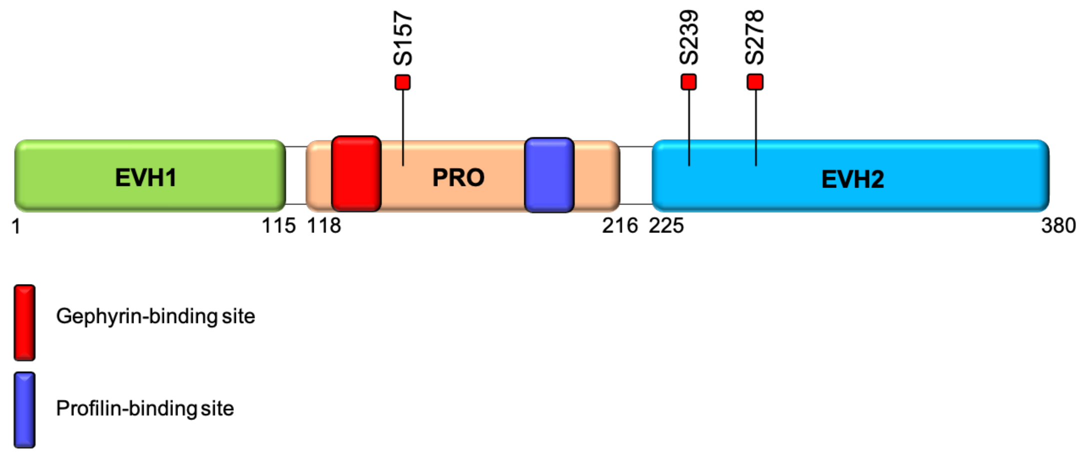

Figure V.6 Schematic representation of VASP's PTMs and the binding sites harbored in the proline-rich region. *PTMs are shown by lines with a red square indicating phosphorylation. The number of the modified residue is indicated on top of the line. Gephyrin and profilin-binding sites are marked by their relative positions in the Pro-rich region (Pro) of VASP, highlighted in red and blue, respectively.*

The ena/VASP family was shown to be essential for the mobility of many membrane-associated proteins and for neuronal positioning during embryogenesis[212]. This family plays a key role in neuronal cells, as demonstrated by Mena-deficient mice that are simultaneously heterozygous for a profilin 1 deletion. These animals show defects in neurulation and die before birth[207]. Profilin is a small protein of ~14-17 kDa and exists in two isoforms, profilin 1 and 2[298]. Both isoforms interact directly with actin monomers (G-actin), VASP and gephyrin[128,131,299]. Furthermore, triple knock-out (ko) mice which were deficient for all three ena/VASP family members (Mena, VASP and EVL) died between embryonic and postnatal ages of E16.5 and P0, while animals containing a single VASP allele were viable and fertile[211]. The triple-ko animals displayed severe defects in neurite initiation and resulted in neuronal ectopias during corticogenesis[211].

In hippocampal neurons, VASP also shows colocalization with SV2 and PSD-95 clusters at excitatory postsynaptic sites[217]. SV2 is the synaptic vesicle glycoprotein 2 present at presynaptic sites, while PSD-95 is the postsynaptic density protein of 95 kDa, thus its name, and it is located at excitatory postsynaptic sites where it functions as scaffolding protein[300]. Via a VASP knockdown approach[217] the protein was observed to regulate the size of spine head areas, which was reduced in its absence. Furthermore, VASP was also found to be critical for the synaptic localization of other scaffolding-proteins such as Homer and Shank. In the absence of VASP, the size of PSD95 and GluR1 clusters decreased while the amplitudes of miniature excitatory postsynaptic currents (mEPSCs) were reduced. Expression of VASP extended the retention time of GluR1 at spines. These observations are in line with a central role of VASP in the regulation of excitatory synaptic signal strength.

This of course raises the question regarding the role VASP and its cousins play at inhibitory synapses? I hypothesize that VASP plays a similar role at inhibitory postsynaptic sites. In the absence of VASP, I would predict that the density of gephyrin at synaptic sites would be reduced resulting in a decrease in $GABA_AR$ and GlyR clusters and weakened mIPSC amplitudes. To demonstrate this, experiments are ongoing using shRNAs to knock down Mena/VASP expression in cultured hippocampal neurons. Bausen *et al.* conducted experiments in hippocampal neurons treated with alkaloids to disrupt the microfilaments[129]. In their findings, they observed that after actin microfilament disaggregation, Mena failed to localize to synapses, while at the same time the number of gephyrin clusters decreased, especially affecting small clusters, which were defined as being smaller than ~5 μm in diameter. While this effect was primarily observed in immature hippocampal neurons, it was less prominent in differentiated neurons[129,164,166]. This observation suggests that Mena/VASP are particularly important during the initial steps of synapse formation, for instance by regulating the deposition of gephyrin beneath the inhibitory postsynaptic membrane. One should also point out that profilin could further modulate the gephyrin-ena/VASP network. Hence, a multi-protein complex could regulate the anchoring of gephyrin clusters to actin filaments via profilin/VASP and might contribute to their stabilization and maintenance.

VI Closing remarks

In the context of this thesis, I have biochemically and enzymatically characterized the inhibitory action of artemisinins upon the PDXK enzyme. First, murine PDXK was kinetically characterized, deriving values of K_m and k_{cat} which were similar to values previously reported by other groups. Second, I could demonstrate that artesunate and artemisinin exhibit a competitive inhibition mechanism and that artemisinin is 6 times stronger inhibitor in comparison with artesunate of PDXK. Finally, I observed that the modification of residues V41 and F43 impairs the enzymatic function of the enzyme, probably because the binding of the substrate is affected by these mutations. Meanwhile, the elimination of the guanidinium moiety of R86 was not enough to impair the binding of artesunate. These results allowed to contribute biochemical data to a multi-disciplinary investigation of the neurotransmission impairment by the anti-malarial drugs artemisinins. This study is particularly relevant as it represents one of only a few reports to date that analyze the impact of drugs on GABAergic neurotransmission and identifying a new presynaptic target protein.

Addressing a second aim of this thesis, I have established a protocol for the elucidation of the cryo-EM structure of full-length gephyrin, the principal inhibitory postsynaptic scaffolding protein, resulting in a preliminary, low resolution structure of the protein at a resolution of 16 Å. The density map is clearly asymmetric and a preliminary interpretation allowed for the placement of a G-domain trimer and an E-domain dimer. Additional improvements of the sample quality will be required to achieve higher resolution, which have been either initiated or are discussed in this work.

In the main part of my thesis, I have molecularly characterized the complex formed by gephyrin and the actin-cytoskeleton related protein Mena/VASP. Using a biochemical and biophysical approach as well as with the use of cell-based studies, the gephyrin and VASP binding sites have been mapped and narrowed to specific regions of the proteins. Therefore, the conclusions of this work are that gephyrin interacts with VASP through its linker region, specifically residues P201-V255. Meanwhile, VASP binds to gephyrin via its proline-rich region, in particular residues P125-Q144. From site-directed mutagenesis studies, I concluded that within the P125-Q144 stretch in VASP, the conserved acidic residues E136 and E137, are critical for the gephyrin-VASP interaction, while the conserved basic residues K142 and R143 are not. The formation of this complex *in vitro* is spontaneous at temperatures $T>\Delta \boldsymbol{H}/\Delta \boldsymbol{S}$, being endothermic and entropically favored. The binding affinity increases at higher temperatures and salt concentrations, exhibiting a low micromolar affinity at physiological temperature. In addition to visualizing complex formation in co-transfected cells, I could demonstrate that the two proteins colocalize at synaptic sites in cultured hippocampal as well as in cortical neurons.

In summary, the data presented in this thesis provide new insights into the formation and stabilization of gephyrin clusters at inhibitory synapses by interactions with the actin-cytoskeleton.

VII Outlook

Amongst the aims of this thesis have been to elucidate the cryo-EM structure of full-length gephyrin and to molecularly characterize the complex formed by gephyrin and members of the actin-cytoskeleton related protein ena/VASP family. While most of the goals were accomplished through this work, some questions remain open. To continue this work, I propose some strategies, which are presented below.

With respect to the first aim, I have described a workflow which provided an initial, low-resolution cryo-EM structure of full-length gephyrin. To improve the resolution, some modifications of the protocol will be required. General recommendations are: (1) Also express gephyrin in insect cells possibly resulting in a more homogenous protein preparation with a decreased flexibility in the linker region. (2) To improve the protein purification protocol by incorporating additional chromatography steps and being more selective in the choice of fractions after the individual chromatography steps. (3) To modify the GraFix protocol by employing different crosslinkers and varying the concentrations. (4) To again try cryo-EM without crosslinking but utilizing samples which were generated by considering the first two steps.

The structural studies with holo-gephyrin provide one avenue to derive the first high resolution structure of the intact protein, however, to increase the chances of success these studies should be extended to the gephyrin-VASP complex. In an initial step the stoichiometry of the complex should be analyzed by SEC-MALS, followed by a low-resolution structural characterization by SAXS and, ultimately, cryo-EM. These studies would define the respective interacting regions beyond what has been mapped by biochemical techniques and would also identify residues which could be targeted in subsequent structure-function studies.

Besides the structural characterization of the interaction between gephyrin and VASP, as a representative member of the ena/VASP family, the functional characterization of this interaction and its physiological relevance need to be further refined. In this sense, one question I would like to answer is how is this interaction modulated? To answer this question, I propose to perform *in vitro* binding tests, like MST and NAGE using phospho-mimetic gephyrin mutants, such as the S222D, S226D, T227D, S268D and S270D mutants to check the interaction with VASP, and, conversely, using phospho-mimetic VASP mutants, such as the S157D variant to investigate the interaction with gephyrin, in order to check whether complex formation is modulated by phosphorylation events. In addition, the colocalization of phosphomimetic mutants of VASP and gephyrin should be characterized in HEK293 cells. Finally, the phosphorylation state of VASP and gephyrin colocalizing at synaptic sites in hippocampal and cortical cultured neurons might be identified via phospho-specific antibodies.

From the perspective of VASP, whether the binding of gephyrin hampers its anti-capping function remains an attractive, yet unproven hypothesis. Substantiating this assumption might be very interesting to complement the data aimed at describing the *in vivo* modulation of this complex. To test and analyze this phenomenon, it will be necessary to analyze the actin-polymerization function of VASP *in vitro* in the presence and absence of gephyrin, either using pyrene-modified actin or TIRF microscopy assays.

The elucidation that the VASP-binding site is in the same region in gephyrin as the DYNLL-binding site prompted the question about a possible interplay between the two gephyrin binding partners. To derive additional insight into the functionality of this binding site, competition binding assays between DYNLL and VASP in their interactions with gephyrin could be performed using MST and ITC. These interactions might also be visualized in cell-based studies, by using co-transfected HEK293 cells as well as cultured hippocampal and cortical neurons and checking for a possible colocalization of DYNLL, VASP and gephyrin via confocal microscopy.

Since the physiological relevance behind this interaction remains a central open question, ongoing knockdown experiments will hopefully help to functionally characterize the physiological role of this interaction. To this end, after the knockdown expression of Mena/VASP proteins via shRNAs, gephyrin/GABA$_A$Rs cluster size and number will be determined as well as electrophysiological recordings of mIPSCs to test whether the absence of Mena/VASP impairs the proper formation of gephyrin clusters and ultimately GABAergic synapses. The final test for the importance of the gephyrin-Mena/VASP interaction will come from rescue experiments in which the gephyrin-binding deficient ΔP125-Q144 VASP variant will be transfected into a Mena/VASP knockdown background. In this setting, the regular actin cytoskeleton-related functions of Mena/VASP will not be impaired and the resulting phenotype should solely be due to the absence of its interaction with gephyrin.

VIII Literature

1 Dale Purves, G. A., David Fitzpatrick, William Hall, Anthony LaMantia, Leonard White, Richard Mooney, and Michael Platt. *Neuroscience*. Sixth edition edn, (2018).

2 Sudhof, T. C. Neurotransmitter release: the last millisecond in the life of a synaptic vesicle. *Neuron* **80**, 675-690, doi:10.1016/j.neuron.2013.10.022 (2013).

3 Dutertre, S., Becker, C. M. & Betz, H. Inhibitory glycine receptors: an update. *J Biol Chem* **287**, 40216-40223, doi:10.1074/jbc.R112.408229 (2012).

4 Sieghart, W. *et al.* Structure and subunit composition of GABA(A) receptors. *Neurochem Int* **34**, 379-385 (1999).

5 Kasaragod, V. B. & Schindelin, H. Structure-Function Relationships of Glycine and GABAA Receptors and Their Interplay With the Scaffolding Protein Gephyrin. *Front Mol Neurosci* **11**, 317, doi:10.3389/fnmol.2018.00317 (2018).

6 Kasaragod, V. B. & Schindelin, H. Structure of Heteropentameric GABAA Receptors and Receptor-Anchoring Properties of Gephyrin. *Front Mol Neurosci* **12**, 191, doi:10.3389/fnmol.2019.00191 (2019).

7 Du, J., Lu, W., Wu, S., Cheng, Y. & Gouaux, E. Glycine receptor mechanism elucidated by electron cryo-microscopy. *Nature* **526**, 224-229, doi:10.1038/nature14853 (2015).

8 Huang, X., Chen, H., Michelsen, K., Schneider, S. & Shaffer, P. L. Crystal structure of human glycine receptor-alpha3 bound to antagonist strychnine. *Nature* **526**, 277-280, doi:10.1038/nature14972 (2015).

9 Huang, X., Chen, H. & Shaffer, P. L. Crystal Structures of Human GlyRalpha3 Bound to Ivermectin. *Structure* **25**, 945-950 e942, doi:10.1016/j.str.2017.04.007 (2017).

10 Huang, X. *et al.* Crystal structures of human glycine receptor alpha3 bound to a novel class of analgesic potentiators. *Nat Struct Mol Biol* **24**, 108-113, doi:10.1038/nsmb.3329 (2017).

11 Miller, P. S. & Aricescu, A. R. Crystal structure of a human GABAA receptor. *Nature* **512**, 270-275, doi:10.1038/nature13293 (2014).

12 Laverty, D. *et al.* Crystal structures of a GABAA-receptor chimera reveal new endogenous neurosteroid-binding sites. *Nat Struct Mol Biol* **24**, 977-985, doi:10.1038/nsmb.3477 (2017).

13 Miller, P. S. *et al.* Structural basis for GABAA receptor potentiation by neurosteroids. *Nat Struct Mol Biol* **24**, 986-992, doi:10.1038/nsmb.3484 (2017).

14 Phulera, S. *et al.* Cryo-EM structure of the benzodiazepine-sensitive alpha1beta1gamma2S tri-heteromeric GABAA receptor in complex with GABA. *Elife* **7**, doi:10.7554/eLife.39383 (2018).

15 Zhu, S. *et al.* Structure of a human synaptic GABAA receptor. *Nature* **559**, 67-72, doi:10.1038/s41586-018-0255-3 (2018).

16 Grudzinska, J. *et al.* The beta subunit determines the ligand binding properties of synaptic glycine receptors. *Neuron* **45**, 727-739, doi:10.1016/j.neuron.2005.01.028 (2005).

17 Langosch, D., Thomas, L. & Betz, H. Conserved quaternary structure of ligand-gated ion channels: the postsynaptic glycine receptor is a pentamer. *Proc Natl Acad Sci U S A* **85**, 7394-7398, doi:10.1073/pnas.85.19.7394 (1988).

18 Patrizio, A., Renner, M., Pizzarelli, R., Triller, A. & Specht, C. G. Alpha subunit-dependent glycine receptor clustering and regulation of synaptic receptor numbers. *Sci Rep* **7**, 10899, doi:10.1038/s41598-017-11264-3 (2017).

19 Sigel, E. & Steinmann, M. E. Structure, function, and modulation of GABA(A) receptors. *J Biol Chem* **287**, 40224-40231, doi:10.1074/jbc.R112.386664 (2012).

20 Gamlin, C. R., Yu, W. Q., Wong, R. O. L. & Hoon, M. Assembly and maintenance of GABAergic and Glycinergic circuits in the mammalian nervous system. *Neural Dev* **13**, 12, doi:10.1186/s13064-018-0109-6 (2018).
21 Tretter, V. *et al.* Gephyrin, the enigmatic organizer at GABAergic synapses. *Front Cell Neurosci* **6**, 23, doi:10.3389/fncel.2012.00023 (2012).
22 Tretter, V., Ehya, N., Fuchs, K. & Sieghart, W. Stoichiometry and assembly of a recombinant GABAA receptor subtype. *J Neurosci* **17**, 2728-2737 (1997).
23 Baumann, S. W., Baur, R. & Sigel, E. Forced subunit assembly in alpha1beta2gamma2 GABAA receptors. Insight into the absolute arrangement. *J Biol Chem* **277**, 46020-46025, doi:10.1074/jbc.M207663200 (2002).
24 Maric, H. M., Mukherjee, J., Tretter, V., Moss, S. J. & Schindelin, H. Gephyrin-mediated gamma-aminobutyric acid type A and glycine receptor clustering relies on a common binding site. *J Biol Chem* **286**, 42105-42114, doi:10.1074/jbc.M111.303412 (2011).
25 Mukherjee, J. *et al.* The residence time of GABA(A)Rs at inhibitory synapses is determined by direct binding of the receptor alpha1 subunit to gephyrin. *J Neurosci* **31**, 14677-14687, doi:10.1523/JNEUROSCI.2001-11.2011 (2011).
26 Tretter, V. *et al.* Molecular basis of the gamma-aminobutyric acid A receptor alpha3 subunit interaction with the clustering protein gephyrin. *J Biol Chem* **286**, 37702-37711, doi:10.1074/jbc.M111.291336 (2011).
27 Brady, M. L. & Jacob, T. C. Synaptic localization of alpha5 GABA (A) receptors via gephyrin interaction regulates dendritic outgrowth and spine maturation. *Dev Neurobiol* **75**, 1241-1251, doi:10.1002/dneu.22280 (2015).
28 Kowalczyk, S. *et al.* Direct binding of GABAA receptor beta2 and beta3 subunits to gephyrin. *Eur J Neurosci* **37**, 544-554, doi:10.1111/ejn.12078 (2013).
29 Essrich, C., Lorez, M., Benson, J. A., Fritschy, J. M. & Luscher, B. Postsynaptic clustering of major GABAA receptor subtypes requires the gamma 2 subunit and gephyrin. *Nat Neurosci* **1**, 563-571, doi:10.1038/2798 (1998).
30 Kneussel, M., Hermann, A., Kirsch, J. & Betz, H. Hydrophobic interactions mediate binding of the glycine receptor beta-subunit to gephyrin. *J Neurochem* **72**, 1323-1326, doi:10.1046/j.1471-4159.1999.0721323.x (1999).
31 Pfeiffer, F., Graham, D. & Betz, H. Purification by affinity chromatography of the glycine receptor of rat spinal cord. *J Biol Chem* **257**, 9389-9393 (1982).
32 Schmitt, B., Knaus, P., Becker, C. M. & Betz, H. The Mr 93,000 polypeptide of the postsynaptic glycine receptor complex is a peripheral membrane protein. *Biochemistry* **26**, 805-811, doi:10.1021/bi00377a022 (1987).
33 Kim, E. Y. *et al.* Deciphering the structural framework of glycine receptor anchoring by gephyrin. *EMBO J* **25**, 1385-1395, doi:10.1038/sj.emboj.7601029 (2006).
34 Sander, B. *et al.* Structural characterization of gephyrin by AFM and SAXS reveals a mixture of compact and extended states. *Acta Crystallogr D Biol Crystallogr* **69**, 2050-2060, doi:10.1107/S0907444913018714 (2013).
35 Herweg, J. & Schwarz, G. Splice-specific glycine receptor binding, folding, and phosphorylation of the scaffolding protein gephyrin. *J Biol Chem* **287**, 12645-12656, doi:10.1074/jbc.M112.341826 (2012).
36 Schwarz, G., Schrader, N., Mendel, R. R., Hecht, H. J. & Schindelin, H. Crystal structures of human gephyrin and plant Cnx1 G domains: comparative analysis and functional implications. *J Mol Biol* **312**, 405-418, doi:10.1006/jmbi.2001.4952 (2001).
37 Liu, M. T., Wuebbens, M. M., Rajagopalan, K. V. & Schindelin, H. Crystal structure of the gephyrin-related molybdenum cofactor biosynthesis protein MogA from Escherichia coli. *J Biol Chem* **275**, 1814-1822, doi:10.1074/jbc.275.3.1814 (2000).

38 Sola, M., Kneussel, M., Heck, I. S., Betz, H. & Weissenhorn, W. X-ray crystal structure of the trimeric N-terminal domain of gephyrin. *J Biol Chem* **276**, 25294-25301, doi:10.1074/jbc.M101923200 (2001).
39 Kasaragod, V. B. & Schindelin, H. Structural Framework for Metal Incorporation during Molybdenum Cofactor Biosynthesis. *Structure* **24**, 782-788, doi:10.1016/j.str.2016.02.023 (2016).
40 Xiang, S., Nichols, J., Rajagopalan, K. V. & Schindelin, H. The crystal structure of Escherichia coli MoeA and its relationship to the multifunctional protein gephyrin. *Structure* **9**, 299-310, doi:10.1016/s0969-2126(01)00588-3 (2001).
41 Krausze, J. *et al.* Dimerization of the plant molybdenum insertase Cnx1E is required for synthesis of the molybdenum cofactor. *Biochem J* **474**, 163-178, doi:10.1042/BCJ20160846 (2017).
42 Kneussel, M. & Betz, H. Clustering of inhibitory neurotransmitter receptors at developing postsynaptic sites: the membrane activation model. *Trends Neurosci* **23**, 429-435, doi:10.1016/s0166-2236(00)01627-1 (2000).
43 Stallmeyer, B. *et al.* The neurotransmitter receptor-anchoring protein gephyrin reconstitutes molybdenum cofactor biosynthesis in bacteria, plants, and mammalian cells. *Proc Natl Acad Sci U S A* **96**, 1333-1338, doi:10.1073/pnas.96.4.1333 (1999).
44 Kuper, J., Winking, J., Hecht, H. J., Mendel, R. R. & Schwarz, G. The active site of the molybdenum cofactor biosynthetic protein domain Cnx1G. *Arch Biochem Biophys* **411**, 36-46, doi:10.1016/s0003-9861(02)00714-2 (2003).
45 Kuper, J., Llamas, A., Hecht, H. J., Mendel, R. R. & Schwarz, G. Structure of the molybdopterin-bound Cnx1G domain links molybdenum and copper metabolism. *Nature* **430**, 803-806, doi:10.1038/nature02681 (2004).
46 Mendel, R. R. The molybdenum cofactor. *J Biol Chem* **288**, 13165-13172, doi:10.1074/jbc.R113.455311 (2013).
47 Sabatini, D. M. *et al.* Interaction of RAFT1 with gephyrin required for rapamycin-sensitive signaling. *Science* **284**, 1161-1164, doi:10.1126/science.284.5417.1161 (1999).
48 Craig, A. M., Banker, G., Chang, W., McGrath, M. E. & Serpinskaya, A. S. Clustering of gephyrin at GABAergic but not glutamatergic synapses in cultured rat hippocampal neurons. *J Neurosci* **16**, 3166-3177 (1996).
49 Kirsch, J. & Betz, H. Widespread expression of gephyrin, a putative glycine receptor-tubulin linker protein, in rat brain. *Brain Res* **621**, 301-310, doi:10.1016/0006-8993(93)90120-c (1993).
50 Kneussel, M. *et al.* Loss of postsynaptic GABA(A) receptor clustering in gephyrin-deficient mice. *J Neurosci* **19**, 9289-9297 (1999).
51 Meyer, G., Kirsch, J., Betz, H. & Langosch, D. Identification of a gephyrin binding motif on the glycine receptor beta subunit. *Neuron* **15**, 563-572, doi:10.1016/0896-6273(95)90145-0 (1995).
52 Prior, P. *et al.* Primary structure and alternative splice variants of gephyrin, a putative glycine receptor-tubulin linker protein. *Neuron* **8**, 1161-1170, doi:10.1016/0896-6273(92)90136-2 (1992).
53 Ramming, M. *et al.* Diversity and phylogeny of gephyrin: tissue-specific splice variants, gene structure, and sequence similarities to molybdenum cofactor-synthesizing and cytoskeleton-associated proteins. *Proc Natl Acad Sci U S A* **97**, 10266-10271, doi:10.1073/pnas.97.18.10266 (2000).
54 Fritschy, J. M., Harvey, R. J. & Schwarz, G. Gephyrin: where do we stand, where do we go? *Trends Neurosci* **31**, 257-264, doi:10.1016/j.tins.2008.02.006 (2008).

55 Paarmann, I., Schmitt, B., Meyer, B., Karas, M. & Betz, H. Mass spectrometric analysis of glycine receptor-associated gephyrin splice variants. *J Biol Chem* **281**, 34918-34925, doi:10.1074/jbc.M607764200 (2006).
56 Saiyed, T. *et al.* Molecular basis of gephyrin clustering at inhibitory synapses: role of G- and E-domain interactions. *J Biol Chem* **282**, 5625-5632, doi:10.1074/jbc.M610290200 (2007).
57 Smolinsky, B., Eichler, S. A., Buchmeier, S., Meier, J. C. & Schwarz, G. Splice-specific functions of gephyrin in molybdenum cofactor biosynthesis. *J Biol Chem* **283**, 17370-17379, doi:10.1074/jbc.M800985200 (2008).
58 Nawrotzki, R., Islinger, M., Vogel, I., Volkl, A. & Kirsch, J. Expression and subcellular distribution of gephyrin in non-neuronal tissues and cells. *Histochem Cell Biol* **137**, 471-482, doi:10.1007/s00418-012-0914-7 (2012).
59 Bedet, C. *et al.* Regulation of gephyrin assembly and glycine receptor synaptic stability. *J Biol Chem* **281**, 30046-30056, doi:10.1074/jbc.M602155200 (2006).
60 Ule, J. *et al.* CLIP identifies Nova-regulated RNA networks in the brain. *Science* **302**, 1212-1215, doi:10.1126/science.1090095 (2003).
61 Tyagarajan, S. K. *et al.* Extracellular signal-regulated kinase and glycogen synthase kinase 3beta regulate gephyrin postsynaptic aggregation and GABAergic synaptic function in a calpain-dependent mechanism. *J Biol Chem* **288**, 9634-9647, doi:10.1074/jbc.M112.442616 (2013).
62 Tyagarajan, S. K. *et al.* Regulation of GABAergic synapse formation and plasticity by GSK3beta-dependent phosphorylation of gephyrin. *Proc Natl Acad Sci U S A* **108**, 379-384, doi:10.1073/pnas.1011824108 (2011).
63 Kuhse, J. *et al.* Phosphorylation of gephyrin in hippocampal neurons by cyclin-dependent kinase CDK5 at Ser-270 is dependent on collybistin. *J Biol Chem* **287**, 30952-30966, doi:10.1074/jbc.M112.349597 (2012).
64 Ghosh, H. *et al.* Several posttranslational modifications act in concert to regulate gephyrin scaffolding and GABAergic transmission. *Nat Commun* **7**, 13365, doi:10.1038/ncomms13365 (2016).
65 Specht, C. G. *et al.* Regulation of glycine receptor diffusion properties and gephyrin interactions by protein kinase C. *EMBO J* **30**, 3842-3853, doi:10.1038/emboj.2011.276 (2011).
66 Bausen, M., Weltzien, F., Betz, H. & O'Sullivan, G. A. Regulation of postsynaptic gephyrin cluster size by protein phosphatase 1. *Mol Cell Neurosci* **44**, 201-209, doi:10.1016/j.mcn.2010.02.007 (2010).
67 Kang, R. *et al.* Neural palmitoyl-proteomics reveals dynamic synaptic palmitoylation. *Nature* **456**, 904-909, doi:10.1038/nature07605 (2008).
68 Dejanovic, B. *et al.* Palmitoylation of gephyrin controls receptor clustering and plasticity of GABAergic synapses. *PLoS Biol* **12**, e1001908, doi:10.1371/journal.pbio.1001908 (2014).
69 Schwarz, G., Mendel, R. R. & Ribbe, M. W. Molybdenum cofactors, enzymes and pathways. *Nature* **460**, 839-847, doi:10.1038/nature08302 (2009).
70 Mendel, R. R. & Leimkuhler, S. The biosynthesis of the molybdenum cofactors. *J Biol Inorg Chem* **20**, 337-347, doi:10.1007/s00775-014-1173-y (2015).
71 Llamas, A., Mendel, R. R. & Schwarz, G. Synthesis of adenylated molybdopterin: an essential step for molybdenum insertion. *J Biol Chem* **279**, 55241-55246, doi:10.1074/jbc.M409862200 (2004).
72 Llamas, A., Otte, T., Multhaup, G., Mendel, R. R. & Schwarz, G. The Mechanism of nucleotide-assisted molybdenum insertion into molybdopterin. A novel route toward metal cofactor assembly. *J Biol Chem* **281**, 18343-18350, doi:10.1074/jbc.M601415200 (2006).

73 Belaidi, A. A. & Schwarz, G. Metal insertion into the molybdenum cofactor: product-substrate channelling demonstrates the functional origin of domain fusion in gephyrin. *Biochem J* **450**, 149-157, doi:10.1042/BJ20121078 (2013).

74 Reiss, J. & Hahnewald, R. Molybdenum cofactor deficiency: Mutations in GPHN, MOCS1, and MOCS2. *Hum Mutat* **32**, 10-18, doi:10.1002/humu.21390 (2011).

75 Bayram, E. *et al.* Molybdenum cofactor deficiency: review of 12 cases (MoCD and review). *Eur J Paediatr Neurol* **17**, 1-6, doi:10.1016/j.ejpn.2012.10.003 (2013).

76 Langosch, D., Hoch, W. & Betz, H. The 93 kDa protein gephyrin and tubulin associated with the inhibitory glycine receptor are phosphorylated by an endogenous protein kinase. *FEBS Lett* **298**, 113-117, doi:10.1016/0014-5793(92)80034-e (1992).

77 Gonzalez-Forero, D. & Alvarez, F. J. Differential postnatal maturation of GABAA, glycine receptor, and mixed synaptic currents in Renshaw cells and ventral spinal interneurons. *J Neurosci* **25**, 2010-2023, doi:10.1523/JNEUROSCI.2383-04.2005 (2005).

78 Zita, M. M. *et al.* Post-phosphorylation prolyl isomerisation of gephyrin represents a mechanism to modulate glycine receptors function. *EMBO J* **26**, 1761-1771, doi:10.1038/sj.emboj.7601625 (2007).

79 Hanus, C., Vannier, C. & Triller, A. Intracellular association of glycine receptor with gephyrin increases its plasma membrane accumulation rate. *J Neurosci* **24**, 1119-1128, doi:10.1523/JNEUROSCI.4380-03.2004 (2004).

80 Fuhrmann, J. C. *et al.* Gephyrin interacts with Dynein light chains 1 and 2, components of motor protein complexes. *J Neurosci* **22**, 5393-5402, doi:20026552 (2002).

81 Maas, C. *et al.* Neuronal cotransport of glycine receptor and the scaffold protein gephyrin. *J Cell Biol* **172**, 441-451, doi:10.1083/jcb.200506066 (2006).

82 Ehrensperger, M. V., Hanus, C., Vannier, C., Triller, A. & Dahan, M. Multiple association states between glycine receptors and gephyrin identified by SPT analysis. *Biophys J* **92**, 3706-3718, doi:10.1529/biophysj.106.095596 (2007).

83 Dahan, M. *et al.* Diffusion dynamics of glycine receptors revealed by single-quantum dot tracking. *Science* **302**, 442-445, doi:10.1126/science.1088525 (2003).

84 Charrier, C., Ehrensperger, M. V., Dahan, M., Levi, S. & Triller, A. Cytoskeleton regulation of glycine receptor number at synapses and diffusion in the plasma membrane. *J Neurosci* **26**, 8502-8511, doi:10.1523/JNEUROSCI.1758-06.2006 (2006).

85 Hanus, C., Ehrensperger, M. V. & Triller, A. Activity-dependent movements of postsynaptic scaffolds at inhibitory synapses. *J Neurosci* **26**, 4586-4595, doi:10.1523/JNEUROSCI.5123-05.2006 (2006).

86 Kralic, J. E. *et al.* Compensatory alteration of inhibitory synaptic circuits in cerebellum and thalamus of gamma-aminobutyric acid type A receptor alpha1 subunit knockout mice. *J Comp Neurol* **495**, 408-421, doi:10.1002/cne.20866 (2006).

87 Serwanski, D. R. *et al.* Synaptic and nonsynaptic localization of GABAA receptors containing the alpha5 subunit in the rat brain. *J Comp Neurol* **499**, 458-470, doi:10.1002/cne.21115 (2006).

88 Loebrich, S., Bahring, R., Katsuno, T., Tsukita, S. & Kneussel, M. Activated radixin is essential for GABAA receptor alpha5 subunit anchoring at the actin cytoskeleton. *EMBO J* **25**, 987-999, doi:10.1038/sj.emboj.7600995 (2006).

89 Burkarth, N., Kriebel, M., Kranz, E. U. & Volkmer, H. Neurofascin regulates the formation of gephyrin clusters and their subsequent translocation to the axon hillock of hippocampal neurons. *Mol Cell Neurosci* **36**, 59-70, doi:10.1016/j.mcn.2007.06.001 (2007).

90 Li, R. W. *et al.* Disruption of postsynaptic GABA receptor clusters leads to decreased GABAergic innervation of pyramidal neurons. *J Neurochem* **95**, 756-770, doi:10.1111/j.1471-4159.2005.03426.x (2005).

91 Alldred, M. J., Mulder-Rosi, J., Lingenfelter, S. E., Chen, G. & Luscher, B. Distinct gamma2 subunit domains mediate clustering and synaptic function of postsynaptic GABAA receptors and gephyrin. *J Neurosci* **25**, 594-603, doi:10.1523/JNEUROSCI.4011-04.2005 (2005).
92 Studer, R. *et al.* Alteration of GABAergic synapses and gephyrin clusters in the thalamic reticular nucleus of GABAA receptor alpha3 subunit-null mice. *Eur J Neurosci* **24**, 1307-1315, doi:10.1111/j.1460-9568.2006.05006.x (2006).
93 Tretter, V. *et al.* The clustering of GABA(A) receptor subtypes at inhibitory synapses is facilitated via the direct binding of receptor alpha 2 subunits to gephyrin. *J Neurosci* **28**, 1356-1365, doi:10.1523/JNEUROSCI.5050-07.2008 (2008).
94 Fang, C. *et al.* GODZ-mediated palmitoylation of GABA(A) receptors is required for normal assembly and function of GABAergic inhibitory synapses. *J Neurosci* **26**, 12758-12768, doi:10.1523/JNEUROSCI.4214-06.2006 (2006).
95 Keller, C. A. *et al.* The gamma2 subunit of GABA(A) receptors is a substrate for palmitoylation by GODZ. *J Neurosci* **24**, 5881-5891, doi:10.1523/JNEUROSCI.1037-04.2004 (2004).
96 Rathenberg, J., Kittler, J. T. & Moss, S. J. Palmitoylation regulates the clustering and cell surface stability of GABAA receptors. *Mol Cell Neurosci* **26**, 251-257, doi:10.1016/j.mcn.2004.01.012 (2004).
97 Jacob, T. C. *et al.* Gephyrin regulates the cell surface dynamics of synaptic GABAA receptors. *J Neurosci* **25**, 10469-10478, doi:10.1523/JNEUROSCI.2267-05.2005 (2005).
98 Schrader, N. *et al.* Biochemical characterization of the high affinity binding between the glycine receptor and gephyrin. *J Biol Chem* **279**, 18733-18741, doi:10.1074/jbc.M311245200 (2004).
99 Dejanovic, B. *et al.* Simultaneous impairment of neuronal and metabolic function of mutated gephyrin in a patient with epileptic encephalopathy. *EMBO Mol Med* **7**, 1580-1594, doi:10.15252/emmm.201505323 (2015).
100 Grunewald, N. *et al.* Sequences Flanking the Gephyrin-Binding Site of GlyRbeta Tune Receptor Stabilization at Synapses. *eNeuro* **5**, doi:10.1523/ENEURO.0042-17.2018 (2018).
101 Maric, H. M. *et al.* Molecular basis of the alternative recruitment of GABA(A) versus glycine receptors through gephyrin. *Nat Commun* **5**, 5767, doi:10.1038/ncomms6767 (2014).
102 Maric, H. M. *et al.* Design and synthesis of high-affinity dimeric inhibitors targeting the interactions between gephyrin and inhibitory neurotransmitter receptors. *Angew Chem Int Ed Engl* **54**, 490-494, doi:10.1002/anie.201409043 (2015).
103 Craig, A. M. & Kang, Y. Neurexin-neuroligin signaling in synapse development. *Curr Opin Neurobiol* **17**, 43-52, doi:10.1016/j.conb.2007.01.011 (2007).
104 Babaev, O. *et al.* Neuroligin 2 deletion alters inhibitory synapse function and anxiety-associated neuronal activation in the amygdala. *Neuropharmacology* **100**, 56-65, doi:10.1016/j.neuropharm.2015.06.016 (2016).
105 Varoqueaux, F., Jamain, S. & Brose, N. Neuroligin 2 is exclusively localized to inhibitory synapses. *Eur J Cell Biol* **83**, 449-456, doi:10.1078/0171-9335-00410 (2004).
106 Kang, Y., Zhang, X., Dobie, F., Wu, H. & Craig, A. M. Induction of GABAergic postsynaptic differentiation by alpha-neurexins. *J Biol Chem* **283**, 2323-2334, doi:10.1074/jbc.M703957200 (2008).
107 Feng, G. *et al.* Dual requirement for gephyrin in glycine receptor clustering and molybdoenzyme activity. *Science* **282**, 1321-1324, doi:10.1126/science.282.5392.1321 (1998).
108 Grosskreutz, Y., Betz, H. & Kneussel, M. Rescue of molybdenum cofactor biosynthesis in gephyrin-deficient mice by a Cnx1 transgene. *Biochem Biophys Res Commun* **301**, 450-455, doi:10.1016/s0006-291x(02)03062-0 (2003).

109 WHO. *Dementia*, <https://www.who.int/news-room/fact-sheets/detail/dementia> (2019).
110 Agarwal, S., Tannenberg, R. K. & Dodd, P. R. Reduced expression of the inhibitory synapse scaffolding protein gephyrin in Alzheimer's disease. *J Alzheimers Dis* **14**, 313-321, doi:10.3233/jad-2008-14305 (2008).
111 Hales, C. M. *et al.* Abnormal gephyrin immunoreactivity associated with Alzheimer disease pathologic changes. *J Neuropathol Exp Neurol* **72**, 1009-1015, doi:10.1097/01.jnen.0000435847.59828.db (2013).
112 Mitew, S., Kirkcaldie, M. T., Dickson, T. C. & Vickers, J. C. Altered synapses and gliotransmission in Alzheimer's disease and AD model mice. *Neurobiol Aging* **34**, 2341-2351, doi:10.1016/j.neurobiolaging.2013.04.010 (2013).
113 Zhang, Y., Bode, A., Nguyen, B., Keramidas, A. & Lynch, J. W. Investigating the Mechanism by Which Gain-of-function Mutations to the alpha1 Glycine Receptor Cause Hyperekplexia. *J Biol Chem* **291**, 15332-15341, doi:10.1074/jbc.M116.728592 (2016).
114 Harvey, K. *et al.* The GDP-GTP exchange factor collybistin: an essential determinant of neuronal gephyrin clustering. *J Neurosci* **24**, 5816-5826, doi:10.1523/JNEUROSCI.1184-04.2004 (2004).
115 Rees, M. I. *et al.* Isoform heterogeneity of the human gephyrin gene (GPHN), binding domains to the glycine receptor, and mutation analysis in hyperekplexia. *J Biol Chem* **278**, 24688-24696, doi:10.1074/jbc.M301070200 (2003).
116 Lionel, A. C. *et al.* Rare exonic deletions implicate the synaptic organizer Gephyrin (GPHN) in risk for autism, schizophrenia and seizures. *Hum Mol Genet* **22**, 2055-2066, doi:10.1093/hmg/ddt056 (2013).
117 Ellis, S. E., Panitch, R., West, A. B. & Arking, D. E. Transcriptome analysis of cortical tissue reveals shared sets of downregulated genes in autism and schizophrenia. *Transl Psychiatry* **6**, e817, doi:10.1038/tp.2016.87 (2016).
118 Um, J. W. *et al.* IQ Motif and SEC7 Domain-containing Protein 3 (IQSEC3) Interacts with Gephyrin to Promote Inhibitory Synapse Formation. *J Biol Chem* **291**, 10119-10130, doi:10.1074/jbc.M115.712893 (2016).
119 Fang, M. *et al.* Downregulation of gephyrin in temporal lobe epilepsy neurons in humans and a rat model. *Synapse* **65**, 1006-1014, doi:10.1002/syn.20928 (2011).
120 Peret, A. *et al.* Contribution of aberrant GluK2-containing kainate receptors to chronic seizures in temporal lobe epilepsy. *Cell Rep* **8**, 347-354, doi:10.1016/j.celrep.2014.06.032 (2014).
121 Soukupova, M. *et al.* Impairment of GABA release in the hippocampus at the time of the first spontaneous seizure in the pilocarpine model of temporal lobe epilepsy. *Exp Neurol* **257**, 39-49, doi:10.1016/j.expneurol.2014.04.014 (2014).
122 Solimena, M. *et al.* Autoantibodies to glutamic acid decarboxylase in a patient with stiff-man syndrome, epilepsy, and type I diabetes mellitus. *N Engl J Med* **318**, 1012-1020, doi:10.1056/NEJM198804213181602 (1988).
123 Butler, M. H. *et al.* Autoimmunity to gephyrin in Stiff-Man syndrome. *Neuron* **26**, 307-312 (2000).
124 Raju, R. *et al.* Autoimmunity to GABAA-receptor-associated protein in stiff-person syndrome. *Brain* **129**, 3270-3276, doi:10.1093/brain/awl245 (2006).
125 Kurt, M. A., Kafa, M. I., Dierssen, M. & Davies, D. C. Deficits of neuronal density in CA1 and synaptic density in the dentate gyrus, CA3 and CA1, in a mouse model of Down syndrome. *Brain Res* **1022**, 101-109, doi:10.1016/j.brainres.2004.06.075 (2004).
126 Hanson, J. E., Blank, M., Valenzuela, R. A., Garner, C. C. & Madison, D. V. The functional nature of synaptic circuitry is altered in area CA3 of the hippocampus in a mouse model of Down's syndrome. *J Physiol* **579**, 53-67, doi:10.1113/jphysiol.2006.114868 (2007).

127 Choii, G. & Ko, J. Gephyrin: a central GABAergic synapse organizer. *Exp Mol Med* **47**, e158, doi:10.1038/emm.2015.5 (2015).
128 Giesemann, T. *et al.* Complex formation between the postsynaptic scaffolding protein gephyrin, profilin, and Mena: a possible link to the microfilament system. *J Neurosci* **23**, 8330-8339 (2003).
129 Bausen, M., Fuhrmann, J. C., Betz, H. & O'Sullivan G, A. The state of the actin cytoskeleton determines its association with gephyrin: role of ena/VASP family members. *Mol Cell Neurosci* **31**, 376-386, doi:10.1016/j.mcn.2005.11.004 (2006).
130 Kirsch, J. *et al.* The 93-kDa glycine receptor-associated protein binds to tubulin. *J Biol Chem* **266**, 22242-22245 (1991).
131 Mammoto, A. *et al.* Interactions of drebrin and gephyrin with profilin. *Biochem Biophys Res Commun* **243**, 86-89, doi:10.1006/bbrc.1997.8068 (1998).
132 Poulopoulos, A. *et al.* Neuroligin 2 drives postsynaptic assembly at perisomatic inhibitory synapses through gephyrin and collybistin. *Neuron* **63**, 628-642, doi:10.1016/j.neuron.2009.08.023 (2009).
133 Fruh, S., Tyagarajan, S. K., Campbell, B., Bosshard, G. & Fritschy, J. M. The catalytic function of the gephyrin-binding protein IQSEC3 regulates neurotransmitter-specific matching of pre- and post-synaptic structures in primary hippocampal cultures. *J Neurochem* **147**, 477-494, doi:10.1111/jnc.14572 (2018).
134 Navarro-Lerida, I. *et al.* Proteomic identification of brain proteins that interact with dynein light chain LC8. *Proteomics* **4**, 339-346, doi:10.1002/pmic.200300528 (2004).
135 Lee, E. Y. *Structural and Biochemical Characterization of Interaction between Gephyrin and Dynein Light Chains*, Stony Brook University, (2009).
136 Wang, H., Bedford, F. K., Brandon, N. J., Moss, S. J. & Olsen, R. W. GABA(A)-receptor-associated protein links GABA(A) receptors and the cytoskeleton. *Nature* **397**, 69-72, doi:10.1038/16264 (1999).
137 Kneussel, M. *et al.* The gamma-aminobutyric acid type A receptor (GABAAR)-associated protein GABARAP interacts with gephyrin but is not involved in receptor anchoring at the synapse. *Proc Natl Acad Sci U S A* **97**, 8594-8599, doi:10.1073/pnas.97.15.8594 (2000).
138 Kins, S., Betz, H. & Kirsch, J. Collybistin, a newly identified brain-specific GEF, induces submembrane clustering of gephyrin. *Nat Neurosci* **3**, 22-29, doi:10.1038/71096 (2000).
139 Grosskreutz, Y. *et al.* Identification of a gephyrin-binding motif in the GDP/GTP exchange factor collybistin. *Biol Chem* **382**, 1455-1462, doi:10.1515/BC.2001.179 (2001).
140 Antonelli, R. *et al.* Pin1-dependent signalling negatively affects GABAergic transmission by modulating neuroligin2/gephyrin interaction. *Nat Commun* **5**, 5066, doi:10.1038/ncomms6066 (2014).
141 Uezu, A. *et al.* Identification of an elaborate complex mediating postsynaptic inhibition. *Science* **353**, 1123-1129, doi:10.1126/science.aag0821 (2016).
142 Guo, Z. Artemisinin anti-malarial drugs in China. *Acta Pharm Sin B* **6**, 115-124, doi:10.1016/j.apsb.2016.01.008 (2016).
143 Tu, Y. Artemisinin-A Gift from Traditional Chinese Medicine to the World (Nobel Lecture). *Angew Chem Int Ed Engl* **55**, 10210-10226, doi:10.1002/anie.201601967 (2016).
144 WHO. *Overview of malaria treatment*, <https://www.who.int/malaria/areas/treatment/overview/en/> (2018).
145 Li, J. *et al.* Artemisinins Target GABAA Receptor Signaling and Impair alpha Cell Identity. *Cell* **168**, 86-100 e115, doi:10.1016/j.cell.2016.11.010 (2017).
146 Ackermann, A. M., Moss, N. G. & Kaestner, K. H. GABA and Artesunate Do Not Induce Pancreatic alpha-to-beta Cell Transdifferentiation In Vivo. *Cell Metab* **28**, 787-792 e783, doi:10.1016/j.cmet.2018.07.002 (2018).

147 van der Meulen, T. *et al.* Artemether Does Not Turn alpha Cells into beta Cells. *Cell Metab* **27**, 218-225 e214, doi:10.1016/j.cmet.2017.10.002 (2018).
148 Kasaragod, V. B. *et al.* Elucidating the Molecular Basis for Inhibitory Neurotransmission Regulation by Artemisinins. *Neuron* **101**, 673-689 e611, doi:10.1016/j.neuron.2019.01.001 (2019).
149 Brewer, T. G. *et al.* Neurotoxicity in animals due to arteether and artemether. *Trans R Soc Trop Med Hyg* **88 Suppl 1**, S33-36, doi:10.1016/0035-9203(94)90469-3 (1994).
150 Wesche, D. L., DeCoster, M. A., Tortella, F. C. & Brewer, T. G. Neurotoxicity of artemisinin analogs in vitro. *Antimicrob Agents Chemother* **38**, 1813-1819, doi:10.1128/aac.38.8.1813 (1994).
151 Crespo-Ortiz, M. P. & Wei, M. Q. Antitumor activity of artemisinin and its derivatives: from a well-known antimalarial agent to a potential anticancer drug. *J Biomed Biotechnol* **2012**, 247597, doi:10.1155/2012/247597 (2012).
152 Liu, X., Cao, J., Huang, G., Zhao, Q. & Shen, J. Biological Activities of Artemisinin Derivatives Beyond Malaria. *Curr Top Med Chem* **19**, 205-222, doi:10.2174/1568026619666190122144217 (2019).
153 Zyad, A., Tilaoui, M., Jaafari, A., Oukerrou, M. A. & Mouse, H. A. More insights into the pharmacological effects of artemisinin. *Phytother Res* **32**, 216-229, doi:10.1002/ptr.5958 (2018).
154 Davis, T. M. *et al.* Penetration of dihydroartemisinin into cerebrospinal fluid after administration of intravenous artesunate in severe falciparum malaria. *Antimicrob Agents Chemother* **47**, 368-370, doi:10.1128/aac.47.1.368-370.2003 (2003).
155 Nontprasert, A. *et al.* Assessment of the neurotoxicity of oral dihydroartemisinin in mice. *Trans R Soc Trop Med Hyg* **96**, 99-101, doi:10.1016/s0035-9203(02)90256-7 (2002).
156 Miller, L. G. & Panosian, C. B. Ataxia and slurred speech after artesunate treatment for falciparum malaria. *N Engl J Med* **336**, 1328, doi:10.1056/NEJM199705013361818 (1997).
157 Elias, Z., Bonnet, E., Marchou, B. & Massip, P. Neurotoxicity of artemisinin: possible counseling and treatment of side effects. *Clin Infect Dis* **28**, 1330-1331, doi:10.1086/517789 (1999).
158 Jigang Wang, C. X., Yin Kwan Wong, Yujie Li, Fulong Liao,Tingliang Jiang, Youyou Tu. Artemisinin, the Magic Drug Discovered from Traditional Chinese Medicine. *Engineering* **5**, 32-39, doi:https://doi.org/10.1016/j.eng.2018.11.011 (2019).
159 O'Neill, P. M., Barton, V. E. & Ward, S. A. The molecular mechanism of action of artemisinin--the debate continues. *Molecules* **15**, 1705-1721, doi:10.3390/molecules15031705 (2010).
160 di Salvo, M. L., Safo, M. K. & Contestabile, R. Biomedical aspects of pyridoxal 5'-phosphate availability. *Front Biosci (Elite Ed)* **4**, 897-913 (2012).
161 Eliot, A. C. & Kirsch, J. F. Pyridoxal phosphate enzymes: mechanistic, structural, and evolutionary considerations. *Annu Rev Biochem* **73**, 383-415, doi:10.1146/annurev.biochem.73.011303.074021 (2004).
162 Percudani, R. & Peracchi, A. A genomic overview of pyridoxal-phosphate-dependent enzymes. *EMBO Rep* **4**, 850-854, doi:10.1038/sj.embor.embor914 (2003).
163 Kasaragod, V. B. *et al.* Pyridoxal Kinase Inhibition by Artemisinins Downregulates Inhibitory Neurotransmission. *bioRxiv*, 2020.2004.2005.026310, doi:10.1101/2020.04.05.026310 (2020).
164 Kirsch, J. & Betz, H. The postsynaptic localization of the glycine receptor-associated protein gephyrin is regulated by the cytoskeleton. *J Neurosci* **15**, 4148-4156 (1995).
165 Kirsch, J., Kuhse, J. & Betz, H. Targeting of glycine receptor subunits to gephyrin-rich domains in transfected human embryonic kidney cells. *Mol Cell Neurosci* **6**, 450-461, doi:10.1006/mcne.1995.1033 (1995).

166 Allison, D. W., Chervin, A. S., Gelfand, V. I. & Craig, A. M. Postsynaptic scaffolds of excitatory and inhibitory synapses in hippocampal neurons: maintenance of core components independent of actin filaments and microtubules. *J Neurosci* **20**, 4545-4554 (2000).
167 van Zundert, B. *et al.* Developmental-dependent action of microtubule depolymerization on the function and structure of synaptic glycine receptor clusters in spinal neurons. *J Neurophysiol* **91**, 1036-1049, doi:10.1152/jn.00364.2003 (2004).
168 Niebuhr, K. *et al.* A novel proline-rich motif present in ActA of Listeria monocytogenes and cytoskeletal proteins is the ligand for the EVH1 domain, a protein module present in the Ena/VASP family. *EMBO J* **16**, 5433-5444, doi:10.1093/emboj/16.17.5433 (1997).
169 Bear, J. E. *et al.* Negative regulation of fibroblast motility by Ena/VASP proteins. *Cell* **101**, 717-728, doi:10.1016/s0092-8674(00)80884-3 (2000).
170 Beneken, J. *et al.* Structure of the Homer EVH1 domain-peptide complex reveals a new twist in polyproline recognition. *Neuron* **26**, 143-154, doi:10.1016/s0896-6273(00)81145-9 (2000).
171 Fedorov, A. A., Fedorov, E., Gertler, F. & Almo, S. C. Structure of EVH1, a novel proline-rich ligand-binding module involved in cytoskeletal dynamics and neural function. *Nat Struct Biol* **6**, 661-665, doi:10.1038/10717 (1999).
172 Small, J. V. Facing up to Mena: Tes(ting) times for EVH1 domains. *Nat Cell Biol* **10**, 118-120, doi:10.1038/ncb0208-118 (2008).
173 Boeda, B. *et al.* Tes, a specific Mena interacting partner, breaks the rules for EVH1 binding. *Mol Cell* **28**, 1071-1082, doi:10.1016/j.molcel.2007.10.033 (2007).
174 Gertler, F. B., Niebuhr, K., Reinhard, M., Wehland, J. & Soriano, P. Mena, a relative of VASP and Drosophila Enabled, is implicated in the control of microfilament dynamics. *Cell* **87**, 227-239, doi:10.1016/s0092-8674(00)81341-0 (1996).
175 Wanner, S. J., Danos, M. C., Lohr, J. L. & Miller, J. R. Molecular cloning and expression of Ena/Vasp-like (Evl) during Xenopus development. *Gene Expr Patterns* **5**, 423-428, doi:10.1016/j.modgep.2004.09.004 (2005).
176 Xanthos, J. B., Wanner, S. J. & Miller, J. R. Cloning and developmental expression of Xenopus Enabled (Xena). *Dev Dyn* **233**, 631-637, doi:10.1002/dvdy.20358 (2005).
177 Gertler, F. B. *et al.* enabled, a dosage-sensitive suppressor of mutations in the Drosophila Abl tyrosine kinase, encodes an Abl substrate with SH3 domain-binding properties. *Genes Dev* **9**, 521-533, doi:10.1101/gad.9.5.521 (1995).
178 Haffner, C. *et al.* Molecular cloning, structural analysis and functional expression of the proline-rich focal adhesion and microfilament-associated protein VASP. *EMBO J* **14**, 19-27 (1995).
179 Han, Y. H. *et al.* Requirement of a vasodilator-stimulated phosphoprotein family member for cell adhesion, the formation of filopodia, and chemotaxis in dictyostelium. *J Biol Chem* **277**, 49877-49887, doi:10.1074/jbc.M209107200 (2002).
180 Ball, L. J., Jarchau, T., Oschkinat, H. & Walter, U. EVH1 domains: structure, function and interactions. *FEBS Lett* **513**, 45-52, doi:10.1016/s0014-5793(01)03291-4 (2002).
181 Brindle, N. P., Holt, M. R., Davies, J. E., Price, C. J. & Critchley, D. R. The focal-adhesion vasodilator-stimulated phosphoprotein (VASP) binds to the proline-rich domain in vinculin. *Biochem J* **318 (Pt 3)**, 753-757, doi:10.1042/bj3180753 (1996).
182 Reinhard, M., Rudiger, M., Jockusch, B. M. & Walter, U. VASP interaction with vinculin: a recurring theme of interactions with proline-rich motifs. *FEBS Lett* **399**, 103-107, doi:10.1016/s0014-5793(96)01295-1 (1996).
183 Krause, M. *et al.* Lamellipodin, an Ena/VASP ligand, is implicated in the regulation of lamellipodial dynamics. *Dev Cell* **7**, 571-583, doi:10.1016/j.devcel.2004.07.024 (2004).
184 Reinhard, M., Jouvenal, K., Tripier, D. & Walter, U. Identification, purification, and characterization of a zyxin-related protein that binds the focal adhesion and microfilament

protein VASP (vasodilator-stimulated phosphoprotein). *Proc Natl Acad Sci U S A* **92**, 7956-7960, doi:10.1073/pnas.92.17.7956 (1995).
185 Zhang, Y., Tu, Y., Gkretsi, V. & Wu, C. Migfilin interacts with vasodilator-stimulated phosphoprotein (VASP) and regulates VASP localization to cell-matrix adhesions and migration. *J Biol Chem* **281**, 12397-12407, doi:10.1074/jbc.M512107200 (2006).
186 Boukhelifa, M., Parast, M. M., Bear, J. E., Gertler, F. B. & Otey, C. A. Palladin is a novel binding partner for Ena/VASP family members. *Cell Motil Cytoskeleton* **58**, 17-29, doi:10.1002/cm.10173 (2004).
187 Ahern-Djamali, S. M. *et al.* Identification of profilin and src homology 3 domains as binding partners for Drosophila enabled. *Proc Natl Acad Sci U S A* **96**, 4977-4982, doi:10.1073/pnas.96.9.4977 (1999).
188 Comer, A. R., Ahern-Djamali, S. M., Juang, J. L., Jackson, P. D. & Hoffmann, F. M. Phosphorylation of Enabled by the Drosophila Abelson tyrosine kinase regulates the in vivo function and protein-protein interactions of Enabled. *Mol Cell Biol* **18**, 152-160, doi:10.1128/mcb.18.1.152 (1998).
189 Lambrechts, A. *et al.* cAMP-dependent protein kinase phosphorylation of EVL, a Mena/VASP relative, regulates its interaction with actin and SH3 domains. *J Biol Chem* **275**, 36143-36151, doi:10.1074/jbc.M006274200 (2000).
190 Krugmann, S. *et al.* Cdc42 induces filopodia by promoting the formation of an IRSp53:Mena complex. *Curr Biol* **11**, 1645-1655, doi:10.1016/s0960-9822(01)00506-1 (2001).
191 Ermekova, K. S. *et al.* The WW domain of neural protein FE65 interacts with proline-rich motifs in Mena, the mammalian homolog of Drosophila enabled. *J Biol Chem* **272**, 32869-32877, doi:10.1074/jbc.272.52.32869 (1997).
192 Ferron, F., Rebowski, G., Lee, S. H. & Dominguez, R. Structural basis for the recruitment of profilin-actin complexes during filament elongation by Ena/VASP. *EMBO J* **26**, 4597-4606, doi:10.1038/sj.emboj.7601874 (2007).
193 Kursula, P. *et al.* High-resolution structural analysis of mammalian profilin 2a complex formation with two physiological ligands: the formin homology 1 domain of mDia1 and the proline-rich domain of VASP. *J Mol Biol* **375**, 270-290, doi:10.1016/j.jmb.2007.10.050 (2008).
194 Jonckheere, V., Lambrechts, A., Vandekerckhove, J. & Ampe, C. Dimerization of profilin II upon binding the (GP5)3 peptide from VASP overcomes the inhibition of actin nucleation by profilin II and thymosin beta4. *FEBS Lett* **447**, 257-263, doi:10.1016/s0014-5793(99)00293-8 (1999).
195 Zimmermann, J. *et al.* Relaxation, equilibrium oligomerization, and molecular symmetry of the VASP (336-380) EVH2 tetramer. *Biochemistry* **41**, 11143-11151, doi:10.1021/bi020379x (2002).
196 Barzik, M. *et al.* Ena/VASP proteins enhance actin polymerization in the presence of barbed end capping proteins. *J Biol Chem* **280**, 28653-28662, doi:10.1074/jbc.M503957200 (2005).
197 Bachmann, C., Fischer, L., Walter, U. & Reinhard, M. The EVH2 domain of the vasodilator-stimulated phosphoprotein mediates tetramerization, F-actin binding, and actin bundle formation. *J Biol Chem* **274**, 23549-23557, doi:10.1074/jbc.274.33.23549 (1999).
198 Prehoda, K. E., Lee, D. J. & Lim, W. A. Structure of the enabled/VASP homology 1 domain-peptide complex: a key component in the spatial control of actin assembly. *Cell* **97**, 471-480, doi:10.1016/s0092-8674(00)80757-6 (1999).
199 Kuhnel, K. *et al.* The VASP tetramerization domain is a right-handed coiled coil based on a 15-residue repeat. *Proc Natl Acad Sci U S A* **101**, 17027-17032, doi:10.1073/pnas.0403069101 (2004).

200 Eigenthaler, M., Nolte, C., Halbrugge, M. & Walter, U. Concentration and regulation of cyclic nucleotides, cyclic-nucleotide-dependent protein kinases and one of their major substrates in human platelets. Estimating the rate of cAMP-regulated and cGMP-regulated protein phosphorylation in intact cells. *Eur J Biochem* **205**, 471-481, doi:10.1111/j.1432-1033.1992.tb16803.x (1992).
201 Bear, J. E. *et al.* Antagonism between Ena/VASP proteins and actin filament capping regulates fibroblast motility. *Cell* **109**, 509-521, doi:10.1016/s0092-8674(02)00731-6 (2002).
202 Applewhite, D. A. *et al.* Ena/VASP proteins have an anti-capping independent function in filopodia formation. *Mol Biol Cell* **18**, 2579-2591, doi:10.1091/mbc.e06-11-0990 (2007).
203 Dent, E. W. *et al.* Filopodia are required for cortical neurite initiation. *Nat Cell Biol* **9**, 1347-1359, doi:10.1038/ncb1654 (2007).
204 Furman, C. *et al.* Ena/VASP is required for endothelial barrier function in vivo. *J Cell Biol* **179**, 761-775, doi:10.1083/jcb.200705002 (2007).
205 Geese, M. *et al.* Contribution of Ena/VASP proteins to intracellular motility of listeria requires phosphorylation and proline-rich core but not F-actin binding or multimerization. *Mol Biol Cell* **13**, 2383-2396, doi:10.1091/mbc.e02-01-0058 (2002).
206 Skoble, J., Auerbuch, V., Goley, E. D., Welch, M. D. & Portnoy, D. A. Pivotal role of VASP in Arp2/3 complex-mediated actin nucleation, actin branch-formation, and Listeria monocytogenes motility. *J Cell Biol* **155**, 89-100, doi:10.1083/jcb.200106061 (2001).
207 Lanier, L. M. *et al.* Mena is required for neurulation and commissure formation. *Neuron* **22**, 313-325, doi:10.1016/s0896-6273(00)81092-2 (1999).
208 Gupton, S. L. & Gertler, F. B. Filopodia: the fingers that do the walking. *Sci STKE* **2007**, re5, doi:10.1126/stke.4002007re5 (2007).
209 Koleske, A. J. Do filopodia enable the growth cone to find its way? *Sci STKE* **2003**, pe20, doi:10.1126/stke.2003.183.pe20 (2003).
210 Menzies, A. S. *et al.* Mena and vasodilator-stimulated phosphoprotein are required for multiple actin-dependent processes that shape the vertebrate nervous system. *J Neurosci* **24**, 8029-8038, doi:10.1523/JNEUROSCI.1057-04.2004 (2004).
211 Kwiatkowski, A. V. *et al.* Ena/VASP Is Required for neuritogenesis in the developing cortex. *Neuron* **56**, 441-455, doi:10.1016/j.neuron.2007.09.008 (2007).
212 Goh, K. L., Cai, L., Cepko, C. L. & Gertler, F. B. Ena/VASP proteins regulate cortical neuronal positioning. *Curr Biol* **12**, 565-569, doi:10.1016/s0960-9822(02)00725-x (2002).
213 Forrester, W. C. & Garriga, G. Genes necessary for C. elegans cell and growth cone migrations. *Development* **124**, 1831-1843 (1997).
214 Gao, F. B., Brenman, J. E., Jan, L. Y. & Jan, Y. N. Genes regulating dendritic outgrowth, branching, and routing in Drosophila. *Genes Dev* **13**, 2549-2561, doi:10.1101/gad.13.19.2549 (1999).
215 Li, W., Li, Y. & Gao, F. B. Abelson, enabled, and p120 catenin exert distinct effects on dendritic morphogenesis in Drosophila. *Dev Dyn* **234**, 512-522, doi:10.1002/dvdy.20496 (2005).
216 Lin, Y. L., Lei, Y. T., Hong, C. J. & Hsueh, Y. P. Syndecan-2 induces filopodia and dendritic spine formation via the neurofibromin-PKA-Ena/VASP pathway. *J Cell Biol* **177**, 829-841, doi:10.1083/jcb.200608121 (2007).
217 Lin, W. H., Nebhan, C. A., Anderson, B. R. & Webb, D. J. Vasodilator-stimulated phosphoprotein (VASP) induces actin assembly in dendritic spines to promote their development and potentiate synaptic strength. *J Biol Chem* **285**, 36010-36020, doi:10.1074/jbc.M110.129841 (2010).
218 Rostaing, P. *et al.* Analysis of synaptic ultrastructure without fixative using high-pressure freezing and tomography. *Eur J Neurosci* **24**, 3463-3474, doi:10.1111/j.1460-9568.2006.05234.x (2006).

219 Gabel, C. V., Antoine, F., Chuang, C. F., Samuel, A. D. & Chang, C. Distinct cellular and molecular mechanisms mediate initial axon development and adult-stage axon regeneration in C. elegans. *Development* **135**, 1129-1136, doi:10.1242/dev.013995 (2008).
220 Dwivedy, A., Gertler, F. B., Miller, J., Holt, C. E. & Lebrand, C. Ena/VASP function in retinal axons is required for terminal arborization but not pathway navigation. *Development* **134**, 2137-2146, doi:10.1242/dev.002345 (2007).
221 Dent, E. W. & Kalil, K. Axon branching requires interactions between dynamic microtubules and actin filaments. *J Neurosci* **21**, 9757-9769 (2001).
222 Schober, J. M., Komarova, Y. A., Chaga, O. Y., Akhmanova, A. & Borisy, G. G. Microtubule-targeting-dependent reorganization of filopodia. *J Cell Sci* **120**, 1235-1244, doi:10.1242/jcs.003913 (2007).
223 Colavita, A. & Culotti, J. G. Suppressors of ectopic UNC-5 growth cone steering identify eight genes involved in axon guidance in Caenorhabditis elegans. *Dev Biol* **194**, 72-85, doi:10.1006/dbio.1997.8790 (1998).
224 Gitai, Z., Yu, T. W., Lundquist, E. A., Tessier-Lavigne, M. & Bargmann, C. I. The netrin receptor UNC-40/DCC stimulates axon attraction and outgrowth through enabled and, in parallel, Rac and UNC-115/AbLIM. *Neuron* **37**, 53-65, doi:10.1016/s0896-6273(02)01149-2 (2003).
225 Moore, S. W., Tessier-Lavigne, M. & Kennedy, T. E. Netrins and their receptors. *Adv Exp Med Biol* **621**, 17-31, doi:10.1007/978-0-387-76715-4_2 (2007).
226 Forsthoefel, D. J., Liebl, E. C., Kolodziej, P. A. & Seeger, M. A. The Abelson tyrosine kinase, the Trio GEF and Enabled interact with the Netrin receptor Frazzled in Drosophila. *Development* **132**, 1983-1994, doi:10.1242/dev.01736 (2005).
227 Bashaw, G. J., Kidd, T., Murray, D., Pawson, T. & Goodman, C. S. Repulsive axon guidance: Abelson and Enabled play opposing roles downstream of the roundabout receptor. *Cell* **101**, 703-715, doi:10.1016/s0092-8674(00)80883-1 (2000).
228 Yu, T. W., Hao, J. C., Lim, W., Tessier-Lavigne, M. & Bargmann, C. I. Shared receptors in axon guidance: SAX-3/Robo signals via UNC-34/Enabled and a Netrin-independent UNC-40/DCC function. *Nat Neurosci* **5**, 1147-1154, doi:10.1038/nn956 (2002).
229 Wills, Z. *et al.* A Drosophila homolog of cyclase-associated proteins collaborates with the Abl tyrosine kinase to control midline axon pathfinding. *Neuron* **36**, 611-622, doi:10.1016/s0896-6273(02)01022-x (2002).
230 Wills, Z., Bateman, J., Korey, C. A., Comer, A. & Van Vactor, D. The tyrosine kinase Abl and its substrate enabled collaborate with the receptor phosphatase Dlar to control motor axon guidance. *Neuron* **22**, 301-312, doi:10.1016/s0896-6273(00)81091-0 (1999).
231 Lebrand, C. *et al.* Critical role of Ena/VASP proteins for filopodia formation in neurons and in function downstream of netrin-1. *Neuron* **42**, 37-49, doi:10.1016/s0896-6273(04)00108-4 (2004).
232 Aszodi, A. *et al.* The vasodilator-stimulated phosphoprotein (VASP) is involved in cGMP- and cAMP-mediated inhibition of agonist-induced platelet aggregation, but is dispensable for smooth muscle function. *EMBO J* **18**, 37-48, doi:10.1093/emboj/18.1.37 (1999).
233 Halbrugge, M., Friedrich, C., Eigenthaler, M., Schanzenbacher, P. & Walter, U. Stoichiometric and reversible phosphorylation of a 46-kDa protein in human platelets in response to cGMP- and cAMP-elevating vasodilators. *J Biol Chem* **265**, 3088-3093 (1990).
234 Loureiro, J. J. *et al.* Critical roles of phosphorylation and actin binding motifs, but not the central proline-rich region, for Ena/vasodilator-stimulated phosphoprotein (VASP) function during cell migration. *Mol Biol Cell* **13**, 2533-2546, doi:10.1091/mbc.e01-10-0102 (2002).

235 Song, H. J. & Poo, M. M. Signal transduction underlying growth cone guidance by diffusible factors. *Curr Opin Neurobiol* **9**, 355-363, doi:10.1016/s0959-4388(99)80052-x (1999).
236 Robert, X. & Gouet, P. Deciphering key features in protein structures with the new ENDscript server. *Nucleic Acids Res* **42**, W320-324, doi:10.1093/nar/gku316 (2014).
237 Gasteiger, E. *et al.* in *The Proteomics Protocols Handbook* (ed John M. Walker) 571-607 (Humana Press, 2005).
238 Lassmann, T., Frings, O. & Sonnhammer, E. L. Kalign2: high-performance multiple alignment of protein and nucleotide sequences allowing external features. *Nucleic Acids Res* **37**, 858-865, doi:10.1093/nar/gkn1006 (2009).
239 Shen, Y., Maupetit, J., Derreumaux, P. & Tuffery, P. Improved PEP-FOLD Approach for Peptide and Miniprotein Structure Prediction. *J Chem Theory Comput* **10**, 4745-4758, doi:10.1021/ct500592m (2014).
240 Thevenet, P. *et al.* PEP-FOLD: an updated de novo structure prediction server for both linear and disulfide bonded cyclic peptides. *Nucleic Acids Res* **40**, W288-293, doi:10.1093/nar/gks419 (2012).
241 Berman, H. M. *et al.* The Protein Data Bank. *Nucleic Acids Res* **28**, 235-242, doi:10.1093/nar/28.1.235 (2000).
242 Schrodinger, LLC. *The PyMOL Molecular Graphics System, Version 1.8* (2015).
243 Källberg, M. *et al.* Template-based protein structure modeling using the RaptorX web server. *Nat Protoc* **7**, 1511-1522, doi:10.1038/nprot.2012.085 (2012).
244 Scheres, S. H. RELION: implementation of a Bayesian approach to cryo-EM structure determination. *J Struct Biol* **180**, 519-530, doi:10.1016/j.jsb.2012.09.006 (2012).
245 Yuan, B., Latek, R., Hossbach, M., Tuschl, T. & Lewitter, F. siRNA Selection Server: an automated siRNA oligonucleotide prediction server. *Nucleic Acids Res* **32**, W130-134, doi:10.1093/nar/gkh366 (2004).
246 Pettersen, E. F. *et al.* UCSF Chimera--a visualization system for exploratory research and analysis. *J Comput Chem* **25**, 1605-1612, doi:10.1002/jcc.20084 (2004).
247 UniProt Consortium, T. UniProt: the universal protein knowledgebase. *Nucleic Acids Res* **46**, 2699, doi:10.1093/nar/gky092 (2018).
248 Li, M. Z. & Elledge, S. J. Harnessing homologous recombination in vitro to generate recombinant DNA via SLIC. *Nat Methods* **4**, 251-256, doi:10.1038/nmeth1010 (2007).
249 Rueden, C. T. *et al.* ImageJ2: ImageJ for the next generation of scientific image data. *Bmc Bioinformatics* **18**, doi:ARTN 529
10.1186/s12859-017-1934-z (2017).
250 Bolte, S. & Cordelieres, F. P. A guided tour into subcellular colocalization analysis in light microscopy. *J Microsc-Oxford* **224**, 213-232, doi:DOI 10.1111/j.1365-2818.2006.01706.x (2006).
251 Jerabek-Willemsen, M. *et al.* MicroScale Thermophoresis: Interaction analysis and beyond. *Journal of Molecular Structure* **1077**, 101-113, doi:10.1016/j.molstruc.2014.03.009 (2014).
252 Dittgen, T. *et al.* Lentivirus-based genetic manipulations of cortical neurons and their optical and electrophysiological monitoring in vivo. *Proc Natl Acad Sci U S A* **101**, 18206-18211, doi:10.1073/pnas.0407976101 (2004).
253 Zufferey, R. *et al.* Self-inactivating lentivirus vector for safe and efficient in vivo gene delivery. *J Virol* **72**, 9873-9880 (1998).
254 Naldini, L. *et al.* In vivo gene delivery and stable transduction of nondividing cells by a lentiviral vector. *Science* **272**, 263-267 (1996).

255 Kwok, F. & Churchich, J. E. Brain pyridoxal kinase. Purification, substrate specificities, and sensitized photodestruction of an essential histidine. *J Biol Chem* **254**, 6489-6495 (1979).
256 Lineweaver, H. & Burk, D. The Determination of Enzyme Dissociation Constants. *Journal of the American Chemical Society* **56**, 658-666, doi:10.1021/ja01318a036 (1934).
257 Dixon, M. The determination of enzyme inhibitor constants. *Biochem J* **55**, 170-171 (1953).
258 Stark, H. GraFix: stabilization of fragile macromolecular complexes for single particle cryo-EM. *Methods Enzymol* **481**, 109-126, doi:10.1016/S0076-6879(10)81005-5 (2010).
259 Ohi, M., Li, Y., Cheng, Y. & Walz, T. Negative Staining and Image Classification - Powerful Tools in Modern Electron Microscopy. *Biol Proced Online* **6**, 23-34, doi:10.1251/bpo70 (2004).
260 Elsinghorst, P. W., di Salvo, M. L., Parroni, A. & Contestabile, R. Inhibition of human pyridoxal kinase by 2-acetyl-4-((1R,2S,3R)-1,2,3,4-tetrahydroxybutyl)imidazole (THI). *J Enzyme Inhib Med Chem* **30**, 336-340, doi:10.3109/14756366.2014.915396 (2015).
261 Hanna, M. C., Turner, A. J. & Kirkness, E. F. Human pyridoxal kinase. cDNA cloning, expression, and modulation by ligands of the benzodiazepine receptor. *J Biol Chem* **272**, 10756-10760, doi:10.1074/jbc.272.16.10756 (1997).
262 Jones, D. C., Alphey, M. S., Wyllie, S. & Fairlamb, A. H. Chemical, genetic and structural assessment of pyridoxal kinase as a drug target in the African trypanosome. *Mol Microbiol* **86**, 51-64, doi:10.1111/j.1365-2958.2012.08189.x (2012).
263 McCormick, D. B., Gregory, M. E. & Snell, E. E. Pyridoxal phosphokinases. I. Assay, distribution, I. Assay, distribution, purification, and properties. *J Biol Chem* **236**, 2076-2084 (1961).
264 Erickson, H. P. Size and shape of protein molecules at the nanometer level determined by sedimentation, gel filtration, and electron microscopy. *Biological procedures online* **11**, 32-51, doi:10.1007/s12575-009-9008-x (2009).
265 Spencer, R. L. & Bland, S. T. in *Stress: Physiology, Biochemistry, and Pathology* (ed George Fink) 57-68 (Academic Press, 2019).
266 Charlesworth, P., Cotterill, E., Morton, A., Grant, S. G. & Eglen, S. J. Quantitative differences in developmental profiles of spontaneous activity in cortical and hippocampal cultures. *Neural Dev* **10**, 1, doi:10.1186/s13064-014-0028-0 (2015).
267 Cesca, F., Baldelli, P., Valtorta, F. & Benfenati, F. The synapsins: key actors of synapse function and plasticity. *Prog Neurobiol* **91**, 313-348, doi:10.1016/j.pneurobio.2010.04.006 (2010).
268 Palacios, J. M., Mengod, G., Grau, M., Picatoste, F. & Blanco, I. Pyridoxal-5'-phosphate as a cofactor for rat brain histidine decarboxylase. *J Neurochem* **30**, 213-216, doi:10.1111/j.1471-4159.1978.tb07054.x (1978).
269 Manoochehr Messripour, A. M. Effects of Vitamin B6 on the Brain Glutamate Pyrovate Transaminase and Glutamate Oxaloacetate Transaminase in Young and Old Rats. *American Journal of Medicine and Medical Sciences* **2**, 33-35, doi:10.5923/j.ajmms.20120201.07 (2012).
270 Krishnamurti Dakshinamurti, S. D., Michael P. Czubryt. in *Handbook of Famine, Starvation, and Nutrient Deprivation* Ch. Vitamin B6: Effects of Deficiency, and Metabolic and Therapeutic Functions, (2017).
271 Dejanovic, B. *et al.* Exonic microdeletions of the gephyrin gene impair GABAergic synaptic inhibition in patients with idiopathic generalized epilepsy. *Neurobiol Dis* **67**, 88-96, doi:10.1016/j.nbd.2014.02.001 (2014).
272 Rao S. T., R., M. G. Comparison of super-secondary structures in proteins. *J Mol Biol.* **76**, 241-256, doi:10.1016/0022-2836(73)90388-4 (1973).

273 Schwarz, G. *et al.* The molybdenum cofactor biosynthetic protein Cnx1 complements molybdate-repairable mutants, transfers molybdenum to the metal binding pterin, and is associated with the cytoskeleton. *Plant Cell* **12**, 2455-2472, doi:10.1105/tpc.12.12.2455 (2000).
274 Formaneck, M. S., Ma, L. & Cui, Q. Effects of temperature and salt concentration on the structural stability of human lymphotactin: insights from molecular simulations. *Journal of the American Chemical Society* **128**, 9506-9517, doi:10.1021/ja061620o (2006).
275 Chen, W.-Y., Huang, H.-M., Lin, C.-C., Lin, F.-Y. & Chan, Y.-C. Effect of Temperature on Hydrophobic Interaction between Proteins and Hydrophobic Adsorbents: Studies by Isothermal Titration Calorimetry and the van't Hoff Equation. *Langmuir* **19**, 9395-9403, doi:10.1021/la034783o (2003).
276 Jia, H., Liggins, J. R. & Chow, W. S. Entropy and biological systems: experimentally-investigated entropy-driven stacking of plant photosynthetic membranes. *Sci Rep* **4**, 4142, doi:10.1038/srep04142 (2014).
277 Whitesides, G. M. & Krishnamurthy, V. M. Designing ligands to bind proteins. *Q Rev Biophys* **38**, 385-395, doi:10.1017/S0033583506004240 (2005).
278 Eftink, M. R., Anusiem, A. C. & Biltonen, R. L. Enthalpy-entropy compensation and heat capacity changes for protein-ligand interactions: general thermodynamic models and data for the binding of nucleotides to ribonuclease A. *Biochemistry* **22**, 3884-3896, doi:10.1021/bi00285a025 (1983).
279 Olsson, T. S., Ladbury, J. E., Pitt, W. R. & Williams, M. A. Extent of enthalpy-entropy compensation in protein-ligand interactions. *Protein Sci* **20**, 1607-1618, doi:10.1002/pro.692 (2011).
280 Fenley, A. T., Muddana, H. S. & Gilson, M. K. Entropy-enthalpy transduction caused by conformational shifts can obscure the forces driving protein-ligand binding. *Proc Natl Acad Sci U S A* **109**, 20006-20011, doi:10.1073/pnas.1213180109 (2012).
281 Breiten, B. *et al.* Water networks contribute to enthalpy/entropy compensation in protein-ligand binding. *J Am Chem Soc* **135**, 15579-15584, doi:10.1021/ja4075776 (2013).
282 Du, X. *et al.* Insights into Protein-Ligand Interactions: Mechanisms, Models, and Methods. *Int J Mol Sci* **17**, doi:10.3390/ijms17020144 (2016).
283 Ryde, U. A fundamental view of enthalpy–entropy compensation. *Med. Chem. Commun.* **5**, 1324-1336, doi:10.1039/c4md00057a (2014).
284 Shen, M., Stukenberg, P. T., Kirschner, M. W. & Lu, K. P. The essential mitotic peptidyl-prolyl isomerase Pin1 binds and regulates mitosis-specific phosphoproteins. *Genes Dev* **12**, 706-720, doi:10.1101/gad.12.5.706 (1998).
285 Gagnon, J. A. & Mowry, K. L. Molecular motors: directing traffic during RNA localization. *Crit Rev Biochem Mol Biol* **46**, 229-239, doi:10.3109/10409238.2011.572861 (2011).
286 Harrell, J. M. *et al.* Evidence for glucocorticoid receptor transport on microtubules by dynein. *J Biol Chem* **279**, 54647-54654, doi:10.1074/jbc.M406863200 (2004).
287 Akhmanova, A. & Hammer, J. A., 3rd. Linking molecular motors to membrane cargo. *Curr Opin Cell Biol* **22**, 479-487, doi:10.1016/j.ceb.2010.04.008 (2010).
288 Roberts, A. J., Kon, T., Knight, P. J., Sutoh, K. & Burgess, S. A. Functions and mechanics of dynein motor proteins. *Nat Rev Mol Cell Biol* **14**, 713-726, doi:10.1038/nrm3667 (2013).
289 Vallee, R. B., Seale, G. E. & Tsai, J. W. Emerging roles for myosin II and cytoplasmic dynein in migrating neurons and growth cones. *Trends Cell Biol* **19**, 347-355, doi:10.1016/j.tcb.2009.03.009 (2009).
290 Muresan, V. & Muresan, Z. Unconventional functions of microtubule motors. *Arch Biochem Biophys* **520**, 17-29, doi:10.1016/j.abb.2011.12.029 (2012).

291 Hansen, S. D., Zuchero, J. B. & Mullins, R. D. Cytoplasmic actin: purification and single molecule assembly assays. *Methods Mol Biol* **1046**, 145-170, doi:10.1007/978-1-62703-538-5_9 (2013).
292 Hansen, S. D. & Mullins, R. D. VASP is a processive actin polymerase that requires monomeric actin for barbed end association. *J Cell Biol* **191**, 571-584, doi:10.1083/jcb.201003014 (2010).
293 Zacchi, P., Antonelli, R. & Cherubini, E. Gephyrin phosphorylation in the functional organization and plasticity of GABAergic synapses. *Front Cell Neurosci* **8**, 103, doi:10.3389/fncel.2014.00103 (2014).
294 Rui, Y. *et al.* Activity-dependent regulation of dendritic growth and maintenance by glycogen synthase kinase 3beta. *Nat Commun* **4**, 2628, doi:10.1038/ncomms3628 (2013).
295 Benz, P. M. *et al.* Cytoskeleton assembly at endothelial cell-cell contacts is regulated by alphaII-spectrin-VASP complexes. *J Cell Biol* **180**, 205-219, doi:10.1083/jcb.200709181 (2008).
296 Benz, P. M. *et al.* Differential VASP phosphorylation controls remodeling of the actin cytoskeleton. *J Cell Sci* **122**, 3954-3965, doi:10.1242/jcs.044537 (2009).
297 Doppler, H. R., Bastea, L. I., Lewis-Tuffin, L. J., Anastasiadis, P. Z. & Storz, P. Protein kinase D1-mediated phosphorylations regulate vasodilator-stimulated phosphoprotein (VASP) localization and cell migration. *J Biol Chem* **288**, 24382-24393, doi:10.1074/jbc.M113.474676 (2013).
298 Krishnan, K. & Moens, P. D. J. Structure and functions of profilins. *Biophys Rev* **1**, 71-81, doi:10.1007/s12551-009-0010-y (2009).
299 Neuhoff, H. *et al.* The actin-binding protein profilin I is localized at synaptic sites in an activity-regulated manner. *Eur J Neurosci* **21**, 15-25, doi:10.1111/j.1460-9568.2004.03814.x (2005).
300 Chua, J. J. E., Kindler, S., Boyken, J. & Jahn, R. The architecture of an excitatory synapse. *Journal of Cell Science* **123**, 819, doi:10.1242/jcs.052696 (2010).

IX Appendices

IX.1 Appendix I

Table IX.1 BLAST analysis of the VASP shRNA against the mouse RefSeq Database

Target	Description	Identity	Alignment(antisense:5'->3')
NR_104069	*Mus musculus Vasp, transcript variant 4, non-coding RNA*	18	2 cagttgataaccacctgc 19 527 cagttgataaccacctgc 510
NM_001282022	*Mus musculus Vasp, transcript variant 3, mRNA*	18	2 cagttgataaccacctgc 19 527 cagttgataaccacctgc 510
NM_001282021	*Mus musculus Vasp, transcript variant 2, mRNA*	18	2 cagttgataaccacctgc 19 527 cagttgataaccacctgc 510
NM_009499	*Mus musculus Vasp, transcript variant 1, mRNA*	18	2 cagttgataaccacctgc 19 527 cagttgataaccacctgc 510
NM_008466	Mus musculus karyopherin (importin) alpha 3 (Kpna3), mRNA	16	2 cagttgataaccacctg 18 1130 cagttgagaaccacctg 1114
NM_001357251	Mus musculus insulin induced gene 2 (Insig2), transcript variant 5, mRNA	14	4 gttgataaccacct 17 1711 gttgataaccacct 1698
NM_178082	Mus musculus insulin induced gene 2 (Insig2), transcript variant 2, mRNA	14	4 gttgataaccacct 17 1542 gttgataaccacct 1529
NM_001271531	Mus musculus insulin induced gene 2 (Insig2), transcript variant 3, mRNA	14	4 gttgataaccacct 17 1535 gttgataaccacct 1522
NM_133748	Mus musculus insulin induced gene 2 (Insig2), transcript variant 1, mRNA	14	4 gttgataaccacct 17 1778 gttgataaccacct 1765
NM_139304	Mus musculus GATA zinc finger domain containing 2B (Gatad2b), mRNA	14	5 ttgataaccacctg 18 3403 ttgataaccacctg 3416
XR_001778742	PREDICTED: Mus musculus uncharacterized LOC108167577 (LOC108167577), ncRNA	14	5 ttgataaccacctg 18 1053 ttgataaccacctg 1066
XM_030254684	PREDICTED: Mus musculus zinc finger protein 644 (Zfp644), transcript variant X35, mRNA	14	3 agttgataaccacc 16 8975 agttgataaccacc 8988
XM_030254676	PREDICTED: Mus musculus zinc finger protein 644 (Zfp644), transcript variant X19, mRNA	14	3 agttgataaccacc 16 8408 agttgataaccacc 8421
XM_030254675	PREDICTED: Mus musculus zinc finger protein 644 (Zfp644), transcript variant X18, mRNA	14	3 agttgataaccacc 16 8596 agttgataaccacc 8609
XM_030254674	PREDICTED: Mus musculus zinc finger protein 644 (Zfp644), transcript variant X17, mRNA	14	3 agttgataaccacc 16 8543 agttgataaccacc 8556
XM_030254673	PREDICTED: Mus musculus zinc finger protein 644 (Zfp644), transcript variant X16, mRNA	14	3 agttgataaccacc 16 8431 agttgataaccacc 8444
XM_030254672	PREDICTED: Mus musculus zinc finger protein 644 (Zfp644), transcript variant X14, mRNA	14	3 agttgataaccacc 16 8412 agttgataaccacc 8425
XM_030254670	PREDICTED: Mus musculus zinc finger protein 644 (Zfp644), transcript variant X12, mRNA	14	3 agttgataaccacc 16 8600 agttgataaccacc 8613

XM_030254669	PREDICTED: Mus musculus zinc finger protein 644 (Zfp644), transcript variant X11, mRNA	14	3 agttgataaccacc 16 8490 agttgataaccacc 8503
XM_030254668	PREDICTED: Mus musculus zinc finger protein 644 (Zfp644), transcript variant X10, mRNA	14	3 agttgataaccacc 16 8465 agttgataaccacc 8478
XM_030254667	PREDICTED: Mus musculus zinc finger protein 644 (Zfp644), transcript variant X8, mRNA	14	3 agttgataaccacc 16 9106 agttgataaccacc 9119
XM_030254666	PREDICTED: Mus musculus zinc finger protein 644 (Zfp644), transcript variant X7, mRNA	14	3 agttgataaccacc 16 8998 agttgataaccacc 9011
XM_030254662	PREDICTED: Mus musculus zinc finger protein 644 (Zfp644), transcript variant X1, mRNA	14	3 agttgataaccacc 16 8971 agttgataaccacc 8984
XR_867391	PREDICTED: Mus musculus predicted gene, 40078 (Gm40078), transcript variant X3, ncRNA	14	3 agttgataaccacc 16 5569 agttgataaccacc 5582
XR_003954506	PREDICTED: Mus musculus predicted gene, 40078 (Gm40078), transcript variant X2, ncRNA	14	3 agttgataaccacc 16 796 agttgataaccacc 809
XR_003954505	PREDICTED: Mus musculus predicted gene, 40078 (Gm40078), transcript variant X1, ncRNA	14	3 agttgataaccacc 16 1057 agttgataaccacc 1070
XM_030252577	PREDICTED: Mus musculus GATA zinc finger domain containing 2B (Gatad2b), transcript variant X4, mRNA	14	5 ttgataaccacctg 18 3662 ttgataaccacctg 3675
XM_006501361	PREDICTED: Mus musculus GATA zinc finger domain containing 2B (Gatad2b), transcript variant X3, mRNA	14	5 ttgataaccacctg 18 3665 ttgataaccacctg 3678
XM_006501360	PREDICTED: Mus musculus GATA zinc finger domain containing 2B (Gatad2b), transcript variant X2, mRNA	14	5 ttgataaccacctg 18 7939 ttgataaccacctg 7952
XM_006501359	PREDICTED: Mus musculus GATA zinc finger domain containing 2B (Gatad2b), transcript variant X1, mRNA	14	5 ttgataaccacctg 18 7935 ttgataaccacctg 7948
XR_880185	PREDICTED: Mus musculus predicted gene 11525 (Gm11525), transcript variant X3, ncRNA	14	6 tgataaccacctgc 19 2396 tgataaccacctgc 2383
XR_880186	PREDICTED: Mus musculus predicted gene 11525 (Gm11525), transcript variant X2, ncRNA	14	6 tgataaccacctgc 19 3238 tgataaccacctgc 3225
XR_003949764	PREDICTED: Mus musculus predicted gene 11525 (Gm11525), transcript variant X1, ncRNA	14	6 tgataaccacctgc 19 4663 tgataaccacctgc 4650
XM_006529892	PREDICTED: Mus musculus insulin induced gene 2 (Insig2), transcript variant X3, mRNA	14	4 gttgataaccacct 17 5813 gttgataaccacct 5800
XM_006529891	PREDICTED: Mus musculus insulin induced gene 2 (Insig2), transcript variant X2, mRNA	14	4 gttgataaccacct 17 1548 gttgataaccacct 1535
XM_006529889	PREDICTED: Mus musculus insulin induced gene 2 (Insig2), transcript variant X1, mRNA	14	4 gttgataaccacct 17 1562 gttgataaccacct 1549

NM_001271532	Mus musculus insulin induced gene 2 (Insig2), transcript variant 4, mRNA	14	4 gttgataaccacct 17 1402 gttgataaccacct 1389
NM_001166625	Mus musculus chemokine (C-C motif) receptor 9 (Ccr9), transcript variant 1, mRNA	13	5 ttgataaccacct 17 1737 ttgataaccacct 1749
NM_009913	Mus musculus chemokine (C-C motif) receptor 9 (Ccr9), transcript variant 2, mRNA	13	5 ttgataaccacct 17 1669 ttgataaccacct 1681
NM_009305	Mus musculus synaptophysin (Syp), mRNA	13	4 gttgataaccacc 16 942 gttgataaccacc 930
NM_019820	Mus musculus cerebellin 3 precursor protein (Cbln3), mRNA	13	7 gataaccacctgc 19 4286 gataaccacctgc 4274
NM_001081326	Mus musculus amylo-1,6-glucosidase, 4-alpha-glucanotransferase (Agl), transcript variant 1, mRNA	13	3 agttgataaccac 15 555 agttgataaccac 567
NM_001362367	Mus musculus amylo-1,6-glucosidase, 4-alpha-glucanotransferase (Agl), transcript variant 2, mRNA	13	3 agttgataaccac 15 555 agttgataaccac 567
NM_001360117	Mus musculus ribonuclease, RNase A family, 6 (Rnase6), transcript variant 2, mRNA	13	3 agttgataaccac 15 1378 agttgataaccac 1366
NM_026278	Mus musculus Lrp2 binding protein (Lrp2bp), mRNA	13	7 gataaccacctgc 19 3123 gataaccacctgc 3111
NR_153407	Mus musculus ribonuclease, RNase A family, 6 (Rnase6), transcript variant 3, non-coding RNA	13	3 agttgataaccac 15 837 agttgataaccac 825
NM_030098	Mus musculus ribonuclease, RNase A family, 6 (Rnase6), transcript variant 1, mRNA	13	3 agttgataaccac 15 1094 agttgataaccac 1082
XR_871331	PREDICTED: Mus musculus predicted gene, 39451 (Gm39451), ncRNA	13	6 tgataaccacctg 18 6797 tgataaccacctg 6809
XM_006511247	PREDICTED: Mus musculus enhancer of mRNA decapping 3 (Edc3), transcript variant X2, mRNA	13	2 cagttgataacca 14 1086 cagttgataacca 1074
XM_011242760	PREDICTED: Mus musculus enhancer of mRNA decapping 3 (Edc3), transcript variant X1, mRNA	13	2 cagttgataacca 14 1353 cagttgataacca 1341
XR_378911	PREDICTED: Mus musculus Lrp2 binding protein (Lrp2bp), transcript variant X2, misc_RNA	13	7 gataaccacctgc 19 3366 gataaccacctgc 3354
XM_006509483	PREDICTED: Mus musculus Lrp2 binding protein (Lrp2bp), transcript variant X1, mRNA	13	7 gataaccacctgc 19 2796 gataaccacctgc 2784
XM_006502287	PREDICTED: Mus musculus amylo-1,6-glucosidase, 4-alpha-glucanotransferase (Agl), transcript variant X1, mRNA	13	3 agttgataaccac 15 890 agttgataaccac 902
XR_001780981	PREDICTED: Mus musculus predicted gene, 46422 (Gm46422), ncRNA	13	5 ttgataaccacct 17 4393 ttgataaccacct 4381
NM_153799	Mus musculus enhancer of mRNA decapping 3 (Edc3), mRNA	13	2 cagttgataacca 14 1377 cagttgataacca 1365

IX.2 Appendix II

Figure IX.1 Co-localization analysis of VASP and gephyrin in COS-7 cells. *COS-7 cell images of GFP-gephyrin (green)/flag-VASP (red) merged channels. Scale bar, 10 µm.*

VASP/Gephyrin

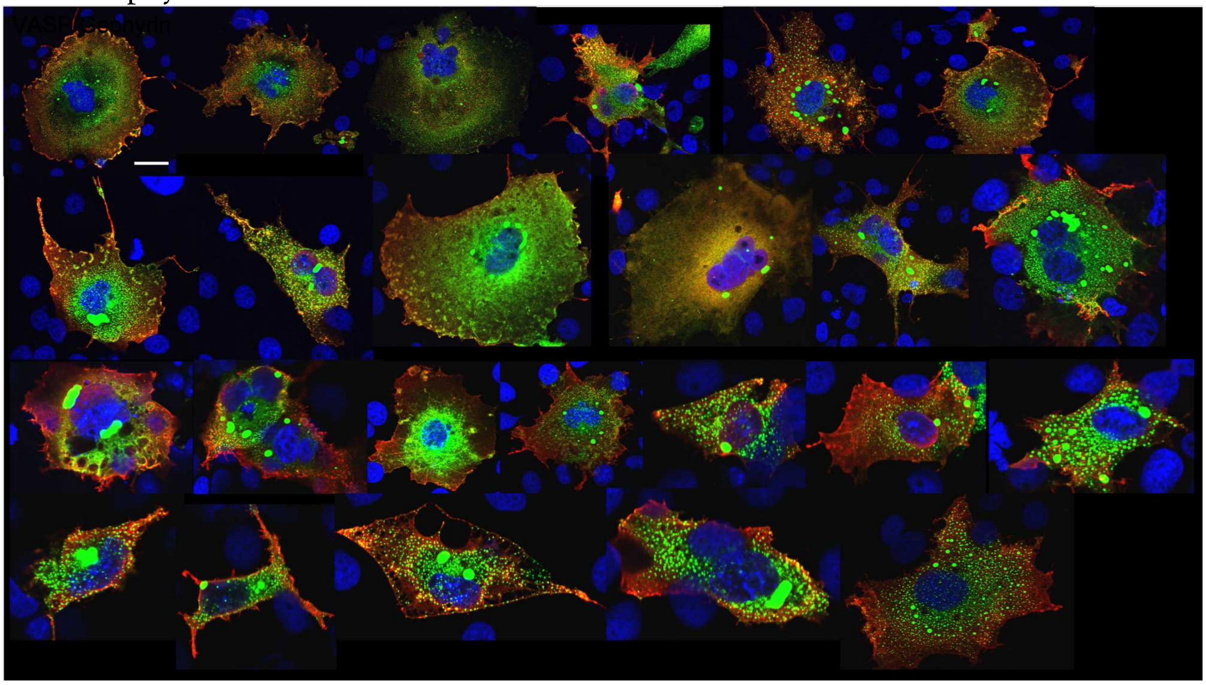

EVH1-PRO/Gephyrin

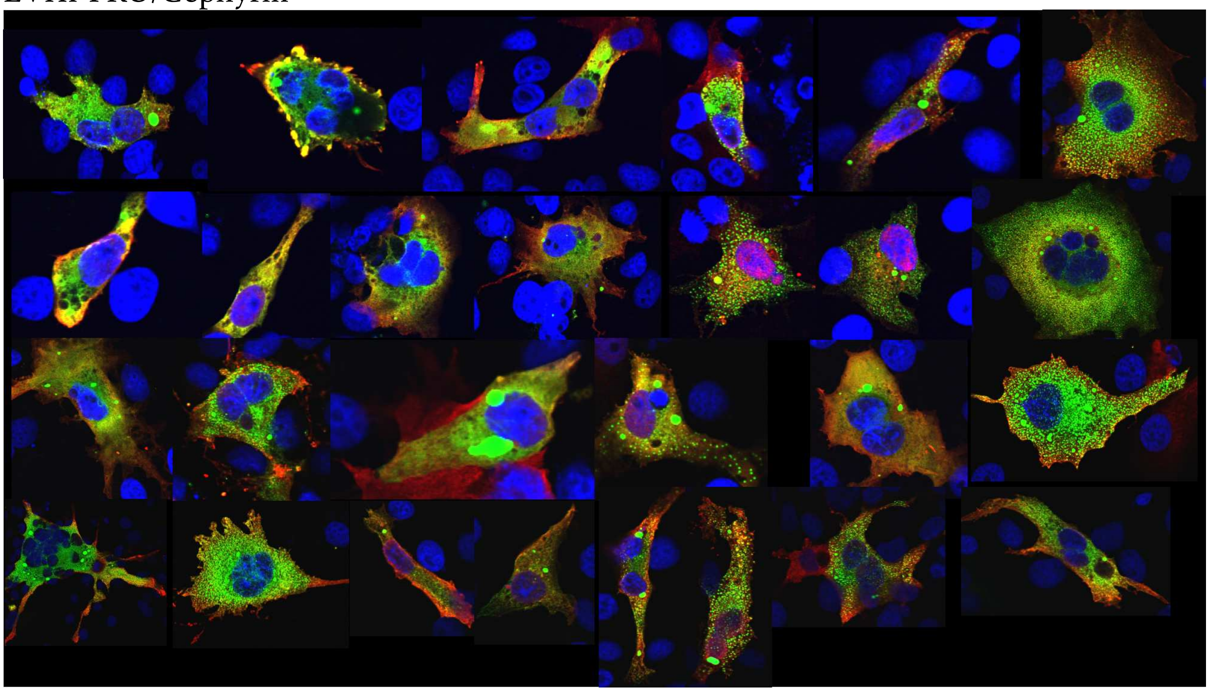

EVH1/Gephyrin

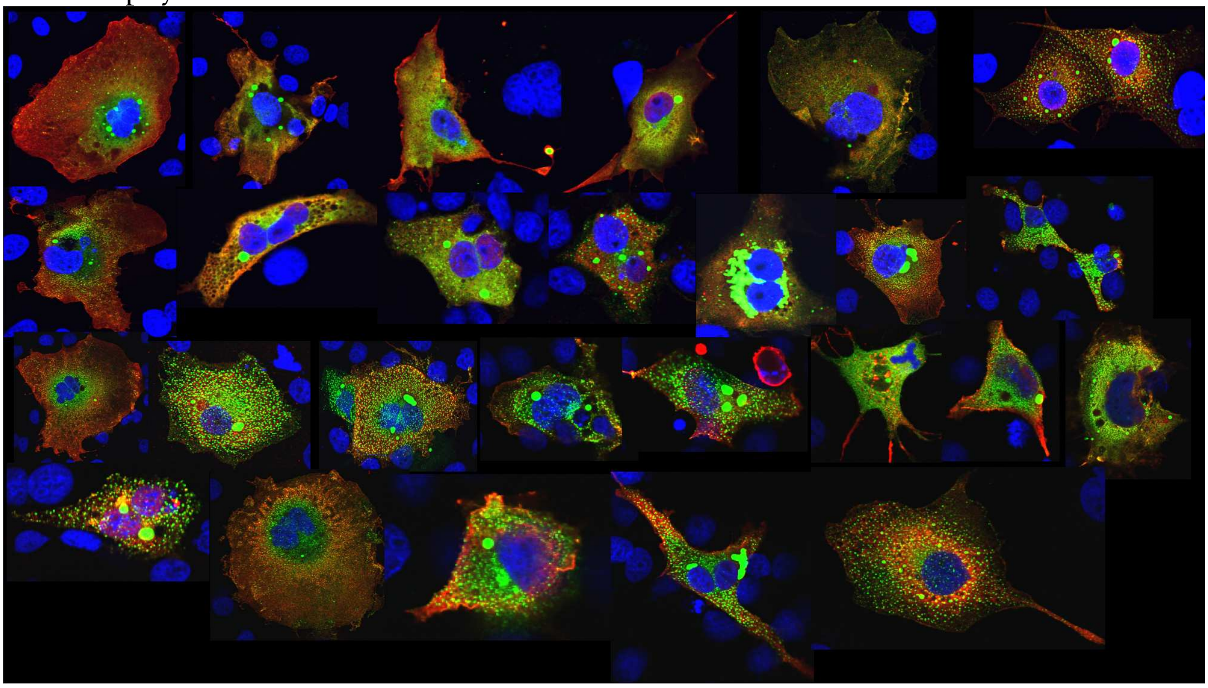

PRO/Gephyrin

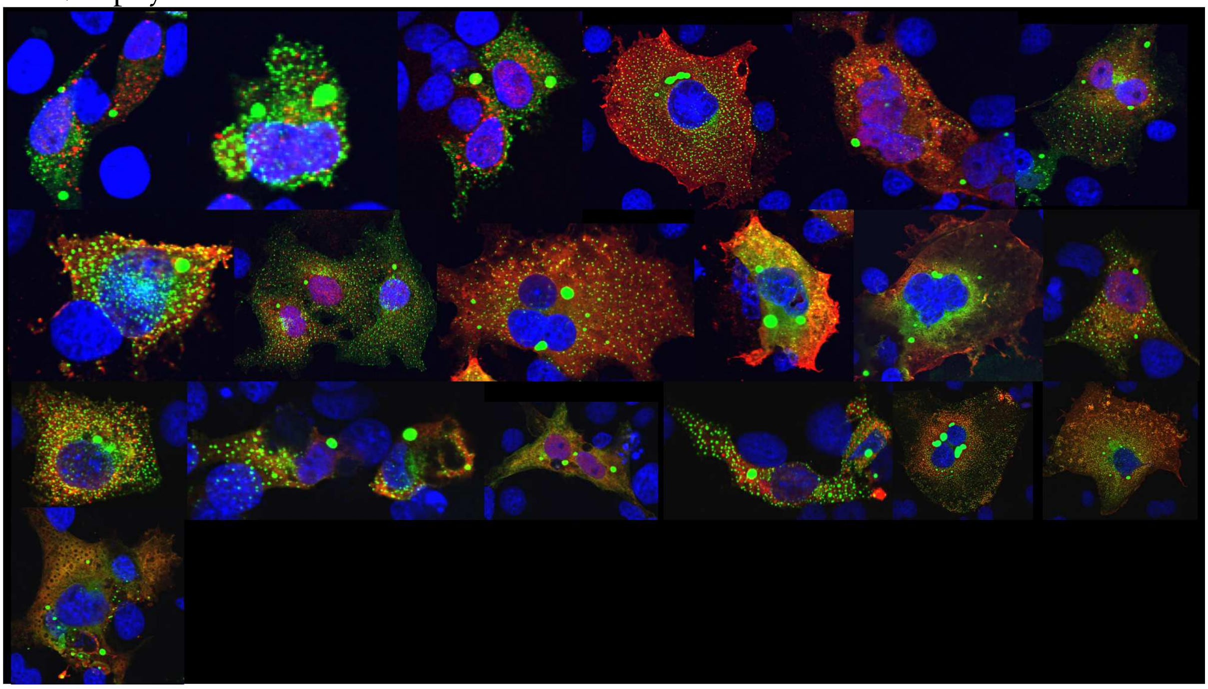

EVH2/Gephyrin

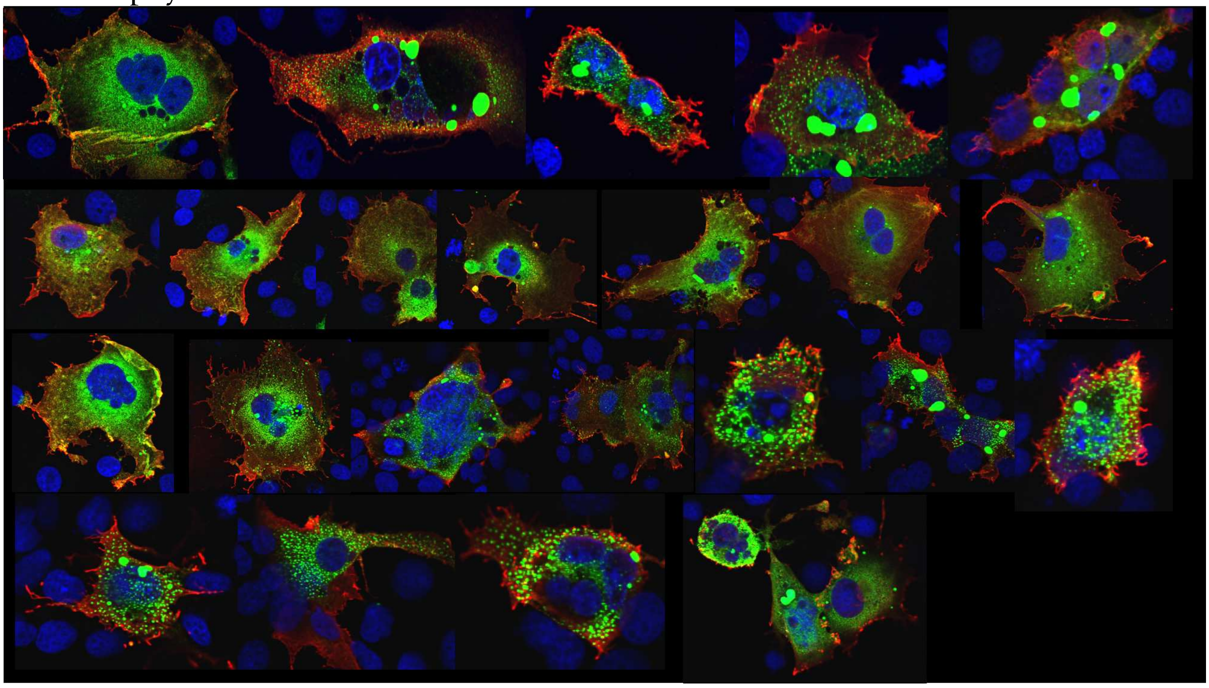

VASPΔ125-144/Gephyrin

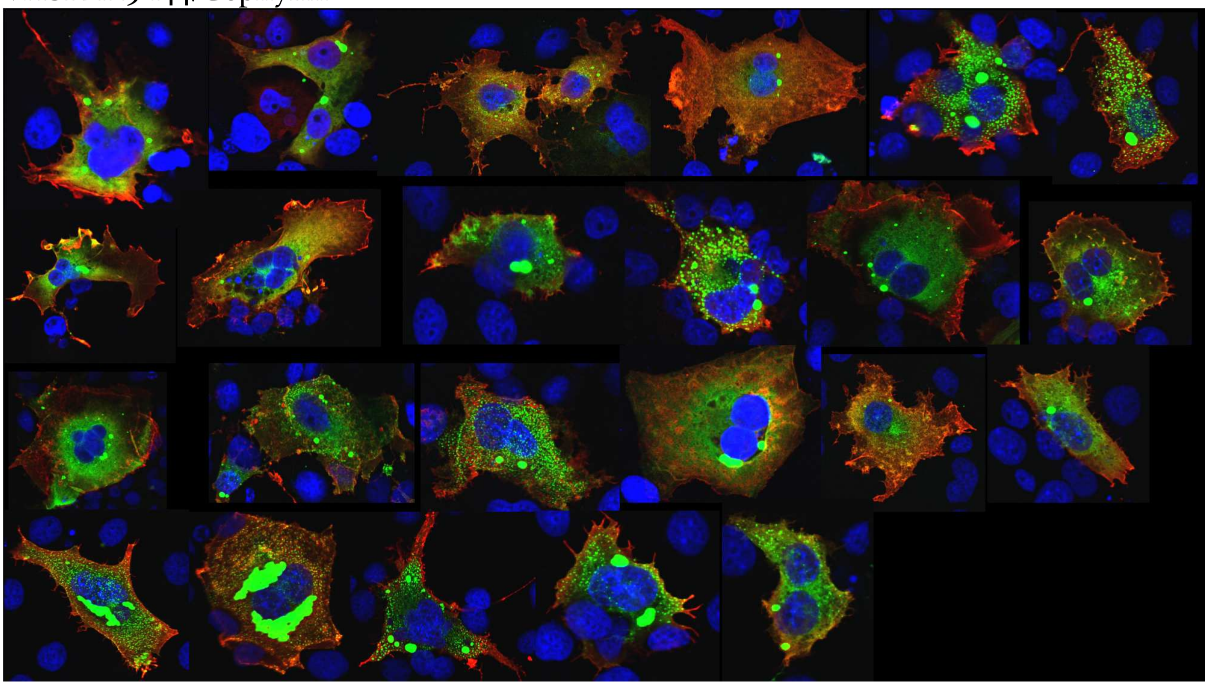

VASP(E136A/E137A)/Gephyrin

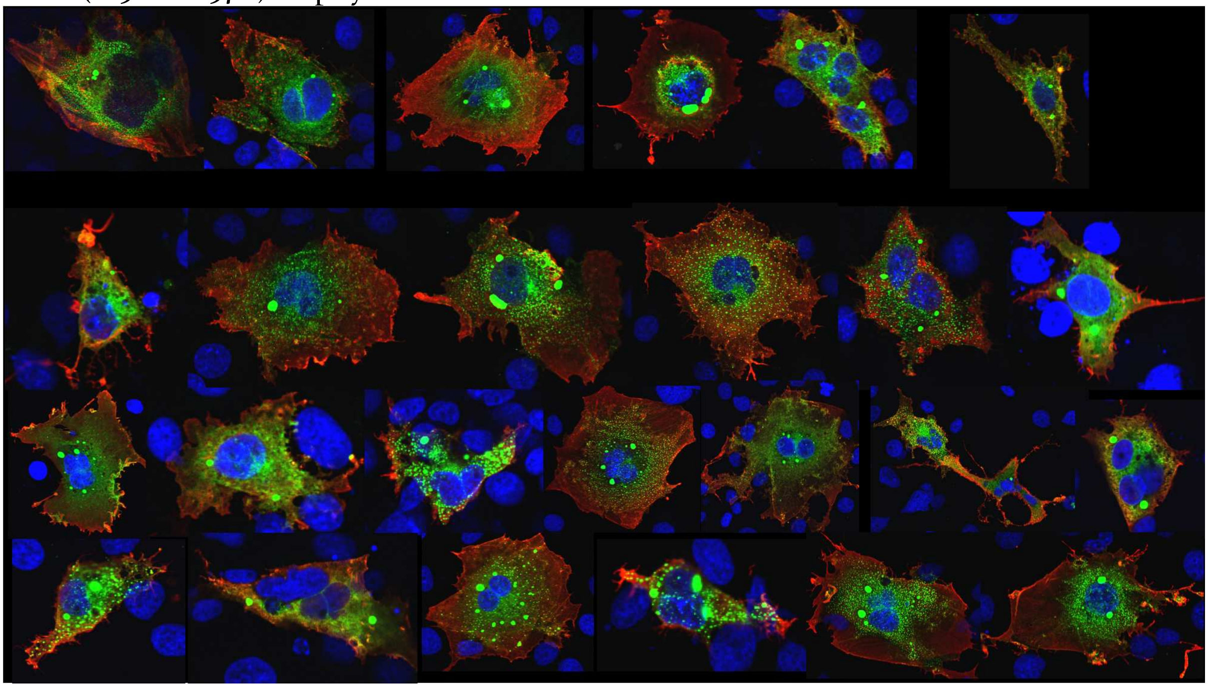

VASP(K142A/Q143A)/Gephyrin

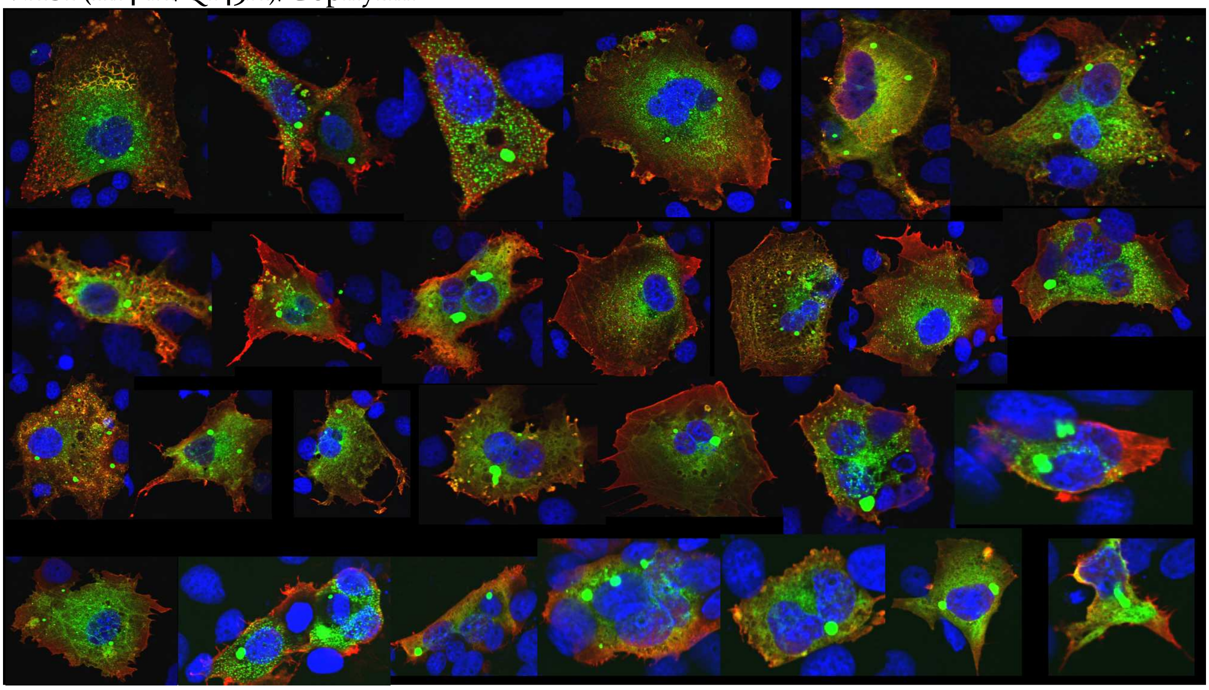

IX.3 Appendix III

Table IX.2 Pearson's coefficients of colocalized VASP (and related constructs) with gephyrin in COS-7 cells.

VASP	EVH1-PRO	PRO	EVH1	EVH2	Δ125-144	E136A/E137A	K142A/R143A
0.385	0.674	0.389	0.123	0.312	0.268	0.221	0.456
0.4	0.653	0.356	0.189	0.316	0.384	0.042	0.303
0.496	0.64	0.65	0.249	0.169	0.122	0.059	0.461
0.557	0.58	0.522	0.286	0.216	0.306	0.194	0.317
0.496	0.607	0.568	0.328	0.184	0.463	0.288	0.357
0.434	0.594	0.473	0.252	0.337	0.057	0.117	0.385
0.381	0.461	0.467	0.182	0.17	0.155	0.137	0.363
0.685	0.289	0.38	0.123	0.219	0.182	0.297	0.308
0.391	0.422	0.447	0.27	0.314	0.328	0.216	0.288
0.562	0.466	0.306	0.307	0.257	0.194	0.282	0.58
0.532	0.204	0.516	0.189	0.223	0.287	0.139	0.465
0.343	0.527	0.465	0.367	0.301	0.02	0.164	0.291
0.325	0.486	0.462	0.235	0.261	0.053	0.114	0.417
0.403	0.523	0.315	0.453	0.169	0.232	0.366	0.372
0.419	0.335	0.47	0.373	0.131	0.411	0.201	0.341
0.31	0.461	0.294	0.182	0.078	0.194	0.098	0.369
0.49	0.523	0.438	0.316	0.179	0.121	0.427	0.344
0.475	0.564	0.548	0.286	0.138	0.333	0.141	0.517
0.576	0.431	0.525	0.344	0.198	0.192	0.206	0.465

0.381	0.281	0.445	0.366	0.302	0.14	0.216	0.387
0.369	0.499	0.377	0.312	0.243	0.18	0.155	0.382
0.408	0.521	0.373	0.302	0.337	0.265	0.285	0.361
0.414	0.457	0.382	0.382	0.314	0.411	0.152	0.456
0.605	0.318	0.537	0.387	0.262	0.136	0.115	0.362
0.652	0.452	0.418	0.392	0.165	0.237	0.334	0.599
0.623	0.607	0.713	0.252	0.313	0.334	0.153	0.58

IX.4 Appendix IV

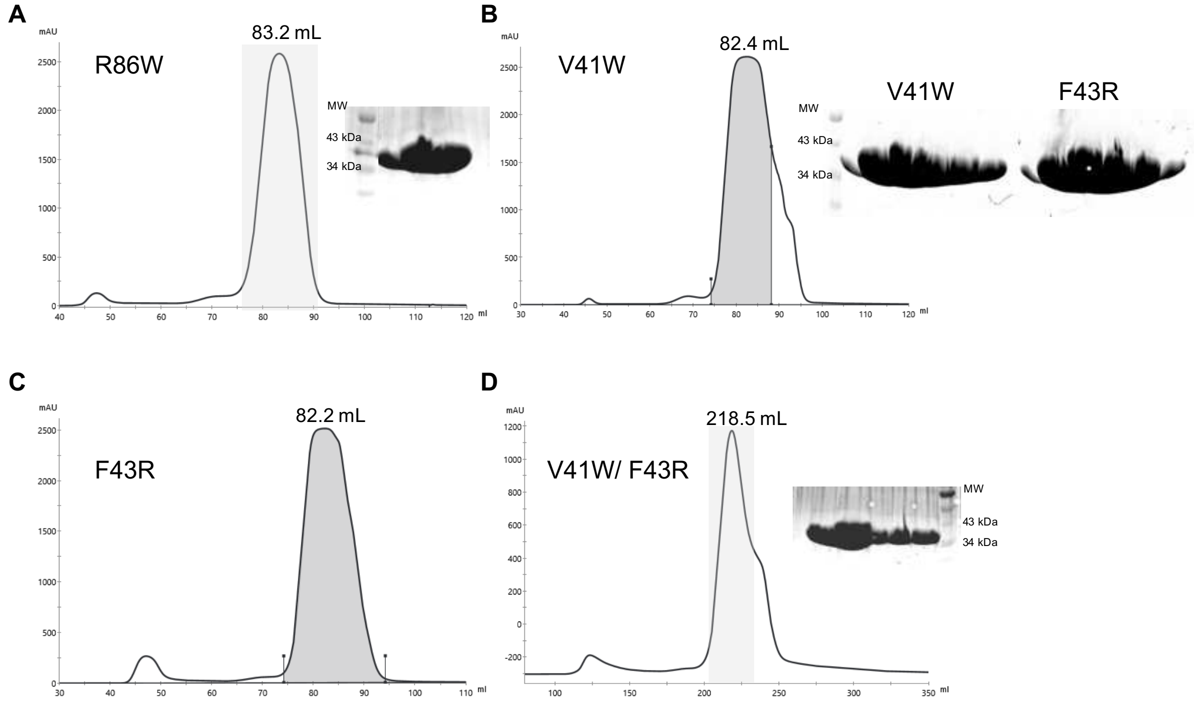

***Figure IX.2 Size exclusion chromatograms of the PDXK mutants used in this study. (A)** R86W, **(B)** V41W, **(C)** F43R, **(D)** V41W/ F43R. Sample purity was analyzed by SDS-PAGE (15% gels) and fractions within the shaded areas were pooled and used in further experiments. Retention times are ~82.5 with SD 200 16/60 (A- C) column and 218.5 mL (D) with the SD 200 26/60 column. This corresponds to 0.67 CV indicating an approximate size of 60 kDa in correspondence with a dimer as expected for PDXK.*

IX.5 List of Abbreviations

Table IX.3 List of abbreviations.

For amino acids, the one or three letter code was used, according to the International Union of Pure and Applied Chemistry (IUPAC) regulations.

Abbreviation	Name
A_{280}	Absorbance at 280
Abl	Abelson tyrosine kinase
ActA	Actin Assembly-inducing protein
AFM	Atomic Force Microscopy
Amp	Ampicillin
AMP-MPT	Adenosine Monophosphate- Metal binding pterin
AMPAR	α-amino-3-hydroxy-5-methyl-4-isoxazole propionic acid receptors
APS	Ammonium persulfate
ARHGEF9	Guanine Nucleotide Exchange Factor Collybistin
aSEC	Analytical Size Exclusion
ATP	Adenosine-5'-triphosphate disodium salt
BLAST	Basic local alignment search tool
BSA	Bovine serum albumin
C. elegans	*Caenorhabditis elegans*
$CaCl_2$	Calcium chloride dihydrate
Cam	Chloramphenicol
CBD	Chitin binding domain
CC	Coiled coil
cDNA	Complementary Deoxyribonucleotide Acid
CIP	Calf intestinal phosphatase
CNS	Central nervous system
Co-IP	Co-Immunoprecipitation
COS-7	CV-1 in Origin with SV40 genes
Cryo-EM	Cryo-electromicroscopy
CV	Column volume
CV-1	*Cercopithecus aethiops* African green monkey fibroblast cell line
D. discoideum	*Dictyostelium discoideum*
D. melanogaster	*Drosophila melanogaster*
DAPI	4', 6-diamidino-2-phenylindole
dATP	2'-Deoxyadenosine 5'-triphosphate, sodium salt
DCC	Deleted in Colorectal Cancer
dCTP	2'-Deoxycytidine 5'-triphosphate, sodium salt
DEAE	Diethylaminoethyl-dextran
dGTP	2'-Deoxyguanosine 5'-triphosphate, sodium salt
DIV	Day *in vitro*
DMEM	Dulbecco's Modified Eagle Medium
DMSO	Dimethyl sulfoxide
DOPA	Aminoacid Dihydroxyphenylalanine, precursor of the neurotransmitters catecholamines
DTT	Dithiothreitol
dTTP	2'-Deoxythymidine 5'-triphosphate, sodium salt

DYNLL-1/2	Dynein LC8 Light Chain
E. coli	*Escherichia coli*
ECD	Extracellular domain
EDTA	Ethylenediaminetetraacetic acid
Ena	Enabled protein
EPSPs	Excitatory postsynaptic potentials
ERK 1/2	Extracellular signal-regulated kinases 1 and 2
EVH1/2	Ena-VASP homology domains 1 and 2
Evl	Ena/Vasp- like protein
FAB	F-actin binding site at EVH2
FCS	Fetal complete serum
FL	Full- length
FP4-Mito	FPPPP-signal peptide to transport to mitochondria
FPLC	Fast protein liquid chromatography
FSC	Fourier Shell Correlation
Fw	Forward primer
GABA	γ-aminobutyric acid
$GABA_A$RAP	$GABA_A$R-associated protein
$GABA_A$Rs	γ-aminobutyric acid type A receptors
GAD	Glutamic Acid Decarboxylase
GephE	E domain of gephyrin
GephG	G domain of gephyrin
GFP	Green Fluorescent Protein
GlyRs	Glycine receptors
GOI	Gen of Interest
GSK 3β	Glycogen Synthase Kinase 3β
HCl	Hydrochloric acid
HEK293	Human embryonic kidney 293
HEPES	4-(2-hydroxyethyl)-1-piperazineethanesulfonic acid
HRP	Horseradish Peroxidase
IgG	Immunoglobulin G
iPSD	Inhibitory Postsynaptic Density
IPSPs	Inhibitory postsynaptic potentials
IPTG	Isopropyl-β-D-thiogalactopyranoside
ITC	Isothermal Titration Calorimetry
IUPAC	International Union of Pure and Applied Chemistry
K_a	Affinity constant
Kan	Kanamycin
KCl	Potassium chloride
K_d	Dissociation constant
KH_2PO_4	Potassium dihydrogen phosphate
K_i	Inhibitory constant
ko	Knock out
L. monocytogenes	*Listeria monocytogenes*
LB-medium	Luria Bertani medium
LIM domain	Lin-11, Isl-1 and Mec-3 domain
ln	Natural logarithm
MA	Magnetic agarose
MALS	Multi-Angle Light Scattering

MEM	Minimal Essential Medium
Mena	Mammalian enabled protein
mEPSCs	miniature Excitatory Postsynaptic Currents
Mg-ATP	Adenosine 5'-triphosphate magnesium salt
Mg_2SO_4	Magnesium sulfate
$MgCl_2$	Magnesium chloride
MgCl2	Magnesium chloride
mGluR	metabotropic Glutamate Receptor
mIPSCs	miniature Inhibitory postsynaptic currents
Moco	Molybdenum cofactor
MOCS1A/1B/2A/2B/3	Molybdenum Cofactor Synthesis 1A/1B/2A/2B/3
m.o.i	Multiplicity of infection
MPT	Metal binding pterin
MST	Microscale Thermophoresis
mTOR	mammalian Target of Rapamycin
Na_2HPO_4	Sodium phosphate dibasic
NaCl	Sodium Chloride
NAGE	Native Agarose gel shift assay
NaOH	Sodium Hydroxide
NCBI	National Center for Biotechnology Information
NEB	New England Biolabs
NH_4Cl	Ammonium Chloride
NS	Negative Stain
OD	Optical density
PCR	Polymerase Chain Reaction
PDB	Protein Data Bank
PDXK	Pyridoxal kinase
PEG	Polyethylene glycol
PFA	Paraformaldehyde
PKA	Protein kinase A
PKG	Protein kinase G
PL	Pyridoxal
pLGIC	pentameric Ligand-gated chloride channels
PLP	Pyridoxal phosphate
PMSF	Phenylmethylsulfonyl fluoride
PNK	Polynucleotide kinase
PRO	Proline-rich region of VASP
PSD	Post-synaptic Density
PSD95	Post-synaptic density protein of 95kDa
PTM	Post-translational modification
qRT-PCR	Quantitative real-time PCR
RS	Restriction Site
Rv	Reverse primer
RVZ	Rudolf Virchow Zentrum
SAXS	Small-angle X-ray Scattering
Scr-shRNA	Scrambled Small hairpin Ribonucleic Acid
SD	Superdex
SDS	Sodium dodecyl sulfate
SDS-PAGE	SDS polyacrylamide gel electrophoresis
SEC	Size Exclusion
Sf9	*Spodoptera frugiperda* 9

SGD	stochastic gradient descent algorithm
SH3	Src-homology 3
SHMT	Serine Hydroxymethyl Transferase
shRNA	Small hairpin Ribonucleic Acid
siRNA	Small interference Ribonucleic Acid
SLIC	Sequence and ligation independent cloning
SV2	Synaptic Vesicle Glycoprotein 2
SV40	Simian Virus 40
TAE buffer	Tris-Acetate-EDTA
TE buffer	Tris-EDTA
TEM	transmission electromicroscope
TEMED	Tetramethylethylenediamin
TIRF	Total Internal Reflection Fluorescence Microscopy
TLE	Temporal Lobe Epilepsy
TLM	G-actin binding site at EVH2
TM	Transmembrane
TMD	Transmembrane domain
Tris	Tris-(hydroxymethyl)-aminomethane
UC	Ultracentrifugation
UCSF	University of California at San Francisco
UV-VIS	Ultraviolet- Visible
VASP	Vasodilator stimulated phosphoprotein
Vel	Turnover ratio or velocity
VSV-G	vesicular stomatitis virus G
WB	Western Blot
wt	Wild type
X. laevis	*Xenopus laevis*
αCAMKII	calcium/calmodulin-dependent protein kinase II
βmE	β-mercaptoethanol
ε_{DNA}	Extinction coefficient of DNA
ξ_{prot}	Extinction coefficient of the protein

List of Figures

List of Tables

List of Publications

1. Vikram Babu Kasaragod*, Anabel Pacios-Michelena*, Natascha Schaefer, Fang Zheng, Nicole Bader, Christian Alzheimer, Carmen Villmann, Hermann Schindelin. Pyridoxal Kinase Inhibition by Artemisinins Downregulates Inhibitory Neurotransmission. bioRxiv 2020.04.05.026310; doi: https://doi.org/10.1101/2020.04.05.026310. (A revised version of the manuscript for PNAS is currently prepared.)

* These authors contributed equally to this work

2. Anabel Pacios-Michelena, Vikram Babu Kasaragod, Hermann Schindelin. Artemisinins and their Impact on Inhibitory Neurotransmission. (Review article, to be submitted to Current Opinion in Pharmacology).

List of International Meetings

Eureka 2019. 14th International GSLS Student Symposium. Poster presentation. Molecular insights into the complex between the vasodilator-stimulated phosphoprotein (VASP) and gephyrin. October 2019.

Meeting in emerging mechanisms for inhibitory synapse plasticity schedule 2018. Poster presentation. Molecular insights into the vasodilator-stimulated phosphoprotein (VASP)-gephyrin interaction. Switzerland, June 2018

Eureka 2018. 13th International GSLS Student Symposium. Poster presentation. Molecular insights into the vasodilator-stimulated phosphoprotein (VASP)- gephyrin interaction. October 2018.

Eureka 2017. 12th International GSLS Student Symposium. Molecular insights into the actin cytoskeleton related proteins interacting with gephyrin. Poster presentation. October 2017.

Eureka 2016. 11th International GSLS Student Symposium. Understanding the molecular basis of actin cytoskeleton related proteins interacting with gephyrin. Poster presentation. October 2016.

Affidavit

I hereby confirm that my thesis entitled **"Molecular insights into the complex formed by the actin cytoskeleton related protein VASP and the inhibitory postsynaptic scaffolding protein gephyrin"** is the result of my own work. I did not receive any help or support from commercial consultants. All sources and/or materials applied are listed and specified in the thesis.

Furthermore, I confirm that this thesis has not yet been submitted as part of another examination process neither in identical nor in similar form.

Würzburg, ...
(Date) (Signature)

Eidesstattliche Erklärung

Hiermit erkläre ich an Eides statt, dass die Dissertation „**Molekulare Einblicke in den Komplex, der durch das mit dem Aktin-Zytoskelett verwandte Protein VASP und Gephyrin, einem Gerüstprotein inhibitorischer postsynaptischer Strukturen, gebildet wird**" eigenständig, d.h. insbesondere selbstständig und ohne Hilfe eines kommerziellen Promotionsberaters, angefertigt und keine anderen als die von mir angegebenen Quellen und Hilfsmittel verwendet zu haben.

Ich erkläre außerdem, dass die Dissertation weder in gleicher noch in ähnlicher Form bereits in einem anderen Prüfungsverfahren vorgelegen hat.

Würzburg, ...
(Datum) (Unterschrift)